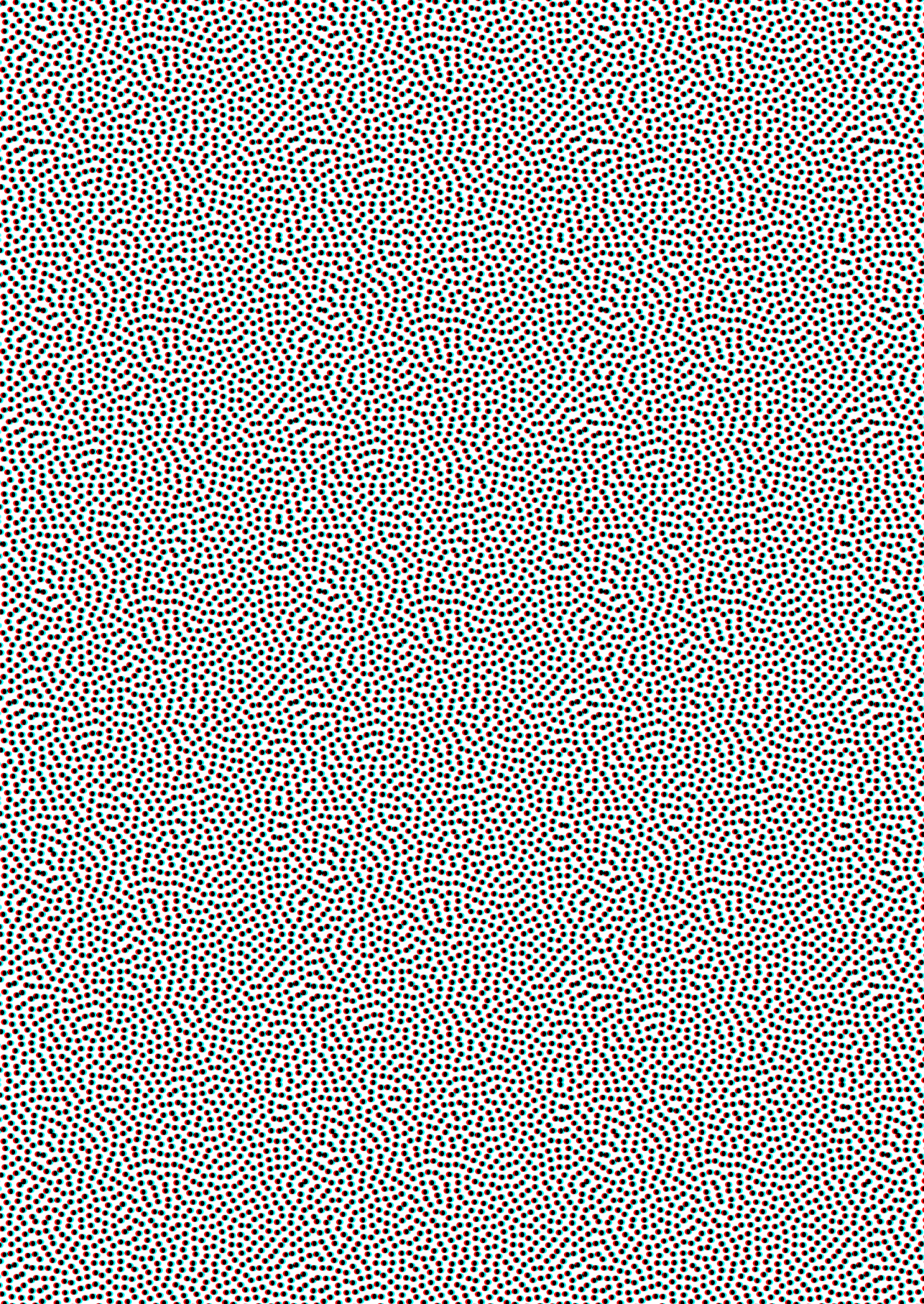


TRAPPING LIGHT IN SOLAR CELLS  
WITH DISORDERED  
HYPERSPPECTRAL UNIFORMITY

ALEXANDER LAMBERTZ





TRAPPING LIGHT IN SOLAR CELLS WITH  
DISORDERED HYPERSPECTRAL UNIFORMITY



UNIVERSITEIT VAN AMSTERDAM

*Trapping Light in Solar Cells with Disordered Hyperspectral Uniformity*

Ph.D. Thesis, University of Amsterdam, March 2026

Alexander Lambertz

ISBN: 978-94-6536-158-1

Cover design by Jan Sobierajski: Front shows the fast-Fourier transform of a hyper-uniform pattern. Backside reveals light coupling to guided mode resonances by this pattern.

The work described in this thesis was performed between November 2021 and March 2026 at NWO-Institute AMOLF, Science Park 104, 1098 XG, and the University of Amsterdam, Science Park 904, 1098 XH, Amsterdam, The Netherlands.

This work is part of the Dutch Research Council (NWO).

A digital version of this thesis is available at:  
<https://ir.amolf.nl> and <https://www.lmpv.nl/Theses/>.

Printed by <https://www.proefschriften.nl>  
Copyright © 2026 by Alexander Lambertz

Trapping Light in Solar Cells with Disordered Hyperspectral Uniformity

ACADEMISCH PROEFSCHRIFT

ter verkrijging van de graad van doctor  
aan de Universiteit van Amsterdam  
op gezag van de Rector Magnificus  
prof. dr. ir. P.P.C.C. Verbeek

ten overstaan van een door het College voor Promoties ingestelde commissie,  
in het openbaar te verdedigen in de Agnietenkapel  
op maandag 22 juni 2026, te 13.00 uur

door Alexander Lambertz  
geboren te Keulen

***Promotiecommissie***

*Promotores:*

prof. dr. E. Alarcón Lladó  
dr. J. van de Groep

Universiteit van Amsterdam  
Universiteit van Amsterdam

*Overige leden:*

prof. dr. A. Polman  
dr. S.A. Mann  
prof. dr. R. Saive  
prof. dr. C. Becker  
  
prof. dr. M.S. Golden

Universiteit van Amsterdam  
Universiteit van Amsterdam  
University of Twente  
Hochschule für Technik und  
Wirtschaft Berlin  
Universiteit van Amsterdam

Faculteit der Natuurwetenschappen, Wiskunde en Informatica

# Contents

<b>1</b>	<b>Introduction</b>	<b>1</b>
1.1	Photonic Innovations in the Quest for Clean Energy	1
1.2	Solar Photovoltaics	4
1.3	Ultrathin Silicon Solar Cells	5
1.4	Disordered Hyperuniformity: Nature's Symphony of Order and Chaos	6
1.5	Outline of the Thesis	8
<b>2</b>	<b>Theoretical Background</b>	<b>11</b>
2.1	Working Principles of Solar Cells	12
2.2	Fundamental Limits to Solar Cells	14
2.3	The Balance between Optical- and Electronic Losses	17
2.4	Light Trapping in Thin Weakly-Absorbing Layers	18
2.4.1	The Yablonovitch (Lambertian) Limit	18
2.4.2	Resonant Scatterers	19
2.4.3	Total Internal Reflection	21
2.4.4	Guided- and Quasi-Guided Modes	22
2.4.5	Momentum of Light and Structure	22
2.5	Ensemble Statistical Properties	25
2.5.1	The Pair-Correlation Function $g_2$	25
2.5.2	The Structure Factor	25
2.5.3	The Power Spectral Density (PSD)	25
2.5.4	Order, Disorder and Hyperuniform Disorder (HUD)	26
2.6	Hyperuniform Disordered Light-Engineered (HUDLE) layers	28
<b>3</b>	<b>Quantifying light coupling to guided modes in semiconductor slabs with arbitrary scattering patterns</b>	<b>31</b>
3.1	Introduction	32
3.2	Results	33
3.2.1	Toolbox for Light Trapping Analysis	35
3.2.2	Principle Demonstration	37
3.2.3	Case Study 1: Impact of Localized Resonances in Scattering Patterns	40
3.2.4	Case Study 2: Modal Coupling in Aperiodic Scattering Arrays	42
3.2.5	Case Study 3: Extracting Coupling Rates and Modal Properties	44
3.3	Conclusions	46
3.4	Methods	46
3.5	Supplementary Information	49
<b>4</b>	<b>Integrating Hyperuniform Disordered Light Trapping Layers in Ultrathin c-Si Solar Cells</b>	<b>53</b>
4.1	Introduction	54
4.2	Results and Discussion	55
4.2.1	Integration of Hyperuniform Nanopatterns into Ultrathin Devices	55
4.2.2	Spectrally-Resolved Characterization	58
4.2.3	Hyperuniform Light-Trapping Mechanism	60

4.2.4	Final Remarks	63
4.3	Conclusion	63
4.4	Materials and Methods	64
4.5	Supplementary Information	67
<b>5</b>	<b>Angular Response Analysis of Ultrathin Solar Cells</b>	<b>75</b>
5.1	Introduction	75
5.2	Results	76
5.2.1	Reflection and Diffraction at Oblique Angles of Incidence	76
5.2.2	Measured and Simulated Angular Photocurrent Response	77
5.2.3	Spectral Response of the Simulated Absorptance versus Angle	79
5.2.4	Effect of AOI on the Visible and Near-Infrared Spectral Ranges	80
5.3	Conclusion	84
5.4	Experimental	84
5.5	Supporting Information	85
<b>6</b>	<b>Self-Assembled HUDLE Patterns</b>	<b>89</b>
6.1	Introduction	90
6.2	Methodology	91
6.2.1	The Phase-Separation Process	91
6.2.2	Impact of Blend Composition	92
6.2.3	Impact of Substrate and Ambient Conditions	95
6.2.4	Selective Dissolution and Etch Transfer	95
6.3	Results	96
6.3.1	Impact on the Light Scattering Properties	97
6.3.2	Tailored Pattern Formation through Process Parameter Variation	98
6.3.3	Enhanced Light Trapping with Self-Assembled HUDLE Patterns	100
6.4	Discussion	103
6.5	Conclusion and Outlook	103
6.6	Experimental	104
6.7	Supplementary Information	109
	<b>List of publications</b>	<b>117</b>
	<b>Author Contributions</b>	<b>119</b>
	<b>Summary</b>	<b>121</b>
	<b>Samenvatting</b>	<b>125</b>
	<b>Acknowledgments</b>	<b>129</b>
	<b>Bibliography</b>	<b>135</b>
	<b>Curriculum Vitae</b>	<b>151</b>

# 1

## Introduction

*“Die Natur kapieren und kopieren (Understand and copy Nature)”*  
— Viktor Schaubberger

### 1.1 Photonic Innovations in the Quest for Clean Energy

Humans live on earth and require energy to live. Energy in the form of biomass for sustenance, hot and cold air for comfort, and electricity to sustain our modern civilization. Though Nature supplies biomass readily without human interaction, the world-wide food, heat and electricity supply all require technologies to secure on-demand availability. Wide-spread adoption of technological advancements and population growth continue to increase the daily world-wide energy demand, rendering energy security one of the great challenges of the 21st century.

The global per-capita primary energy consumption varies widely, from under 5 kWh/day in equatorial regions to over 440 kWh/day in Iceland and roughly 580 kWh/day in Qatar (Fig. 1.1). Today, energy production majorly relies on fossil fuels—finite resources whose extraction grows costlier, scars landscapes, destroys habitats, and produces volatile supply chains. Continued combustion of these fuels has raised atmospheric CO<sub>2</sub> concentrations, accelerates climate change, and threatens planetary habitability [1]. These rising environmental and socio-economic concerns make a shift away from fossil fuels urgent, motivating a widespread effort in harvesting the planet’s renewable energy flows.

The idea to use Earth’s renewable energy to generate electricity is not new. In 1891, Nikola Tesla argued that humanity would eventually “attach their machinery to the very wheelwork of nature” [2]. Five years later, he guided the first large hydroelectric power plant installation near Niagara Falls, which delivered ~ 37 MW of sustainable electricity, followed by a second installation of ~ 40 MW in 1903 [3, 4]. This established hydropower as the main source of electricity until the 1930s [5]. Since then, electricity demand has grown roughly a hundredfold and continues rising with population and technological development [6, 7]. While hydropower is geographically constrained, wind and solar resources can be harvested across much of the globe. Replacing a substantial fraction of fossil energy, therefore requires massive

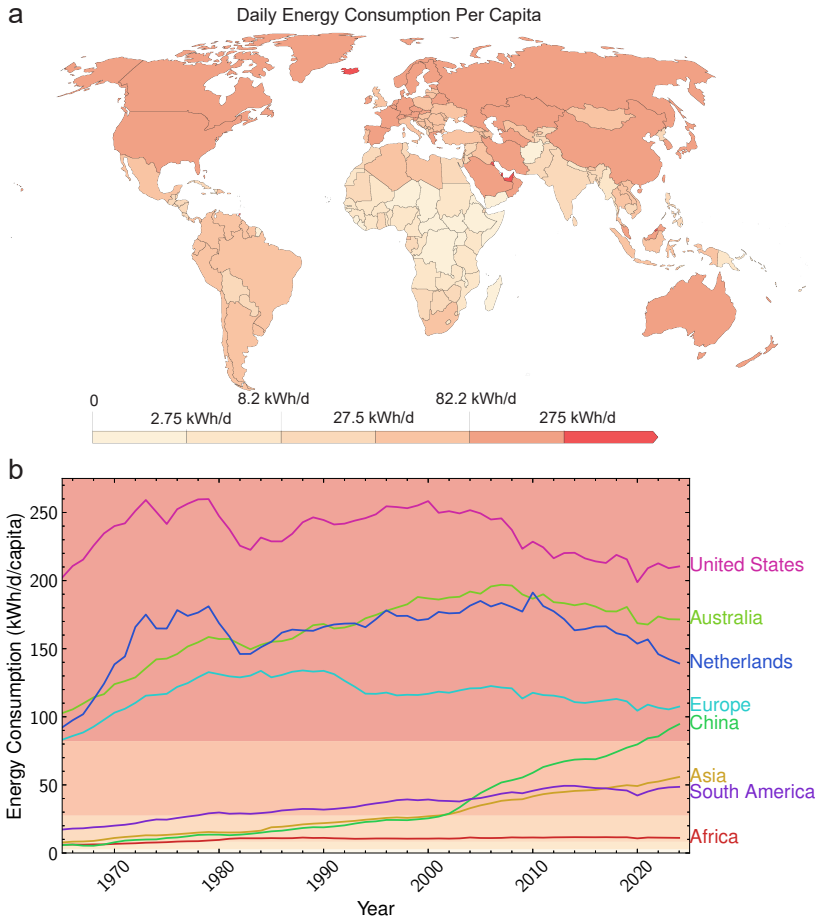


**Figure 1.1: World-wide energy consumption per day and capita**

**a** World map of daily energy consumption per person. **b** Historic trends of daily energy consumption per person for selected regions.

additional renewable capacity—and to avoid past mistakes, it is imperative to do so efficiently, durably, and with recyclable materials. Meeting these simultaneous goals is challenging because the design trade-offs are often antagonistic: higher efficiency can demand more or higher-grade materials, raising cost, complicating manufacturing, and making end-of-life recycling harder. Technological improvements advance slowly to established, low-cost production lines, and especially the highly-concentrated photovoltaic industry creates strong inertia against innovations [8].

Photonics provides a promising route forward. Photonic materials exploit intrinsic light-matter interactions to perform optical and optoelectronic functions without continuous external power input. The field of photonics emerged in the mid-20th century, deriving its name in analogy to electronics: by introducing structures on subwavelength scales, photonic

## 1.1 Photonic Innovations in the Quest for Clean Energy



**Figure 1.2: Photonic solutions improve technology across the bank**

*Photonic concepts applied to devices and their manufacturing process can greatly enhance efficiency and sustainability in the energy sector, urban development, agriculture and electronics/computing devices. Adapted from [9].*

materials engineer optical band structures so that otherwise ordinary materials exhibit sophisticated optical behaviors, mimicking the complexity of silicon-based integrated circuits.

Advances in 21st-century nanofabrication—enabling deterministic patterning at ever smaller scales—have unlocked unprecedented capabilities to improve optoelectronic devices through photonics [10–12], from light management in smartphones and wearables [13] to enhanced radiative cooling for industrially-large heat sinks [10, 14]. Photonic principles harbor benefits throughout renewable-energy technologies and sustainable manufacturing [14, 15]: to improve laser cutting and annealing [11, 16], enable nondestructive quality monitoring [17], and aid characterization of electronic components during production [17, 18]. The range of potential benefits includes broad improved functionality, reduced energy consumption, and simplified production workflows [13, 14, 16] (Fig. 1.2). The advantages of photonics-enhanced concepts are not limited to device- and product performance alone, but can have significant impact on the manufacturing process and lead to a reduction of energy- and material use beyond the field of energy production [15, 16], e.g. in water purification, renewable fuel and chemical production, agriculture, and computing [13, 15]. Photonic solutions can substantially lower society’s future energy demand and help enable a circular, low-waste economy [14, 15].

The introduction of photonics concepts to solar photovoltaics has already demonstrated substantial improvements at laboratory scales [19–21] and will continue to be a central component in the transition required to maintain a habitable environment [22, 23]. To maximize the impact of photonics in the energy production sector, these concepts must be readily implementable in industrial processes [22, 24, 25]. While photonics provide a promising pathway toward a sustainable civilization [23, 26], they cannot generate energy on their own; a robust solar cell manufacturing industry is essential for harnessing this potential in practical applications [22, 27].

## 1.2 Solar Photovoltaics

Solar cells generate electricity wherever sunlight is available, enabling truly decentralized power production and reducing dependence on long transmission networks and complex international supply chains. Their modular design—spanning tiny centimeter-scale cells in calculators up to square-meter modules for rooftops and ground-mounted arrays—lets installations be precisely sized for anything from portable electronics to utility-scale plants. No other renewable source—neither geothermal, wind, nor hydropower—matches the versatility of solar panels across this broad spectrum of energy needs.

In 2024, renewable energy technologies accounted for approximately 32 % of global electricity consumption, marking a record high. This includes 14 % from hydropower, 8 % from wind, 7 % from solar photovoltaics (PV), and 3 % from biomass and waste [28]. Remarkably, power generation from solar PV has doubled roughly every three years since 2016, with a notable increase in 2024 that surpassed all other renewable technologies combined, contributing 485 TWh compared to 432 TWh [28]. These substantial gains highlight the essential role of solar PV in the transition to renewable energy, emphasizing the urgent need for sustainable production methods and effective end-of-life recycling strategies.

Silicon dominates the photovoltaic market, making up about 97 % of production globally [29]. Leveraging advancements from the electronics sector, silicon materials have established a leading position in the solar energy market. Recent improvements have allowed silicon panels to offer warranties that exceed 40 years, providing a significant advantage over wind turbines and other solar technologies. As older solar panels from the early 2000s approach the end of their expected 20-year lifespan, considering their entire life cycle—from production to recycling—is becoming increasingly important. A significant portion of energy consumption and emissions in PV manufacturing stems from wafer production. Currently, nearly all wafers are obtained via the Czochralski method [30–32]. This method entails pulling a mono-crystalline ingot from a liquid pool of highly purified polysilicon, a process that is both slow and energy-intensive. In particular, the energy requirement to achieve higher purities increases markedly; for instance, the energy consumption ranges from 50 to 65 kWh/kg for 9N silicon wafers (99.999999 % purity) to between 65 and 80 kWh/kg for 11N [33]. This substantial energy demand is particularly concerning due to the associated kerf losses during wafer sawing, which lead to the disposal of a significant fraction—up to 45 %—as contaminated waste [34, 35]. Consequently, a considerable portion of the energy utilized in the creation of high-quality wafers is lost. Moreover, since many solar cells are produced using energy derived from fossil fuels, this process presents a contradiction to their sustainability profile.

The cumulatively installed capacity surpassed 2.2 TW of solar energy in 2024 is expected to increase by as much as a factor of 10 by 2050, necessitating a paradigm shift toward more circular solar PV production practices [28, 36]. A key strategy in this transition is to drastically reduce the absorber thickness [37–41]. Reducing the thickness by a factor of 10 or more, not only multiplies the solar cell area per kg silicon, but also offers opportunities to produce wafers more sustainably, or avoid the wafering process altogether. Therefore, a shift in the production towards ultrathin devices could accelerate the transition to sustainable energy production enormously.

### 1.3 Ultrathin Silicon Solar Cells

Reducing the wafer thickness simultaneously lowers manufacturing costs and the material requiring recycling. Further simplifying the device architecture could allow the next generation of silicon-based photovoltaics to significantly reduce their environmental impact while maintaining efficiencies above 20%. From an electronics perspective, thinner layers offer further opportunities to reduce necessary purification levels of the absorber material. When material thickness reaches  $\sim 110\ \mu\text{m}$  or less, alternatives to the energy-intensive Czochralski wafer-fabrication method become economically viable [42]. Exemplary alternatives include epitaxy [43–46], epi-free [47], Si spalling [48], and stress-induced lift-off [49]. Figure 1.3 compares the efficiencies of solar modules versus absorber thickness for different carrier lifetimes [40]. The module efficiencies correspond to advanced hetero-junction concepts such as SHJ [50, 51] and TOPcon [52, 53]. In these high-efficiency devices, the bulk carrier lifetime becomes a significant limitation for thick active layers. For a moderate lifetime of 1 ms, the optimum thickness measures  $50\ \mu\text{m}$  and thicker layers lead to a reduction in module efficiency. Interestingly, in the limit of very thin absorbers  $t \sim 10\ \mu\text{m}$ , the curves of different carrier lifetime collapse into a small range of module efficiency variation, highlighting that the efficiency of ultrathin devices depends only little on the bulk crystal quality. This is significant, since it suggests that ultrathin solar cells could be manufactured with lower-grade silicon as a starting material, opening the possibility to recycle de-commissioned solar modules into new ultrathin devices with comparable performance characteristics [54].

Nonetheless, thinner materials present challenges; reduced thickness leads to diminished light absorption and lower current production. The indirect band gap in crystalline silicon entails poor absorption characteristics near its band gap ( $\lambda \sim 1100\ \text{nm}$ ), requiring layers of substantial thickness to absorb 99% the usable solar irradiance (Fig. 1.4a). In fact, to reach this level of absorptance close to the band gap, the required thickness of material exceeds 1 mm. With only one micrometer of absorber thickness, the absorption of wavelengths  $\lambda \gtrsim 425\ \text{nm}$  is incomplete and substantially limits performance (Fig. 1.4b). Throughout the wavelength range  $400\ \text{nm} \leq \lambda \leq 1100\ \text{nm}$ , a flat slab of  $1\ \mu\text{m}$  (blue) only absorbs  $\sim 38\%$  on average. This persistent challenge continues to oppose the transition to ultrathin wafers in the photovoltaics industry, despite substantial achievements at laboratory scales to increase

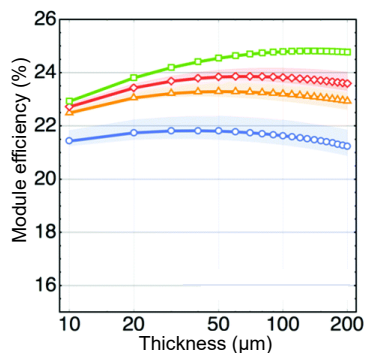


**Figure 1.3: Silicon PV module efficiency versus thickness**

Module efficiency is plotted for different crystal qualities, which are quantified by their bulk carrier lifetimes: 5 ms (green), 1 ms (red), 500  $\mu\text{s}$  (orange), and 100  $\mu\text{s}$  (blue). Adapted from [40].

## Introduction

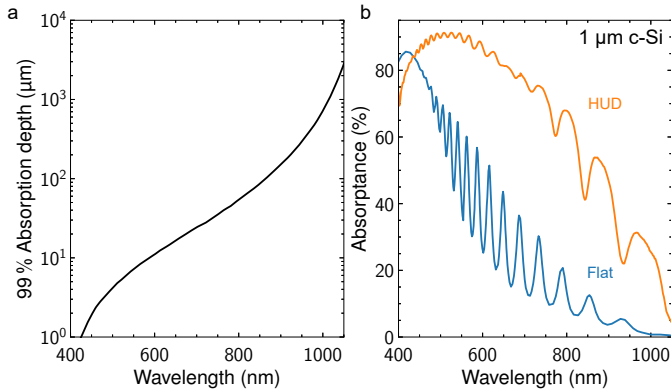


**Figure 1.4: Ultrathin silicon absorbers.**

(a) Absorber thickness versus wavelength, showing the required thickness to absorb 99% in crystalline silicon. (b) Experimentally measured absorbance in a 1 μm-thick silicon layer versus wavelength, where the front side is either flat (blue) or patterned (orange). Published among others by the author in [55].

absorbance through the introduction of photonics-enhanced scattering structures.

Particularly, a combination of photonics principles with an extraordinary class of structures has recently shown record absorbance in substrates of this thickness (orange) [55]. This class bridges seemingly opposing concepts of order and disorder into a third type of matter states: disordered hyperspectral uniformity, or hyperuniform disorder (HUD) for short. The intrinsic correlations within these apparently chaotic yet homogeneous arrangements harbor exciting abilities when integrated with light management schemes, leading to an average absorbance of ~ 61 %, thus a relative improvement greater than 60 % compared with a flat layer. As this marks only the first step towards highly-efficient ultrathin solar cells, a complete device that proves these enhancements experimentally is highly sought after. In this thesis, we set out to realize this dream and strive towards a deeper understanding of HUD and its benefits, which continue to be unveiled.

## 1.4 Disordered Hyperuniformity: Nature's Symphony of Order and Chaos

While exceptional performance improvements have been achieved with the implementation of photonic nanostructures into photovoltaic devices, most of these have focused on producing either highly-ordered arrays of identical unit elements, or instead using fully random patterning approaches. Recently, however, a third class of materials has attracted interest from many different scientific disciplines, which can be regarded as a mixture of these polar opposites, or a bridge between order and chaos: disordered hyperuniformity. Though omnipresent in Nature, its 'hidden' order has kept it camouflaged in plain sight for centuries of scientific investigation, and since its discovery, signatures of hyperuniformity continue to be revealed in the most unexpected realms of the physical world.

The principles behind hyperuniformity are literally universal- found in the formation

## 1.4 Disordered Hyperuniformity: Nature's Symphony of Order and Chaos

of galaxies and aggregates of stars as well as in the early stages of the universe itself [56, 57]. Hyperuniformity extends from these astronomical scales down to atomic dimensions. For instance, a single atomic layer (2D material) of amorphous silicon dioxide [58] (quartz glass) exhibits the same property: a suppression of density fluctuations at large length scales. Before we turn to mathematical descriptions (in Chapter 2), however, let us consider further examples in Nature to gain an intuitive understanding and discover the qualitative criteria indicative of a hyperuniform distribution. In the biological world, disordered hyperuniformity is commonly encountered and continues to be discovered in more unexpected locations, such as butterfly wings [59], bacterial motility [60], cellular geometries [61], and the webbing of biological tissues [62]. A most striking example was found in the eyes of a chicken. To evenly distribute color receptors on the retina, evolution has exploited the characteristic optical properties of this extraordinary class. Qualitatively, HUD can be described by the simultaneous fulfillment of requirements considering vastly different length scales: at long range, they homogeneously fill all regions while avoiding falling into any sort of apparent ordering. At short distances, HUD locations appear fully random, yet never violate a minimum separation among each other. Translated to the locations of color receptors in the chicken's eye, these rules assure the presence of a receptor close to any location on the retina on the one hand. On the other hand, there is a minimum separation distance between identical receptor types. The absence of long-range order is crucial as it would produce unwanted diffractive effects impeding image clarity, while a pair of closely-spaced receptors would enable cross talk and limit the spatial resolution of the bird's vision [63].

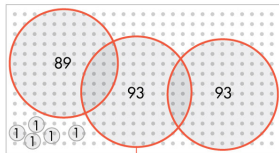
This qualitative description is illustrated by a so-called "ring-toss" experiment (Fig. 1.5). We start with the ordered lattice (left). Where ever we draw a circle of a certain radius within the periodic distribution, the number of points within the circle will show only small variations. As we decrease the radius towards the dimensions of the unit cell, these variations will become smaller since they occur around the circumference of the circle, which shrinks in proportion to the radius. In a (Poisson) random distribution, great variation is observed at all length scales (circle diameters). In this case, the variance is proportional to the area of the ring and grows quadratically in two dimensions. Finally, in a hyperuniform distribution (right), we find variations similar to the random distribution when the drawn circle is small, but

### FINDING HIDDEN ORDER

Imagine repeatedly tossing a ring onto a field of dots and counting the number of whole dots inside the ring each time it lands.

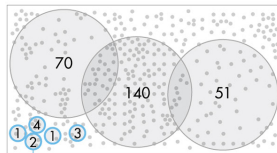
#### Ordered lattice

The number of enclosed dots per ring toss varies more for large rings than for small rings. This is because all the variation occurs along the ring's edge and so is proportional to the ring's perimeter.



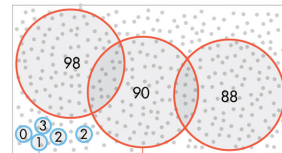
#### Random distribution

The variation in the number of enclosed dots is proportional to the ring's area, since the density of dots varies throughout the ring. This means the variation can become extreme on large scales.



#### Hyperuniform distribution

For small rings, the variation is similar to that of a random distribution. But the variation is proportional to the ring's perimeter rather than its area, so for large rings, the variation resembles that of a lattice.



Similar variance in number of dots per large ring toss

Similar variance per small ring toss

**Figure 1.5: Ring-toss experiment**

This experiment illustrates the variance dependence on length scales in ordered, disordered, and hyperuniform-disordered ensembles. Adapted from [64].

## Introduction

as the diameter grows, the variance grows more slowly than the circle area. At large length scales, the variations are more comparable to the periodic case. This indicates a constraint randomness, or correlated disorder, leading to a homogeneous distribution of points- yet absent of perfect order. This property has profound impact on the photonic functionality of a scattering layer when the scattering objects are arranged in such a way, and has demonstrated record-shattering absorptance enhancements when applied to an ultrathin film of crystalline silicon (Fig. 1.4). In this thesis, we explore the advantages of hyperuniform disorder when applied to ultrathin silicon solar cells.

## 1.5 Outline of the Thesis

In this thesis, we set out to realize ultrathin silicon solar cells with hyperuniform light trapping, and strive towards a deeper understanding of HUD and its benefits, which continue to be unveiled. What are the mechanisms within HUD that enable very high absorptance? Does the greater absorptance similarly improve power conversion efficiency in actual devices? How would such devices compare with solar cells featuring ordered arrays, and what implications arise under real-world conditions? How can we implement these structures at scales relevant for the photovoltaics industry?

To explore these questions, we begin by deepening our understanding of light-matter interactions, photonics principles, and ensemble statistics (**Chapter 2**). In this chapter, we further introduce crucial metrics and characterization methods to describe and evaluate the complex optical responses involving disordered nanostructures.

Next, as many questions remain open, and analytical tools so far insufficiently describe the intricate relations of light-matter interactions in photonic devices, we establish a numerical toolbox to analyze and quantify light propagation and absorption in arbitrarily complex device stacks (**Chapter 3**). Here, we take the Fourier perspective to elucidate the connection between the geometry of a scatterer, their mutual spatial arrangement, and the momentum distribution of the trapped and absorbed light. These insights establish disordered hyperuniformity as a promising approach for improving light absorption in weakly-absorbing substrates, such as ultrathin solar cells.

In **Chapter 4**, we design and fabricate 4.8  $\mu\text{m}$ -thin silicon solar cells with periodic and hyperuniform-disordered photonic structures, and study the effect of different pattern types on the absorption and conversion efficiencies of a large number of identical devices. The optoelectronic characterization reveals significant differences between periodic- and HUD-type solar cells. It shows substantial improvements in HUD-type cells over periodic ones, particularly in spectral regimes where incomplete absorption challenges performance.

To assess the effectiveness under real-world conditions, we explore the angular response of these devices in **Chapter 5**, which provides insights into the electricity production throughout the solar cycle of one day. Once more, marked differences between order and disorder arise in these measurements, revealing an important contradiction in the design of photonic nanopatterns that is typically overlooked: the simultaneous optimization for normal incidence and a balanced angular response leads to opposing design directives.

Finally, for the successful implementation of our findings into solar cell manufacturing processes at industrially relevant scales, we explore an alternative to the slow and costly nanolithographic fabrication of HUD structures. In **Chapter 6**, we adopt a large-area self-assembly method based on phase-separated immiscible polymer blends, which have shown the ability to produce near-hyperuniform structures. Advancing on previous studies of these systems, we design and build a controlled-atmosphere enclosure to ensure identical

starting conditions between deposition runs. With this improved stability of the process, we identify critical macroscopic parameters that enable tuning of morphological and nanoscale properties of the formed layers. When the patterns are transferred into a substrate, these changes translate to tailorable light scattering properties, suitable to enhance absorption in ultrathin Si slabs. Our findings extend beyond photovoltaic devices and silicon as the primary material, which opens up opportunities to simultaneously simplify and optimize other mass-produced optoelectronic devices.

In summary, we first develop a numerical toolbox to reveal the underlying mechanisms of the exceptional light-matter interactions observed in disordered hyperuniform device layers, which enables characterization and optimization of all kinds of scattering layers for optically active devices. Subsequently, by fabricating a large number of ultrathin solar cells incorporating HUD designs as well as periodically-patterned and flat reference cells, we demonstrate the superior ability of HUD to trap and utilize photons otherwise lost to incomplete absorption. The performance metrics strongly depend on the angle of incidence of light, and the simultaneous optimization of trapping layers for oblique and normal incidence requires careful design of the momentum-space of ensembles, which we prove with a series of experiments and simulations at oblique insolation conditions. Finally, to maximize the ultimate impact of our findings, we replace slow nanolithography with a self-assembly method to obtain comparable HUD designs at large scales, where we demonstrate effortless tunability of the scattering response by simple alterations of process conditions and chemical compositions. Altogether, this work provides fundamental insights into real device performance with disordered hyperuniform concepts, and lays significant groundwork for the economical production of highly-efficient ultrathin silicon solar cells, which can revolutionize the photovoltaics landscape within the next generation.



# 2

## Theoretical Background

This chapter aims to briefly summarize and deepen physical and mathematical concepts which are relevant for the understanding of light-matter interaction in thin slabs exhibiting weak absorption. We begin with a description of (silicon) photovoltaics, where we introduce the basic working principles, operating conditions, and fundamental limits. To approach these limits, we highlight the trade-off between optical and electronic performance, which impacts any optoelectronic device, and motivate a necessity for better understanding of nanophotonic light-matter interactions and engineered scattering layers. A scattering layer can be understood as a combination of microscopic features describing the nanoscale properties (i.e. form factor), and the structural correlations arising at large length scales (i.e. structure factor). Both form- and structure factor influence light scattering properties and relate to each other, rendering suitable analysis tools vital to elucidate the consequences of particular design choices. To analyze these individually, we first investigate the scattering properties of an exemplary Si cylinder isolated in air. Since we are interested in the capabilities of a specific scattering morphology to enhance absorptance in thin weakly-absorbing layers, we next investigate (quasi-)guided-mode dispersion in thin slabs. Light trapping describes the coupling of external radiation into these guided modes and requires efficient and targeted diffraction, which depends on the spatial-frequency content of a scattering layer at short and long distances. Here, we analyze spatial momentum maps of different particle distributions by their correlations, structure factor, and power-spectral density, which afford complementary insights into the full scattering response of tailored nanopatterns. Finally, we motivate hyperuniform disorder combined with resonant nanostructures for highly-efficient, broadband scattering layers for implementation in ultrathin solar cells.

## 2.1 Working Principles of Solar Cells

The conversion of energy carried by light to an electric current can be summarized in a few steps. (1) Absorption of light in the semiconductor material creates an electron-hole pair, where the hole represents an available (empty) bound electronic state. (2) The electron and hole are separated from each other and diffuse to specific regions, which allow entry only to one type of charge (positive holes or negative electrons). (3) The charges are extracted by individual conductors that are connected through an external circuit. (4) The extracted charges produce a current in the external circuit, deliver their energy to the circuit load, and recombine at the opposite terminals of the solar cell.

Many different architectures that fulfill these basic requirements have been conceived and more are continuously being developed to improve the extraction potential while reducing resistance and other loss mechanisms. For step (1), a semi-conducting material is required with a band gap energy that can be overcome by solar radiation. The charge separation in step (2) can be achieved by e.g. doping (homojunction), thus introducing foreign elements into the semiconductor, which in turn favors one type of charge over the other. Alternatively, the semiconductor can be combined with another (semi-conducting) material, which likewise preferably allows one carrier type only (heterojunction). Finally, as a third option, step (2) and (3) can be combined by employing so-called selective contacts, which simultaneously separate and extract charges from the bulk semiconductor material. In chapter 4, we fabricate an ultrathin solar cell that combines several of these ideas with crystalline silicon as the semiconductor.

The band diagram of our solar cell is sketched in Fig. 2.1, with an undoped (intrinsic, i-Si) layer at the center making up the bulk of the semiconductor material. Towards the extremities at the left and right side, the silicon is p- and n-doped, respectively, which initiates charge separation of electron-hole pairs created in the bulk region. The excitation of a bound electron by sunlight is visualized by an arrow ( $\lambda$ ), which excites a negatively charged electron ( $e^-$ ) from its bound state in the valence band (lower black line) to the conduction band (upper black line) and leaves a hole ( $h^+$ ) in the valence band. The electron and hole diffuse to the cathode and anode, respectively, accelerated by the relative difference in doping levels, which is indicated by the bending bands, where electrons prefer downhill while holes traverse in the upwards direction towards their respective Fermi levels (horizontal dashed lines). The Fermi energy is split into positive ( $E_{Fp}$ , red) and negative ( $E_{Fn}$ , blue) quasi Fermi levels by the presence of (photo-)excited carriers. At the anode side, an additional layer of  $\text{NiO}_x$  acts as a selective contact, which blocks the entry of electrons (indicated by a reversing arrow). The terminals are connected by the external circuit (green solid line) through which charge carriers flow, power the load (e.g. a fan shown at the bottom), and ultimately recombine at the opposite terminal. This completes the circuit and the recombined charge carriers are ready to be excited again by an incoming photon. Ergo, the solar cell.

In this thesis, we use crystalline silicon due to its abundance, low-cost, stability, non-toxicity, and established position in the solar industry. A number of alternative semiconductor materials aim to rival silicon-based technology in the market, promising high-efficiency, lightweight, cheap, and easy-to-fabricate solar panels. Matching the benign, omnipresent, and stable nature of silicon, however, presents a formidable challenge. As we attempt to highlight in this work, the promises claimed by competing materials can be fulfilled by silicon-based solar cells as well, but necessitate a paradigm shift towards ultrathin devices.

Any new technological advancements require benchmarking against existing solutions, and for solar cells, a set of basic rules is established for fair comparison among the different approaches. The standard testing conditions (STC) are defined to establish comparability

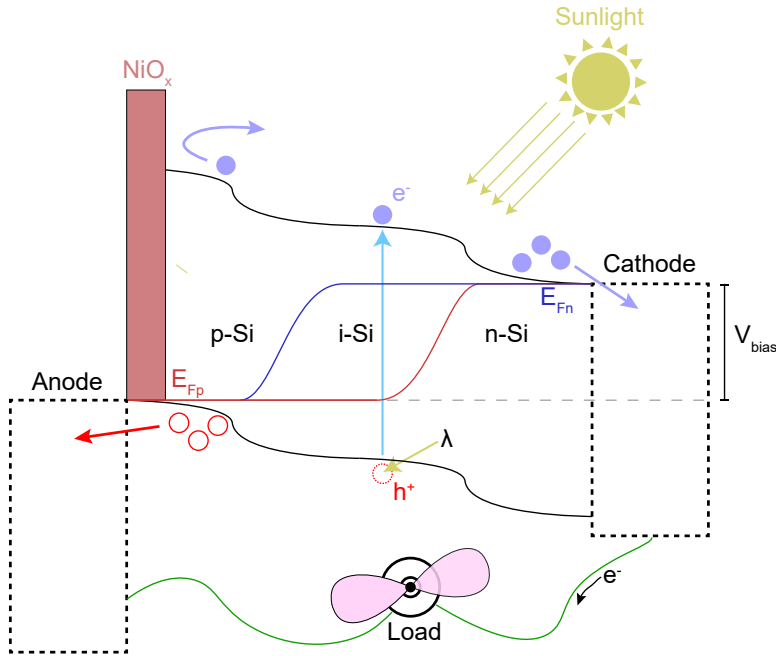


**Figure 2.1: Band-structure schematic of a p-i-n-junction solar cell close to open-circuit potential**

Solar cell from left to right: Anode (Ag),  $\text{NiO}_x$  selective contact, p-doped Si, intrinsic Si, n-Si, Cathode (Al). The Fermi energy splits into two quasi-Fermi levels at the p-side  $E_{Fp}$  (red solid line) and at the n-side  $E_{Fn}$  (blue solid line). Incident light ( $\lambda$ ) creates a pair of electron  $e^-$  and hole  $h^+$ . The potential of the electron-hole pair is given by the difference of the quasi-Fermi levels  $E_{ch} = E_{Fn} - E_{Fp} = qV_{bias}$  with electron charge  $q$ .

between photovoltaic devices tested anywhere in the world. They state that measurements are to be performed at a cell temperature of  $25^\circ\text{C}$  and  $1000\text{ W}\cdot\text{m}^{-2}$  irradiance of an AM1.5G-compliant spectrum (International Standard IEC 60904-3 [65]) under normal incidence. The AM1.5G spectrum (Fig. 2.2) corresponds to the solar radiation impinging onto a sun-facing plane, which is tilted  $37^\circ$  relative to the horizontal. At perpendicular incidence to this plane, the sunlight is transmitted (filtered) through about 1.5 times the surface-normal atmospheric thickness, which is denoted by the number. The suffix “G” denotes that both diffuse and direct, thus *global*, “G”, irradiance is included. Direct illumination refers to perpendicular incidence onto the tilted plane, while light collected from all other directions contributes to the diffuse component. The diffuse component thus comprises sunlight reflected off other surfaces onto the tilted plane.

The irradiance (Fig. 2.2a) varies greatly across the  $250\text{ nm} < \lambda < 2000\text{ nm}$  spectral range, with most power available around  $\lambda \sim 500\text{ nm}$ . A semiconductor absorbs light with greater energies than its bandgap. Hence, the usable solar spectrum depends on the specific material employed. Crystalline silicon has a bandgap energy of  $E_G = 1.12\text{ eV}$  ( $\sim 1100\text{ nm}$ ) at room temperature and thereby absorbs a considerable fraction of the solar irradiance. Since every absorbed photon can create exactly one electron-hole pair, the number of absorbed photons

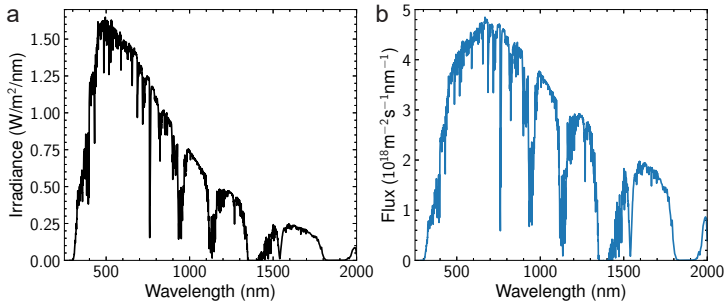


**Figure 2.2: Solar spectrum at the earth's surface**  
 Solar irradiance (a) and photon flux (b) according to the AM1.5G standard spectrum.

per unit time determines the maximum achievable current, while the individual photon energy only needs to be greater than the bandgap. The number of photons per unit time and area ( $\# \text{photons}/\text{s}/\text{m}^2$ ) versus wavelength (Fig. 2.2b) appears notably different from the irradiance spectrum. The maximum flux occurs in the region  $500 \text{ nm} < \lambda < 900 \text{ nm}$ , with a peak at  $\lambda = 669 \text{ nm}$ . Efficient utilization of irradiance at these wavelengths is key to achieve good performance. To approach the theoretical limit of efficiency, however, the absorption and conversion of all above-bandgap photons have to be optimized.

## 2.2 Fundamental Limits to Solar Cells

When a solar cell is illuminated and connected to an external circuit, it provides a flow of charges (current  $I$ ) at a certain potential (voltage  $V$ ). The resistance of the load produces a backwards-directed electromotive force  $V_L$  which opposes the flow of current. When  $V = V_L$ , the current through the circuit remains constant and a steady state is reached. The steady-state power  $P = I(V) \cdot V$  delivered by the solar cell thereby depends on the counter voltage  $V_L$  produced by the load and follows the characteristic current-voltage ( $IV$ -) curve of the solar cell.

The  $IV$ -curve of an ideal solar (black line in Fig. 2.3) shows maximum current at  $V = 0$ , which decreases slowly as the voltage is raised. Beyond a certain voltage, the current begins to fall sharply towards zero. The current value at  $V = V_L = 0$  is known as the short-circuit current  $I_{sc}$  or short-circuit current density  $J_{sc} = I_{sc}/A$ , where  $A$  denotes the area of the cell. The voltage at zero current is called open-circuit voltage  $V_{oc}$  and corresponds to the maximum potential at which charge carriers are extractable. The voltage-dependent power (red curve) rises near linearly at low voltages and reaches a peak value close to the knee point beyond which the current significantly drops. This “maximum power point” (mpp, denoted by a star), corresponds to the operating voltage at which the power delivered to the external load is maximized for a given illumination condition.

The power conversion efficiency of solar- ( $P_{in}$ ) to electric power ( $P_{out}$ ) is defined at the mpp by the ratio ( $P_{in}/P_{out}$ ):

$$\eta = \frac{P_{out}}{P_{in}} = \frac{V_{mpp} \cdot I_{mpp}}{P_{in}} = \frac{V_{mpp} \cdot J_{mpp}}{I_{in}}, \quad (2.1)$$

with solar irradiance (or intensity, insolation, power per area)  $I_{in} = P_{in}/A$ . The efficiency is

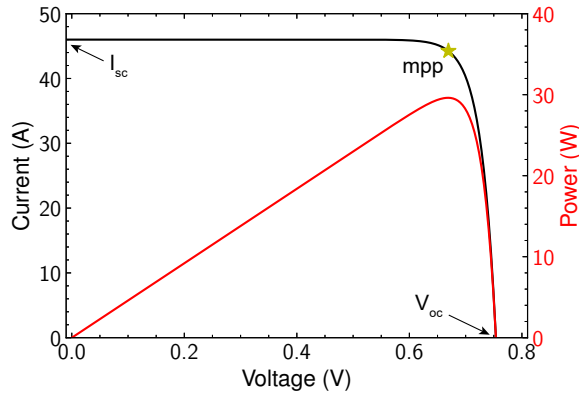


**Figure 2.3: Current-Voltage characteristics of an ideal solar cell**

Current (black) and power (red) delivered to an external load and versus bias voltage for an ideal solar cell. The maximum-power point (mpp) is marked with a star, short-circuit current  $I_{sc}$  and open-circuit voltage  $V_{oc}$  are indicated by arrows. The curves roughly correspond to an ideal c-Si solar cell.

commonly quantified by the characteristic short-circuit current and open-circuit voltages through the introduction of the fill factor  $FF$ :

$$FF = \frac{I_{mpp} V_{mpp}}{I_{sc} V_{oc}}. \quad (2.2)$$

The fill factor gives great insights into the (non-)ideality of a real solar cell. While in an ideal solar cell, the junction behaves like a perfect one-way street and there is no resistance to the extraction of charge carriers, there are no real materials exhibiting these properties. Instead, leakage currents rise in proportion to the voltage difference across the cell, which diminish  $I(V)$  as the voltage increases and thereby lead to a greater slope of  $I(V)$  at  $V < V_{mpp}$ . In addition, any ohmic resistance within the semiconductor and contacting layers cause an additional drop in voltage as the current rises from zero at  $V_{oc}$  to  $I_{mpp}$ , which reduce the slope of  $I(V)$  between these voltages. Both effects individually decrease the fill factor, since the maximum power point shifts to smaller voltage- and current values, while  $V_{oc}$  and  $I_{sc}$  remain unaffected.

The conversion of solar energy to electricity is thermodynamically limited, and the ultimately attainable efficiency depends on the bandgap energy of the semiconductor material. The theoretical efficiency limit results from a detailed-balance (DB) analysis under steady-state operation, where the current results from the balance of generative- and loss currents. Solar and thermally generated electron-hole pairs contribute to current, while radiative recombination (black body radiation), due to the finite temperature of the solar cell, comprises a loss channel. Though other loss channels exist in real solar cells, e.g. Shockley-Reed-Hall and Auger recombination, these are disregarded in the detailed balance. Furthermore, it is assumed that all above-bandgap photons are absorbed and create exactly one electron-hole pair. This assumptions carries great impact, because the utilization efficiency of a photon strongly depends on its energy. As a result of these simplifications, the detailed balance limit is solely a function of the bandgap of the semiconductor (Fig.2.4). The shape of the efficiency

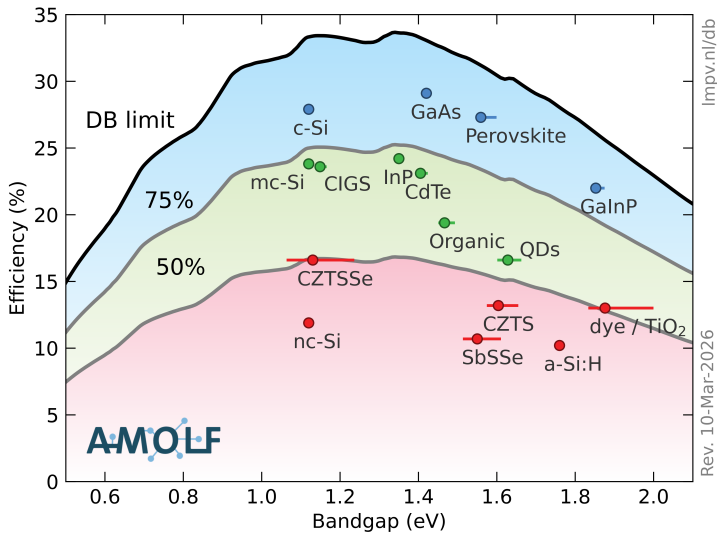


**Figure 2.4: Detailed-Balance limit of single-junction solar cells**

Ultimate theoretical efficiency versus bandgap energy (black curve). Colored dots represent the best-performing experimental solar cell devices per semiconductor material (given next to the dot), as of March 10th, 2026. Horizontal lines indicate materials with tunable bandgaps. Experimental results are categorized by shaded regions highlighting the attained fraction of the DB limit. Graphic obtained from [www.lmpv.nl](http://www.lmpv.nl) [66, 67].

limit (black curve) results from the balance between the extraction potential  $U = qV$  and total number of absorbed photons  $N_{\text{ph}} = I/q$ , with electron charge  $q$ , both of which relate to the bandgap. A larger bandgap increases the potential but leads to fewer absorbed photons of the AM1.5G spectrum, since only photons with greater energy than the bandgap energy can contribute to current, which determines the shape of  $\eta \propto UN_{\text{ph}}$ . The DB limit reveals that the highest efficiencies are achievable with semiconductor bandgaps in the range  $1.1 < E_G < 1.4 \text{ eV}$ , which includes crystalline silicon. Besides c-Si, only three other semiconductor materials have led to efficiencies greater than 75% of the DB limit, which highlights the challenges in material science to produce compound materials that reach high levels of crystal purity. In particular, the defect density in crystalline silicon needs to be exceptionally low, since the typical absorber layers are up to hundreds of times thicker than those in other (direct-bandgap) materials. The required purification demands substantial thermal energy, and the considerable thickness of silicon absorbers stems primarily from their poor optical absorption at wavelengths near the bandgap. With appropriate light-management strategies, the minimum thickness needed to achieve nearly-complete absorption can be reduced substantially, which mitigates the requirement of high crystal purity and leads to a balance between electronic extraction and optical absorption properties.

## 2.3 The Balance between Optical- and Electronic Losses

The fundamentals of light-matter interaction in semiconductors lies at the heart of nearly all optoelectronic devices, such as solar cells, photo- and light-emitting diodes and photo-detectors, CCD cameras, etc. In all of these examples, efficiency and performance are linked on the one hand to the ability to fully absorb (or extract) light of a certain frequency, and on the other hand, to extract (or inject) charge carriers with minimal resistance and loss of potential. These requirements are in mutual contradiction for real-world photosensitive devices, because the absorbed fraction of light increases with the thickness of the material, while resistance to the current extraction and losses related to imperfections in the material diminish when the thickness is reduced. Inversely, for light-emitting devices, a thicker material layer increases the probability of radiative recombination of the injected electron-hole pairs, while a thinner material increases the escape probability of generated photons and limits their chances for re-absorption. Hence, the optimization of any optoelectronic device depends upon a balance between optical and electronic losses.

The optimal thickness for a solar cell thus depends on semiconductor's electronic quality, represented by the carrier diffusion length  $L_D$ , and light-absorption properties  $\alpha$ , which are intrinsic to the material. The upper efficiency limit results from the balance of these losses as a function of thickness. Figure 2.5 reveals vastly different optimized thicknesses depending on the semiconductor material. Absorptance corresponds to the double-pass limit, thus assuming a perfect back reflector. In case of crystalline silicon (blue), the solid line represents the double-pass limit while the dashed line corresponds to the  $4n^2$ -limit (Lambertian/Yablonovitch), which is introduced in the following section. In the context of mass-produced devices, the time, cost, and reliability of the manufacturing process often impose additional constraints on the feasibility of any device architecture. Consequently,

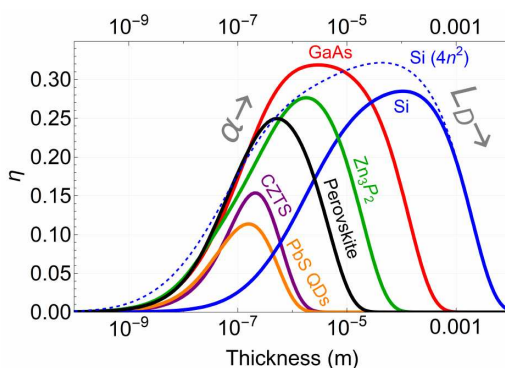


**Figure 2.5: Efficiency dependence on absorber thickness**

Power conversion efficiency  $\eta$  versus absorber thickness for different solar cell absorber materials: Copper/Zinc/Tin/Sulfur (CZTS, purple), Lead-Sulfate quantum dots (PbS QDs, orange), Perovskite (black), Gallium-Arsenide (GaAs, red), Zinc-Phosphite ( $Zn_3P_2$ , green), and Silicon (Si, blue solid). The calculated optical absorption  $\alpha$  corresponds to the double-pass absorption limit versus thickness in the respective materials, and for Si, the Yablonovitch  $4n^2$  light-trapping limit is included additionally (blue dashed). Adapted from [68].

employing thicker material layers to achieve complete absorption necessitates higher quality to minimize increased electronic losses, which leads to significant increases in cost and production time (see also Introduction sec. 1.2). Improving light-capturing efficiency in thin substrates, however, can be achieved with much lower energy expenditure, for example, by incorporating surface corrugations.

### 2.4 Light Trapping in Thin Weakly-Absorbing Layers

The most common strategy employed in silicon photovoltaics to improve light trapping is random pyramidal texturing by a wet-etching process in a bath of potassium hydroxide (KOH), which selectively removes certain facets of the silicon crystal structure [69, 70]. Vertically upright pyramids of micron-size dimension are then easily obtained by a suitable orientation of the crystal with respect to the device architecture. When light at normal incidence impinges on the side face of a pyramidal structure at the absorbers surface, it is refracted into the substrate under an angle, which increases the optical path length inside the absorbing material, effectively increasing its apparent thickness. This strategy, though first implemented in solar cell already  $\sim 40$  years ago [71], continues to comprise the primary approach in the large-scale production of conventional silicon solar cells. In the next iteration of solar cell designs, however, the standard wafer thickness is projected to decrease the currently still ambitious target of  $110\ \mu\text{m}$ , by as much as an order of magnitude [72], which will ultimately render random pyramidal texturing with KOH unsuitable, since the feature sizes of the created pyramids falls in the same order of magnitude as the cell thickness.

In order to overcome the incomplete absorption in materials thinner than the absorption length of light, and where conventional pyramidal texturing is unsuitable, sub-wavelength structures implemented at different levels of the device architecture have proven exceptionally viable [73–78]. Modern lithographic tools allow deterministic control of object morphologies at the single-digit nanometer scale, enabling tailored sub-wavelength geometries which exploit photonics for ultimate light management. Before taking a closer look at these advanced concepts requiring precise control, however, we consider a prominent example case of a fully random patterning approach.

#### 2.4.1 The Yablonoitch (Lambertian) Limit

When light impinges on a flat, weakly-absorbing slab at normal incidence (Fig. 2.6a), a considerable fraction reaches the rear interface without being absorbed and exits the slab. The absorbed intensity fraction in this process is known as single-pass absorptance, where the optical path length is equal to the thickness of the slab. By adding a reflector at the rear interface (b), the optical path is effectively doubled, leading to the double-pass absorptance limit. So far, the interfaces are considered flat, such that the incident light retains its vertical direction within the slab. If instead, the front (or rear) interface features corrugations, light diffracts into the slab at different angles (c). The wave traveling at an angle covers a larger distance within the material before reaching the back reflector as well as on the way back to the front interface. Thereby, the optical path length is enhanced by scattering into the plane of the absorber. In 1982, Yablonoitch derived a fundamental upper bound for light absorption for such slabs by assuming complete randomization of light directions within the substrate [79]. In the Lambertian (isotropic) scattering limit, the path-length enhancement for normally incident light is increased up to  $4n^2$ , where  $n$  denotes the refractive index of the absorber. Practically, this limit implies that ideal diffuse internal scattering increases

## 2.4 Light Trapping in Thin Weakly-Absorbing Layers

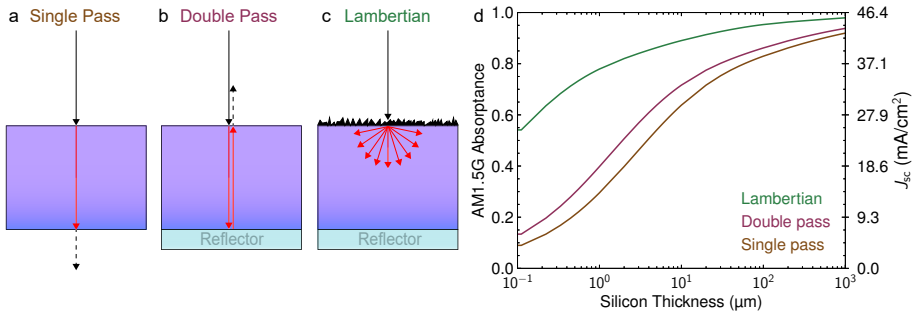


**Figure 2.6: Common absorption limits in thin substrates**

Schematic of light interacting with a thin substrate indicated by arrows. The optical path length inside the absorber is highlighted by red arrows for a single-pass (a), double-pass (b), and Lambertian (c) limit. (d) AM1.5G-averaged absorbance of wavelengths  $\lambda \in [300, 1200]$  nm versus silicon thickness for the limits (a,b,c).  $J_{sc}$  is calculated from the AM1.5G photon flux under the assumption every photon creates exactly one electron-hole pair.

the effective optical thickness — and thus the probability of photon absorption — by up to a factor of  $4n^2$  without changing the material absorption coefficient. This has profound impact on the average absorbance, especially for very thin absorber layers (Fig. 2.6d). At  $1 \mu\text{m}$  thickness, the single pass absorption of  $\sim 25\%$  increases to  $\sim 40\%$  by adding a back reflector (double-pass), while reaching almost  $80\%$  in the Lambertian light-trapping limit. The average absorbance is calculated by weighing the absorbance at each wavelength with the photon flux of the AM1.5G spectrum (Fig. 2.2b), and the right-hand ordinate axis in Fig. 2.6d displays the corresponding maximum photocurrent  $I_{sc}$  normalized to a solar cell area of  $1 \text{ cm}^2$ .

The Lambertian limit underpins many light-trapping strategies: textured front surfaces and rough or diffusing rear reflectors aim to approximate the isotropic internal angular distribution to approach the  $4n^2$  enhancement. The  $4n^2$  limit considers zero reflectance from the front interface, which is difficult to achieve for a broad spectral range in real devices. Therefore, a solar cell exhibiting a true Lambertian response across the whole solar spectrum has not been achieved so far. Although the term limit suggests an upper boundary, photonic concepts such as localized resonances, angular restrictions, and coupling to guided modes can be combined to achieve even higher absorbance, albeit typically within a limited spectral or angular range.

### 2.4.2 Resonant Scatterers

Sub-wavelength inclusions which differ in refractive index from the surrounding dielectric medium give rise to strong optical responses due to shape-dependent resonances. The underlying mechanism differs if the inclusions are metallic (plasmonic response [80]) or dielectric (Mie response [81]). Plasmons are quasi-particles comprised of coherent oscillations of free electrons on the surface of a metal particle. When light excites such a particle, the coupling between the incident field and the electromagnetic field produced by the oscillating charges creates strong scattering effects, which can be exploited in light management techniques. Mie-resonances, in contrast, occur within dielectric nanostructures. Here, the the strong polarizability of the material supports oscillations (of the bound electron orbitals relative

## Theoretical Background

to the fixed positive charges) analogous to a mass-and-spring mechanical system, which similarly couple to external electromagnetic waves. Hence, both the sources of the induced fields (free versus bound electrons) as well as the location (at the surface versus in the bulk) differ fundamentally between plasmonic- and Mie-type of resonances. In particular, limited coherence and mutual scattering of the free electrons in plasmonic particles lead to (thermal) losses of electromagnetic energy, which reduce the re-radiated field intensity and heat the material. Nevertheless, both plasmonic- and Mie-resonance supporting nanoparticles have been included in advanced solar cell designs and lead to substantial improvements of their optoelectronic response [82–88].

In this thesis, we implement Mie-resonant structures, which besides reduced optical losses offer the ability to tailor the spectral response by engineering their precise shape. The geometric tunability arises from the confinement of electromagnetic energy within the particle. As an example, let us consider a Si nanocylinder suspended in vacuum that is axially excited by a plane wave (Fig. 2.7). The high refractive index of silicon ( $3 < n < 5.5$ ) strongly compresses the electric field and retards it with respect to parts of the wave passing next to it. This secondary retarded field interferes with the incident wave and produces scattering. If the dimensions are such that dielectric displacement currents can form closed loops within the cylinder (2.7a), a standing-wave is formed for certain wavelengths, which stores and re-radiates substantial amounts of power [89].

The scattering spectrum a cylinder of height  $h = 100$  nm and diameter  $d = 100$  nm exhibits strong wavelength dependence, featuring a pronounced peak at  $\lambda = 496$  nm with nearly tenfold enhancement (c). The scattering cross-section normalized to the geometrical projection of the cylinder indicates that the optical footprint of the cylinder in air is about ten times larger than its geometrical area normal to the incident field. Thereby, a substantial fraction of the incident field is scattered away from the normal direction, both at the location of the cylinder and extending into its vicinity [90]. The spectral location of the peaks changes as a function of the cylinder dimensions, i.e. shifting to larger wavelengths when the diameter is increased  $d = 100$  nm (blue)  $\rightarrow d = 125$  nm (green).

When a number of such cylinders are combined into a scattering layer, the scattering response results from a convolution of the angular- and spectral responses of the individual object with the total scattering response of the ensemble [91]. Furthermore, slightly varying

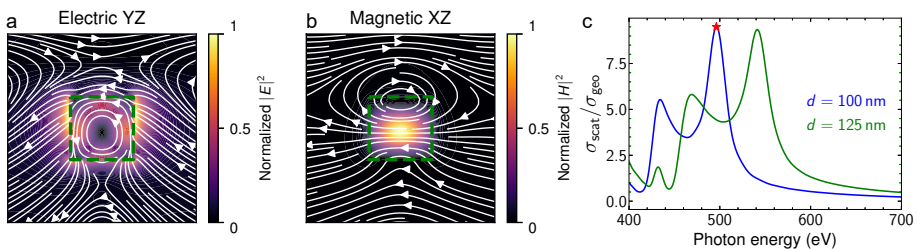


**Figure 2.7: Mie resonance of a Si cylinder in air**

Electric- (a) and magnetic- (b) field plots of a magnetic-dipole resonance at 496 nm. Arrows indicate the direction of the electric- and magnetic fields, respectively. Si cylinder dimensions are height  $h = 100$  nm and diameter  $d = 100$  nm, and its location is indicated by a dashed frame. (c) Normalized scattering cross-section of Si cylinders in air versus wavelength. Two diameters are shown,  $d = 100$  nm and  $d = 125$  nm, height  $h = 100$  nm in both. The red star marks the wavelength corresponding to the field plots in (a) and (b).

the dimensions of cylinders across the scattering layer leads to a substantial broad-band scattering enhancement through the spectral distribution of the scattering peaks associated with the changing parameter. These combined effects open up a vast parameter space and necessitate careful optimization for specific operating wavelengths.

Overall, the resonant scattering behavior of nanoscale objects situated at a material interface redirects light into off-normal directions within the material. Light trapping describes the process of coupling incident light into guided modes of a substrate, which depend on total internal reflection.

### 2.4.3 Total Internal Reflection

Total internal reflection occurs when light travels through a material with a refractive index  $n_2$  greater than that of the surrounding medium with index  $n_1$ , and strikes the interface at an angle exceeding the critical angle. The critical angle  $\alpha_c$  follows from Snell's law:

$$n_1 \sin \alpha_1 = n_2 \sin \alpha_2, \quad (2.3)$$

where  $\alpha_{1,2}$  denote the angles with respect to the interface normal in materials of  $n_{1,2}$ , respectively. It implies that light impinging at angles  $\alpha_2 > \arcsin(n_1/n_2) \equiv \alpha_c$  cannot refract out of the higher-index material  $n_2$ . Snell's law reflects momentum conservation at flat interfaces for the interface-parallel wavevector component  $k_{\parallel}$ :

$$k_{\parallel,1} = \frac{2\pi}{\lambda_0} n_1 \sin \alpha_1 = \frac{2\pi}{\lambda_0} n_2 \sin \alpha_2 \equiv k_{\parallel,2}, \quad (2.4)$$

with vacuum wavelength  $\lambda_0$ .

The momentum domain simplifies the description of scattering, diffraction and refraction of light. When  $k_{\parallel} < |k_0|$  (Fig. 2.8a), light refracts in- and out of the material, while light is trapped by total internal reflection for  $k_{\parallel} > |k_0|$  (b). When the thickness of the material is on the order of the wavelength, however, also the guided-mode structure affects the trapping of light.

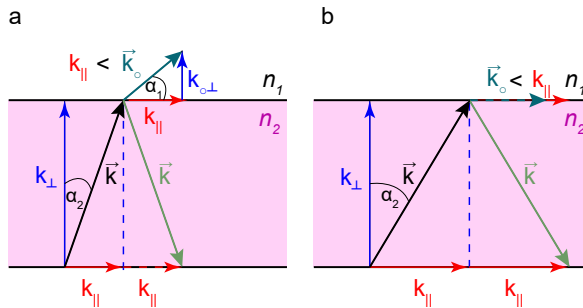


**Figure 2.8: Refraction and total internal reflection at a flat material/air interface**  
 Schematic of refraction (a) and total internal reflection (b) at an interface between air ( $n_1$ ) and a material  $n_2$ .  $\vec{k}_0/\vec{k}$  denotes the wavevector in air/material, respectively, where  $|\vec{k}| = \sqrt{k_{\perp}^2 + k_{\parallel}^2}$  with interface-normal  $k_{\perp}$  and interface-parallel  $k_{\parallel}$  components.

### 2.4.4 Guided- and Quasi-Guided Modes

Maxwell's equations guarantee the continuity of the electric field and its first derivative across any optical interface. It implies that the interface-parallel (in-plane) momentum component  $k_{\parallel}$  for trapped light must not only exceed the wavevector in the surrounding media, but further adhere to the boundary conditions imposed by the optical interface. These optical states (modes) within the waveguide are characterized by specific allowed values of  $k_{\parallel}$  at each wavelength.

The maximum number of modes relates to the thickness of the waveguide and the refractive index contrast with its surroundings, indicated by the critical angle  $\alpha_c$ :

$$m_{\max} = \frac{kt \cos \alpha_c}{\pi} + 1, \quad (2.5)$$

with thickness  $t$  and the one is added for order  $m = 0$ . Eq. 2.5 reveals a linear dependence of the number of optical states on the thickness of the trapping layer, assuming other conditions remain unchanged. As  $t$  becomes significantly larger than  $k^{-1}$ , the mode profiles overlap and merge into a continuum of states. Consequently, all waves with  $k_{\parallel} > k_c$  will be supported in thick layers. Conversely, when the thickness is comparable to the wavelength in the material, only distinct  $k_{\parallel}$  states exist (Fig. 2.9).

The colored rings (a,c) representing the modes'  $k_{\parallel}$  reveal a strong spectral dependence, due to the dispersive  $n(\lambda)$  characteristic of silicon. As a consequence, modes at long wavelengths occur at smaller  $k_{\parallel}$  values than at short wavelengths. The black inner circle encloses the escape cone, where  $k_{\parallel} = \sqrt{k_x^2 + k_y^2} < k_0$ . As these in-plane momenta correspond to angles smaller than  $\alpha_c$ , total internal reflection does not occur and light can refract out of the slab, thus "escape". The right column in Fig. 2.9 displays the mode dispersion against wavelength for thicknesses 200 nm (b) and 1  $\mu\text{m}$  (d), where the color scale indicates an onset of incomplete absorption at  $\lambda \geq 400$  nm versus  $\lambda \sim 450$  nm in the thin and thicker slabs, respectively. At long wavelengths, coupling to guided modes is essential to achieve greater absorptances.

The optical states are bound by total internal reflection, hence they cannot be excited by external radiation incident on a flat air-/material interface. Coupling to modes is afforded by adding corrugations (structure) to the interface, which imparts sufficient in-plane momentum to diffract light into the guided-mode regime. The principle of reciprocity implies that light trapped in a guided mode can also escape into the surrounding space upon interaction with the structured interface. Since the corrugations allow the in- and out-coupling of light to and fro a guided mode, it is termed a "leaky-" or quasi-guided mode.

### 2.4.5 Momentum of Light and Structure

As we have seen in the previous sections, light in a finite material with larger refractive index  $n$  than its surrounding can become trapped by total internal reflection, when its in-plane momentum component exceeds the magnitude of its total momentum vector in the surrounding media. Similarly, the spatial features, i.e. the distances associated with peaks and troughs in a corrugated surface, can be described in terms of (spatial) momentum in reciprocal space. The momentum-view of structures affords great insights into the distribution of spatial frequencies and (an-)isotropy in the plane, and allows extraction of periodicity and other characteristics of interest.

By virtue of an abrupt change of refractive index over a length  $l$  of a peak or trough in the pattern, normally incident light may be scattered into the higher-index material to acquire in-plane momenta that are increased or decreased by an amount of  $\Delta k_{\parallel} = \pm 2\pi/l$ , as a result

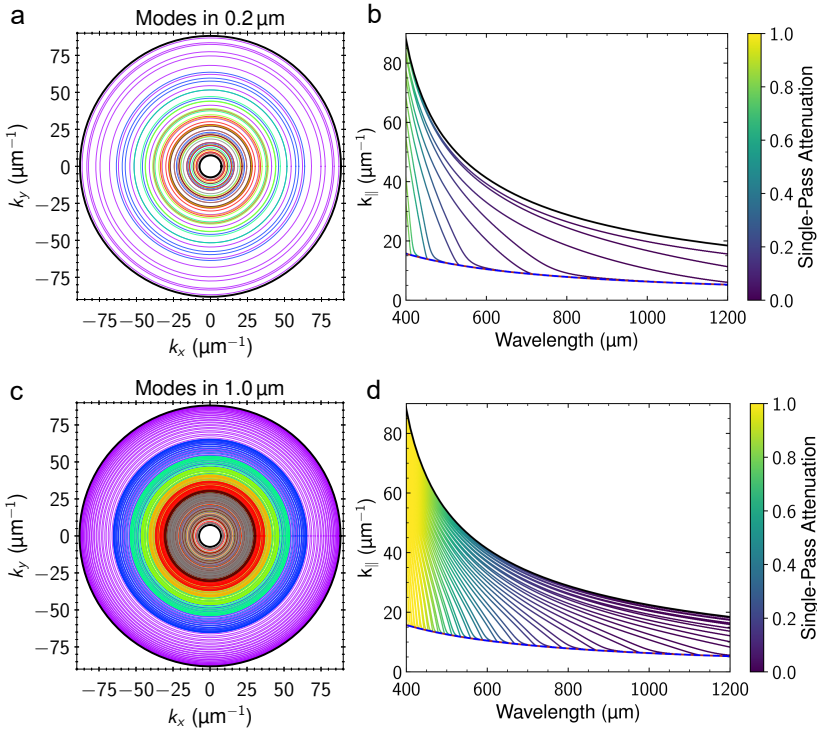


**Figure 2.9: Guided mode representation and dispersion in ultrathin silicon**

Guided modes in a silicon slab in air with thickness 200 nm (a,b) and 1  $\mu\text{m}$  (c,d). Left column: Modes as colored lines in the  $k_x, k_y$ -plane for wavelengths  $400 \text{ nm} \leq \lambda \leq 800 \text{ nm}$  in 50 nm steps. Colors approximate those of light in the visible, and gray represents  $\lambda = 800 \text{ nm}$ . Inner black circles corresponds to a radius of  $k_0$  at 800 nm and outer circles to  $k$  at 400 nm. Right column: In-plane momentum  $k_{\parallel}(\lambda)$  against wavelength with color-coded absorptance within a single-pass through the slab. Lower blue/red curve represents the light line and upper black curve the maximum wavevector within the material.

of interference from wavefronts scattered by the peaks or troughs in different spatial locations. If the corrugations are periodically arranged, the scattering interference can afford additions of integer multiples of  $\Delta k \cdot m$  to the in-plane momentum of the scattered light, which gives rise to the diffraction orders  $m \in [0, \pm 1, \pm 2, \dots]$ . Thus, there is an inherent link between the momentum distribution of spatial characteristics in a scattering layer and the distribution of light momenta that are scattered by this layer. If there is an overlap between in-plane momentum of a diffracted beam of light and a guided mode of the structure into which the light is scattered, coupling to the mode occurs and a so-called guided-mode resonance (GMR) is created [92, 93]. For the function of the optoelectronic device to either absorb or extract light within- or from the material, GMRs provide significant enhancements and tailoring their properties becomes key in reaching higher efficiencies.

Figure 2.10 illustrates the momentum characteristics of different structure types and indicates the in-plane momenta  $k_{\parallel}$  into which light can be diffracted. The inner circle  $k_0$

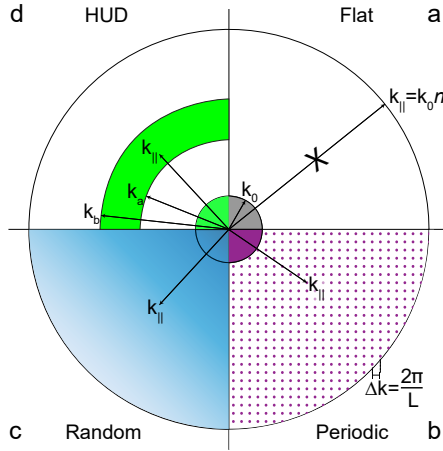


**Figure 2.10: Momentum-domain illustration of different scattering approaches**  
 Interface-parallel plane  $k_x, k_y$  in momentum space. The quadrants represent different structure types: **(a)** Flat (no structure); **(b)** Periodic; **(c)** Random; **(d)** hyperuniform disordered (HUD). Allowed optical states in each quadrant are marked as dots/shaded regions. The circles represent the free-space wavevector  $k_0$  (inner circle) and the wavevector inside the material  $k$  (outer circle).

encloses all allowed momenta in free space and the outer circle marks the maximum wavevector within the material  $k = k_0 n$ . Normal incident light  $k_{\parallel} = 0$  appears at the origin and gains in-plane momentum through scattering off the structure. Depending on the structure type, possible  $k_{\parallel}$  values are constrained and only certain optical states can be populated.

At a flat interface (quadrant a), in-plane momentum is conserved (as in Fig. 2.3) and only values within  $k_0$  are allowed. In the case of a square-lattice periodic grating (b), allowed states correspond to the harmonic series of the lattice vector  $\Delta k_{\text{periodic}} = \frac{2\pi}{L} (m + n)$  with periodicity  $L$  and  $m, n \in \mathbb{Z}$  for the mutually orthogonal directions along  $k_x, k_y$ . As such, overlap with the guided mode rings (Fig. 2.9) occurs only in distinct locations that are wavelength-dependent. Due to the strong dispersion, coupling to modes over a broad spectral range cannot be achieved with a singular parameter of periodicity [75]. A fully random distribution corresponds to a periodicity approaching infinity  $L \rightarrow \infty$ , and consequently allowed states merge into a continuum  $\Delta k_{\text{random}} \rightarrow 0$ . In turn, incident light is spread over all possible momenta and can couple to all modes. Thereby, random distributions are suited to populate all modes also for broad incident light spectra. There is, however, no control to target specific  $k_{\parallel}$  values or to prevent scattering into the escape cone  $k_{\parallel} < k_0$ . The momentum content of disordered hyperuniform patterns (d) shows a third type of distribution, which shares certain similarities with both periodic and random types. On the one hand, allowed states (green ring) form a continuum as in a random configuration. On the other hand, all of them fall within an interval of  $k_{\text{HUD}} \in [k_a, k_b]$ , with other  $k_{\parallel}$  forbidden— as in a periodic arrangement. Aligning the green ring with the  $k$ -vectors of the guided modes of a thin silicon slab offers intriguing prospects to optimize light trapping within the thin layer while simultaneously minimizing diffraction within the light cone. To understand where these peculiarities in disordered hyperuniformity originate, we introduce some statistical metrics which allow to look under the hood of these distributions.

## 2.5 Ensemble Statistical Properties

### 2.5.1 The Pair-Correlation Function $g_2$

The pair correlation function  $g_2$  is a fundamental statistical quantity, because it contains information about interparticle forces and system structure that can be measured experimentally through scattering techniques. It measures the probability of finding a particle at distance  $r$  from another particle, normalized by the average particle density. A value of 1 means particles are randomly distributed at that distance, while values greater than 1 indicate clustering or attraction, and values less than 1 indicate avoidance or repulsion. At short distances,  $g(r)$  typically shows peaks corresponding to nearest-neighbor shells and the preferred spacing between particles, which reflects the underlying structure of the system. At large distances, a random distribution approaches 1, while greater values reflect long-range correlations.

For a distribution of  $N$  particles in the  $x, y$  plane with coordinates  $x_{i,j}, y_{i,j}$  with  $i, j \in [1, N]$ ,  $g_2$  corresponds to:

$$g_2(r) = \frac{1}{N} \sum_{i=1}^N \sum_{j \neq i} \delta(r - |\mathbf{r}_i - \mathbf{r}_j|), \quad (2.6)$$

where

$$|\mathbf{r}_i - \mathbf{r}_j| = \sqrt{(x_i - x_j)^2 + (y_i - y_j)^2}. \quad (2.7)$$

### 2.5.2 The Structure Factor

To quantitatively describe statistical properties, such as order and disorder, the structure factor  $S(k)$  provides a complementary measure to  $g_2(r)$  in momentum space as a function of the spatial momentum  $k$ . It is defined as the Fourier transform of the total correlation function  $h$  [94, 95]:

$$S(k) = 1 + \rho \int h(r) e^{ik \cdot \mathbf{r}} d\mathbf{r}, \quad (2.8)$$

with total correlation function:

$$h(r) = g_2(r) - 1, \quad (2.9)$$

where  $g_2$  represents the pair-correlation function.

The structure factor provides invaluable insights into the spatial correlations of a scattering layer. Since  $g_2$  and consequentially the structure factor solely represent spatial coordinates, however, they contain no information about the local geometry (form factor), which strongly impacts the scattering response. The finite dimensions of the scattering objects alter the spatial momentum content of the scattering layer by introducing additional distances, which is captured by the power spectral density.

### 2.5.3 The Power Spectral Density (PSD)

The power spectral density (PSD) is a powerful tool for analyzing the spatial frequency content of topographies by decomposing them in momentum space. It operates on complete 2D spatial maps rather than discrete sets of point coordinates, requiring either continuous or discretized height data across the entire domain. The PSD is calculated as the squared magnitude of the 2D Fourier transform of the height function  $H(x, y)$ .

## Theoretical Background

Consider, for instance, an arrangement of  $N$  identical disks with radius  $r$  and center coordinates  $(x_i, y_i)$  in the  $xy$ -plane. In this case,  $H(x, y)$  can be written as:

$$H(x, y) = \sum_{i=1}^N \Theta \left( r - \sqrt{(x - x_i)^2 + (y - y_i)^2} \right), \quad (2.10)$$

with Heaviside step function  $\Theta$ . The PSD is then obtained as:

$$\text{PSD}(k_x, k_y) = |\mathcal{F}\{H(x, y)\}|^2 = \left| \int \int_{-\infty}^{\infty} H(x, y) e^{-i(k_x x + k_y y)} dx dy \right|^2, \quad (2.11)$$

where  $\mathcal{F}$  denotes the 2D Fourier transform and  $(k_x, k_y)$  are the wave vectors in momentum space.

### 2.5.4 Order, Disorder and Hyperuniform Disorder (HUD)

Figure 2.11 compares ordered, disordered, and hyperuniform-disordered arrangements of disks in a  $A = 15 \times 15 \mu\text{m}^2$  observation window and their statistical properties. In real space (top row, a), the difference between order and disorder is immediately apparent, while the degree of correlations in the HUD distribution is not easily quantifiable, despite being visually homogeneous (and somewhat pleasing to the eye).

The pair-correlation analysis (b) shows values oscillating around  $g_2(r) = 1$  for an ordered arrangement (left), except for  $g_2 = 0$  when  $r < L$  with periodicity  $L$ . The values of  $g_2$  depend on the sampling radius  $dr$ , and exhibits small oscillation amplitudes if  $dr = L$  is set, i.e. sampling at the periodicity  $L = 500$  nm. In case of oversampling  $dr = L/4$ ,  $g_2$  shows increased aggregation at radii corresponding to the mutual distances of lattice coordinates in all directions, and repulsion at other distances. As the radius increases, the impact of sampling reduces and oscillations about  $g_2 = 1$  decrease in amplitude, owing to the fact that mutual distances between lattice coordinates merge into a continuum as  $r \rightarrow \infty$ . Due to the finite observation window, however,  $g_2(r)$  decreases towards zero for  $r > 7 \mu\text{m}$ . Both the choice of sampling and finite regions impact the representation of arrangements in numerical methods and requires investigation so as to avoid artifacts in the obtained measures. In case of (hyperuniform-) disorder, we sample at the smallest inter-particle distance found in the observation window, which avoids artificial aggregation/repulsion traces at most distances. The calculated  $g_2(r)$  produces similar oscillations around  $g_2 = 1$  in disordered (Poisson-random, middle) and HUD (right) distributions, although with increased frequencies and smaller amplitudes. At small  $r$ , the oscillations of Poisson random show the greatest amplitudes, and exhibit a more uniform distribution as  $r$  increases up to the finite window limit at  $r \sim 7.5 \mu\text{m}$ . The HUD arrangement shows features of both previous ensemble types. The oscillation amplitudes are smallest in this distribution, while their frequency (pertaining to the minimum inter-particle distance) lies in-between order and disorder. Most notably, there is a minimum radius  $r \sim 400$  nm, below which  $g_2 = 0$  as in the periodic case. This observation highlights the minimum separation kept in HUD arrangements despite being disordered at small length scales, and the strongly reduced oscillation amplitudes warrant a homogeneous distribution especially at large  $r$  (length scales), absent of void regions seen in the random case (a, middle).

The structure factor  $S(k)$  follows from Fourier transform of  $g_2$  (row b), which we calculate for the finite window dimensions shown in (a). The finite extent limits the resolution  $\Delta k_{\min} = \pi/(15 \mu\text{m})$ , which impacts the constructive/destructive interference due to the limited set of contributing Fourier coefficients. As a consequence, the delta peaks of the

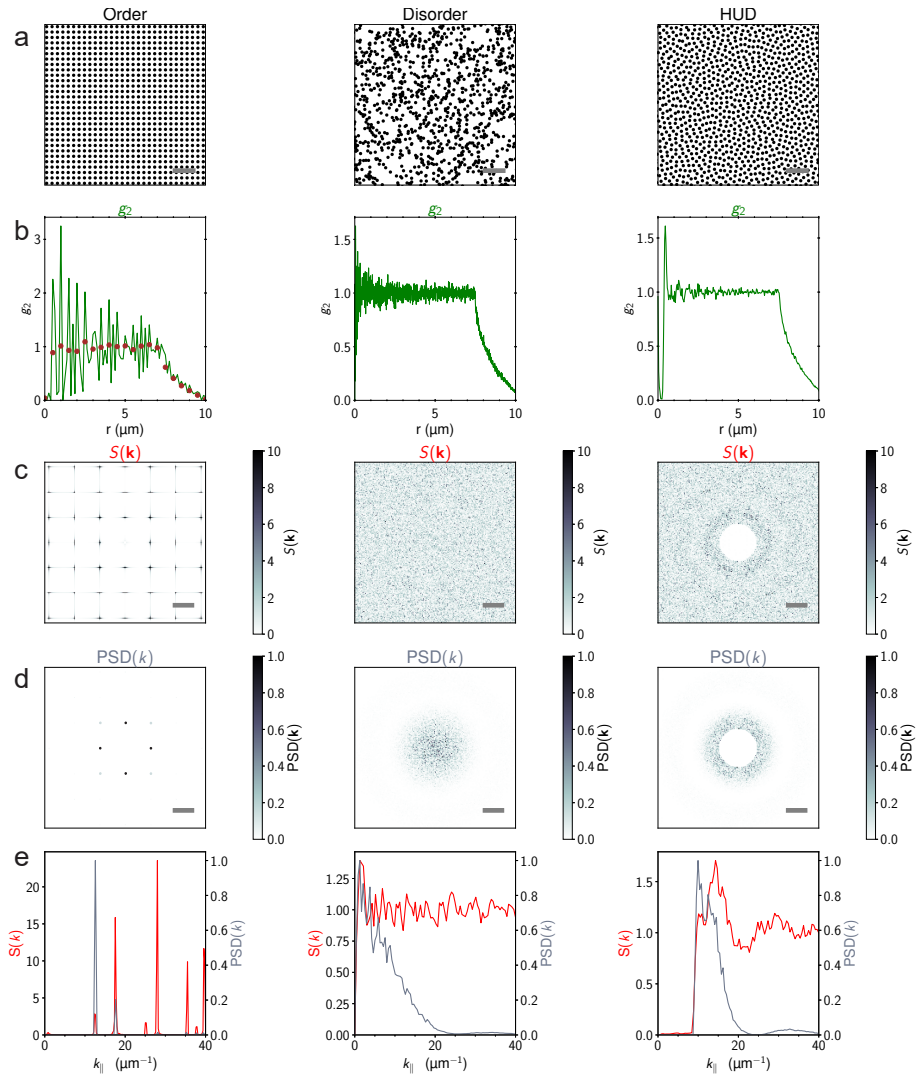


**Figure 2.11: Ensembles in real- and Fourier space**

From top to bottom row: (a) Distributions of disks in real space; (b) pair-correlation function  $g_2$ ; (c) 2D structure factor  $S(\vec{k})$ ; (d) 2D power spectral density  $\text{PSD}(\vec{k})$ ; (e) radial averages of  $S(k)$  and  $\text{PSD}(k)$ , for ordered/periodic (left column), disordered/random (middle), and HUD (right). Scale bars are  $2\mu\text{m}$  in (a) and  $10\mu\text{m}^{-1}$  in (c,d). The diffraction spots of the periodic PSD (d, left) are enlarged to increase visibility.

ordered arrangement (left) appear as rectangular stars instead of sharp dots, similar to the diffractive effect in transmission grating with a small number of slits. The locations of the stars correspond to the reciprocal lattice vectors  $k_{x,y} \in \frac{2\pi}{L}(m_x, m_y)$ , with integers  $m_x, m_y$  representing the orders along  $k_x, k_y$ , respectively. The disordered arrangement (b, middle) shows a homogeneous  $S(\vec{k})$  with no pronounced features, since all spatial frequencies (inverse distances) are uniformly represented. The HUD (right) again shares similarity with both order and disorder, exhibiting a homogeneous distribution of  $S(\vec{k})$  akin to random, which is delimited in its wavevector ranges  $k_{\parallel} \in [k_a, k_b]$  (cp. with Fig. 2.10). Similar to the periodic structure factor, the regions outside of this interval show extremely small values of  $S(\vec{k})$ . Specifically,  $S(\vec{k}) = 0$  for  $\vec{k} \rightarrow 0$  in hyperuniform distributions [94]. For this HUD arrangement in particular,  $S(\vec{k}) = 0$  for  $\vec{k} \in [0, k_c]$ , where  $k_c \sim 8 \mu\text{m}^{-2}$ , forming a black disk in the center of  $S(\vec{k})$ . This property, classified by a vanishing structure factor for a continuous momentum range extending from zero, is termed stealthy disordered hyperuniformity [95]. The absence of small in-plane momenta enables stealthy HUD distributions to avoid light scattering into the escape cone in the same manner as sub-wavelength periodic arrays.

The PSD (row c) closely resembles the structure factor of each arrangement at small wavevectors but decays rapidly at larger spatial frequencies. For the periodic distribution (left), only the first set of diffraction orders is clearly visible. For the disordered (middle) and HUD arrangements (right), the PSD intensity is greatly reduced at  $k_{\parallel} \gtrsim 20 \mu\text{m}^{-1}$ . The difference at larger  $k_{\parallel}$  between PSD( $\vec{k}$ ) and  $S(\vec{k})$  arises from their definitions: (1) The one added to the Fourier transformation in case of the latter but not for the former. (2) The normalization to particle density  $\rho$  only in case of  $S(\vec{k})$ . (3) The sources of real-space data, which is pixelated (image) data for the whole region in PSD versus particle center locations alone in  $S(\vec{k})$ . Specifically at large  $k_{\parallel}$ , point (3) carries two implications: Firstly, the maximum  $k_{\parallel}$ -vector is limited to the Nyquist frequency  $k_{\text{max}} = \pi/d$ , where  $d$  denotes the pixel size of the source image [96]. Secondly, the PSD captures the impact of the local scatterer geometry, while  $S(\vec{k})$  only represents their mutual distance distributions.

The similarities and differences between power spectral density and structure factor are compared by their radial averages in row (e). For the ordered arrangement (left), the peak locations align but show large differences in relative amplitudes. In disorder (middle) and HUD (right), the decay of PSD intensity at large  $k_{\parallel}$  is especially evident, and traces of the disk radius  $r_d = 150 \text{ nm}$  impacting the profiles is visible at  $k_{\parallel} \gtrsim 21 \mu\text{m}^{-1}$ , corresponding to the inverse diameter value  $(2\pi/3 \sim 20.9) \mu\text{m}^{-1}$ .

The statistical analysis reveals the profound differences between order, disorder, and HUD arrangements, which translate to particular light-scattering responses when they are implemented at a material interface. The highlighted advantages and shortcomings of both PSD and structure factor lead to a more complete view to predict and characterize optical responses for ordered and disordered scattering layers alike.

## 2.6 Hyperuniform Disordered Light-Engineered (HUDLE) layers

The ring-like- or doughnut-resembling momentum-space signature of HUD structures, when translates into a light-scattering layer, inherits novel and exciting properties. As we have seen in sec 2.4.5, the distribution of light from a scattering interface follows the spatial momentum distribution of the scatterers in that layer. In combination with the limited optical states in ultrathin substrates (sec. 2.4.4), the tuning of scattering momenta via the periodicity in

## 2.6 Hyperuniform Disordered Light-Engineered (HUDLE) layers

ordered arrangements presents a distinct advantage. Since the optical states are subjected to dispersion, however, the simultaneous optimization of a broad spectral range of wavelengths is highly constrained and light trapping only occurs at specific locations throughout the spectrum. A broad-band response is leveraged by the introduction of disorder, which enable a homogeneous distribution of scattering light across the whole momentum range. At any rate, light trapping necessitates a minimum scattering momentum to couple incident light to guided modes (cp. sec. 2.4.3). Therefore, a considerable fraction of the evenly scattered intensity falls within the escape cone leading to reduced absorptance.

The combination of both seemingly opposing principles in hyperuniform disorder highlights their distinct advantage for light-trapping applications: a broad-band response with tailored properties. By excluding spatial frequencies overlapping with the escape cone from the PSD (or structure factor), the majority of light is scattered into the guided-mode regime. Here, coupling to modes is supported for all wavelengths, due to the continuous PSD features within this momentum range. This combination renders HUD particularly suited for broad-band light-trapping in ultrathin device layers.

The stringent mathematical formulation of HUD criteria are broken when objects are placed in HUD arrangements and a binary topography is obtained [97]. The resulting structures classify as “near-” hyperuniform and are termed “hyperuniform-disordered light engineered” (HUDLE) layers in this thesis [98]. We investigate two distinct types of ‘decorations’ of HUD point patterns, where the first kind consists of holes (termed HUDLE Holes) placed at each location, where the disk diameter provides an additional tuning knob to tailor the spectral scattering efficiency (cp. sec. 2.4.2). The second approach features a wall-network (labeled HUDLE Walls), obtained by a Delauney-tessellation protocol, where the wall widths predominately impact the spectral response [99].

Scanning-electron microscope images of the HUDLE patterns and an optimized periodic design (Periodic), serving as a reference, are shown in Fig. 2.12. Before incorporating these patterns into solar cells and characterizing their performance in ch. 4, we first develop a numerical toolbox to analyze simulated absorptance data and extract light-trapping properties.

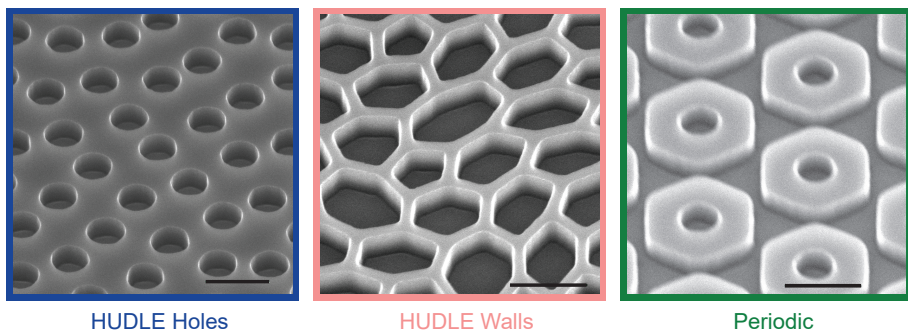


**Figure 2.12: HUDLE and periodic patterns**  
Tilted scanning-electron microscope images of HUDLE Holes (left), HUDLE Walls (middle), and periodic (right) patterns. Scale bars: 500 nm.



# 3

## Quantifying light coupling to guided modes in semiconductor slabs with arbitrary scattering patterns

Optimizing broadband optical absorption in thin semiconductor layers using nanopatterned light-trapping structures remains a major challenge as the applicability of existing models is restricted. When absorbing layers are thinned to the wavelength scale, guided mode bands discretize and statistical limits are no longer applicable. Coupled-mode theory can make accurate predictions for narrow-band excitation of structures with only a few sufficiently separated modes in order to determine a suitable periodicity, but when localized resonances are introduced in the scattering unit and resonant peaks start overlapping, no further design directives are extractable from it. Here, we present a numerical approach to obtain quantitative information from full-field simulations on the energy- and momentum-resolved scattering and absorption distributions for both periodic and arbitrary non-periodic nanopatterns. This enables tailoring of the pattern parameters to steer light into specific guided modes and analyze their absorptive properties and trapping capabilities. We demonstrate the applicability of this toolbox using three case studies in which we assess the impact of localized Mie resonances and (quasi-)random structural correlations on the modal absorption, including the numerical retrieval of coupling- and loss rates. From this complete picture of the absorption profile, key insights can be derived for the rational design of many optoelectronic device applications.

### 3.1 Introduction

Light absorption in semiconductor substrates poses an important challenge that underlies a wide range of modern optoelectronic technologies. In particular, for applications where the substrate is thinner than the absorption length of light, it becomes critical to modify the light-matter interaction beyond simple refraction by introducing sub-wavelength nanostructures on the surface of the substrate. In fact, such nanopatterned light scattering layers crucially combine their function as anti-reflection coating with their ability to trap light inside the thin absorber substrate to maximally enhance the optical absorption. While optimization routines for their nanoscale geometry have become well established for monochromatic conditions (e.g. light-emitting diodes (LEDs) [100, 101], photonic power converters [102, 103], or grating couplers [104, 105]), optimizing the combined anti-reflection and light trapping properties for broadband illumination conditions remains remarkably challenging. At the same time, it directly impacts the performance of broadband optoelectronic devices, including photo-detectors [106–108], multi-color LEDs [109–111], and photovoltaics [73, 112, 113].

Light trapping occurs when incident waves are scattered into the plane of the substrate with in-plane momentum components  $k_{\parallel}$  larger than the free-space wave vector  $k_0 < k_{\parallel} \leq k_{\text{Mat}}$ , i.e. into the guided mode regime, where  $k_{\text{Mat}} = 2\pi n_{\text{Mat}} \lambda^{-1}$  denotes the wave vector inside the material with refractive index  $n_{\text{Mat}}$  at free-space wavelength  $\lambda$ . When the thickness of the material is reduced, the continuum of optical states transitions into a finite number of distinct modes. As a consequence, not all photons that attain a  $k_{\parallel}$  within the above interval through diffraction will be effectively trapped and optical absorption is inefficient. As such, light scattering into the plane of the absorber needs to be tailored to the modal structure at each photon energy. Furthermore, since each mode is characterized by a specific dispersive absorption rate, targeting specific modes is key yet often elusive, since the modal dispersion of a full device stack involving multiple layers and nanostructures is not easily obtained.

In literature, the several prototypical geometries have been explored extensively, namely complete order (i.e. periodic gratings) or disorder (fully random). Random roughening techniques such as pyramidal texturing [114] and sandblasting [115] are facile to fabricate but offer little control over the unit cell and size. Instead, to achieve better control, identical unit elements, such as pillars, holes, and non-isotropic shapes, are tailored geometrically to support Mie- [116] or plasmon resonances [82] and placed in optimized (periodic) arrangements [117–120]. There are several models to describe the scattering response of such prototypical geometries, which typically explore an ultimate upper limit for absorption under a restrictive set of assumptions. For thick and weakly-absorbing substrates with random textures, the statistical (Yablonovitch)  $4n^2$ -limit describes the thermodynamic maximum of optical absorptance. This limit has later been extended to also include the strongly-absorbing parts of the spectrum [121], but crucially assumes a continuum of states as well as uniform population of all optical states and is therefore restricted to thick absorbing layers only.

For thin substrates on the other hand, where modal overlap can be neglected, temporal coupled-mode theory (CMT) can find an upper limit for absorption with periodic patterns [122]. The predicted ultimate absorption enhancement is intrinsically narrow-band, and is greatly reduced when broadband enhancement is considered [123]. Furthermore, absorptance is strongly overestimated when the thickness or periodicity is increased and resonances start to overlap. To address this, a model that accommodates overlapping resonances was developed recently [124]. This presents a major step forward to retrieve accurate predictions for the actual absorption enhancements rather than deriving an upper limit for it. Despite its applicability to absorber thicknesses in-between the restrictive cases mentioned above, the model applies only to periodic structures, ignores the scattering properties of the

individual nanostructures within the unit cell, assumes equal coupling rates to all modes and a bulk-like density of optical states that neglects the specific mode structure of the device. These simplifying assumptions often obscure intricate relations between absorption and coupling rates, which give rise to large discrepancies between the model's predictions and experiments.

More recently, structures other than fully random or periodic – such as correlated random or disordered hyperspectral uniformity – have been proposed [99] and initial experiments demonstrate enhanced optical absorption by matching the pattern's spatial frequencies to the modes supported in the thin substrates [55, 125–127]. In this context, there are no models available that accommodate such tailored patterns and go beyond the assumptions described above. As a consequence, finite-element methods which solve Maxwell's equations in spatially and temporally discretized full-wave simulation volume are commonly employed. Forward-design optimizations therein typically employ a single figure of merit (e.g., total absorptance over a spectral range) while varying a range of free parameters, which makes the process computationally expensive and opaque. At the same time, electromagnetic field data obtained from such simulations contain crucial information that can be leveraged to elucidate the role of the scattering unit cell, the arrangement of scatterers, and the geometry of the active layer.

Here, we present a numerical toolbox that employs energy-momentum resolved absorption data retrieved from full-field simulations to offer quantitative insights into mode-resolved absorption and coupling properties. It is compatible with arbitrary (non-periodic) scatterer layouts of considerable size and realistic finite—absorbing—substrate effects, free of restrictive assumptions, and enables physically interpretable optimization beyond brute-force absorptance optimization sweeps. To illustrate its use, we first compare the energy-momentum resolved scattering spectra of a periodic structure on a semi-infinite lossless substrate versus a finite absorptive substrate, and extract mode-resolved absorption efficiencies. Next, we use the toolbox to: (i) investigate the impact of localized resonances within the scattering pattern on the modal; (ii) study modal coupling in aperiodic (Poisson random and hyperuniform) scattering arrays; and (iii) extract modal properties and coupling rates directly from the absorption heatmaps. Numerical quantification of mode-resolved coupling efficiencies, trapping, and absorptive properties offered by our toolbox provides actionable guidance for the design of device-optimized broadband light-scattering nanopatterns and offers data to refine and validate (semi-)analytical models and their assumptions.

## 3.2 Results

To illustrate the situation, we consider the generic case of a plane wave incident on a finite, weakly-absorbing substrate situated on a perfect mirror (Fig. 3.1). For a flat slab (panel a), light impinges perpendicular to the interface and is partly reflected by the front surface and partially transmitted into the substrate. Since the substrate is weakly absorbing, a considerable fraction reaches the perfect mirror at the bottom, where it is reflected. The reflected wave reaches again the top interface, where it is partially transmitted and reflected again. Interference between the downwards and upwards traveling waves gives rise to Fabry-Pérot oscillations in the absorptance (Fig. 3.1c, black) and reflectance spectra, which enhance absorptance at certain wavelengths. All partial waves retain their parallel wave vector (in-plane momentum) in all parts of the system.

A common approach to enhance the optical absorption is to include a periodic corrugation to the top interface (panel b). Indeed, the absorptance (Fig. 3.1c, green) and reflectance spectra are greatly modified by diffraction. The interaction of the normally incident light with

## Quantifying light coupling to guided modes in semiconductor slabs with arbitrary scattering patterns

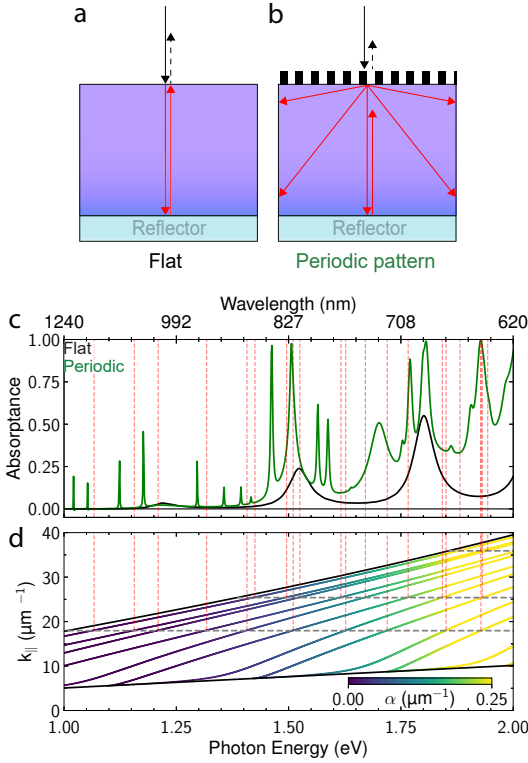


**Figure 3.1: Illustration of light trapping in ultrathin weakly absorbing substrates**

Illustration of a plane wave incident onto a weakly-absorbing slab on a perfect mirror, where the slab surface is either flat (a) or periodically patterned (b). (c) Full-wave FDTD-calculated absorbance spectra for a 500 nm-thick Si slab for a flat (black) and periodically patterned (green) top surface with period  $p = 350$  nm. (d) Dispersion diagram of a 500 nm c-Si slab in air. The lower/upper black solid lines represent the light line in air and silicon, respectively. In between these lies the guided-mode regime, where the colored lines correspond to the dispersion curves of the modes, with the color indicating their dispersive absorption coefficient.

the patterned layer imparts interface-parallel momentum components to the reflected and transmitted partial waves. Due to the periodicity ( $p = 350$  nm), in-plane momenta changes occur in quanta of  $\Delta k_{\parallel} = \sqrt{(2\pi m/p_x)^2 + (2\pi n/p_y)^2}$ , where  $m, n \in \{0, 1, 2, \dots\}$  and  $p_x = p_y = p$  in a square lattice with periodicities  $p_x, p_y$  along the orthogonal directions  $x, y$ , respectively. Comparing the absorbance spectra between these cases (Fig. 1c), we observe a substantial broad-band improvement at photon energies  $E_{\text{ph}} > 1.5$  eV for the patterned slab, while both spectra show similar values at low energies, with the exception of a series of sharp peaks.

To identify the origin of the peaks, one may compare the guided modes supported by the substrate in air with the in-plane momentum offered by the periodic structure (Fig. 3.1d). At their intersection, in-plane momentum matching of a diffraction order of the grating a guided mode is fulfilled, and incident light is coupled to the guided mode to form a guided-mode

resonance (GMR) [92].

The scattering efficiency and coupling to such GMRs at each photon energy crucially depends on the scattering layer properties, such as unit-cell geometry and area filling fraction, leading to greatly varying coupling rates ( $\gamma_e$ ) across the energy spectrum. At the same time, the intrinsic loss rate ( $\gamma_i$ ; corresponding to optical absorption) equally depends on photon energy and the momentum of the individual modes through the group velocity ( $v_g$ ):  $\gamma_i = \alpha_m \cdot v_g$  [128]. Here,  $\alpha_m$  is the mode's absorption coefficient, which is color coded in Fig. 3.1c. However, comparing the absorption peaks in Fig. 3.1b with the crossings in Fig. 3.1c shows that the GMR peaks are clearly displaced from the crossing points. The observed spectral shifts result from the modified modal dispersion due to the nanopatterned grating on top of the absorber, which is neglected in simple mode solvers. The large variations in peak height, on the other hand, clearly highlight that there are strong variations in the relative rates at which light is coupled in/out of the GMRs and absorbed by the GMR throughout the spectral range of interest. Finally, an additional complication in the description of the scattering properties is the presence of the interference fringes (i.e. Fabry-Pérot), which are commonly ignored in conventional CMT models.

This simplified example of a periodic structure on a thin slab already highlights the challenge: wavelength and angle-dependent scattering properties of the individual nanoparticles, strongly varying absorption coefficients, and non-negligible Fabry-Perot complicate the optical absorption far beyond the realms of established models. Additionally, more complex non-periodic and non-random structure factors for broadband scattering layers further challenge the established models [129]. As such to optimize light scattering and absorption in such advanced devices approaching the theoretical limits, scattered power and momentum distribution for all photon energies need precise quantification, and the ability to track their dependence on the design parameters becomes crucial.

### 3.2.1 Toolbox for Light Trapping Analysis

Here, we propose a numerical toolbox that enables detailed quantification of energy and momentum-resolved light absorption in arbitrarily complex scattering layers and systems. The methodology is outlined as follows: the device layers are set up in a FDTD simulation environment (Fig. 3.2a). The source injects a plane wave towards the stack, which is absorbed either by materials in the stack or the perfectly-matched layer (PML) boundary located above the source plane. Electromagnetic fields are calculated in discrete time intervals until the residual power residing in the system falls below a predetermined auto-shutoff threshold (see methods). Two monitors are used to record the local electromagnetic fields and power flux in reflectance (between the PML and source) and inside the flat absorbing layer close to the scattering interface where light is transmitted into the substrate. Since only the net transmitted power is stored in the monitors (the difference between the transmitted power in both directions normal to the monitor plane), the transmittance monitor contains only the power fraction absorbed in the device. Due to its close vicinity to the scattering layer, the recorded power contains both contributions from the evanescent near-fields of the scattering units as well as propagating modes in the uniform absorber layer. Next, we perform a near-to-far-field transformation of the transmitted near-fields (Fig. 3.2b). In essence, this transformation decomposes the local near-field data into a set of plane waves of different wavevectors. By selecting only physical solutions, the evanescent portions are omitted and only propagating waves are retained. From the coefficients of the basis set of sine waves, we obtain the angular distribution (in-plane momenta  $k_{\parallel}$ ) of the absorbed power fractions within the absorbing layer (Fig. 3.2c), which resemble a diffraction pattern or back-focal

## Quantifying light coupling to guided modes in semiconductor slabs with arbitrary scattering patterns

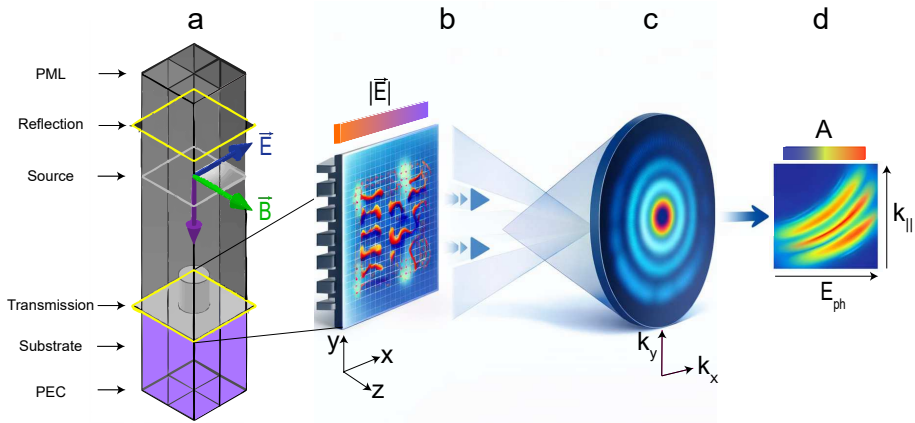


**Figure 3.2: Methodology to obtain energy and momentum-resolved absorption** (a) Employ finite-difference time-domain simulations to obtain near-field profiles inside the (finite) substrate close to the scattering layer. (b) Perform near- to far-field transform to retrieve propagation properties. (c) Radial averaging of in-plane momentum distribution  $|k_{||}|$  at each photon energy. (d) Integrate scattered power into specific momentum channels to display absorbance and coupling efficiencies for specific guided modes.

plane image in Fourier space. From this, we calculate the radially-averaged absorbance versus  $k_{||}$ -magnitude at each photon energy and display the result in an energy-momentum resolved heatmap (Fig. 3.2d). Crucially, this three-dimensional momentum- and energy-resolved data enables the isolation of individual resonant features that would otherwise be indistinguishable in a regular frequency spectrum, and thereby allows one to compute relevant physical quantities of isolated GMRs, such as propagation constant, absorption coefficient, group velocity, and coupling rates to free space channels.

We acknowledge the existence of other numerical toolboxes similar to the one presented here. However, none of these offer simultaneous computation of layer-by-layer momentum-resolved absorbance, coupling rates, and the extraction of mode-dispersion diagrams from the same simulation, and/or are limited to infinite and/or periodic systems. Here, we provide a brief overview of their similarities and differences.

First, RETOP [130] is a dedicated near-to-far-field transformation tool that can operate on near-field data obtained with RCWA, finite-difference and finite-element methods. It allows the extraction of momentum-resolved by-layer absorbance, but has no option to solve for guided-mode resonances, and extract other relevant physical quantities off the shelf. Furthermore, since it is comprised of a MATLAB code collection, the calculations are considerably slower than our method, which uses the multi-processing API of the simulation suite. Second, MANlite [131] is a solver for quasi-normal modes and thus handles absorptive materials, and operates on near-field data sets obtained by the finite-element method. Thereby, it can handle finite systems and disorder, but does not compute (momentum-resolved) absorbance or coupling rates. Third, RETICOLO [132] is an RCWA implementation that only handles infinite, periodic systems. It can provide dispersion diagrams but does not include light excitation, therefore does not compute (momentum-resolved) absorbance or coupling rates. The computational demand of this method increases rapidly when nano-

structures and 3D shapes are included, due to the increased number of necessary momentum points to accurately represent the scattering layer, which practically limits its ability to handle large unit cells and dense scatterer arrangements.

Additionally, analytical approaches to derive dispersion in the presence of small dielectric permittivity perturbations have been developed [133, 134], and Brillouin-Wigner perturbation theory handles also stronger perturbations [135]. Furthermore, finite-difference or finite-element eigenmode solvers (ANSYS [136], COMSOL [137], and more) are in principle capable of finding modes in arbitrary systems. These, however, require pre-existing knowledge to filter out non-physical results, typically do not handle finite and non-periodic systems well, and are incapable of calculating by-layer absorptance and coupling rates. In contrast, our toolkit resolves individual modal absorption contributions and coupling rates between free-space and guided-mode channels in arbitrary three-dimensional, dispersive and non-periodic structures.

### 3.2.2 Principle Demonstration

To illustrate the merits of the toolbox, we first study a model system comprised of a square-lattice periodic grating on a non-dispersive and lossless semi-infinite substrate with  $n = 3.55$ . The most fundamental insight is provided by a heatmap that illustrates the light distribution as a function of the in-plane momentum and photon energy in the substrate as a fraction of the incident power upon a single scattering event (Fig. 3.3a). The white curve denotes the light line in air, which marks the onset of the guided mode regime, and the color represents the fraction of power per unit wavevector normalized to the incoming power at that photon energy. The heatmap shows bright horizontal lines at  $k_{\parallel} = 0$  as well as specific non-zero momentum values.

A periodic grating scatters light exclusively into its corresponding diffraction orders, which, for a square lattice, occur at in-plane momenta given by:

$$k_{\parallel}^2 = (2\pi i/p)^2 + (2\pi j/p)^2, \quad (3.1)$$

with  $i, j \in [0, \pm 1, \pm 2, \dots]$  indicating the diffractive order in the  $x$  and  $y$  direction, respectively, labeled as  $(i, j)$ . The power fraction in each diffraction channel reduces with both decreasing photon energy and increasing diffraction order. The normalized power spectral density (PSD) of the periodic pattern (Fig. 3b) highlights the power diffracted into each order, showing dominant scattering into the  $(i, j) = (\pm 1, 0)$  channel. The decrease in power in this channel for lower photon energies results from the wavelength-dependent scattering efficiency of the grating's unit cell.

For light trapping, the total power fraction scattered beyond the light line in air ( $\equiv k_c$ ) is of particular interest. As such, in Fig. 3.3c, we integrate and classify power fractions at each photon energy as back-scattered (i.e. reflected, red), scattered into the substrate with  $k_{\parallel} < k_c$  (gray), and scattered beyond the light line with  $k_{\parallel} \geq k_c$  (blue). The shaded regions confirm the observation that at low photon energies, nearly all forward scattered power falls within the escape cone, while for larger energies, increasingly more power is diffracted into the guided-mode regime. This analysis provides insights into the grating's scattering efficiency and enables a quantitative study of the coupling strength to specific diffraction orders. As such, it enables the de-convolution of the respective impact of the lattice pitch and unit-cell geometry on the angular scattering profile at each photon energy. For a semi-infinite and lossless substrate, this analysis is limited to a single pass scattering event, and predictions of the exact absorption spectra of a finite absorbing slabs with such periodic patterns remain elusive.

## Quantifying light coupling to guided modes in semiconductor slabs with arbitrary scattering patterns

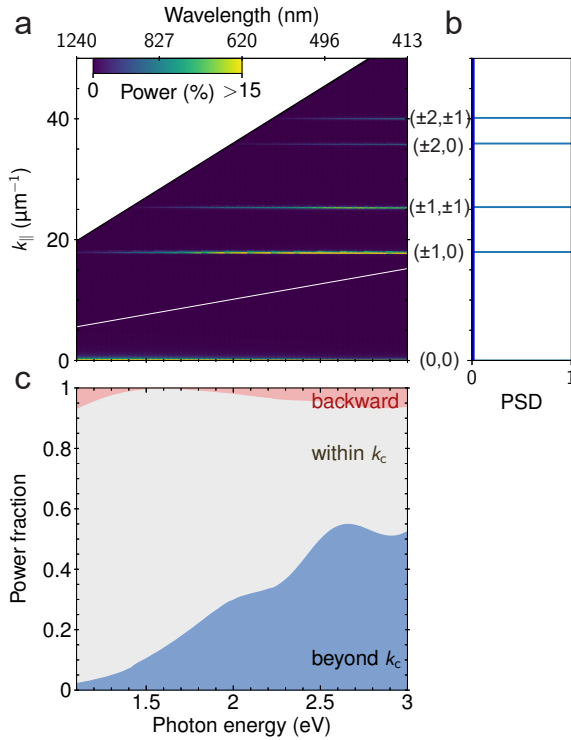


**Figure 3.3: Momentum-energy resolved scattering efficiency of a periodic grating on a semi-infinite, lossless, and non-dispersive substrate**

(a) Power distribution as a function of in-plane momentum and photon energy (color) of incident light scattered into a semi-infinite, non-absorbing substrate ( $n = 3.55$ ) by a periodic grating comprised of pillars with radius  $r_{\text{pillar}} = 75$  nm, height  $h_{\text{pillar}} = 75$  nm, and  $n_{\text{pillar}} = 3.55$ . At each photon energy, the sum over all momenta equals the transmittance into the substrate and, in the absence of absorption, is equal to  $(1-R)$ . (b) Normalized power spectral density (PSD) of the periodic grating. The diffraction channels are labeled by their order in the square lattice. (c) Reflectance (red, top) and integrated transmittance within (gray, middle), and beyond the light line (blue, bottom).

Next, we aim to obtain accurate absorption characteristics for a real thin-film device in which discrete waveguide modes play a central role. As such, we consider a thin (finite) substrate to include the effects of back reflections and interference inside the slab, and also take into account optical absorption in the material. We use the same 500 nm thick slab of c-Si as an example, and place a non-absorbing and non-dispersive periodic grating on its top surface, as well as a perfect reflector underneath (Fig. 3.4). In contrast to Fig. 3.3a, the color scale in Fig. 3.4a now represents the absolute absorptance that includes multiple scattering events inside of the absorber. To do this, we leverage the fact that the near-field monitor data collection only records net transmitted powers. While the methodology remains unchanged, in the previous example, all power transmitted through the grating was eventually absorbed

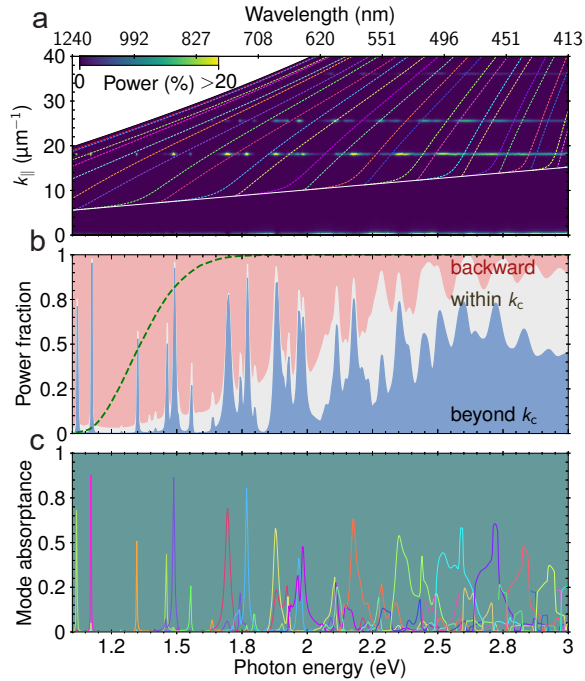


**Figure 3.4: Absorbance in a 500 nm Si substrate on a PEC with a periodic grating**  
 (a) Absorbed power distribution as a function of in-plane momentum and photon energy (color) for a 500 nm silicon slab with periodic grating comprised of pillars with radius  $r_{\text{pillar}} = 75$  nm, height  $h_{\text{pillar}} = 75$  nm and  $n_{\text{pillar}} = 3.55$ . (b) Integrated power fractions for reflectance (red), and absorbance for momentum within (gray) and beyond the escape cone (blue). (c) Extracted modal absorbance highlighting how each individual GMR contributes to the total absorbance in (b). Colors match those in (a).

by the perfect-matched layer (PML) boundary inside of the substrate, thus suppressing any reflection. For a finite absorber, the perfect reflector at the bottom of the layer enables multiple interactions with the scattering layer which enables out-coupling from the substrate. Out-coupled power fractions are subtracted from the monitor data and the remainder solely quantifies power absorbed in the substrate.

The heatmap (Fig. 3.4a) shows similar bright horizontal lines as in Fig. 3.3a, yet here they become strongly modulated across the spectrum, and for  $1 \text{ eV} < E_{\text{ph}} < 2 \text{ eV}$  they appear as distinct spots only at specific photon energies where momentum matching with the grating reciprocal lattice vector is fulfilled (i.e. crossings of solid and dashed lines in Fig. 3.1c). At these specific locations in the momentum-energy ( $k$ - $E$ ) plane, light trapping occurs through the resonant excitation of GMRs. The extreme absorbance enhancements beyond 90 %, e.g. at  $\sim 1.13 \text{ eV}$ , are almost entirely due to scattering beyond the light line, which provides direct further evidence of coupling to these guided modes. Crucially, our numerical analysis enables the integration of the absorbance around distinct spots in the  $k$ - $E$  plane to yield the fraction of light absorbed by coupling to the corresponding GMR. This presents the compelling

## Quantifying light coupling to guided modes in semiconductor slabs with arbitrary scattering patterns

opportunity to identify the (combination of) corresponding guided-mode resonance(s) for each spectral peak and infer their properties using a simple mode solver [138].

To do this, we start with the guided modes of 500 nm c-Si in air, which are displayed as dashed lines and overlaid with the heatmap in Fig. 3.4a. At each photon energy, we can assign the GMRs to the nearest mode and extract its contribution to total absorption (Fig. 3.4c). Similar to Fig. 3.1b, the presence of the nanopatterned grating modifies the modal properties of the slab, and as such the peaks in absorption due to a GMR are slightly displaced from the mode branches that are calculated without taking the grating into account. The scattering layer with sub-wavelength periodicity gives rise to an effective-medium refractive index [139, 140], which red-shifts the guided modes with respect to the assumed air-cladding (i.e.  $n > 1$ ). To take into account this modified modal structure in the analysis, we employ a rationally motivated asymmetric integration environment around each mode in the process of allocating absorbed power to specific modes (see Methods).

We note that the modal decomposition of the absorptance (Fig. 3.4c) aligns well with the peaks observed in Fig. 3.4b, where for most GMRs the majority of absorption is attributed to a single mode and supported by higher-order modes only in small amounts. Especially when GMRs occur at different  $k_{\parallel}$  at a similar photon energy (e.g. around 1.9 eV), the decomposition by modal contribution lends valuable insights into the scattering efficiency and provides the means to de-convolute the effect of light trapping from Fabry-Pérot resonances.

These results so far highlight how our numerical toolkit enables momentum-resolved insights in the absorptance for finite and absorptive semiconductor layers, including the contribution of individual GMRs for fully periodic systems that are already well-studied in literature. In the following, we will capitalize on the generic applicability of our numerical toolbox and turn our attention to scenarios which are recondite or otherwise intractable with other approaches. We first study the influence of localized resonances, before turning our attention to non-periodic systems with varying degrees of spatial correlations.

### 3.2.3 Case Study 1: Impact of Localized Resonances in Scattering Patterns

One of the important assumptions in both the statistical analysis of light absorption in randomly textured thick slabs as well as CMT for thin slabs is that the coupling efficiency to all available modes is identical. This assumption is imperative to simplify the theoretical analysis, yet undermines the complex frequency- and angular dependent scattering response of the individual nanostructures that comprise most scattering patterns. In this first case study, we investigate the influence of localized resonances on the coupling efficiency to waveguided modes. To this end, we analyze and compare the optical absorption for two different pillar heights in an otherwise unchanged scattering layer (Fig. 3.5). The pillar dimensions are  $r = 75$  nm,  $h = 75$  nm (left column) and  $r = 75$  nm,  $h = 175$  nm (right column). By increasing the height above  $\sim 100$  nm, vertical electric and magnetic current loops characteristic of localized (Mie) resonances are supported at lower photon energies, which about triples the scattering efficiency and promotes scattering into larger in-plane momentum values [89]. Analogous to Fig. 3.4b, the area under the curves is subdivided into different shades to denote the fraction of power that is reflected (red), scattered within the escape cone (gray) and beyond (blue). Relative to the total scattering efficiency, the larger pillar scatters more light beyond and less into the escape cone than the smaller pillar, yet at the same time, it shows increased reflectance.

In the integrated power fractions (Figs. 3.5b,e) and as a consequence of the increased pillar height, the peak absorption for most GMR changes and additional peaks appear. As a

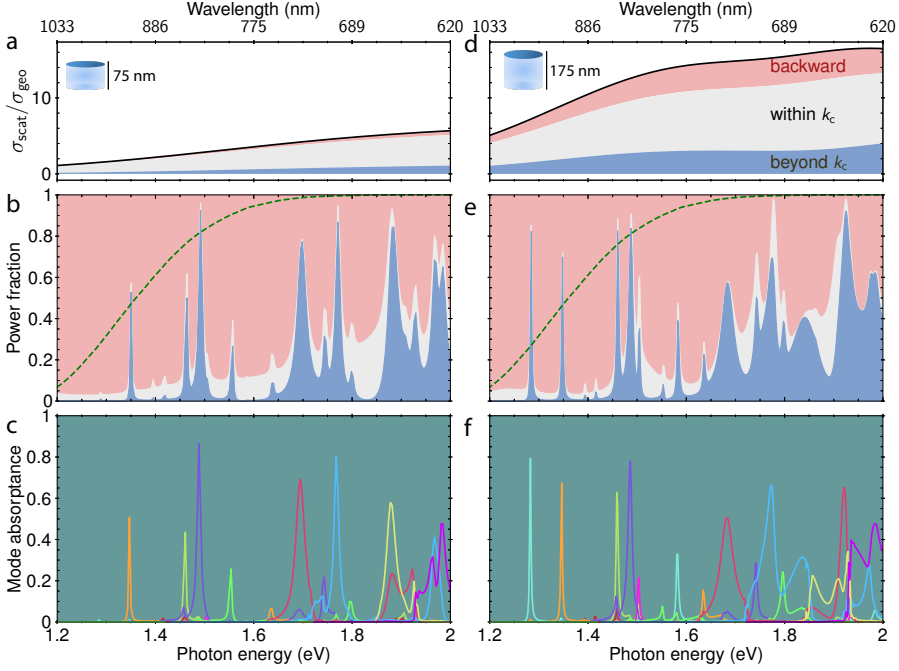


**Figure 3.5: Effect of localized resonances on periodic scattering patterns**

**Top row:** Direction-resolved scattering cross-sections for a pillar ( $r = 75$  nm,  $n = 3.55$ ) with heights  $h = 75$  nm (**a**) and  $h = 175$  nm (**d**) on a semi-infinite, dispersion-less substrate ( $n = 3.55$ ). **Middle row:** Integrated power fractions by momentum and photon energy for back-reflected (red), transmitted into (gray) and beyond (blue) the escape cone for the shorter (**b**) and taller (**e**) pillar in a square lattice ( $p = 350$  nm). Green dashed curve denotes the Lambertian  $4n^2$ -limit [79]. **Bottom row:** Modal decomposition versus photon energy for short (**c**) and tall (**f**) pillar.

result, the GMR peak occurring at  $\sim 1.3$  eV, which is hardly noticeable for  $h = 75$  nm (Fig. 3.5b), becomes strongly pronounced in Fig. 3.5e with a single mode contributing above 50%<sub>abs</sub> to the total absorbance. In contrast to that, the absorption peak at  $\sim 1.48$  eV (purple) decreases in height as the pillar height increases.

Despite being limited in applicability in its conventional form, CMT does offer a very valuable framework to assess the coupling conditions for a single isolated GMR, yet does not apply to strongly overlapping resonance peaks in the absorption spectra. Here, we capitalize on the energy- and momentum-resolved information from the toolbox, which allows one to isolate single resonances by their  $k_{\parallel}$  dependence and in turn, apply the coupled-mode formalism. The amplitude of a GMR in the frequency domain is typically described by a form of the temporal coupled-mode theory equation [122, 141]:

$$A(\omega) = \frac{\gamma_i \gamma_e}{(\omega - \omega_0)^2 + (\gamma_i + N\gamma_e)^2 / 4}, \quad (3.2)$$

with loss-rates  $\gamma_i$  due to internal absorption, and  $\gamma_e$  due to coupling to  $N$  free-space channels,

## Quantifying light coupling to guided modes in semiconductor slabs with arbitrary scattering patterns

at driving frequency  $\omega$  and with resonance frequency  $\omega_0$ .

According to Eq. 3.2, the GMR amplitude is governed by the ratio of flux rates  $\gamma_e$  of the  $N$  input/output ports and the intrinsic loss  $\gamma_i$  of the mode. At critical coupling, i.e.  $\gamma_i = N\gamma_e$ , unity absorptance can be achieved. In broadband optoelectronic devices, one typically achieves the highest averaged absorptance across the spectrum when the system is operated in the over-coupling regime [124]. However, to achieve (near-)unity absorption at resonant frequencies, one would target critical coupling instead. The external coupling rate  $\gamma_e$  increases with the pillar height, while the intrinsic loss remains unchanged. The diminution of the absorption peak at  $\sim 1.48$  eV as a result of increased pillar height is thus indicative of a transition from close to critical coupling to the over-coupling regime  $N\gamma_e > \gamma_i$ , leading to reduced absorptance of the GMR.

The light trapping observed in both examples can yield absorptance beyond the Lambertian  $4n^2$ -limit [79] (green dashed curve in Fig. 3.5c,f) as predicted by coupled-mode theory [122, 123], yet the effect is of narrow-band character and the averaged absorptance stays far below this limit. As evidenced by Figs. 3.4 and 3.5, such a periodic grating, despite being sub-wavelength in its lattice parameter, does not afford a broad-band light trapping effect that is desirable in many optoelectronic applications including thin-film solar cells. In fact, significant absorption enhancement by light trapping is limited to the number of momentum matching conditions between guided-mode branches and diffraction orders. As the periodicity is increased, the number of matches increases. At the same time, however, additional diffraction channels in free space are created. Despite creating more GMRs with the larger periodicity, the overall scattering efficiency diminishes drastically and with it the power scattered beyond the light line (cp. Fig. 3.11).

### 3.2.4 Case Study 2: Modal Coupling in Aperiodic Scattering Arrays

In order to obtain absorption enhancements that are truly broad-band in nature, it is necessary to avoid patterns with extreme degrees of order and instead regard nanostructures with continuous PSD features, such as random or correlated-disordered systems. Except for trivial statistical cases, such as the common assumption of homogeneous light distribution across all available in-plane momenta, there are typically no tools available to study the coupling to guided modes, including the effect of spatial correlations and nanoscale geometries on the momentum distribution and absorptance spectrum of broad-band incident light.

We will now apply our toolbox to two distinct cases of aperiodic systems that exhibit continuous features in their PSD (see Fig. 3.6 inset), and thereby can couple incident light to intervals of in-plane momenta rather than single discrete values. Retrieving the modal absorption for such non-periodic structures on thin absorbing slabs lies well beyond what statistical and CMT models can offer, and as such poses a unique model system to assess the capabilities of the numerical toolbox.

The left column in Fig. 3.6 considers a Poisson-random distribution of pillars with  $r = 75$  nm and  $h = 175$  nm (see methods for the pattern generation procedure). The continuous PSD (middle) translates into scattering of light to all available in-plane momenta albeit with varying intensity. Bright lines are visible in the heatmap (Fig. 3.6a) and reveal enhanced absorption profiles that follow the dispersion of the guided modes (see also Fig. 3.1c). Instead of the discrete GMRs seen for periodic examples, here the peaks appear as sub-branches to all available guided modes. In fact, momentum matching conditions occur at any in-plane momentum where the PSD of the pattern and guided modes overlap. At photon energies below  $\sim 1.8$  eV, in-plane momentum values suitable for light trapping fall within an interval of  $k_{\parallel} \in [5, 30] \mu\text{m}^{-1}$ . However, the PSD of the random pattern features significant intensity also

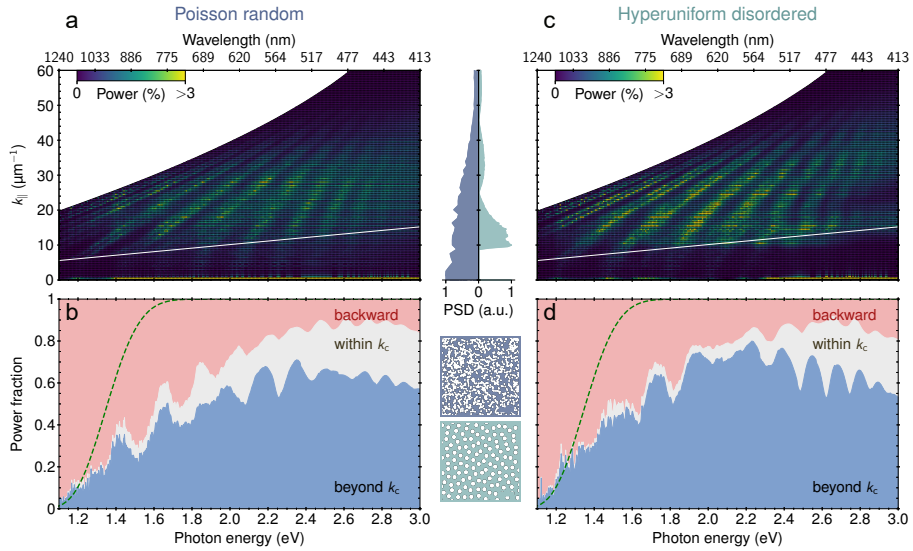


**Figure 3.6: Energy and momentum resolved absorptance for aperiodic scattering layers** Heatmaps (a,c) and integrated power fractions (b,d) are shown for a 500 nm slab of *c*-Si on a perfect mirror, where the top surface of the silicon is patterned with Poisson-random (a,b) or hyperuniform (c,d) arrangement of nanopillars with height  $h = 175$  nm,  $n = 3.55$ , and conformally coated with a 72 nm anti-reflective layer ( $n=1.81$ ). Real space and PSD of the Poisson-random (blue) and hyperuniform (green) pattern are shown in the middle. Green dashed curves in b,d represent the Lambertian  $4n^2$ -limit.

for wavevectors outside of this range. While smaller in-plane momentum values associate with increased escape cone losses, larger in-plane momentum values present in the scattering pattern contribute to haze[142], and thereby reduce the scattering efficiency into the  $k_{\parallel}$ -range of guided modes. As a consequence, the integrated power fractions (Fig. 3.6b) show reduced scattered into the guided-mode regime for photon energies  $1.4 \text{ eV} < E_{\text{ph}} < 2 \text{ eV}$ . Any PSD intensity at  $k_{\parallel} < 5 \mu\text{m}^{-1}$ , on the other hand, leads to scattering within the escape cone and similarly reduces the overall absorptance.

By including some degree of spatial correlations in the pattern generation, the PSD can be tailored without compromising its continuous features for large wavevector intervals. A special class of such arrangements exhibits disordered hyperspectral uniformity, or hyperuniform disorder, which describes a system featuring randomness at small length scale but suppressed density fluctuations at larger scales, thus producing long-range homogeneity in the absence of Bragg peaks [94]. In other words, the PSD vanishes as the momentum approaches zero. In previous works, disordered hyperuniform patterns have shown to result in record-breaking absorption enhancements in ultrathin Si layers[55], which could enhance optoelectronic performance in complete ultrathin Si solar cells [73, 75]. They are of particular interest in broad band optical devices due to their inherent ability to tailor occurrences of specific in-plane momentum values and thereby leverage a non-uniform spectral response with more or less spatial correlations.

In the right column of Fig 3.6, we study a pattern featuring so-called stealthy hyperuniform

## Quantifying light coupling to guided modes in semiconductor slabs with arbitrary scattering patterns

disorder[95, 99]. The term “stealthy” pertains to the property that  $\text{PSD}(k_{\parallel}) = 0$  for  $k_{\parallel} \in [0, k_l]$ , meaning that the PSD is suppressed for all wavevectors up to  $k_l$ , where  $k_l \sim 8\mu\text{m}^{-1}$  in this particular case. Despite the limited number of points in our finite lateral simulation window of  $5 \times 5 \mu\text{m}^2$ , the PSD is strongly suppressed for all  $k_{\parallel} < 8\mu\text{m}^{-1}$  and most of the intensity is concentrated within the interval  $k_{\parallel} \in [9, 18] \mu\text{m}^{-1}$  (see center column and Fig. S3.10), which covers the majority of the guided mode regime down to photon energies of 1 eV. The heatmap reveals that the continuous PSD again results in continuous guided mode resonances that enhance the absorption (Fig. 3.6c), similar to the random pattern in (Fig. 3.6a). Since the PSD is tailored towards  $k$ -values near the Si bandgap, scattering into the GMRs is more efficient than for the random pattern for photon energies up to about 2.2 eV, resulting in strongly enhanced integrated absorption in this spectral range (Fig. 3.6d). In addition, the suppression of small wavevectors results in reduced scattering within the escape cone, which is again corroborated by the small gray-shaded region in the integrated power fractions (Fig. 3.6d).

Since a minimum of about 25 particles is needed to evoke spatial correlations in a simulation environment [59, 143], optimizing these arrangements for specific applications or devices demands significant computational resources and time, yet provides minimal insight into why certain parameter sets yield better performance than others. With our toolkit, the precise contribution to absorption in terms of momentum and energy domains can readily be retrieved and impacts of parameter variations traced to the coupling conditions of individual modes.

### 3.2.5 Case Study 3: Extracting Coupling Rates and Modal Properties

As observed in Fig. 3.4a, the modal structure of a device obtained through mode solving of a simplified device layer structure typically provides incorrect dispersion curves. Here, we instead retrieve the modal properties directly from the absorption heatmaps as function of momentum and energy, and analyze the properties of guided-mode resonances in both domains simultaneously. In literature, absorption peaks are generally analyzed in the frequency domain only, and contain information from all accessible in-plane momentum contributions, i.e. from all modes with resonances in the frequency interval  $\Delta\omega$ . With our approach, we can select small  $\Delta k_{\parallel}$ -intervals and examine the resonance peak versus photon energy of guided-mode resonances in isolation and extract their specific properties. Hence, the additional dimension of momentum provides an artisanal circumvention of the common obstacle of overlapping resonance peaks in the absorption spectrum. By combining the information from both domains, we retrieve the mode propagation and absorption parameters directly from the simulation data. Extracted real mode data of this kind allow to gauge (semi-)analytic models, validate their assumptions, analyze the impact of changes that yield identical results (e.g. pillar height), and extend models to previously elusive cases such as non-periodic, correlated-random or other designs featuring more exotic PSDs and (multiple) scatterer geometries.

As an example, we examine an excerpt (Fig. 3.7a) of the heatmap in Fig. 3.6b and extract slices at 1.247 eV (Fig. 3.7b) and at  $k_{\parallel} = 20.5 \mu\text{m}^{-1}$  (Fig. 3.7c) and observe GMRs in both energy- and momentum domain separately. The GMR occurring at the crossing of the slices differs significantly in shape and full width at half maximum (FWHM) when viewed in either domain, despite reaching approximately the same peak absorbed power fraction. We fit a series of Lorentzians to the peaks in both domains in order to quantify their properties (dashed lines). The peak position of the lorentzian fits corresponds to the propagation constant  $\beta$  of the mode associated with the GMR, while the FWHM in the energy domain  $\text{FWHM}_e$  relates to the modal

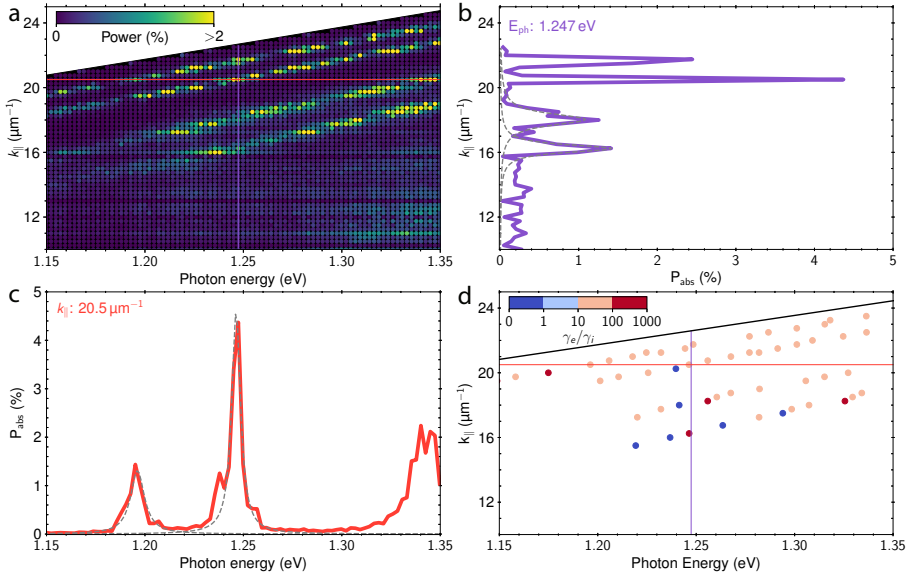


**Figure 3.7: Retrieving modal dispersion from energy-momentum heatmaps**

(a) Excerpt of the heatmap Fig. 3.6b with colored lines indicating slices in momentum- (vertical) and energy space (horizontal) used for (b,c). (b) Slice of  $k_{||}$  versus absorbed power fraction at 1.246 eV with Lorentzians fitted to the GMR peaks (dashed gray curves). (c) Slice of absorbed power fraction versus photon energy at  $k_{||} = 19.75 \mu\text{m}^{-1}$  and Eq. 3.2 fitted to the central GMR peak (dashed gray curve). (d) Detected GMR peaks are plotted with color denoting the quotient of the rates  $\gamma_e/\gamma_i$  (coupling condition), which are extracted from fits such as in (c).

loss rate  $\text{FWHM}_e = 2\gamma_i$ . From the quotient of the  $\text{FWHM}_{e/m}$  in the energy-/momentum domain, respectively, we can extract the group velocity  $v_G = d\omega/dk \equiv \text{FWHM}_e/\text{FWHM}_m$ .

Next, we leverage the fact that a single peak can be isolated and fit Eq. 3.2 to the GMR peak in the energy domain to extract  $\gamma_e, \gamma_i$  and  $N$  directly from the simulation. From this, we calculate the coupling condition  $\gamma_e/\gamma_i$  and use this to color-code the identified GMRs in Fig. 3.7d. The PSD of the hyperuniform pattern (Fig. 6) lies exclusively outside of the escape cone in the examined energy range, therefore we set  $N = 1$ . We observe that most GMR are moderately over-coupled with  $30 < \gamma_e/\gamma_i < 130$ , and only a few detected peaks are under-coupled. None of the peaks are close to critical coupling  $\gamma_e/\gamma_i = 1$ . As opposed to investigating a single GMR's response to a change in the scattering layer design parameters, Fig. 3.7d reveals the impact for a large collection of GMRs in momentum and energy domains simultaneously. With this method, changes to pattern parameters can be traced to the coupling condition of individual GMR across the entire energy and momentum range, thus providing insightful figures of merit for optimization routines targeting specific applications.

Altogether, these three examples demonstrate the ability to, on the one hand, analyze the impact of local scatterer geometry on the coupling rates to individual GMRs, and, on the other hand, trace the momentum space distribution of light when scattered by arrangements of scatterers that exhibit complex disordered PSD signatures. Furthermore, we show that by application of the CMT formalism, guided-mode parameters are extractable directly

## Quantifying light coupling to guided modes in semiconductor slabs with arbitrary scattering patterns

from energy- and momentum-resolved absorptance heatmaps, which allow gauging the predictions of dispersion analysis from analytical models. In the future, we plan to utilize the insights provided by the toolbox to combine individual particle scattering responses with the momentum distribution of their structural arrangement to advance existing models of absorptance and dispersion in complex device architectures.

### 3.3 Conclusions

In summary, we provide a novel numerical method to study light absorption and coupling to waveguide modes in arbitrary scattering structures on thin semiconductor slabs, enabling quantification of coupling efficiencies well beyond the established frameworks for fully random or periodic structures. Since the numerical method relies solely on a far-field projection of the local electromagnetic fields, this analysis is also applicable to engineered random designs that exhibit correlations over large length scales. Using a periodic geometry as a model system, we reveal the complex momentum- and energy-dependent scattering efficiencies into distinct diffraction channels for semi-infinite and lossless substrate. Next, we highlight how the model offers a quantitative assessment of the absorptance of individual and discrete optical modes in thin semiconductor slabs. We apply the toolkit to three case studies that are incompatible with the assumptions and abilities of existing models. First, we investigate the effect of localized resonances in the periodic unit cell and qualitatively assess their impact on the coupling condition of GMR across the momentum-/energy landscape. Second, we simulate large domains of patterns with and without strong spatial correlations, which result in improved broad-band absorptance by offering continuous bands of diffraction channels rather than discrete values as their periodic counterparts. By classifying absorbed power fractions by their in-plane momenta, we show how the PSD of the scattering layer dictates the coupling into the guided-mode regime and can substantially enhance absorptance over large spectral ranges. Third, using a combined analysis of a GMR peak in both momentum and energy space, we illustrate how mode propagation and absorption properties can be extracted directly from energy-momentum absorptance heatmaps and enable calculation of modal coupling rates. Our numerical approach thus proves a versatile tool to aid in the understanding of light coupling and absorption in complex device stacks featuring nano-patterns with arbitrary power-spectral densities and scatterer geometries. It enables the evaluation of critical physical quantities and provides the missing link between simplified analytical models and practical device optimizations.

### 3.4 Methods

#### Simulation Setup and Details

Simulations are performed with the commercial software ANSYS Optics Lumerical. We use 2.5 meV resolution in photon energy and the simulations run until a predetermined auto shutoff level of  $1 \times 10^{-5}$  or less is reached. The shutoff level represents the fraction of the injected energy that has not yet been absorbed by either material or PML. The material constants of c-Si are modeled using 16 coefficients and a tolerance of  $1e-4$  (see fits in Fig. 9). The mesh consists of cubical Yee cells with fixed side lengths  $\leq 5$  nm in the pattern region, while automatic conformal meshing with a minimum mesh size  $\leq 10$  nm is used elsewhere. The largest simulations featuring  $5 \times 5 \mu\text{m}^2$  lateral dimension and 500 nm absorber thickness require approximately 80 GB of RAM.

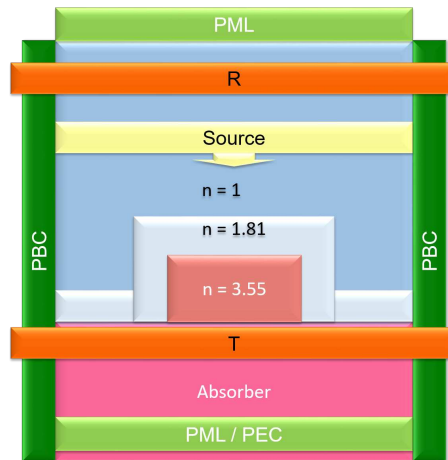


**Figure 3.8: Schematic of the simulation layout**

The boundaries are perfectly-matched layers (PML) at the top and perfect electric conductors (PEC) or PML at the bottom, depending on the type of simulation. Periodic boundary conditions (PBC) are employed at the lateral boundaries. The source injects a plane wave downwards towards the absorber stack. Above the source, the reflection monitor R is located and transmission (T) is recorded at the top of the absorber, one mesh cell below the interface to increase numerical stability. The top interface of the absorber is decorated with the scattering layer with  $n = 3.55$ , which is conformally coated with an anti-reflective layer with  $n = 1.81$ .

The finite absorbing simulations in this work feature a PEC boundary condition and are normalized to power transmitted into the substrate. The scattering layer is a non-dispersive and non-absorbing and thereby introduces artificial discontinuities of  $\epsilon$  at the scatter layer - substrate interface. If instead, the scattering layer is chosen as dispersive and absorbing, transmittance differs from (1-reflectance) by the amount of (parasitic) absorption in the patterned layer, since the transmission monitor is located just below this interface. Here, we choose the non-absorbing scattering layer variant so that the power scattered into the substrate is not affected by parasitic absorption at the expense of increased reflectance by the scattering layer and  $n$  discontinuity.

## Far-Field Projection

The resolution in momentum (the step- or bin size) in the far field transforms is inherently limited by the simulation extent parallel to the monitor used for transformation. In the case of periodic patterns, this limit can be extended indefinitely by using multiple periods for the transformation. For aperiodic structures, however, increasing the far field periods imposes artificial diffraction orders and modifies the momentum space result.

The computational demand of the transformation is related to the number of Yee cells in the monitor data as well as the resolution chosen for the virtual screen onto which the expanded waves are projected. Hence, the resolution in the far field needs to be sufficient to account for the desired momentum resolution, which itself is limited by the lateral extend in the case of aperiodic patterns.

## Quantifying light coupling to guided modes in semiconductor slabs with arbitrary scattering patterns

The finite lateral dimension gives rise to a sinc envelope in the projection, since the fields at the simulation boundaries are truncated. To ensure any ensuing line broadening is comparable for all simulation types, comparable source field dimensions are employed. Here, the number of periods and far field resolution are determined by the desired momentum resolution  $k_{\text{step}}$  according to the formula:

$$p_{\text{FF}} = 2 \times S_{\text{sourcefield}}, \quad (3.3)$$

with the targeted source field extent  $S_{\text{sourcefield}} = 2\pi/k_{\text{step}}$ . If the lateral extend ( $l$ ) of an aperiodic pattern is smaller than ( $S_{\text{sourcefield}}$ ), the number of periods is chosen as  $p = S_{\text{sourcefield}}/l + 1$ .

The resolution of the far field screen is determined by the required number of bins at each wavelength through the formula:

$$R_{\text{FF}} = 4 \times k_{\text{max}}/k_{\text{step}} + 1, \quad (3.4)$$

where  $k_{\text{max}} = 2\pi n_{\text{mat}}/\lambda$  denotes the maximum wavevector of light in the material of refractive index  $n_{\text{mat}}$  in which the monitor is embedded. The pre-factor 4 is introduced to account for both positive and negative momentum values, and the maximum resolution afforded by the source field extent, while the added one results in exactly one bin at  $k_{\parallel} = 0$ .

Next, the desired momentum resolution is translated into solid angle steps, in which the far field projection is integrated to obtain the fractions of power scattered up to the momentum value of each integration step. The heatmaps result from the difference between integrated far field power fractions of adjacent momentum bins and represents the total scattered power into each momentum bin.

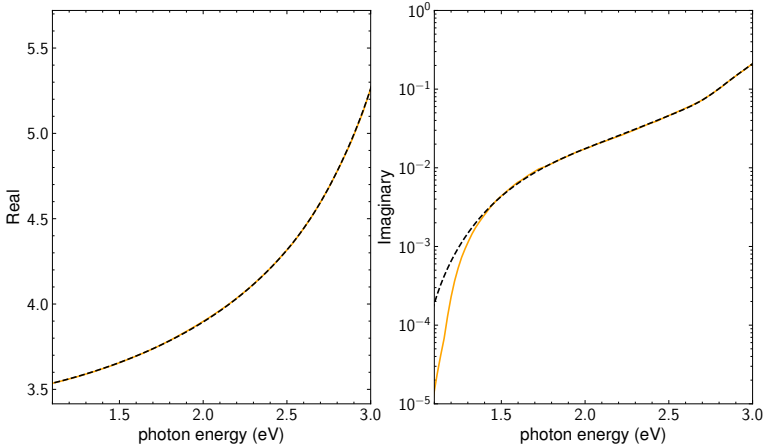


**Figure 3.9: Refractive index fits for silicon**

The material constants are approximated using a polynomial function with 16 coefficients for the (1-3) eV range. The fit over-estimates absorption below  $\sim 1.3$  eV, which significantly accelerates convergence at these photon energies, but has no bearing on the mutual comparability among simulations.

## GMR Modal Attribution

To attribute GMRs to modes obtained with the simple mode solver [138] in the presence of a distorting nanopattern, we proceed as follows: Beginning with the lowest mode order, we collect the absorptance in the  $k_{\parallel}$  vicinity at each photon energy. Since a cladding with increased refractive index causes a red-shift of the modal dispersion, this implies larger  $k_{\parallel}(\omega)$  of the actual modes. To accommodate the shift, we expand the integration environment asymmetrically towards the maximum in-plane momentum or the propagation constant  $\beta$  corresponding to the previous mode order.

For the zeroth mode, the integration interval at each  $E_{\text{ph}} = \hbar c k_0$  thus comprises  $\beta^0 - 2dk < k_{\parallel} < k_{\text{max}} = k_0 n_{\text{mat}}$  with propagation constant  $\beta^0$  from the simple mode solver for mode order 0, the momentum step size (bin size) of the heatmap  $dk$ , and the maximum momentum  $k_{\text{max}}$  within the material of index  $n_{\text{mat}}$ . For mode order  $n$ , the interval changes to  $\beta^n - 2dk < k_{\parallel} < \beta^{n-1} - 2dk$ . In this manner, double counting of GMRs is avoided at the expense of a preference for attributing absorption to lower mode numbers. Furthermore, all power scattered into the guided mode regime will be attributed to a mode.

## Random Pattern Generation

Coordinates are generated using the NumPy [144] random discrete number generator based on the PCG64 method. At each coordinate, a pillar is added within a  $5 \times 5 \mu\text{m}^2$  area until a filling fraction of approximately 50% is achieved. In order to avoid truncation artifacts due to imposed periodic boundary conditions in the lateral direction of the simulation volume, periodic boundary conditions for the placement of pillars are employed. The finite lateral size combined with the periodic boundary conditions impose a small degree of spatial correlation [129] and artificial diffractive orders at in-plane momentum intervals of  $1.26 \mu\text{m}^{-1}$ .

## Peak Detection and Coupling Condition Calculation

In the slices of absorption versus momentum or energy taken from the heatmaps, peaks are detected using the RamanSPY [145] python package. In momentum space, standard Lorentzian functions are fitted to peaks with a prominence (peak amplitude over background) above 0.2% at each photon energy, from which the key parameters center, amplitude and full-width at half-maximum (FWHM) are extracted. In energy space, we fit Eq. 3.2 to the peaks in order to extract  $\gamma_e, \gamma_i$  directly. We use  $N = 1$  if the PSD shows no significant intensity below  $k_c$  (sub-wavelength periodicity and hyperuniform pattern). Further physical quantities are extracted by combining the fit parameters from both energy and momentum domain, such as the group velocity  $v_G = d\omega/dk = \text{FWHM}_e / \text{FWHM}_m$  from the ratios of the  $\text{FWHM}_{e,m}$  from fits in energy and momentum space, respectively, and in turn the mode refractive index  $n_m = c/v_G$  with light speed in vacuum  $c$ .

## 3.5 Supplementary Information

### Real Space Design and PSD of patterns

Fig. 3.10 shows distinct power spectral densities for three different configurations. The PSD of periodic (a) features sharp peaks at the momentum values corresponding to the diffraction orders, while the PSD in case of a random pattern (b) is continuous across the frequency spectrum with diminishing intensity. The correlated-disordered, or hyperuniform distribution

## Quantifying light coupling to guided modes in semiconductor slabs with arbitrary scattering patterns

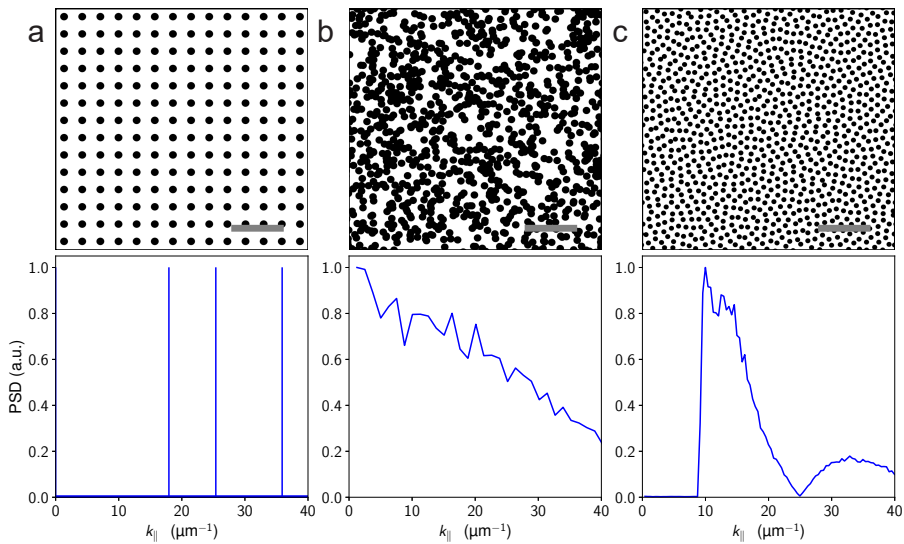


**Figure 3.10: Real space images and PSD of the investigated patterns**

*a* periodic, *b* random, *c* hyperuniform-disordered pillars. Top row: Real space images, scale bar  $1\ \mu\text{m}$  in *a, b* and  $5\ \mu\text{m}$  in *c*. Bottom row: Normalized power spectral density calculated from real-space images above.

of disks in (c) shares features with both periodic and random: A continuous intensity delimited within a certain range of momentum values with no intensity below a threshold momentum value  $\sim 8\ \mu\text{m}$ .

### Additional Simulations

To highlight the effect of sub-wavelength periodicity on scattering beyond the escape cone, Fig. 3.11 shows the same pillar configuration as in Fig. 4 of the main text for periodicities  $p = 350, 600,$  and  $900\ \text{nm}$ . A larger periodicity increases the number of diffraction orders available for scattering at the expense of reduced scattering efficiency into each order and additional diffraction orders into free space for wavelengths that are smaller than the period. In the integrated power fractions, the power scattered beyond the escape cone diminishes steadily as the periodicity increases and with it the overall absorptance. At low photon energies, significant absorptance enhancements can still be observed and quantified by analyzing the coupling conditions as demonstrated in case study 3 of the main text.

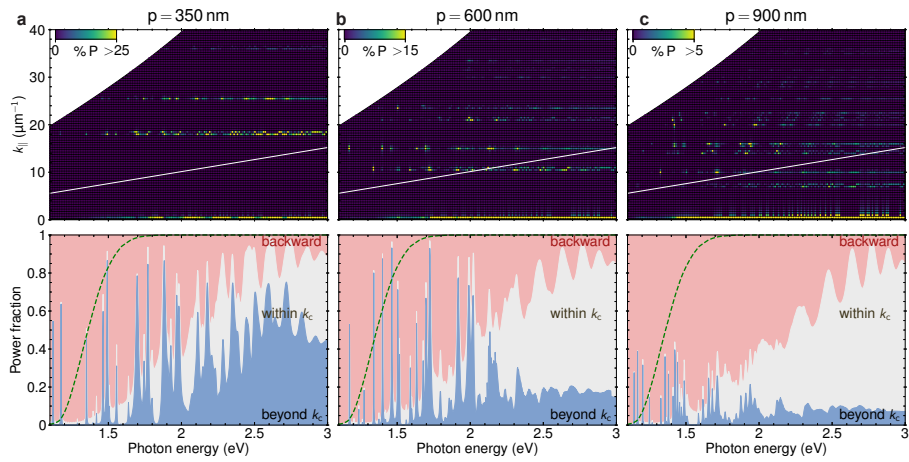


**Figure 3.11: Periodic grating of pillars on 500 nm Si for different periodicities**

The pillar dimensions are equivalent to Fig. 4 of the main text with  $h = 75$  nm and  $r = 75$  nm. The periodicities are 350 nm (a), 600 nm (b), and 900 nm (c). Top row: Heatmaps of the absorptance versus momentum and energy. Bottom row: Integrated power fractions of reflectance (backward, red), and absorptance in the substrate subdivided into fractions within (gray) and beyond (blue) the escape cone.



# 4

## Integrating Hyperuniform Disordered Light Trapping Layers in Ultrathin c-Si Solar Cells

In ch. 2, we introduced theoretical concepts of hyperuniform disordered arrangements (HUD) and investigated their anti-reflective and light-trapping properties with a numerical toolbox in ch. 3. Their ability to couple incident light of a broad spectrum to multiple guided modes of a thin weakly-absorbing layer, while avoiding escape cone losses, affords HUDLE patterns superior absorptance enhancements compared with periodic and random patterning approaches. Ultrathin crystalline silicon solar cells require advanced light trapping to compensate for weak near-infrared (NIR) absorption. Here, we integrate HUDLE nanopatterns with high-quality surface passivation in  $4.8\ \mu\text{m}$  c-Si cells and demonstrate robust device operation enabled by broadband coupling to guided modes. HUDLE layers enhance the fraction of power scattered beyond the escape cone by up to 30 % in the NIR and increase average EQE by > 50 % over flat cells and 10 % over periodic designs from 750 nm - 1000 nm. We directly compare periodic and hyperuniform nanopatterns and show that the continuous spatial frequency distribution of HUDLE leads to more homogeneous coupling of light into guided modes. Importantly, this optical enhancement is achieved without compromising open-circuit voltage or fill factor, demonstrating compatibility between advanced nanophotonics and high electronic quality in ultrathin devices. These results establish hyperuniform disorder as a powerful photonic design strategy for ultrathin silicon photovoltaics.

## 4.1 Introduction

The increasing global demand for sustainable energy sources has driven the development of solar cell technologies, with crystalline silicon (c-Si) solar cells dominating the photovoltaic market [146]. Despite their dominance, conventional c-Si solar cells face limitations in terms of weight, cost, and flexibility, particularly for emerging applications such as building-integrated photovoltaics and in the mobility sector [147]. A promising approach to overcome these limitations is to reduce the thickness of c-Si absorbers to the micrometer scale [40, 114]. However, c-Si solar cells with absorber thickness below  $10\mu\text{m}$  experience severe optical losses [114], as conventional light-management strategies—such as micron-scale pyramidal texturing—are incompatible with such thin devices [41, 148]. To compensate, advanced nanoscale light-trapping schemes must enhance absorption without degrading electronic quality. At these thicknesses, surface recombination becomes a dominant source of dark current, and any increase in surface area from nanostructuring proportionally intensifies recombination losses, resulting in reduced open circuit voltage and fill factor [149–151]. This creates a stringent trade-off between optical enhancement and electronic performance.

Recent advancements in nanofabrication and light trapping strategies have shown promise in improving the performance of ultrathin Si solar cells [77, 114]. Pattern design strategies to enhance light absorption include periodic arrays of inverted nanopylamids [73, 74, 152] and nanocones [78], random patterns through deep reactive ion etching [153] or using a random nanoparticle mask [154, 155], multi-resonant periodic arrays [75, 156, 157], and engineered random patterns [143, 158]. Control over light scattering in these structures is afforded by diffraction orders of the periodic arrays [74], localized Mie resonances [116], or a combination of both [75, 159, 160]. Building on these advances, power conversion efficiencies up to 13.7% [78] and 15.7% [73] have been achieved with solar cells of only  $10\mu\text{m}$  thickness.

To enable high-efficiencies with even thinner absorber layers requires scattering patterns that are tailored to the wafer thickness. Here, the scattering properties of engineered random light trapping structures with disordered hyperspectral uniformity (or hyperuniform disorder, HUD) [94] presents a compelling opportunity: the placement of Mie-like scatterers in a mutual spatial arrangement that exhibits long-range uniformity yet no sharp diffraction peaks. Instead, the ensemble features a bounded but isotropic and continuous interval of spatial frequencies, thereby combining advantages of periodic and random patterns instead of sacrificing one desirable property for the other [99, 113, 161].

This work experimentally validates broadband guided-mode coupling in functioning ultrathin solar cell devices by integrating Hyperuniform Disordered Light Engineered (HUDLE) scattering patterns with  $4.8\mu\text{m}$ -thick c-Si absorbers. Our device architecture intentionally omits a metallic back reflector, thereby providing a clean platform to directly probe the front-surface scattering efficiency of the HUDLE layer into large in-plane momenta. While the strong scattering capabilities of HUDLE layers were previously demonstrated through enhanced absorption in  $1\mu\text{m}$ -thick c-Si slabs,[55] here we show that the broad scattering frequency band of the HUDLE results in more efficient near-infrared photocurrent generation compared to periodic patterns. Using spectrally resolved reflectance and external quantum efficiency measurements in combination with wave-optics simulations, we directly correlate the structure factor of hyperuniform patterns with their momentum-resolved scattering response in a functioning ultrathin device. We show that the continuous spatial frequency band of HUDLE textures enables broadband coupling of near-infrared photons into guided modes, in contrast to the discrete diffraction channels of periodic lattices. Importantly, despite the increased surface area introduced by HUDLE nanostructuring, we experimentally demonstrate that the open-circuit voltage and fill factor remain uncompromised, confirming

that the intricate hyperuniform textures are compatible with high-quality surface passivation in ultrathin architectures.

Together, these results establish hyperuniform disorder as a powerful framework for engineering light–matter interactions in optically thin semiconductor slabs.

## 4.2 Results and Discussion

### 4.2.1 Integration of Hyperuniform Nanopatterns into Ultrathin Devices

To experimentally probe enhanced optical absorption in ultrathin light absorbers, we integrate hyperuniform disordered light engineered (HUDLE) nanopatterns into 4.8  $\mu\text{m}$ -thick c-Si solar cells fabricated on silicon-on-insulator substrates (Fig. 1a). The absence of a metallic back reflector in this architecture ensures that light trapping arises solely from front-surface scattering, providing a controlled platform to directly evaluate coupling into large in-plane wave vectors beyond the escape cone (Fig. 1b). By comparing flat, periodic, and hyperuniform nanopatterns fabricated on the same wafer, we isolate the role of the spatial frequency distribution in governing guided-mode excitation and photocurrent generation.

The spatial frequencies in both the HUDLE and periodic nanopatterns were carefully designed to maximize the absorption of the solar spectrum. Arrays of sub-wavelength structures can scatter and diffract incident light into the absorbing layer beyond the escape cone of light (i.e. at angles beyond the critical angle) [162]. This leads to total internal reflection and thereby light trapping if the in-plane momentum of scattered light matches those of the guided modes of the thin-film absorber [163]. Crucially, the distribution of the scattered light across the range of wave vectors directly dictates the (subset of) guided modes into which light is coupled. Here, guided modes are standing-wave solutions to Maxwell's equations in the absorbing layer that enable in-plane propagation, thereby strongly increasing the optical path length. This is essential for ultrathin devices where a wide range of photon energies are not fully absorbed within a single-pass through the absorbing layer, since a 5  $\mu\text{m}$ -thick c-Si film only absorbs  $< 50\%$  at wavelengths  $\lambda \gtrsim 750 \text{ nm}$  (See supplementary information Fig. 4.6). Namely, light trapping is particularly crucial for near infrared (NIR) photons.

To illustrate this, Fig. 4.1b shows the angular distribution of light scattered off the (patterned) air-silicon interface. Light entering silicon through a flat surface (i.e. without nanostructuring, left) will acquire in-plane momenta exclusively within the escape cone. As such, light trapping cannot occur. Applying a periodic structuring with a periodicity  $p$  on the order of the wavelength of light (middle) introduces diffractive orders at distinct in-plane momenta  $k_{\parallel} = \sqrt{(2\pi m/p)^2 + (2\pi n/p)^2}$ , where the integers  $m, n \in \{0, \pm 1, \pm 2, \dots\}$  represent diffraction orders along the mutually orthogonal 2D lattice directions. The angles associated with these  $k_{\parallel}$  can lie beyond the escape cone and result in light trapping, but only at discrete wavelengths where  $k_{\parallel}$  matches one of the guided modes [122]. In contrast, the continuous spatial frequencies in hyperuniform disordered nanopatterned surfaces (right) offer a continuous range  $k_{\parallel} \in [10, 20] \mu\text{m}^{-1}$ , which falls within the momentum range of the guided modes at the edge of the light line (see Fig. 4.7). This facilitates optimal access to guided modes in the absorber over a broad spectral range, while minimizing reflection losses within the escape cone.

The engineered nanopatterns are transferred into functioning devices by etching approximately 245 nm into the top layer of the solar cell stack. To enable statistically meaningful

## Integrating Hyperuniform Disordered Light Trapping Layers in Ultrathin c-Si Solar Cells

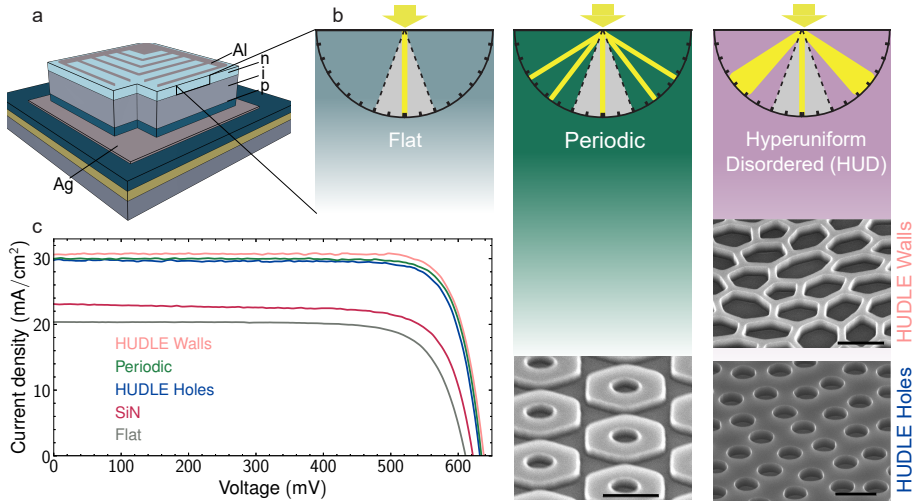


**Figure 4.1: Schematic, operation principle, and performance metrics of 4.8  $\mu\text{m}$ -thick c-Si solar cell devices**

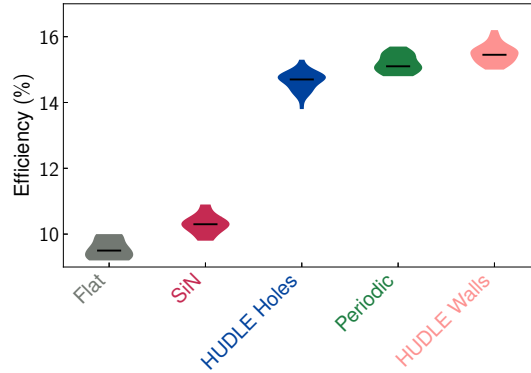
(a) Sketch of the ultrathin solar cell device grown on a silicon-on-insulator (SOI) wafer with an initial device layer thickness of  $2\ \mu\text{m}$  to serve as the seed, on top of a  $500\ \text{nm}$  buried silicon dioxide layer separating the device from the  $500\ \mu\text{m}$  thick Si handle wafer. (b) Illustrative representation of light scattering and diffraction through different surface morphologies: flat (left), periodic nanopattern (middle), and hyperuniform disordered nanopattern (HUD, right). The corresponding scattering patterns into the substrate are highlighted as yellow lobes in the polar plots where the gray shaded area indicates the escape cone of light. Scanning Electron Micrographs of Periodic and two HUDLE designs are also shown (scale bars:  $500\ \text{nm}$ ). (c) Current-voltage characteristics obtained at 1-sun illumination for the best performing solar cell of each type.

comparisons, large-area ( $\text{cm}$ -scale) fields of each design (two HUDLE designs, one periodic reference and unpatterned) are defined on the same wafer. After etching, we passivate the front surface by subjecting the wafer to dry thermal oxidation to form a layer of silicon dioxide. Part of the unpatterned wafer is also subjected to  $\text{SiN}_x$  deposition, to improve anti-reflectance. Individual  $1.6 \times 1.6\ \text{mm}^2$  devices are subsequently formed by mesa isolation and contact deposition. Note that the p-type contact is not formed as a full-area back electrode but is instead contacted laterally at the mesa sidewalls, such that no reflective metallic layer is present beneath the active area, and thus ensuring that optical enhancement originates from front-surface scattering rather than cavity effects (see device sketch Fig. 4.8). This fabrication approach yields  $\sim 25$  of nominally identical devices per pattern type, all processed and passivated simultaneously on the same wafer. As a result, differences in performance can be directly attributed to the nanopattern design rather than variations in material quality or processing conditions.

The current–voltage ( $J$ – $V$ ) characteristics of the best-performing cells of each pattern type under AM1.5G illumination are shown in Fig. 4.1c, with the corresponding photovoltaic parameters summarized in Fig. 4.2a. As a baseline, the flat cell with  $\text{SiO}_2$  passivation already reaches  $\sim 90\%$  of the single-pass absorption limit of  $4.8\ \mu\text{m}$  Si (Fig. 4.6). Adding a  $\text{SiN}_x$  anti-

Table 1: Photovoltaic parameters for the best devices

Pattern	$J_{sc}$ (mA cm <sup>-2</sup> )	$V_{oc}$ (mV)	FF (%)	Efficiency (%)
Flat	20.4 ± 0.4	618	79.1	10.0 ± 0.3
SiNx	23.1 ± 0.5	622	76.2	10.9 ± 0.3
HUDLE Holes	29.8 ± 0.6	632	81.3	15.3 ± 0.5
Periodic	30.0 ± 0.6	634	82.3	15.7 ± 0.5
HUDLE Walls	30.6 ± 0.6	638	82.7	16.2 ± 0.5

**Figure 4.2: Photovoltaic parameters and efficiency statistics**

(a) Table of performance parameters for the best solar cells of each type. (b) Statistical spread and efficiency comparison of the same set of devices ( $N = 25$  for patterned/flat,  $N = 9$  for  $\text{SiN}_x$ ), demonstrating reproducible performance across nanopattern types.

reflection layer further increases the short-circuit current density by  $\sim 3 \text{ mA/cm}^2$ , yielding  $J_{SC} = 23.1 \text{ mA/cm}^2$ , close to the double-pass absorption limit of the SOI stack ( $\sim 25 \text{ mA/cm}^2$ ). This confirms the excellent electronic quality of the p-i-n junction and charge collection. The high  $V_{OC}$  of the unpatterned cells further indicates effective surface passivation, which is particularly critical for ultrathin absorbers where surface recombination dominates [164, 165].

Introducing nanopatterns at the front surface substantially enhances device performance through combined anti-reflection and light-trapping effects. The structured cells exhibit up to a 50 % relative increase in  $J_{SC}$  compared to the flat reference. In addition, all patterned devices maintain fill factors above 80 % and show consistently high  $V_{OC}$  values, indicating that the increased surface area does not introduce additional recombination losses. Dark  $J$ - $V$  analysis using the two-diode model [166] (Fig. 4.9) reveals comparable recombination parameters ( $J_{01}$ ) for flat and patterned cells, confirming preserved surface passivation quality. This demonstrates that hyperuniform nanopatterning can be integrated into ultrathin silicon solar cells without compromising the electrical performance.

We note that the best-performing device, incorporating a HUD wall network, reaches a very high power conversion efficiency of  $(16.2 \pm 0.5) \%$ . Although this value is derived from unmasked measurements and is therefore not intended as a certified record, all device types were fabricated on the same wafer and characterized under identical conditions. As such, the relative differences in efficiency directly reflect the impact of the nanopattern design. Fig. 4.2b shows the statistical distribution of efficiencies measured across multiple devices fabricated on the same wafer. The median efficiencies confirm the systematic improvement for the nanopatterned designs, particularly in the HUD wall network. The small device-to-device variation highlights the robustness of the platform and enables statistically meaningful

comparison of the different nanopattern geometries.

## 4.2.2 Spectrally-Resolved Characterization

While the current–voltage characteristics establish overall performance differences between the nanopattern designs, they do not reveal the spectral origin of these enhancements. To disentangle anti-reflection effects from genuine light-trapping contributions, we perform spectrally resolved reflectance and external quantum efficiency (EQE) measurements for flat and patterned device types (Fig. 4.3a and b, respectively). The shaded regions in b-d visualize the uncertainty of the EQE measurements, which are dominated by fluctuations of the incoming laser power.

To interpret the spectral response, we distinguish between two wavelength regimes:  $\lambda < 600$  nm and  $\lambda > 800$  nm. At short wavelengths, absorption in silicon is sufficiently strong that most photons are absorbed within a single pass through the 4.8  $\mu\text{m}$ -thick device. As a result, interference features are largely absent in this spectral range, and (1-R) therefore predominantly probes the anti-reflective (AR) performance of the front surface rather than any absorption enhancement from light trapping.

The presence of nanopatterning improves AR compared to the flat reference, as expected. Among the patterned designs, the periodic structure exhibits the strongest AR performance. This trend is consistent with its highest air filling fraction (Periodic: 46.6%; HUDLE Walls: 45.7%; HUDLE Holes: 31.7%), which lowers the effective refractive index of the patterned layer and thereby reduces the index contrast at the air–silicon interface. At the same time, the spectral position of the reflectance minimum differs between the designs, indicative of variations in the effect of the  $\text{SiO}_2$  overlayer formed during oxidation. Because all patterns share the same wafer and oxide thickness, the anti-reflection condition cannot be independently optimized for each structure.

At short wavelengths, the EQE shows a similar trend to (1-R). Since (1-R) closely represents absorption within the device in this wavelength range, the ratio  $\text{EQE}/(1-R)$  serves as a proxy for the internal electrical quantum efficiency ( $\text{IQE}_{el}$ ) (Fig. 4.3c).  $\text{IQE}_{el}$  gives insights into extraction efficiency of photo-generated electron-hole pairs, and, to a large extent, is independent of the photon energy that created the electron-hole pairs [167]. All devices here show similar  $\text{IQE}_{el}$  values of approximately 75% – 80% for  $480 \text{ nm} < \lambda < 580 \text{ nm}$ , confirming that nanopatterning does not significantly affect carrier collection efficiency. The sharp decrease in  $\text{IQE}_{el}$  for  $\lambda < 470$  nm is attributed to parasitic absorption in the front contact, which is typical for c-Si homojunction devices [168].

At longer wavelengths ( $\lambda > 800$  nm), (1-R) no longer directly represents absorption in the active layer, as it includes both useful absorption and parasitic absorption in the underlying silicon substrate. In this regime, all (1-R) spectra exhibit pronounced Fabry–Pérot (FP) oscillations, consistent with the free spectral range expected from the 4.8  $\mu\text{m}$  device thickness together with the additional 2  $\mu\text{m}$  silicon seed layer. These high-frequency oscillations are further modulated by lower-frequency FP features arising from the 500 nm buried  $\text{SiO}_2$  layer. The amplitude of the FP oscillations in (1-R) is strongly reduced by the presence of the nanopatterns. This suppression indicates that a significant fraction of incident light is redistributed into large in-plane momenta beyond the escape cone, thereby diminishing coherent back-reflection within the stack. The resulting damping of interference fringes provides first evidence of enhanced light trapping by the nanopatterns.

We further assess the light-trapping performance of the different nanopatterns by evaluating the ratio  $\text{EQE}/(1-R)$  (Fig. 4.3d). In general,  $\text{EQE}/(1-R) = \text{IQE}_{opt}(\lambda)\text{IQE}_{el}(\lambda)$ , where

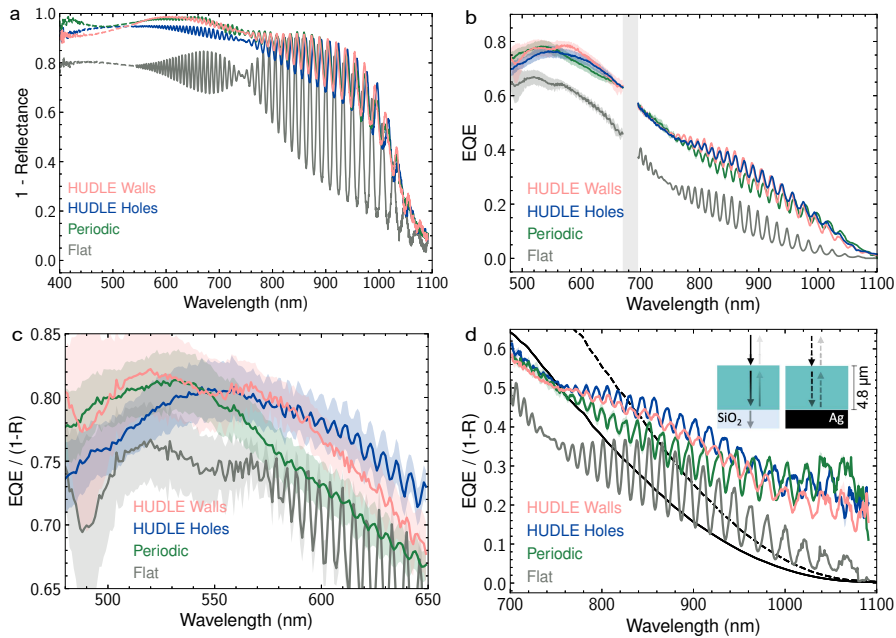


**Figure 4.3: Spectral optoelectronic analysis**

Measured  $(1-R)$  (a) and external quantum efficiency (b) spectra of flat and patterned cells. Reflection measurements are collected using two different setups, where the spectral regions of each setup are indicated using dashed and solid lines (see methods section). The shaded region in (b) highlights the wavelength range that is inaccessible to our experimental set-up. EQE divided by  $(1-R)$  for visible (c) and NIR (d) spectral ranges. The double-pass absorption limit of a  $4.8\ \mu\text{m}$ -thick Si slab on  $\text{SiO}_2$  mirror (black solid line) and on Ag mirror (black dashed line) is also shown in (d).

$IQE_{opt}$  denotes the probability of a photon to be absorbed within the active layer [169]. Assuming comparable carrier extraction properties among all devices (i.e., similar  $IQE_{el}$ , as supported by Fig. 4.3c), which is reasonable given their common wafer origin and identical junction and back-contact architectures, variations in  $EQE/(1-R)$  in the near-infrared can be attributed primarily to differences in  $IQE_{opt}$ . Under this assumption, the HUDLE designs exhibit the strongest light-trapping performance in the (750 – 950) nm spectral range. While the periodic pattern enhances  $IQE_{opt}$  by  $\sim 30\%$  relative to flat, HUDLE structures achieve an improvement of nearly 65%, corresponding to an additional  $\sim 30\%$  gain over the periodic design.

For reference, we also calculate the optical absorption of a  $4.8\ \mu\text{m}$ -thick Si layer on either  $\text{SiO}_2$  or an ideal Ag mirror (solid and dashed black curves, respectively), assuming zero front-surface reflectance. These configurations represent the double-pass absorption limits for our device thickness. Notably, all nanopatterned designs exceed this limit for wavelengths above  $\sim 850\ \text{nm}$ , providing further evidence of enhanced optical path length through guided-mode excitation. Altogether, the combination of reflectance and quantum efficiency measurements gives evidence that our hyperuniform designs more efficiently trap light inside the absorbing

layer in the NIR spectral region. In the following, we examine the origin of this improved light trapping by investigating the light scattering properties of HUDLE layers.

### 4.2.3 Hyperuniform Light-Trapping Mechanism

Generally speaking, efficient light trapping requires suppressed scattering within the escape cone ( $k_{\parallel} < k_c$ ), while enhancing redistribution of light into large  $k_{\parallel}$  to couple to guided modes. The angular scattering response of a nanostructured interface is governed by the convolution of individual scatterer response (form factor) and their spatial correlations (structure factor), yielding the power spectral density (PSD). The PSD defines the distribution of spatial frequencies for coupling light into the waveguide modes of the slab.

HUDLE patterns are engineered such that their structure factor vanishes near  $k_{\parallel} = 0$  (similar to periodic patterns) and exhibits a continuous band of spatial frequencies within a prescribed interval  $k_1 \leq k_{\parallel} \leq k_2$  [55]. See, for instance, the real-space point distribution and structure factor of the HUDLE holes pattern (Fig. 4.4a). The suppressed density fluctuations at large length scales produces a broad annular feature in momentum space while maintaining a “dark” central region (Fig. 4.7). When scatterers are placed at these hyperuniform locations (e.g. holes), the resulting PSD, given by the squared-Fourier transform of the real space image (Fig. 4.4b), extends beyond the ideal HUD interval due to convolution with the scatterer form factor. Crucially, however, the suppression of small  $k_{\parallel}$  and the continuous momentum distribution are preserved, as shown by the PSD of the holes pattern in Fig. 4.4b, right. Hyperuniformity therefore ensures both minimal small-angle scattering and broadband access to guided-mode momenta.

To elucidate the spectral dependence of this behavior, we analyze the response of the individual hole geometry embedded at the air-Si interface (Fig. 4.4c,d). A cross-sectional SEM image of an as-fabricated HUDLE Holes sample is displayed in Fig. 4.4c, with a dashed frame highlighting an individual hole. The calculated scattering cross section of such an individual hole, embedded in a non-absorbing, dispersion-less medium ( $n = 3.5$ ) and coated with 55 nm of SiO<sub>2</sub>, exhibits resonances corresponding to localized dipolar and Fabry-Pérot-like modes (green triangles in Fig. 4.4d). To highlight the differences in directionality, we also plot the breakdown of scattering power over the different angular ranges in Fig. 4.4d. Importantly, a substantial fraction of the forward-scattered power is directed beyond the escape cone, particularly at longer wavelengths near the dipole resonance. This indicates that the basic scattering unit preferentially redistributes near-infrared photons into large in-plane momenta and thereby provides coupling to guided modes. However, the overall device response cannot be understood from single-scatterer behavior alone. The full optical response arises from the interplay between individual scattering resonances and the collective spatial correlations encoded in the structure factor. We therefore simulate the complete nanopatterns and evaluate the  $k_{\parallel}$ -resolved transmitted power (Fig. 4.5).

Figure 4.5a,c,e show the calculated fractions of scattered/transmitted power (color scale) as a function of in-plane momentum and photon energy for all nanopattern types. The HUDLE Holes pattern (Fig. 4.5a) distributes scattered power continuously across the engineered momentum band (indicated by dotted white vertical lines) and maintains substantial scattering beyond  $k_c$  throughout the near-infrared range. This broad redistribution of in-plane momenta ensures sustained coupling to guided modes even at longer wavelengths. More specifically, the integrated power fractions (Fig. 4.5b) show that throughout the entire spectrum, the HUDLE Holes pattern redirects more than a third of the incident power beyond the escape cone in a single pass through the scattering pattern. This fraction decreases at

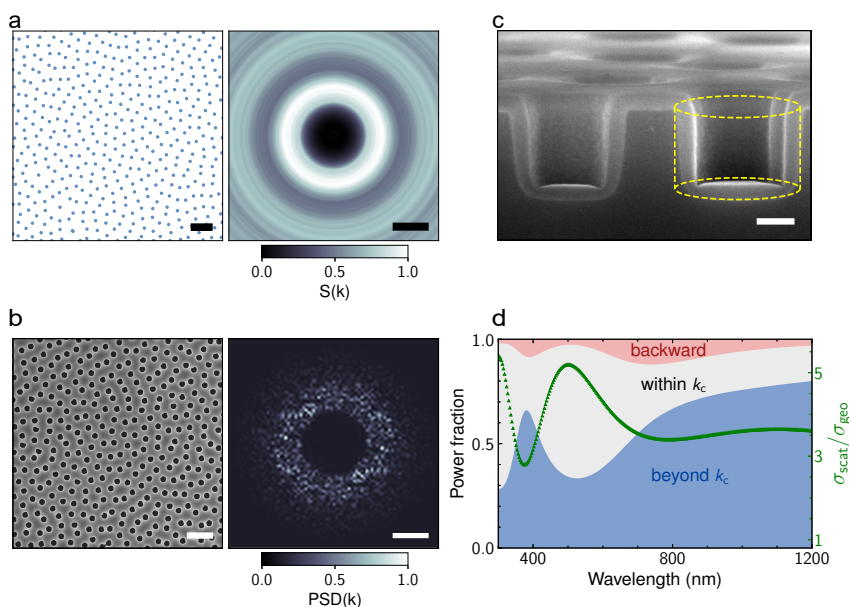


**Figure 4.4: Light trapping mechanism of HUDLE layers**

(a) HUDLE Holes real space locations (left) and their corresponding structure factor  $S(k)$  (right). (b) SEM image of an as-fabricated HUDLE Holes pattern (left) and 2D fast-Fourier transform (FFT, right), obtained from it after Otsu thresholding and subtracting its mean intensity. Scale bars in (a) and (b) are  $1\ \mu\text{m}$  and  $10\ \mu\text{m}^{-1}$  for real- and Fourier space images, respectively. (c) Cross-sectional SEM image of the as-fabricated sample with HUDLE Holes pattern, where the scattering object is highlighted by a dashed frame and the scale bar is  $100\ \text{nm}$ . (d) Scattering cross-section (green triangles) and direction-resolved scattered power fractions of a typical scattering object of the HUDLE Holes pattern; a hole ( $n=1$ ) coated with  $55\ \text{nm}$   $\text{SiO}_2$  located at a silicon-air interface ( $n_{\text{Si}}=3.5$ ,  $k_{\text{Si}}=0$ ) of  $180\ \text{nm}$  radius and  $245\ \text{nm}$  height. Power fractions are displayed as shaded areas with reflection at the top (red), forward scattering into the escape cone ( $k_{\parallel} < k_c$ ) in the middle (gray), and forward scattering beyond the critical angle ( $k_{\parallel} > k_c$ ) at the bottom (blue).

lower energies, which is in equal parts due to increasing reflectance and small-angle forward scattering.

In contrast, the periodic design redistributes light into a limited number of discrete diffraction orders (Fig. 4.5c). As the wavelength increases, the number of diffraction orders beyond the light line decreases, which reduces the fraction of power coupled into guided modes and limits near-infrared light trapping. The total fraction of power scattered beyond  $k_c$  scales with the number of diffraction orders available [75]. The consequences at small photon energies are clearly seen in the breakdown of scattered power (Fig. 4.5d), where the power scattered beyond the escape cone drastically drops for energies  $< 1.5\ \text{eV}$  ( $830\ \text{nm}$ ).

Finally, the HUDLE Walls (Fig. 4.5e,f) exhibit a similar overall behavior, but with the scattered power more strongly concentrated within the engineered momentum interval of the design. This corresponds to the pronounced peak in their PSD (Fig. 4.7), more closely

## Integrating Hyperuniform Disordered Light Trapping Layers in Ultrathin c-Si Solar Cells

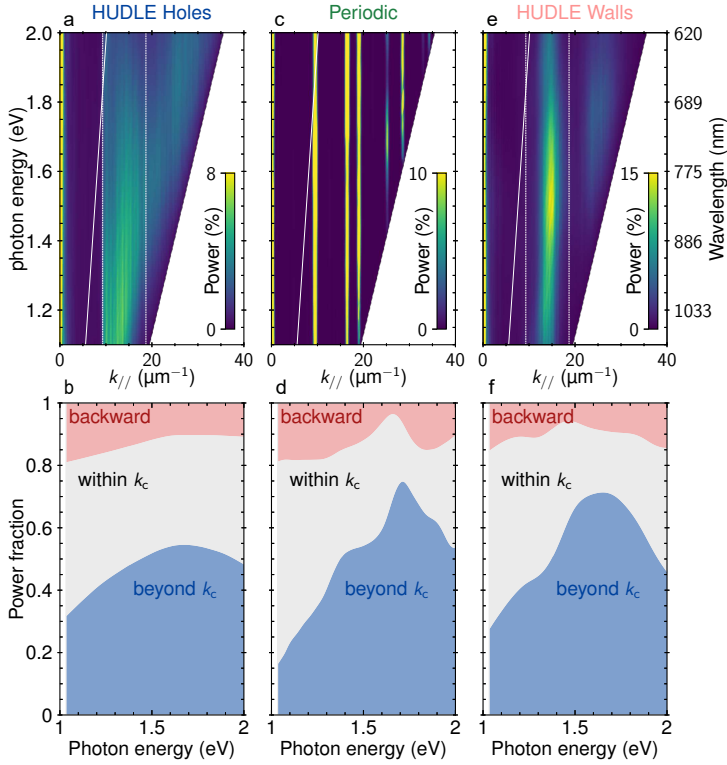


**Figure 4.5: Momentum-resolved light trapping analysis of complete patterns**

Top row: Simulated power distribution of light transmitted through a semi-infinite air-Si interface as a function of in-plane momentum and photon energy for the HUDLE Holes pattern (a, left), Periodic (c, middle) and HUDLE Walls (e, right). The white solid line represents the light line (critical angle) and vertical dashed lines denote in-plane momentum limits of the HUD design. Bottom row: Integrated power fractions of light scattered by the nanostructures. Reflected power fraction (backward) shown in red at the top, power scattered into the escape cone (within  $k_c$ ) gray in the middle, and power scattered beyond the critical angle (beyond  $k_c$ )  $k_{\parallel} > k_c$  in blue at the bottom for Periodic (b), HUDLE Holes (d), and HUDLE Walls (f) as a function of photon energy.

resembling a periodic structure. Comparing the integrated power scattered beyond the escape cone for the different designs (Fig. 4.5b,d,f) reveals that both HUDLE patterns redistribute a larger fraction of light into  $k_{\parallel} > k_c$  in the near-infrared than the Periodic, consistent with their enhanced  $IQE_{\text{opt}}$ . Among the two hyperuniform designs, the HUDLE Holes exhibit the highest fraction of power beyond  $k_c$  in the NIR, in direct agreement with their superior  $IQE_{\text{opt}}$  in this spectral range.

Altogether, the combination of (i) suppressed small-angle scattering and (ii) broadband, continuous momentum redistribution overlapping with the guided-mode dispersion enables hyperuniform nanopatterns to outperform periodic designs in ultrathin absorbers. This momentum-space picture provides a direct physical explanation for the superior near-

infrared  $IQE_{opt}$  measured in the HUDLE devices.

#### 4.2.4 Final Remarks

The device architecture presented in this work is not intended to maximize absolute power conversion efficiency. Instead, it serves as a controlled platform to directly probe front-surface scattering and guided-mode coupling in ultrathin absorbers. Despite the high material quality and excellent surface passivation demonstrated by the preserved  $V_{OC}$  and fill factor, the current device stack contains intrinsic limitations. The thick emitter and  $2\ \mu\text{m}$  seed layer introduce parasitic absorption, and the lack of a reflective back interface prevents recovery of light scattered below the critical angle. The persistence of Fabry–Pérot oscillations in the long-wavelength reflectance spectra indicates that a non-negligible fraction of incident light remains in the zeroth diffraction order and is not redistributed into high in-plane momenta.

We predict that replacing the buried oxide with a Ag mirror and further improving the anti-reflection coating in the  $5\ \mu\text{m}$ -thick solar cell with the periodic pattern would yield an increase in efficiency of more than 3%<sub>absolute</sub>, resulting in  $\sim 19\%$  efficient devices (assuming unchanged values for  $V_{OC}$  and fill factor, see Fig. 4.10). We expect similar improvements for the HUDLE devices.

Finally, we note that the electron-beam lithography used here to create the nanopatterns is incompatible with industrially-scalable solar cell fabrication. Ideally, the nanopatterns are created using vacuum-free processes at room temperature and are completed in a single or few steps. At the same time, large-area nanofabrication methods compatible with both our feature sizes and industrial throughput have previously been published [170, 171] and realized for solar cells. These include substrate-conformal nano-imprint lithography [172, 173] and engineered self-assembly methods adapted to produce the feature sizes and spatial correlations presented in this work [125, 126].

### 4.3 Conclusion

In summary, we demonstrate the integration of hyperuniform disordered nanopatterns into  $4.8\ \mu\text{m}$ -thick crystalline silicon solar cells and establish their photonic operation through combined electrical measurements and momentum-resolved simulations. By intentionally omitting a metallic back reflector, our device platform isolates front-surface scattering and enables a direct assessment of coupling into large in-plane wave vectors.

Spectrally resolved reflectance and EQE measurements allow us to separate optical and electronic contributions to device performance. We show that all nanopatterns preserve electronic collection efficiency, with comparable  $IQE_{el}$ , open-circuit voltage, and fill factor. In contrast, hyperuniform designs substantially enhance the optical contribution to the internal quantum efficiency,  $IQE_{opt}$ , in the near-infrared spectral range.

Numerical simulations reveal that this enhancement directly correlates with increased redistribution of optical power beyond the escape cone and broadband overlap of the hyperuniform momentum band with the guided-mode dispersion of the ultrathin absorber. Compared to periodic patterns, hyperuniform textures maintain stronger scattering into large in-plane wave vectors at long wavelengths, leading to superior near-infrared photon-to-electron conversion.

Our results establish hyperuniform disorder as a robust nanophotonic strategy for ultrathin silicon photovoltaics and provide a framework for designing scattering layers tailored to specific absorber thicknesses.

## 4.4 Materials and Methods

### Design Optimization

The HUDLE Walls design is generated according to the method described by Florescu et al. [99], and the optimization of HUDLE Holes and HUDLE Walls for ultrathin silicon solar cells is described elsewhere [55]. The hexagonal periodic pattern with a periodicity of 765 nm is based on a ring-resonator design with dimensions tailored to support Mie resonances in the near-infrared spectral range.

### c-Si Epitaxial Growth

A 4.8  $\mu\text{m}$ -thick c-Si layer is grown by reduced-pressure chemical vapor deposition (RPCVD) at 1000 °C on a (100)-oriented SOI wafer. The thickness of the buried oxide layer of the SOI is 500 nm and the device (seed) layer is 2  $\mu\text{m}$ . The epitaxially grown c-Si multilayer consists of  $p^+/p/i/n/n^+$  doped layers of (600/300/2800/300/600) nm thickness, respectively, from the seed layer to the top of the device. Doping levels are analyzed using 4-point probe measurements and are found to be  $(8 \cdot 10^{19}/1 \cdot 10^{18}) \text{ cm}^{-3}$  for  $(p^+/p)$  with boron dopants and  $(5 \cdot 10^{19}/1.2 \cdot 10^{17}) \text{ cm}^{-3}$  for  $n^+/n$  layers with phosphorous dopants, respectively. A cross-sectional sketch of the solar cell stack is displayed in Fig. 4.8.

### Nanostructure Fabrication

The nanostructures are fabricated using electron-beam lithography (EBL), using a RAITH Voyager system. A positive tone resist AR-P 6200 (CSAR 62, 4% in Anisole) is spin-coated on the epitaxially grown c-Si, exposed, and developed in penta-acetat, ortho-xylene, and Methyl isobutyl ketone (MIBK)/isopropanol (IPA) ratio 9:1. The reactive ion etch of Si (Lam Research TCP 9400 Poly Etcher) uses 100 sccm HBr, 40 sccm  $\text{Cl}_2$ , 5 sccm  $\text{O}_2$ /He at a background pressure of 6.0 torr and 250 W forward RF power.

### Solar Cell Fabrication

Individual cells are galvanically isolated by a sequence of optical lithography using a Heidelberg instrument MLA 150, followed by resist development and Si etch of 4.3  $\mu\text{m}$  to reveal the  $p^+$ -doped layer at the base of the solar cell stack. We use the same etch recipe as above. After mesa etching and resist removal, the wafer is placed into a dry oxidation oven at 1000 °C to grow 55 nm silicon dioxide on all exposed Si surfaces. Next, 80% of the wafer is covered while the exposed regions receive 31 nm of  $\text{SiN}_x$  using plasma-enhanced chemical vapor deposition (PlasmaTherm Shuttlelock). This thickness is chosen to minimize reflection while accounting for the 55 nm  $\text{SiO}_2$  underneath. Front contact regions are defined using optical lithography (Heidelberg system). Subsequently the  $\text{SiO}_2$  (and  $\text{SiN}_x$ ) in the contact regions is removed using 20:1 buffered oxide etch. Electron-beam evaporation is used to deposit the contact layers consisting of Ti/Al (10/300 nm). Subsequently, the same procedure is repeated to deposit NiOx/Pt/Ag (5/40/160 nm) as the back contact layers. Finally, the wafer is placed in a rapid thermal annealer (RTA AllWin 610) in forming gas at 450 °C in order to reduce contact resistance between the Si and metal layers. The cells' active areas measure  $(0.0196 \pm 0.0004) \text{ cm}^2$  without front metal contacts, obtained through calibrated microscope images (See Figs. 4.12-4.14). Only the active area is used for calibration of the current density and justified by additional EQE measurements with light excitation only on the bus bars,

contacts, and next to the cell mesa (Fig. 4.11), which show negligible current contribution from metalized or galvanically isolated regions.

## JV-Curve Measurements

We use a Newport Solar simulator (94062A Class ABA) as a source that outputs an AM1.5G spectrum. The intensity is close to one sun but can vary by a few percent. The intensity is measured using a calibrated solar cell (Newport Oriel 91150V Reference Cell and Meter) before and after each measurement of every device. Current measuring and voltage sourcing are performed by a source-measure unit (Agilent B2902A). Measurements are performed with two leads which combine voltage sourcing and current sensing through the same contact point. Each cell's *JV*-curve is measured four times in direct succession. Selected cells are also measured in a different setup using a G2V solar simulator and Keithley 2400 SMU and show power conversion efficiencies within the range of uncertainty of the first setup.

## Dark-JV Measurements

We use a Keithley 2450 SMU and four point probes to perform the *JV* measurements in the dark. The voltage is swept manually with an array of set voltage points since the currents are close to the sensitivity limit of the device of  $\sim 10$  fA. At each point, the voltage drop across the cell is measured and then multiple current measurements with 200 ms integration time are performed. Measured values that are within 2 % of each other are averaged and others discarded. If the current measurement deviates by more than an order of magnitude from the adjacent current points, it is likewise discarded. The obtained spectra are analyzed using the 2-diode-model [174] to extract the dark saturation current densities as well series and shunt resistance.

## Reflectance

Reflectance is measured using two different setups for wavelengths  $400 < \lambda < 550$  nm and  $550 < \lambda < 1100$  nm, in which calibration is performed using either a flat polished silicon reference wafer or a protected silver mirror (Thorlabs PF10-03-P01) for the latter range. The setup for short wavelengths is a reflectance/thickness meter (Filmetrics F40). The setup for longer wavelengths is based on a Witec  $\alpha$ 300R microscope using a  $5\times$  objective (NA=0.13) and a halogen illumination source.

## External Quantum Efficiency

The EQE setup is custom-built using a Witec microscope, a super-continuum laser (NKT), and an acousto-optic tunable filter (NKT SuperK Select). A pre-amplifier (Stanford Research Systems SR570) and a lock-in amplifier (Stanford Research Systems SR830) are used for current measurements. The incoming laser is periodically interrupted by a chopper wheel rotating at (40 – 65) Hz. The spot size measures approximately  $50\ \mu\text{m}$  in diameter and is placed in the center between the metal fingers. No optical or electronic biasing is applied. The optical power at the sample position is measured with a power meter (Thorlabs PM100D), and the electronic readout circuit is gauged with a calibrated Si photodiode (Thorlabs FDS1010-CAL). The AM1.5G spectrally-averaged and integrated EQE spectra fall short of the measured  $J_{SC}$  from *JV* measurements but retain the relative difference between patterning types. This is partly due to the inaccessibility of the full wavelength range necessary for faithful comparison

## Integrating Hyperuniform Disordered Light Trapping Layers in Ultrathin c-Si Solar Cells

and partly to the absence of biasing. The latter reduces effectiveness of charge-separation by the p-i-n junction as well as conductance in the highly p-doped layer at the cell base, which also transports carriers laterally to the metal back contacts located at the circumference of the cell. As a consequence, there is increased recombination in the dark regions of the cells. Since this systematic error is equivalent for all pattern types and measurements, the relative EQE comparison remains valid.

### Angular-Resolved Scattering Analysis

All simulations are performed using the finite-difference time-domain (FDTD) simulation software (ANSYS Lumerical 2023 R2.3). The scattering cross-section of a single hole (Fig. 4.4d) is obtained using a total-field/scattered field (TFSF) source with large lateral dimensions  $4 \times 4 \mu\text{m}^2$  and collected using a 3D monitor box from which all scattered intensities are integrated. For the power fractions in Fig. 4.4d, only the monitors parallel to the source-plane are used, which capture most of the forward/backward directed scattering power independently. Through far field transformation of the near fields captured by the monitor inside the substrate, the in-plane momenta of the scattered intensities are obtained and integrated for the ranges within and without the escape cone.

For the full HUDLE pattern simulations (Fig. 4.5), the transmitted powers are also obtained through FDTD, where we simulate a single pass through the scattering layer. The simulation boundaries are perfectly-matched layers (PML) in the directions normal to the air-Si interface. In the lateral direction, we utilize approximately  $15 \times 15 \mu\text{m}^2$  area to include the entire nanopattern design. The large lateral dimension is necessary due to periodic boundary conditions applied here, which for smaller areas give rise to unrealistic diffraction orders. In case of the periodic pattern, a single unit cell is simulated and for the far field analysis, a number of unit cells is chosen such that the total lateral area is approximately equal to  $15 \times 15 \mu\text{m}^2$ , which facilitates faithful comparison with the hyperuniform designs. Simulations are performed with a spectral resolution of 3 nm and convergence is assumed once the total power residing in the simulation volume has decreased to  $10^{-5}$  of its initial value either through absorption in the material or by the PML. Simulations are performed with 4 nm minimum mesh step throughout, except for the total device stack and optimized design (Fig. 4.10), where the same is used in the nanopattern region and ( $\pm 100$ ) nm around it, but increased to 8 nm in the rest of the simulation volume.

## 4.5 Supplementary Information

### Absorption Limits

Figure 4.6 shows the absorptance spectrum in  $5\ \mu\text{m}$  Si assuming no front-surface reflectance and either a silver back reflector at the rear (Ag) or the reflectance of the  $\text{SiO}_2/\text{Si}$  interfaces of the SOI wafer ( $\text{SiO}_2\text{-Si}$ ), calculated using transfer matrix method (TMM) under normal incidence of coherent light [175]. At around  $720\ \text{nm}$ , the double-pass within the SOI structure coincides with the single-pass absorption limit due to a standing wave (Fabry-Pérot resonance) inside the buried oxide layer of the SOI, which suppresses reflection back into the absorbing layer. This nodal point is likewise observed in the EQE and reflectance measurements (Fig. 3 in the main text).

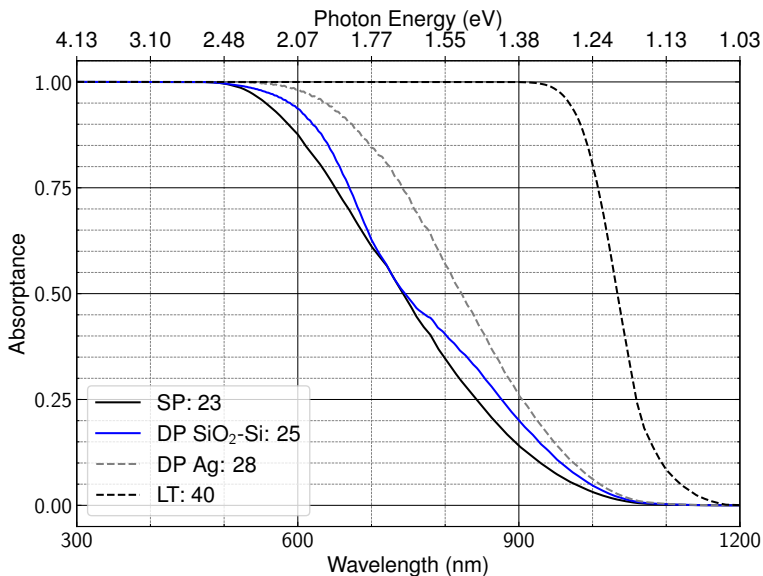


**Figure 4.6: Absorption limits in  $5\ \mu\text{m}$  silicon slab.**

The fraction of absorbed light as a function of wavelength for a single pass (SP), double pass with  $\text{SiO}_2/\text{Si}$  reflector in SOI (DP  $\text{SiO}_2\text{-Si}$ ), double pass with Ag reflector (DP Ag), and lambertian light trapping (Yablonoitch  $4n^2$  limit [79], LT). Legend shows AM1.5G-averaged  $J_{\text{SC}}$  in  $\text{mA}/\text{cm}^2$ .

## PSD Profiles

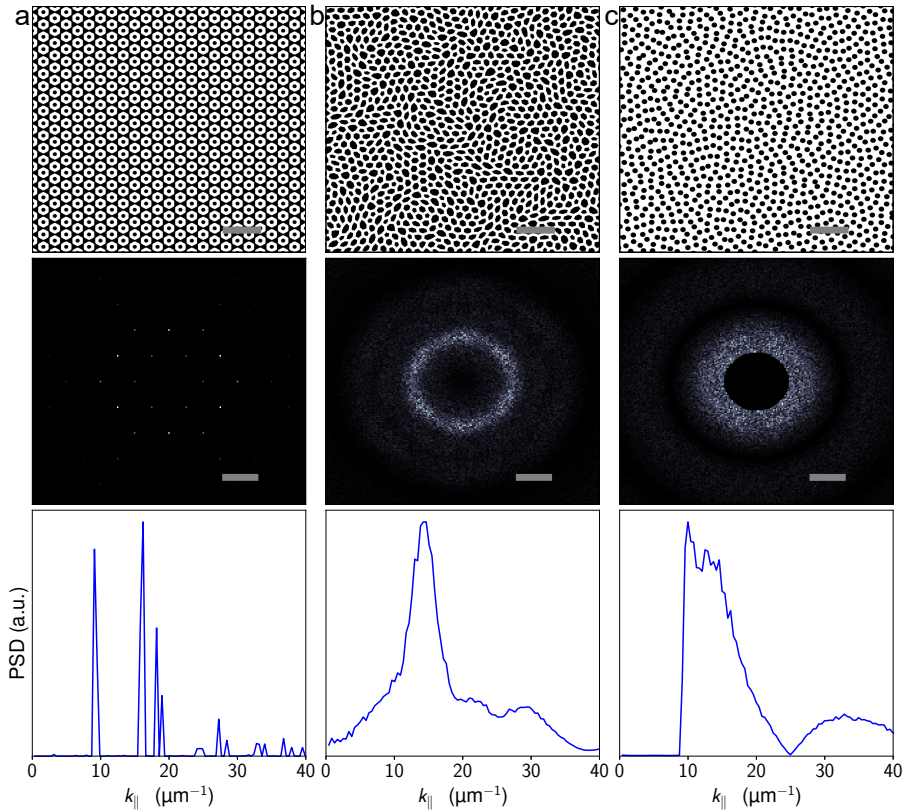


**Figure 4.7: Power spectral density of nanopatterns**

*Real-space image (top row), 2D FFT (middle row) and radial average of FFT (bottom row) of Periodic (a), HUDLE Walls (b), and HUDLE Holes (c). Scale bars are  $2\mu\text{m}$  and  $10\mu\text{m}^{-1}$  top and bottom row, respectively. White regions in the top row are protruding.*

Figure 4.7 displays real- and momentum-space images of the pattern designs. The 2D FFT (middle row) are calculated from the shown  $15 \times 15\mu\text{m}^2$  excerpts of the images in the top row. As a consequence, the resolution of the FFT and its radial average (bottom row) limited by the relatively lateral dimensions.

## Solar Cell Stack Schematic

The solar cell (Fig. 4.8) is grown on top of a SOI wafer (bottom three layers), using the top device layer of  $2\mu\text{m}$  thickness as the seed layer of epitaxy. The vertical p-i-n junction is then formed sequentially, followed by nanopatterning and mesa etching, which defines the galvanically isolated individual devices (slimmer layers at the top).

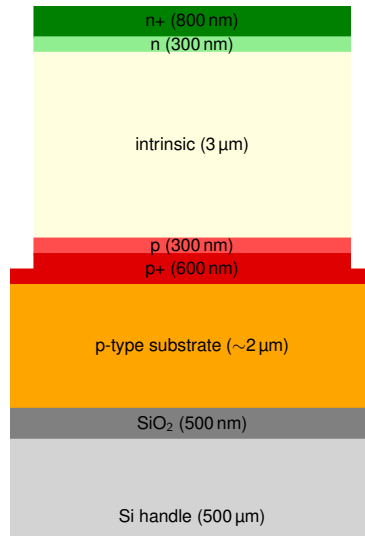


**Figure 4.8: Solar cell stack on SOI.**

*Schematic of the as-grown solar cell stack on SOI platform. The slimmer top layers represent the mesa region, which is defined by optical lithography and etched to reveal the p+-region at the base. The latter also serves as the lateral carrier transport layer to the metal back contacts which are evaporated into the etched trenches.*

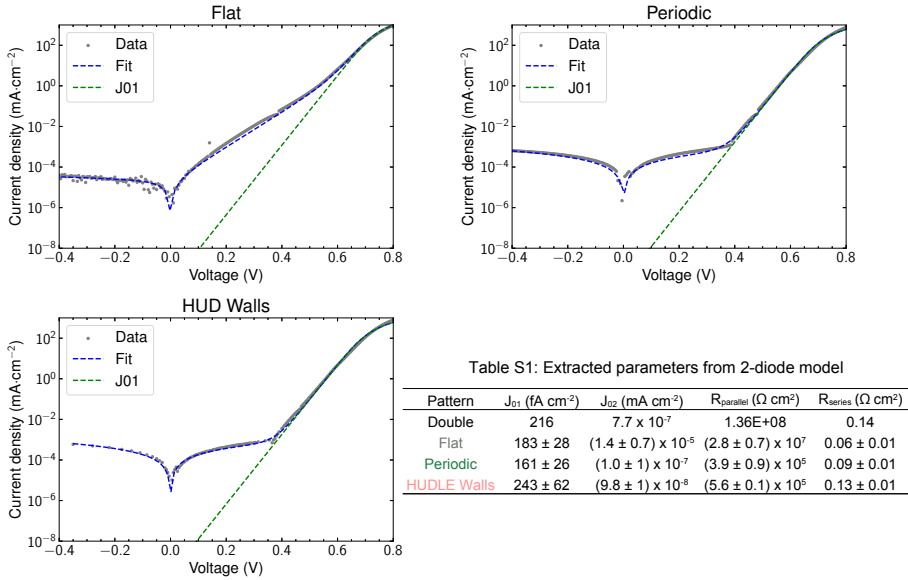
## Double-Diode Model

Figure 4.9 shows measurements of  $J$ - $V$  curves without illumination and a 2-diode model fit. The fit parameters are listed in table S1. Double corresponds to a  $3\ \mu\text{m}$ -thick solar cell fabricated using the same equipment and processes and features a multi-resonant nanoblock array [75]. The fit parameter  $J_{01}$  corresponds to recombination processes in the bulk and at the surface of the device. Since the values are very similar among flat and patterned devices of this work as well as the  $3\ \mu\text{m}$  device Double, it shows that the patterning of the surface followed by thermal oxidation does not notably increase the recombination velocity at this interface. The ideality factor for diode  $J_{02}$  is set to 2. Due to noise in the measurement apparatus, the fit of  $J_{02}$  is suboptimal and varies much among the shown devices.

## Absorptance Simulation

Figure 4.10 displays the simulated absorptance spectrum of our device stack and an optimized design consisting of  $4.8\ \mu\text{m}$ -thick Si solar cell on Ag each with the periodic nanopattern. The AM1.5G-averaged short-circuit current calculated through integration of the entire spectrum yields  $35.9\ \text{mA}/\text{cm}^2$ .

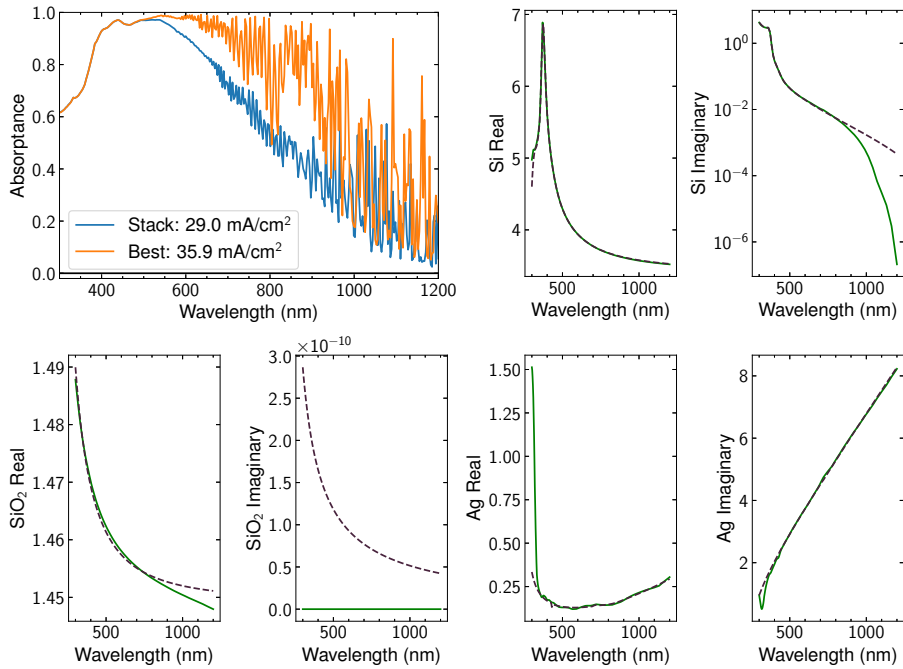
# Integrating Hyperuniform Disordered Light Trapping Layers in Ultrathin c-Si Solar Cells



**Figure 4.9:** 2-Diode model fitted to dark J-V measurements of flat, periodic and HUD devices and a table S1 of parameters extracted from the model. The plots show the measured data as grey dots, the 2-diode-model fit as blue dashed, and the extracted  $J_{01}$  diode with ideality factor  $n \equiv 1$  as dashed green curves. The uncertainty is taken from the standard deviation of fit parameters from multiple measurements on the same cell type weighed by  $(1 - \text{RMSE})$ , with the root means square error RMSE obtained from each fit. The first row “Double” in S1 corresponds to a  $3\mu\text{m}$ -this solar cell on the same platform with multi-resonant arrays [75].

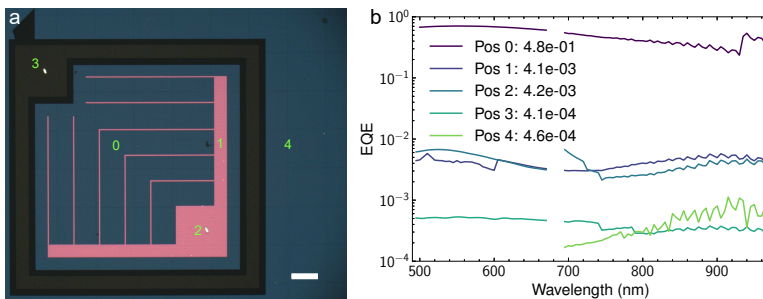
## Spatial EQE Measurements

Figure 4.11 displays EQE measurements performed at different locations of the cell mesa. When the excitation laser spot is focused solely on the frontside metalization (Position 1,2), the contribution weighed by area to  $J_{\text{sc}}$  is on the order of 0.2%. Contributions from the backside contact and the galvanically-isolated surrounding regions are negligible, and the measured currents are at the lower limit of the sensitivity range of our setup.



**Figure 4.10: Simulated absorbance of the periodic nanostructure for the SOI stack and optimized design.**

Upper left: Absorption spectrum of the simulated device stack and an optimized design with  $4.8\mu\text{m}$  Si on a Ag. The AM1.5G-averaged short-circuit current amounts to  $35.9\text{ mA/cm}^2$  (range 300 – 1200) nm and the expected efficiency given the fill factor and open-circuit voltage of the best measurement reaches about 19%. Remaining panels: Visualization of the refractive index data and fit for real and imaginary parts of simulated materials. Solid green represents the material data obtained from Palik [176] and dashed black the polynomial fit used for the simulations.



**Figure 4.11: EQE at different cell positions**

**a** Calibrated microscope image showing the different spot locations. Scale bar  $200\mu\text{m}$ . **b** External quantum efficiency versus wavelength at the different positions shown in (a). Visible range at position 4 produced no stable lock-in signal. Device type: HUDLE Holes.

## Solar Cell Micrographs

Calibrated bright-field microscope images of each of the five cell types; Flat, SiN coated, Periodic, HUDLE Holes, and HUDLE Walls are shown.

Images are taken after characterization and thus show scratches in the contact pads from the probe contacts and possibly dirt or damage that may or may not have been present during the measurements. In case of a nanopattern or SiN, the entire cell region and the surrounding surface is nanostructured or coated, including also the back contact metal regions and beyond. This is visible by the different background colors of the different cell types. Outer cell dimension including back contact region measures  $2 \times 2 \text{ mm}^2$ . The inner cell dimensions measure  $1.6 \times 1.6 \text{ mm}^2$  and subtracting the top left corner of  $0.3 \times 0.3 \text{ mm}^2$ , the total cell area becomes  $2.47 \text{ mm}^2$ . The metalization from bus bars, fingers and the front contact patch in sum cover  $(0.51 \pm 0.04) \text{ mm}^2$ , leaving an active area of  $(1.96 \pm 0.04) \text{ mm}^2$ . The error for the metal coverage results from measuring all cells using an algorithm of masking and thresholding as well as manual masking of the metal areas and cell device.

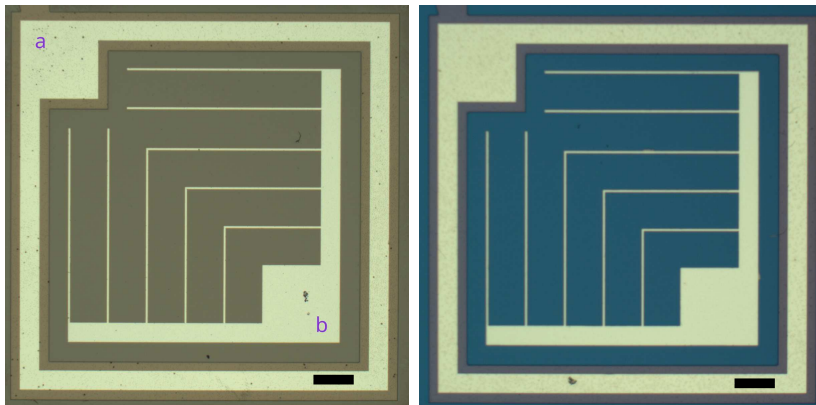


**Figure 4.12:** Flat  $\text{SiO}_2$ -only (left) and  $\text{SiN}_x/\text{SiO}_2$  (right) devices. The back contact metalized region is located in a trench circumscribing the cell mesa with a large p-contact patch at (a). The front metal grids consist of fingers joining on the face of the cell and connected to larger bus bars at two sides of the mesa and at their junction a larger n-contact patch is placed (b). Scale bars  $200 \mu\text{m}$ .

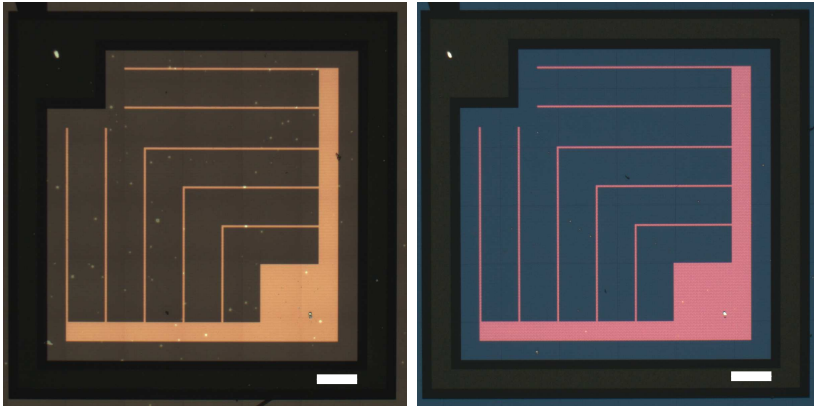


**Figure 4.13:** HUDLE Holes (left) and HUDLE Walls (right) devices. Scale bars 200  $\mu\text{m}$ .

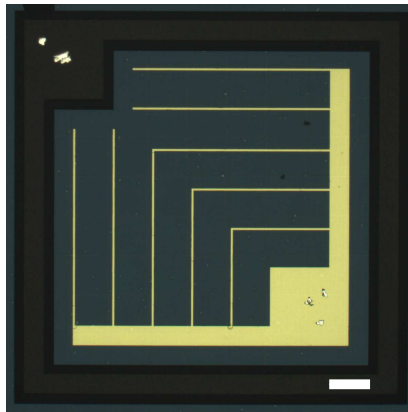


**Figure 4.14:** Device with periodic nanostructures. The metal contacts evaporated onto the patterned cell obtain structured color appearance in reflection. Scale bars 200  $\mu\text{m}$ .



# 5

## Angular Response Analysis of Ultrathin Solar Cells

### 5.1 Introduction

In ch. 3, we investigated the scattering and light-trapping properties of periodic and disordered nanopatterns, and in ch. 4, we evaluated their performance when integrated into ultrathin silicon solar cells. Thus far, these investigations have focused exclusively on normal-incidence illumination. In real-world scenarios, however, solar cells seldom operate under such Standard Testing Conditions (STC). Their photovoltaic performance is often challenged by elevated temperatures, partial shading, and oblique angles of light incidence, leading to substantial deviations from STC performance. Particularly, the angle of light incidence is a crucial factor affecting photonic performance, as it profoundly influences the effectiveness of anti-reflection and light-trapping layers. This variation can alter the quantum efficiency of power conversion across all wavelengths throughout the day. Most ultrathin devices feature surface corrugations, which simultaneously improve light in-coupling, anti-reflection and light trapping. A commonly used approach is to employ periodic patterns. If the lattice constant is smaller than the operating wavelength, no diffraction channels exist in air under normal incidence. As the angle of incidence is increased, however, the diffraction orders can shift into the light cone and provide additional free-space channels to which trapped light can couple, thereby reducing the optical absorption in the cell. As we have shown in previous chapters, disordered patterns including HUDLE layers exhibit no distinct diffraction peaks. Instead, the power spectral density (PSD, see Fig. 4.7) shows a homogeneous isotropic distribution of spatial frequencies in a delimited band in momentum space. The onset of PSD intensity in our HUDLE layers is similarly tailored to fall outside of the escape cone at normal incidence, yet it is equally subjected to a shift with the angle of incident light. The intrinsically isotropic character of HUDLE layers promises resilience to changes in the angle of incidence.

This chapter experimentally examines the effect of angle of incidence on light absorption and conversion into electricity in patterned solar cell devices. We capitalize on the ultrathin c-Si solar cells fabricated in the previous chapter to investigate differences in the light trapping capabilities of different HUDLE layers compared to periodic patterns and flat surfaces.

## 5.2 Results

### 5.2.1 Reflection and Diffraction at Oblique Angles of Incidence

Before we study the angle-dependent scattering properties of the HUDLE cells, we first briefly review the impact of non-normal incidence on flat layer stacks. The performance of solar cells under varying angles of incidence (AOI) is dictated by changes to the anti-reflective (AR) and light-trapping properties. Anti-reflective coatings commonly rely on destructive interference of partial reflectances from their top and bottom interfaces, and thus on the phase change during a double-pass through the AR layer. Since this propagation phase depends on the AOI, the reflectance minimum shifts to shorter wavelengths as the angle increases [177, 178]. To illustrate the impact of AOI on the AR performance, we plot the angle-dependent (AM1.5G-averaged) reflectance of the full device stack with a 55 nm thick SiO<sub>2</sub> layer as an AR coating (Fig. 5.1a). The resulting effect on the reflectance remains small up to AOI ~ 50° and increases rapidly at larger angles. As the AOI deviates from zero, the polarization of light begins to play a role, since the Fresnel reflection coefficients differ between s- and p-polarization. While s-polarized light experiences a monotonic increase in reflectance, the reflectance of p-polarized light decreases up to the Brewster angle, which is defined as  $\theta_B = \arctan(\frac{n_2}{n_1})$ , with refractive indices  $n_1, n_2$  of the materials comprising the interface. For AOI beyond  $\theta_B$ , the reflectance increases sharply. The p-polarized reflectance does not vanish at the Brewster angle in (a), due to the wavelength averaging and additional reflectance from other interfaces within the stack.

For off-normal incidence, transmitted light is refracted into the absorbing layer at an angle, which leads to a path-length increase dictated by Snell's law  $\Delta L \leq n / \sqrt{n^2 - 1}$ , with  $n$  the refractive index of the material (cp. Theory sec. 2.4.3). For c-Si for instance,  $3 < n < 4$  for  $\lambda \gtrsim 600$  nm, which results in a small path length enhancement of (3-6) % (blue dots). As such,

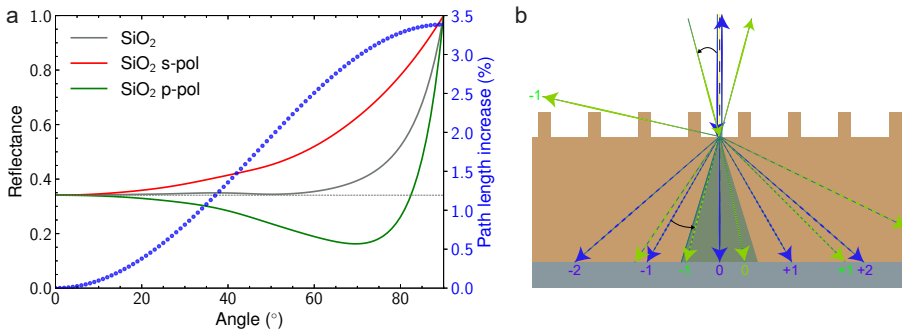


**Figure 5.1: Angular dependence of reflectance and diffraction**

**a** AM1.5G-averaged reflectance versus AOI for the full device stack, where the AR consists of a 55 nm-thick SiO<sub>2</sub> layer. Individual contributions of p- (green) and s-polarized (red) reflectances are shown as well as the path-length increase (blue dots)  $\Delta L_{\text{inc}} = (\sec \theta_t - 1)$  at  $\lambda = 600$  nm. **b** Schematic of light scattering by an air-material interface with sub-wavelength periodic corrugations. At normal incidence (blue set of arrows), only the zeroth order falls into the escape cone inside of the material (shaded region around the arrow labeled “0”). At larger AOI, the diffraction orders shift (green set of arrows) and also non-zero diffraction orders appear in free space.

the angular dependence of absorption for an ultrathin flat device relies upon the balance between counter-acting effects of increased reflectance and path-length.

In the presence of surface corrugations, the absorption length can be enhanced far beyond that of refraction through light trapping. This is of particular relevance in ultrathin c-Si based solar cells, in which the indirect band gap of Si leads to incomplete absorption in the near-infrared- and to some extent in the visible spectral ranges. Here, the angle-dependent performance is further influenced by the particular structural correlations and nanogeometry of the scattering units. For the periodic nanopattern with (square lattice) periodicity  $p = 765$  nm, its diffraction orders fall outside of the light cone for all wavelengths  $\lambda \geq p$  at normal incidence (Fig. 5.1b, blue dashed arrows) and enable coupling to guided modes. When the AOI is increased (green set of arrows), the diffraction orders shift into the escape cone and no longer contribute to light trapping. On the one hand, a periodicity that is slightly smaller than the operating wavelength approaches the fundamental limit of light trapping [122, 123] and can enhance absorption well beyond the Lambertian limit (cp. Theory sec. 2.4.1). The angle at which additional in-air diffraction channels appear, on the other hand, also becomes smaller as the periodicity approaches the wavelength of operation.

## 5.2.2 Measured and Simulated Angular Photocurrent Response

To evaluate device performance under oblique illumination, we measure current-voltage ( $IV$ ) characteristics at angles of incidence (AOI) ranging from  $\theta = 0$  to  $\theta = 60^\circ$  in steps of  $5^\circ$ . An AM1.5G-certified solar simulator is coupled to a large-diameter optical fiber ( $D = 50$  mm) mounted on a goniometer, producing a collimated, unpolarized beam much larger than the cell area. The intensity is calibrated to one sun at normal incidence using a calibrated reference solar cell. At each angle, three consecutive  $IV$  measurements are recorded and averaged. As the AOI increases, the projected illumination on the device decreases according to  $\cos\theta$  (Fig. 5.2a). To account for this geometric effect, we normalize the obtained current density  $J_{sc}$  by  $\cos\theta$  (Fig. 5.2b). A device with angle-independent performance would therefore exhibit a constant corrected  $J_{sc}$  as a function of AOI.

The measured  $J_{sc}$  as a function of angle for all cell types (Fig. 5.2c) show distinct behaviors: depending on the cell type, the corrected  $J_{sc}$  at a given off-normal incidence can exceed or fall below its normal-incidence value. The lowest overall values are observed for the unpatterned reference device (gray, labeled  $\text{SiO}_2$ ), where a flat 55 nm-thick  $\text{SiO}_2$  layer on the Si cell provides passivation and anti-reflection. For this device, the corrected current remains nearly angle-independent up to approximately  $45^\circ$ , and decreases only slightly at larger AOI. In contrast to this, adding an additional 31 nm-thick silicon nitride layer (red, labeled “ $\text{SiNx}$ ”) on top of the  $\text{SiO}_2$  leads to a steady increase of the corrected  $J_{sc}(\theta)$  above the cosine dependence for all angles up to  $55^\circ$ .

The device incorporating an optimized periodic pattern ( $p = 765$  nm, green) exhibits a pronounced angular enhancement of the corrected  $J_{sc}$ . Its lowest value occurs at normal incidence, while for all off-normal angles,  $J_{sc}$  exceeds the cosine-scaled value with a maximum around  $\theta = 40^\circ$ .

The HUDLE-Holes-patterned cell (blue) shows a markedly different angular response without strong angular enhancement of  $J_{sc}$ . In fact, the corrected current decreases progressively at AOI  $\theta \gtrsim 15^\circ$ . The device incorporating the HUDLE Wall Network (salmon) exhibits an angular response that combines features of both the HUDLE Holes and periodic designs, consistent with the numerical scattering analysis in ch. 4, sec. 4.2.3. For angles up to  $35^\circ$ , the corrected  $J_{sc}(\theta)$  exceeds the cosine-law, similar to the periodic case. At  $35^\circ$ , both the periodic and HUDLE-Wall-network cells reach nearly identical currents ( $\sim 26 \text{ mA}\cdot\text{cm}^{-2}$ ). At

## Angular Response Analysis of Ultrathin Solar Cells

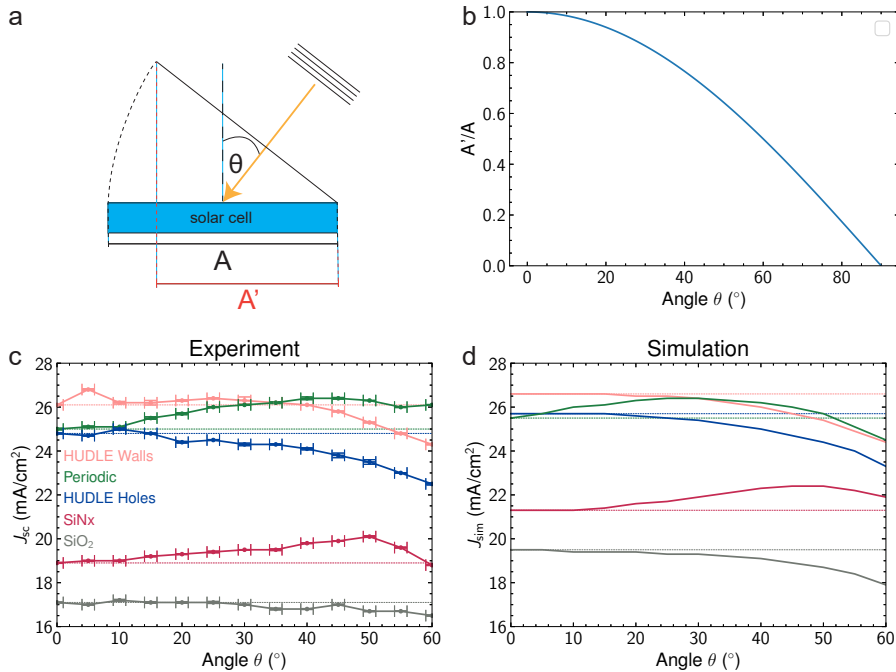


**Figure 5.2: Angular dependence of solar cells**

**a** Schematic of the projected illumination area under an angle. **b** Cosine law for angle dependent projection area. **c** Measured short-circuit current density  $J_{sc}$  vs. angle of incidence for the different cell types. **d** Simulated photo-current density  $J_{sim}$  versus angle for the different designs.  $J_{sim}$  is obtained by weighing the absorptance spectrum with the AM1.5G photon flux under the assumption that each absorbed photon creates one electron-hole pair. Dashed lines in (c,d) represent the cosine-corrected current versus angle.

larger angles ( $> 45^\circ$ ), however, the current density in the HUDLE Walls device deviates below the cosine-law and decreases slightly more rapidly than for the HUDLE Holes. Overall, the angle-dependent  $IV$  measurements reveal a stronger negative deviation from the cosine-law prediction for HUDLE devices than for periodic at large angles.

To further elucidate the origin of the diverging trends of different cell types, we perform RCWA simulations of the full device stack (see Fig. 4.8) under varying angles of incidence (Fig. 5.2d). Comparing (c) and (d) shows an overall good correspondence between the experimental and simulations results. Nevertheless, several clear differences stand out: (1) We note an offset in the absolute values and a different ranking between periodic and HUDLE Holes cell types, which we attribute partly to the internal-quantum efficiency (IQE). The  $\text{IQE}(\lambda) < 100\%$  is not reflected in simulations and affects the cell types differently due to its wavelength dependence. (2) Reflectance differences in the visible may arise from the digitization of scattering layers, which are submerged in a flat layer of SiO<sub>2</sub> in simulation, while being thermally and conformally grown from all exposed Si surfaces in the experiment. (3) For HUDLE designs, imposed periodic boundary conditions in the simulations create artificial diffraction orders of large periodicity (box size  $\sim (6\mu\text{m})^2$ ), which increase in-air

diffraction. As a consequence of these combined numerical limitations, the offset between simulation and experiment is larger for flat ( $J_{\text{sim}} - J_{\text{sc}} \sim 2.5 \text{ mA}\cdot\text{cm}^{-2}$ ) than for patterned devices ( $J_{\text{sim}} - J_{\text{sc}} = (0.5 - 0.7) \text{ mA}\cdot\text{cm}^{-2}$ ). Nonetheless, the good overall agreement of the trends versus AOI between simulation and experiment warrant further inspection of the spectral properties predicted by the simulations.

### 5.2.3 Spectral Response of the Simulated Absorbance versus Angle

We now look into the origin of the observed deviations from the cosine-prediction by analyzing the simulated spectral response of each type in more detail. At normal incidence (Fig. 5.3a), we observe notable differences in the shape of the spectra of the  $\text{SiO}_2$ -only and  $\text{SiO}_2/\text{SiN}_x$  flat devices, where the former shows a flat absorbance profile in the visible, while the latter forms a broad peak and exhibits significantly lower absorbance at  $\lambda < 500 \text{ nm}$ . Beyond  $\lambda \sim 600 \text{ nm}$ , the absorbance diminishes quickly for both types. In this spectral range, the absorption length surpasses the absorber thickness and light is no longer fully absorbed in a single- or double-pass through the active layer. Interference with the incoming radiation gives rise to strong Fabry-Pérot (FP) oscillations that show a nodal point at  $\sim 720 \text{ nm}$ , where the

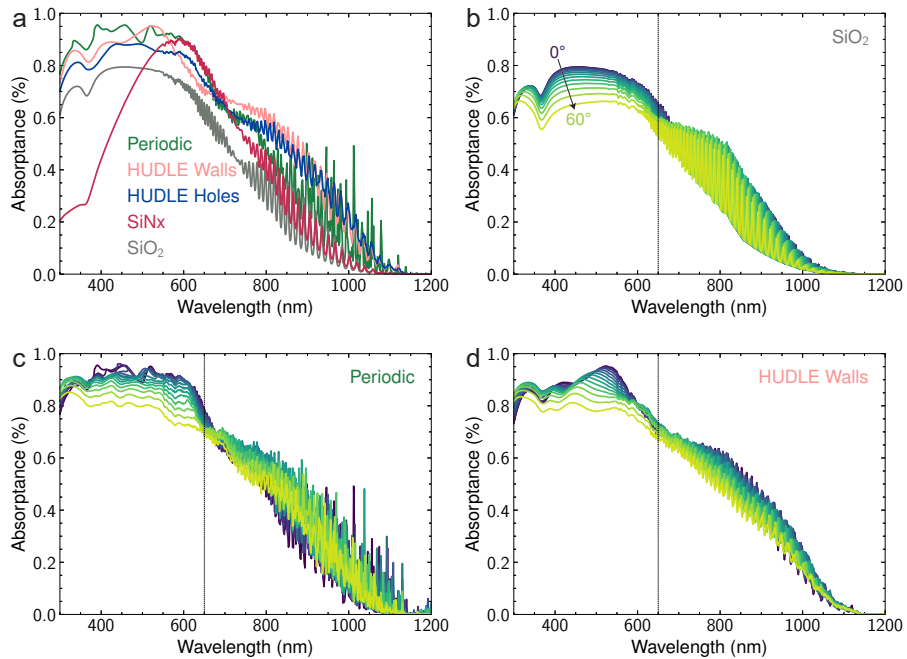


**Figure 5.3: Simulated absorbance spectra at normal and oblique AOI**

*Absorbance spectra of all cell types at normal incidence (a). Absorbance spectra at different AOI in  $10^\circ$  steps against wavelength for flat  $\text{SiO}_2$ -only (b), periodic (c), and HUDLE Walls (d) cell types. The vertical line in b-d marks the wavelength at which the double-pass absorption limit of the  $(4.8 + 2) \mu\text{m}$  active- and seed layer of the solar cell stack falls below 95%.*

500  $\mu\text{m}$ -thick buried oxide layer (see device schematic Fig. 4.8) suppresses any back reflection due to a standing wave (FP resonance) inside of it.

To assess the influence of non-zero AOI, we plot the spectrally-resolved absorptance at different AOI as a function of wavelength. For the flat  $\text{SiO}_2$ -only device (Fig. 5.3b), we observe a steady decrease with angle in the visible range, while the absorption appears more constant in the NIR. The periodic device type shows the overall best absorptance in the visible, reaching above 90 % between 400 nm and 600 nm (a). At oblique AOI (c), absorptance in this spectral range decreases steadily with angle, similar to the flat  $\text{SiO}_2$ -only reference. In the NIR, the FP oscillations originating from the finite device stack are modified by sharp peaks corresponding to diffraction orders of the periodic grating, which improve the angular-dependent absorptance with respect to the  $\text{SiO}_2$ -only device (see also the absorptance heatmap versus wavelength and angle in Fig. 5.9).

Devices featuring a HUDLE layers exhibit large absorptance values in the near-infrared spectral range at normal incidence (a). In the visible, the HUDLE Holes pattern's absorptance profile shares similarity with the  $\text{SiO}_2$ -only flat device, and achieves only slightly increased values. For  $650 \text{ nm} < \lambda < 900 \text{ nm}$ , the HUDLE Holes pattern falls in-between the absorptance values of the HUDLE Walls and periodic pattern. At longer wavelengths  $\lambda > 900 \text{ nm}$ , the HUDLE patterns show less pronounced FP amplitudes than the periodic and flat device types, and no sharp diffraction peaks as seen in the periodic pattern. The HUDLE Wall network achieves good absorptance across the spectrum at normal incidence (a), reaching similar values as the periodic device in the visible and comparable to HUDLE Holes in the NIR. The spectral dependence on AOI (d) shows steadily decreasing absorptance in the visible. In the NIR spectral range, a strong decrease in absorptance occurs only at larger angles of incidence. Additional angle-resolved spectra of  $\text{SiN}_x$  and HUDLE Holes, and heatmaps of all types are plotted in the SI (Figs. 5.8-5.9).

Overall, the spectrally-resolved absorptance comparison among cell types shows pronounced differences in the visible and near-infrared regimes, and the divergent trends with respect to the cosine correction are traceable to the relative contributions to  $J_{\text{sc}}$  and  $J_{\text{sim}}$  from these spectral ranges.

### 5.2.4 Effect of AOI on the Visible and Near-Infrared Spectral Ranges

We continue by studying the role of AOI on the device absorption more thoroughly. We separate the visible- and NIR- contributions by splitting the simulated spectra at 650 nm (dashed horizontal line in Figs. 5.3(b-d) and integrating the two contributions separately. Around 650 nm, transmission into the (parasitic) seed and handle layers of the SOI wafer starts to impact the absorptance of longer wavelengths. Absorptance in the visible range is therefore governed by the AR properties of the device, while the NIR performance predominantly bears on light-trapping and increases in the optical path length with increasing AOI.

Both unpatterned devices show equal contribution from the visible spectral range (Fig. 5.4a) for  $\theta \leq 5^\circ$ , which is remarkable, considering their divergent shapes of the absorptance spectra at small wavelengths. The explanation lies in the calculation of  $J_{\text{VIS}}$  through convolution with the AM1.5G spectrum, which provides about twice as many photons at  $\lambda \sim 650 \text{ nm}$  compared with  $\lambda \sim 400 \text{ nm}$  (see sec. 2.1). For  $\theta > 10^\circ$ , however, there are strong deviations from the horizontal reference line in both cases, where the  $\text{SiO}_2/\text{SiN}_x$  type contributes more to  $J_{\text{sim}}$ , while the  $\text{SiO}_2$ -only device falls below the cosine-corrected line. The  $\text{SiO}_2$  layer affords sub-optimal AR properties for the flat device, which only reaches a peak absorptance close to 80 % at  $\sim 450 \text{ nm}$  (cp. Fig. 5.3a). An ideal AR coating produces a

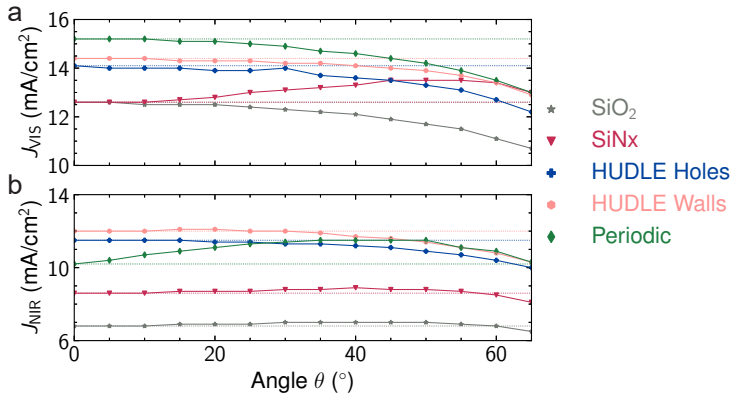


**Figure 5.4: Spectrally-separated  $J_{\text{sim}}$  as function of AOI**

$J_{\text{sim}}$  (solid line) is split into contributions from the visible (a) and NIR (b) parts for wavelengths shorter and longer than  $\lambda = 650 \text{ nm}$ , respectively. The spectra are color-coded for  $\text{SiO}_2$ -only (gray),  $\text{SiN}_x$  (red), HUDLE Holes (blue), HUDLE Walls (salmon), and periodic (green). Dashed lines represent the cosine-corrected current versus angle.

reflection minimum at  $\sim 637 \text{ nm}$ , where the AM1.5G spectrum provides the largest photon flux [179] (cp. Fig. 2.2). To improve absorptance, the additional  $\text{SiN}_x$  layer thickness of  $31 \text{ nm}$  shifts the reflectance minimum close to this value, given the  $55 \text{ nm}$   $\text{SiO}_2$  underneath. As a result, peak absorptance of the  $\text{SiN}_x$  device occurs at  $\lambda \sim 595 \text{ nm}$ . The addition of  $\text{SiN}_x$  on top of  $\text{SiO}_2$ , however, causes a non-sequential refractive index progression from the bulk Si to air, since  $n_{\text{Si}} > n_{\text{SiO}_2} < n_{\text{SiN}_x}$ , which entails unfavorable anti-reflective properties away from the reflectance minimum. Especially at low wavelengths ( $\lambda < 500 \text{ nm}$ ), this leads to the lowest absorption among all device types.

Instead, in the NIR range, both unpatterned types show near-identical trends with a slight improvement due to path-length enhancements at angles  $15^\circ < \theta < 55^\circ$ . This analysis explains the diverging trends versus AOI between the two flat device types: The  $J_{\text{sc}}$  of the  $\text{SiO}_2$ -only type pertains mostly to electron-hole pairs generated from high-energy photons that are fully absorbed within a double-pass through the device layer and necessitate good AR performance. As the angle is increased, the increased path lengths for NIR photons is insufficient to counter-act the rising reflectance, leading to a below-cosine current reduction. The double layer  $\text{SiO}_2/\text{SiN}_x$ , in contrast, most efficiently absorbs photons in the range of the reflectance minimum of the AR coating ( $500 \text{ nm} < \lambda < 700 \text{ nm}$ ), where incomplete absorption in the double pass through the device becomes the limiting factor. Particular in this range, enhanced optical path lengths lead to an increase in cosine-corrected  $J_{\text{sc}}$  up to large AOI. In addition, the refractive-index stacking of the AR layers, which causes increased reflectance for short wavelengths at normal incidence, shows reduced reflectance as the AOI increases and leads to overall enhancement in combination with the improvements in the NIR range.

For the periodic cell type,  $J_{\text{VIS}}$  follows the reference line to about  $10^\circ$  and falls below it at greater AOI. As such, the above-cosine overall current response (Fig. 5.2c) with angle is exclusively due to the NIR improvement. In fact, the cosine-corrected  $J_{\text{NIR}}$  remains above its value at normal incidence up to  $\theta = 65^\circ$ . The steady current increase at  $5^\circ < \theta < 40^\circ$  arises from enhanced diffraction into guided modes as the angle of incidence grows, which enhances the effective optical path length inside the absorber. At larger angles, however,

two effects reduce the photocurrent: the Fresnel reflectance increases, and the second-order diffraction channel for wavelengths  $\lambda \leq 600$  nm shifts into the escape cone at  $\theta > 40^\circ$  (see grating Eq. calculation and plot in sec. 5.5, Fig. 5.6). Because this spectral range coincides with both the double-pass absorption limit of the device and the peak of the AM1.5G photon flux, the additional loss of this diffraction channel has a pronounced impact. Overall, the periodic grating maintains enhanced photocurrent over a broad angular range, demonstrating that for optimally chosen periodicities, its discrete diffraction channels can be particularly effective under oblique illumination.

The HUDLE Holes device shows similar trends in both visible and near-infrared. In both parts of the spectra, below-cosine-dependence is observed at all non-zero AOI. This behavior is consistent with the exceptional near-infrared (NIR) light trapping already present at normal incidence (described in ch. 4), which leaves limited room for additional path-length enhancement at oblique angles. In the visible spectral range, the photocurrent is constrained by sub-optimal anti-reflection at normal incidence, due to the relatively high Si filling fraction of the scattering layer and its correspondingly large effective-medium refractive index. In the near-infrared range, the HUDLE Holes pattern shows negative deviation from the cosine reference. As the angle increases, reflectance losses become more pronounced and diffraction into free-space channels grows. In particular, the dominant peak of the HUDLE Holes power spectral density (PSD) at  $k_{\parallel} \sim 10 \mu\text{m}^{-1}$  progressively shifts into the escape cone (see ch. 2, Fig. 2.11 or ch. 4, Fig. 4.7c). The PSD shift with AOI is illustrated in Fig. 5.5, which shows the dominant PSD intensity wavevectors at normal incidence (blue ring) situated just outside the escape cone (gray disk at the center). At an oblique incidence, the corresponding wavevector is displaced from the origin (exemplary  $\Delta k$ ). The location of the PSD intensity ring shifts in accordance (turquoise ring), and partially overlaps with the escape cone. The corresponding maximum wavelength showing in-air diffraction is plotted versus AOI in the supporting information (Fig. 5.6). In combination with increasing reflectance in the visible, these effects lead to the observed negative deviation from the cosine-law prediction at large angles.

The HUDLE Wall network is likewise affected by an overlap of PSD and escape cone at increasing AOI. In contrast to HUDLE Holes, the HUDLE Wall's PSD peak intensity occurs in a more delimited momentum range, which is centered around a larger value of  $k_{\parallel} \sim 15 \mu\text{m}^{-1}$  (Fig. 4.7b). Therefore, the HUDLE Walls support a larger range of AOI before in-air diffraction sets in, which is corroborated by a negative deviation of HUDLE Walls from  $\theta \sim 35^\circ$  versus  $\theta \sim 20^\circ$  in HUDLE Holes. In the visible range, the HUDLE Walls follows the cosine dependence up  $\theta = 15^\circ$ , similar to the periodic pattern. As the AOI increases, the deviation below this reference is smaller for HUDLE Walls than Periodic, which can also be inferred from the spectral absorptance versus AOI (Fig. 5.3c,d). The pronounced absorptance peak at  $\lambda \sim 525$  nm of the HUDLE Walls at normal incidence reduces in amplitude and shifts to lower wavelengths with increasing AOI, which ultimately leads to the flattening of the absorptance profile in the visible at  $\theta = 60^\circ$ . At large angles ( $\theta \sim 60^\circ$ ), HUDLE Walls and periodic device types show a similarly flat absorptance profile with an average absorptance slightly below 80 %.

Overall, the NIR performance of all pattern types is similar at normal incidence, and with the exception of HUDLE Holes, increase above the cosine reference for a wide range of angles. From this analysis, it is verified that the difference in total  $J_{\text{sc}}$  compared among the patterning approaches almost exclusively originates in the visible range, where the AR properties of the scattering layer govern the absorptance. In terms of trapping NIR photons, the periodic type exhibits significant improvement at oblique incidence, whereas the HUDLE patterns follow more closely the cosine dependence for a wide range of AOI. Here, the distinct PSD features of HUDLE versus periodic dictate the balance between increased optical path

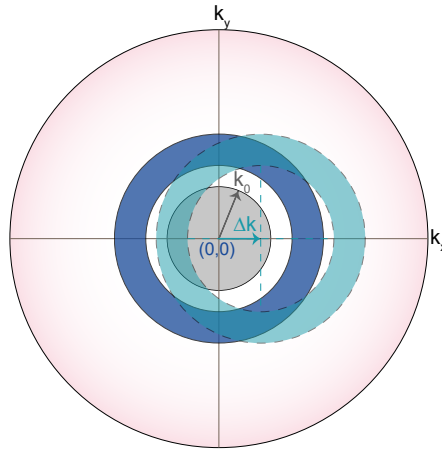


**Figure 5.5: HUDLE diffraction versus AOI**

*Momentum-space ( $k_x, k_y$ -plane) representation of the HUDLE Holes PSD at normal incidence (blue) and at an angle (turquoise). The escape cone is visualized as a gray disk at the origin  $(0,0)$  with radius of the free-space wavevector  $k_0$ , and the angle of oblique incidence is denoted by an arrow  $\Delta k$  along  $k_x$ .*

length and additional in-air diffraction channels. In the visible, we notice two different behaviors pertaining to the overall shape of the absorptance profile in this spectral range. A flat absorptance profile as seen for  $\text{SiO}_2$ , Periodic and HUDLE Holes (Fig. 5.3a), always leads to a reduction below the cosine correction with increasing AOI, while the peaks associated with  $\text{SiN}_x$ - and HUDLE Walls devices can lead to enhancement above the corrected current values. The distinction between last two lies in the precise location of the peak at normal incidence. Here, the  $\text{SiN}_x$  peak occurs at larger wavelengths and progresses from  $\lambda \sim 590$  nm to  $\lambda \sim 550$  nm between  $\theta = 0$  and  $\theta = 60^\circ$ , thus retaining significant overlap with the AM1.5G peak flux range  $\lambda \in [550, 750]$  nm. The HUDLE Wall Network, in contrast, shows maximum absorptance at  $\lambda \sim 525$  nm at normal incidence, and shifts to  $\lambda \sim 450$  nm at  $60^\circ$ , accompanied by a strong reduction in peak amplitude. The combination of both effects reduces the averaged absorptance in HUDLE Walls by an increase of front-surface reflectance.

In the design and optimization of periodic and HUDLE trapping layers alike, the impact of AOI needs to be assessed thoroughly for applications with omnidirectional light incidence. On the one hand, by targeting larger in-plane momentum values in the PSD, a broader range of angles is supported before additional in-air diffraction channels occur. On the other hand, the reduced (pseudo-) periodicity, or average spacing between scatterers, poses limitations to the design of the scattering unit and can decrease the absorptance at normal incidence, for which a periodicity approaching the operating wavelength affords the greatest enhancements. In the visible range, the angular dependence pertains to the overall shape of the absorptance spectrum. A flat profile follows closely the cosine dependence, while in the presence of a localized peak, the peak location and shift dictate the angular response. If the peak overlaps with the AM1.5G photon flux peak region at normal incidence, absorptance reduces drastically with AOI, due to peak-amplitude reduction and a shift to smaller wavelengths. To achieve more robust operation at oblique incidences, one would instead target a reflectance minimum

at a wavelength slightly larger than that of the AM1.5G flux maximum, such that the peak progression with angle traverses the peak region and leverages the reduced peak amplitude.

### 5.3 Conclusion

In summary, we investigate the angular dependence of ultrathin c-Si solar cells with different kinds of light-trapping structures and flat devices with planar AR coating both experimentally and in simulation. The simulations are in good agreement with the experimental observations and provide insights into the spectrally-resolved absorptance changes with angle. The optoelectronic performance in the visible or near-infrared spectral ranges respond differently as the AOI increases, due to changes to front-surface reflectance and optical path lengths inside the absorbing layer. Depending on the cell type and scattering layer, the irradiance-corrected photocurrent may increase or decrease with respect its value at normal incidence, as a result of the balance between the competing effects of both spectral ranges. We find that the optimized periodic pattern produces the least short-circuit current at normal incidence and reaches a maximum at  $\sim 40^\circ$  in experiments, due to a large improvement in the NIR spectral range. Cells with a HUDLE pattern show a different response, with little or no angular enhancement of absorptance in both visible and near-infrared.

Crucially, we identify a mutual contradiction in the design of scattering layers for normal versus oblique incidence. Light trapping with tailored momentum-space show best performance at normal incidence when the PSD peak lies close to the light line. For the best performance under oblique incidence angles of light, however, PSD features at larger in-plane momentum values prevent in-air diffraction for a greater range of incident angles.

### 5.4 Experimental

#### IV Measurements

We use a solar simulator (SCIENCETECH A4 Solar LightLine) as a light source. The lamp is equipped with a large-diameter ( $d=50$  mm) optical fiber that emits a collimated beam with AM1.5G certified spectrum. The output port is attached to a goniometer on a custom-built stage. The working distance is about 30 cm and the beam spot is much larger than the cell area. The intensity is adjusted at normal incidence using a calibrated solar cell (Newport Oriel 91150V Reference Cell and Meter) before and after each angle sweep. The tolerances of illumination were  $(1.00 \pm 0.02)$  suns. The cell is connected to a source-measure unit (Keithley 2450 SMU), which sweeps the potential from -0.05 V to 0.65 V three times consecutively at each angular position. We begin at normal incidence and increase the AOI in steps of  $5^\circ$ . All measurements at each position are averaged and the error is calculated by Gaussian error propagation. The cell area is normalized to the active area of the device (excluding metal regions) and measures  $0.0196 \pm 0.004 \text{cm}^2$ .

#### Transfer-Matrix Method (TMM) Calculations

TMM calculations are performed using the python TMM library [175]. The handle layer of the solar cell stack is modeled infinitely long, the dimensions of other layers are as given in Fig. 5.1a. In panel (b) of the same figure, the reflectance spectra are integrated by weighing each wavelength with the AM1.5G photon flux.

## RCWA Simulations

Rigorous coupled wave analysis (RCWA) simulations are performed with the RCWA implementation in ANSYS Lumerical [136]. The simulation volume includes a  $6 \times 6 \mu\text{m}^2$  excerpt of the HUDLE patterns designs (shown in Fig. 4.7). The accuracy in RCWA simulations depends on the chosen number of wavevectors  $N_k$ . We choose  $N_k > 3400$  as a compromise between simulation time and accuracy. The error in  $J_{\text{sim}}$  compared with  $N_k = 3900$  measures  $\sim 0.01$  (See Fig. 5.7).

## 5.5 Supporting Information

### Diffraction-Order Dependence on AOI

The shift of diffraction orders with angle is displayed in Fig. 5.6, obtained from the grating equation:

$$d [\sin(\theta) + \sin(\theta_o)] = m\lambda, \quad (5.1)$$

with (pseudo-) periodicity  $d$ , AOI  $\theta$  and  $\sin(\theta_o) \equiv 1$ . The ordinate value indicates the onset of in-air diffraction for wavelengths  $\lambda \leq \lambda_{\text{esc}}$  at each angle for diffraction orders  $m = (\pm 1, 0)$  (solid),  $m = (\pm 2, 0)$  (dashed), and  $m = (\pm 1, \pm 1)$  (dash-dotted). For disordered designs, the pseudo-periodicity corresponds to the momentum value at peak PSD intensity (cp. Fig. 4.7).

### RCWA Convergence

Figure 5.7 displays the absorptance spectra of the HUDLE Holes pattern with number of momentum points  $N_k = 3457$  (purple) versus  $N_k = 3969$  (teal). The difference in calculated

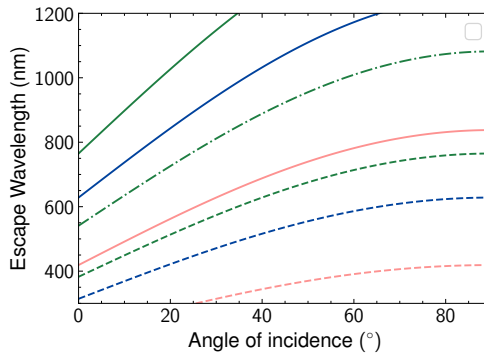


**Figure 5.6: Maximum wavelength of in-air diffraction versus angle.**

Wavelength corresponding to the in-plane momentum of diffraction versus AOI,  $\lambda_{\text{max}} = 2\pi \cdot k_{\parallel, d}^{-1}$ , where  $k_{\parallel, d} = 2\pi/d$ , with  $d$  corresponding the (pseudo-) periodicity of periodic (green), HUDLE holes (blue), and HUDLE walls (pink), obtained from the grating equation. This “escape wavelength” corresponds to the maximum wavelength that diffract into air for the first (solid lines) and second order (dashed lines), and (1, 1) order for periodic only (dash-dotted). For aperiodic patterns, the “pseudo-periodicity” is obtained from the peak momentum value in the pattern’s PSD.

## Angular Response Analysis of Ultrathin Solar Cells

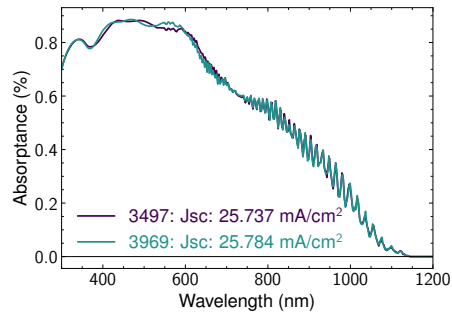


### Figure 5.7: RCWA simulation accuracy

RCWA simulation comparison for a the stack featuring the HUDLE Holes pattern, where the number of  $k$ -points  $N_k$  is increased from 3497 to 3969. The difference in AM1.5G-calculated current density measures  $\sim 0.047 \text{ mA/cm}^2$ .

$J_{\text{sim}}$  measures  $\sim 0.047 \text{ mA/cm}^2$ .

## Additional Simulation Spectra

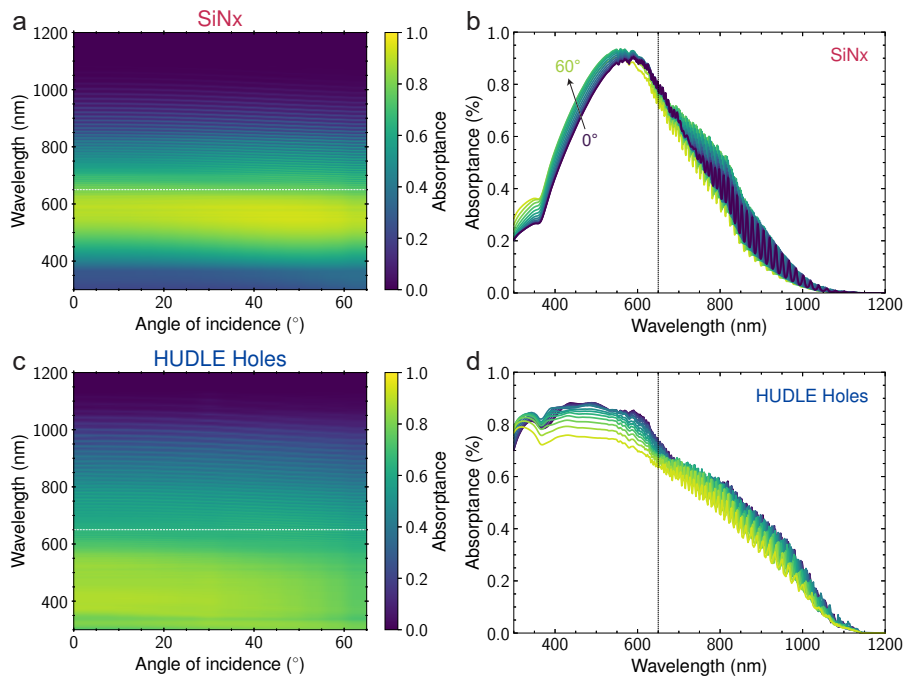


**Figure 5.8: Simulated absorbance versus angle for SiN<sub>x</sub> and HUDLE Holes patterns**  
Absorbance heatmap and spectra for flat SiO<sub>2</sub>/SiN<sub>x</sub> (a,b) and HUDLE Holes (c,d) devices versus angle of incidence.

## Angular Response Analysis of Ultrathin Solar Cells

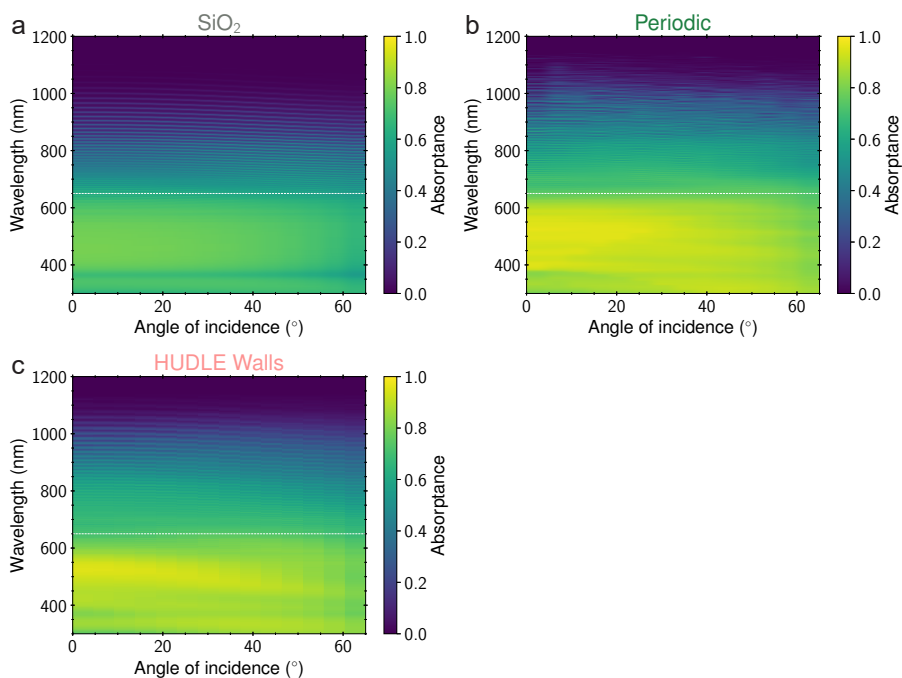


**Figure 5.9: Additional simulated absorptance heatmaps**

Simulated absorptance heatmaps versus wavelength and angle for SiO<sub>2</sub>-only, Periodic, and HUDLE Walls patterns. White horizontal line marks the distinction between visible and NIR spectral ranges.

# 6

## Self-Assembled HUDLE Patterns

In the previous chapters, we have seen significant improvement of in-coupling and light trapping in ultrathin solar cells when carefully designed nanostructures are implemented at their surface. Suitable control over the in-/out-coupling of light can enhance the performance of practically any optoelectronic device. The structures investigated in the previous chapter involved complex design optimization routines followed by slow and costly nanolithographic processes, which are not scalable. To capitalize on the benefits of engineered light trapping layers at industrially relevant scales, the slow and costly fabrication techniques need to be replaced with low-cost and high-throughput methods, compatible with in-line manufacturing schemes such as roll-to-roll. Immiscible blend lithography has shown promise in creating self-assembled nanopatterns at larger scales. However, challenges in yield and reproducibility hinder its industrial implementation. Here, we combine a controlled environmental enclosure with a meticulous fabrication routine to demonstrate the ability to independently tune crucial parameters in the resulting nanocomposites. When translated into an etch mask through selective dissolution of one constituent, the tailored arrangement of holes or pillars can be effectively transferred onto arbitrary substrates using common top-down or bottom-up techniques. We demonstrate the efficacy of the resulting anti-reflective and light-trapping patterns through full-wave optical simulations and experiments on ultrathin weakly-absorbing substrates. Our results tackle one of the standing challenges of immiscible blend lithography and may be extendable beyond spin-coating deposition routes to other, line-compatible deposition methods such as slot-die- or spray-coating.

## 6.1 Introduction

Large-area self-assembled nanopatterns have garnered substantial interest in recent years due to their promising applications in optoelectronics and photonics [180–183]. Although a wide range of fabrication techniques have been developed to create these nanopatterns, most methods have focused on producing fully random structures as these tend to be more straightforward to realize [184–187]. In contrast, achieving precise mutual inter-particle distances and tailored nanoscale geometries of scatterers poses a much greater challenge [171]. At the same time, such control of the spatial arrangement of scatterers is essential for photonic applications, as it dictates the optical response of materials [91, 188–190]. While the simplest and most reproducible methods rely on close packing of identical spheres in two dimensions, which afford no control over inter-particle distances and produce ordered self-assembled arrangements [171, 191], introducing a controllable degree of disorder can substantially extend the functionality and performance, especially in large-bandwidth applications [129, 192, 193].

In particular, correlated-disordered—or tailored-random—patterns are of special interest, as carefully imposed constraints on the positions and geometry of scatterers enable independent control over the angular and spectral response of the nanopattern [91, 129, 194, 195]. A notable subset thereof exhibits disordered hyper-spectral uniformity, commonly referred to as hyperuniform disorder (HUD) [94, 161]. Although such structures are statistically isotropic and non-periodic, their structure factor  $S(k_{\parallel})$  vanishes for momenta below a finite cutoff  $k_c$ , i.e.  $S(k_{\parallel}) = 0$  for  $k_{\parallel} \in [0, k_c]$  [196]. This behavior signifies the suppression of density fluctuations at large length scales, or equivalently, that the number variance  $\sigma^2(r)$  within a spherical sampling window of radius  $r$  (in  $d$  dimensions) grows more slowly than the window volume ( $\propto r^{a < d}$ ) for large  $r$  [197]. From an optical perspective, this property manifests as the suppression of small-angle scattering and a preferential redistribution of scattered light into in-plane momenta exceeding  $k_c$ . When appropriately engineered, these momenta can be shifted outside the escape cone, thereby promoting coupling into guided optical modes that enhance light absorption (see ch. 3 and [75, 150, 198–200]).

Despite these appealing characteristics, the rational design and optimization of near-hyperuniform disordered light-engineered (HUDLE) layers with targeted functionalities remains inherently challenging [201]. To date, no direct computational framework exists for generating real-space patterns that simultaneously enforce prescribed mutual structural correlations and controlled object-size distributions. As a result, correlated-disordered nanopatterns are typically realized using iterative optimization schemes [95, 99, 202], deep-learning approaches [203], or inverse-design methodologies [91, 204]. Furthermore, the deterministic fabrication of such nanopatterns often suffers from limitations in throughput, scalability, and long-term durability, rendering these approaches less suitable for large-area or industrial-scale production [172, 205].

Motivated by these limitations, a growing number of more unconventional experimental strategies for producing hyperuniform structures over large areas have emerged, including the self-assembly of monodisperse dielectric spheres [125], spinodal decomposition [206–208], and phase separation processes [209–211]. The phase-separation route offers distinct advantages in creating light-scattering nanostructures. In this process, a blend of immiscible constituents (polymers) is dissolved in a common solvent and cast onto a substrate. As the solvent evaporates, the phases de-mix and form separated domains with tunable characteristics. Depending on the phase-map trajectory, either isolated, locally confined islands are created (nucleation and growth), or the phase separation results in spinodal decomposition, producing uniformly distributed, connected structures [212, 213]. The

phase-separation approach provides a sophisticated platform for designing complex optical nanomaterials [214]. In contrast to colloidal assembly methods, the size of the isolated structures is not fixed by the colloidal dimensions, and instead controlling the domain size distribution offers additional degrees of design freedom.

Despite the potential of the phase-separation approach, reproducibility remains a major bottleneck, with low fabrication yields further impeding the translation of these methods to production-ready implementations. The substrate condition prior to and during the deposition as well as environmental conditions strongly impact reproducibility and yield and need careful regulation [126, 215]. Various controlling parameters may play a pivotal role in defining the resulting structural properties, including temperature, relative humidity (RH), molecular weight (MW), composition ratio (R), and spin-coating time, acceleration and speed. As the phase-separation process is extremely sensitive to these parameters, they present an opportunity to influence and control the resulting morphology. While an impact of each of these parameters has been identified [126, 216, 217], no study has thus far been presented that analyzes the complex interplay between structural and geometric properties as a consequence of single-parameter variations.

Here, we address these challenges by introducing a robust method for the consistent fabrication of nanopatterns with tunable structural characteristics, specifically tailored to targeted optoelectronic applications. Capitalizing on the stability of the process, we tune the structural properties of nanogeometry and spatial distribution of the ensemble separately by varying macroscopic process parameters such as the molecular weight of the constituents and their mutual mixing ratios in a common solvent. We demonstrate the correlation between power spectral density and light scattering properties with Fourier-space reflectance measurements, providing insights into the efficacy of the fabricated phase-separation patterns. To assess the applicability of our patterns for light trapping, we conduct simulations analyzing the spectrally- and momentum-resolved light-scattering characteristics of experimentally realized pillar structures. Finally, we measure absorptance in ultrathin weakly-absorbing substrates after patterning with the self-assembly route, which shows substantial enhancements across the entire wavelength range compared to an unpatterned reference. Overall, our results demonstrate the fabrication of nanopatterns with controlled correlated disorder based on the phase-separation process, thereby providing the means to produce large-area near-hyperuniform nanopatterns for solar cell applications.

## 6.2 Methodology

### 6.2.1 The Phase-Separation Process

The methodology for obtaining self-assembled nanopatterns using polymer-blend lithography (PBL) is schematically shown in Fig. 6.1a, steps (1) to (7). This is based on the phase-separation process of two immiscible polymers, say PMMA and PS, which first requires the dissolution of both polymers in a common solvent and thorough mixing. At this step, the ternary homogeneous blend is in a stable state (1). In parallel, the substrate is placed on a hot plate to remove any adsorbed water molecules (2). Afterwards, the solution is spin-coated on the substrate, the solvent starts evaporating, and the polymer concentration in the film rises rapidly (3). At this point, the polymer-polymer interactions become more frequent and the system destabilizes, leading to phase separation. Subsequently, the sample is placed on a second hotplate to bake out the remaining solvent and sedate the phase-separated morphology (4). Upon complete solvent evaporation, the de-mixed polymer film is “frozen”

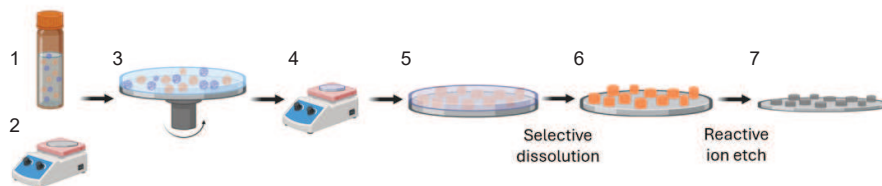


**Figure 6.1: Immiscible blend lithography methodology**

*Schematic of the process flow for obtaining near-hyperuniform self-assembled scattering nanopatterns: (1) A blend of Poly(methyl methacrylate) (PMMA) and polystyrene (PS) are dissolved in the common solvent Methyl Ethyl Ketone (MEK) and subsequently deposited onto a dehydrated substrate (2) through spin-coating (3). The rapid condensation precipitates the polymers onto the substrate as the solvent evaporates. The substrate is transferred to a hotplate for post baking (4). The resulting structure is comprised of distinct domains PS domains embedded in a PMMA host matrix (5). Using a selective solvent (acetic acid), solely the PMMA phase is dissolved and an etch mask of PS pillars isolated on the substrate's surface remains (6). The pillar morphology is transferred into the substrate by reactive-ion etch (7).*

in a meta-stable or unstable state. The final film consists of isolated island domains of one polymer hosted in a matrix of the other (5) [216, 218]. The relative solubility of the two polymers in the common solvent determines which of the two polymers forms the island domains. Here, we use methyl-ethyl-ketone (MEK), for which the PMMA exhibits larger solubility and thereby forms the host matrix. If toluene or tetrahydrofuran is used as the common solvent, the higher solubility of PS would result in PMMA islands instead [216].

The segregated polymer film is subsequently transformed into an etching mask by selectively dissolving one of the two polymer components (6). If the host matrix is removed, isolated polymer islands remain on the substrate. These islands are characterized by a defined radius and inter-island spacing, which together determine the structure factor of the resulting pattern layer. Notably, the complementary morphology, obtained by removing the islands instead of the matrix, yields the same structure factor, as the spatial correlation function governing the lateral ordering remains unchanged. The masked substrate is then etched, for example, by reactive ion etching, thereby transferring the mask topology into the underlying material (7).

Achieving targeted morphologies through the polymer blend process thus requires high-level control over the process parameters. In the following, we describe the fundamental mechanisms underlying process in more detail and highlight the role of the polymer blend composition and environmental parameters on the resulting structure.

## 6.2.2 Impact of Blend Composition

To understand the mixing process of two polymer types ( $A$  and  $B$ ) in more detail, we first turn to a thermodynamic description of the blending process developed by Higgins and Flory [219]. This model is based on a simplified lattice model where components are (de-)mixed at constant volume (Fig. 6.2). The fixed number of sites in the lattice model represents the constant volume, and the two immiscible polymer types (blue/white) are distributed across the sites, forming connected chains. The number of possible configurations decreases with chain length, which illustrates a decrease in mixing entropy. The model assumes equal

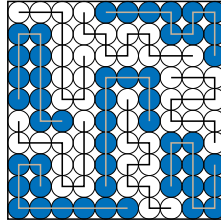


**Figure 6.2: Flory-Huggins theory**

2D-lattice model of mixing two immiscible polymer types with chain lengths of 10 each at constant volume (fixed number of sites). The chain length limits the number of possible permutations.

volumes of the monomers and no change upon mixing, so they can each occupy any lattice location. The Helmholtz free-energy in this case takes the form [220]:

$$\Delta \bar{F}_{\text{mix}} = \Delta \bar{U}_{\text{mix}} - T \Delta \bar{S}_{\text{mix}}, \quad (6.1)$$

where  $\Delta \bar{S}_{\text{mix}}$  is the entropic contribution at a single lattice site,  $T$  is the temperature, and  $\Delta \bar{U}_{\text{mix}}$  denotes the pre-site energy of mixing.

The entropic term can be described by:

$$\Delta \bar{S}_{\text{mix}} = k \left( \frac{\phi}{N_A} \ln \phi + \frac{(1-\phi)}{N_B} \ln (1-\phi) \right), \quad (6.2)$$

where the degree of polymerization  $N_{A,B}$  of polymers A,B, always favors mixing but becomes small as the polymer chain lengths (molar weight) increases.

On the other hand, the free energy of mixing at a specific lattice site is given by:

$$\Delta \bar{U}_{\text{mix}} = \chi \phi (1-\phi) kT. \quad (6.3)$$

Here,  $\phi = f_A = 1 - f_B$  is the volume fraction of one of the two polymer types, and  $k$  is Boltzmann's constant. The enthalpic contribution to the free energy of mixing is governed by the interaction parameter  $\chi$ , which quantifies the difference of interaction energies in the mixture and can be either positive (opposing mixing) or negative (promoting mixing). It is defined as:

$$\chi_{AB} \equiv \frac{z}{2} \left( \frac{2u_{AB} - u_{AA} - u_{BB}}{kT} \right), \quad (6.4)$$

where  $u_{ij}$  denotes the pairwise interaction energy between neighboring segments  $i$  and  $j$ , and  $z$  is the lattice coordination number (e.g.,  $z = 4$  in two dimensions and  $z = 6$  in three dimensions). In other words,  $\chi$  quantifies the energy difference between the pairwise interaction  $u_{AB}$  of the polymers compared with their pure component states  $u_{AA, BB}$ . Because interactions with the substrate-blend and blend-air interface are not directly considered in the definition of Flory-Huggins, the mean-field Flory-Huggins theory lumps everything that is not captured by the model into the  $\chi$  parameter [220].

The parameter  $\chi$  can be experimentally determined in neutron scattering experiments and tabulated values for a number of case studies have been published [209, 221].  $\chi$  reflects the functional dependence of  $\Delta \bar{F}_{\text{mix}}$  on many parameters in the system, and it typically assumes a complex dependence upon the composition, chain length, and temperature [220]. Through its contribution to the free energy,  $\chi$  ultimately governs the thermodynamic

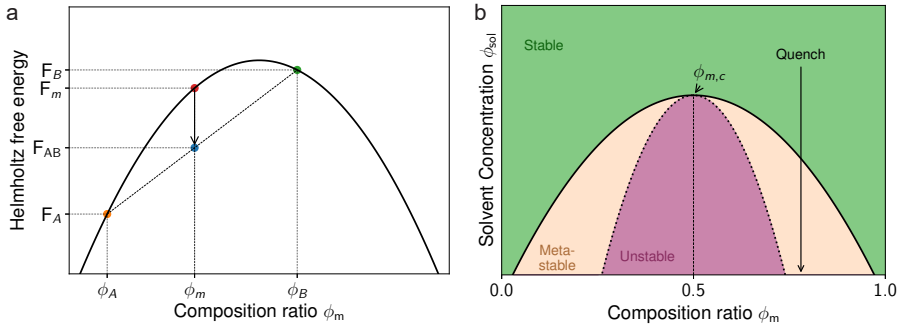


**Figure 6.3: Phase diagram for binary polymer blend and spin-coating process**

**a** Helmholtz free energy  $F$  for an unstable binary polymer blend (solid curve). The instability implies  $F_{\text{mix}} > F_{\text{AB}}$  such that the system can lower its free energy by demixing (phase-separation). The total system composition  $\phi_m = f_A\phi_A + f_B\phi_B$  separates into a linear combination of distinct phases that occupy volume fractions  $f_{\text{A,B}}$  with their phase compositions  $\phi_{\text{A,B}}$ . **b** Gibbs free energy in the ternary blend of polymers A,B dissolved in solvent C. The solvent evaporation quenches the system from a stable state at low polymer content (green region) onto the abscissa in a metastable (beige) or unstable state (rose) region of the remaining binary blend.

stability of the homogeneous blend. Phase separation occurs when the mixed state becomes thermodynamically unstable with respect to composition fluctuations. For a blend of total composition  $\phi_m$ , the homogeneous free energy  $F_{\text{mix}}(\phi_m)$  must exceed that of a phase-separated state  $F_{\text{AB}}(\phi_m)$ , which is given by linear combination of the individual phases (Fig. 6.3a). Thermodynamic instability corresponds to  $F_{\text{mix}}(\phi_m) > F_{\text{AB}}(\phi_m)$ , as the system lowers its free energy by de-mixing. This translates to a concave shape of  $F(\phi_m)$  (solid line in Fig. 6.3a), or  $\partial^2 F_{\text{mix}}/\partial(\phi_m)^2 < 0$ . In this regime, infinitesimal composition fluctuations grow spontaneously, leading to spinodal decomposition. Outside the spinodal but inside the binodal region (meta-stable), phase separation proceeds via nucleation and growth. The latter leads to the desired phase separation of isolated islands of one of the polymers.

In the experiments, the two polymers are dissolved in a common solvent C, forming a ternary system. The binary Flory–Huggins description must therefore be extended to account for polymer–solvent interactions by introducing additional interaction parameters  $\chi_{\text{AC}}$  and  $\chi_{\text{BC}}$ , where the solvent is described as a monomer with  $N_{\text{C}} \equiv 1$ .

In contrast to the incompressible lattice model at constant volume, solvent evaporation during spin coating changes the total volume of the system. The appropriate thermodynamic potential is therefore the Gibbs free energy at constant pressure [214]:

$$\Delta G_m = -nkT \left\{ \begin{array}{l} \frac{f_A}{N_A} \ln f_A + \frac{f_B}{N_B} \ln f_B + \frac{f_C}{1} \ln f_C \\ + \chi_{\text{AB}} f_A f_B + \chi_{\text{BC}} f_B f_C + \chi_{\text{AC}} f_A f_C \end{array} \right\}, \quad (6.5)$$

with total number of monomers  $n = n_A + n_B + n_C$ , where  $n_X = f_X \cdot n$ .

As the solvent evaporates, the overall composition shifts continuously toward the polymer-rich region of the ternary phase diagram. This corresponds to a vertical trajectory in composition space in Figure 6.3b, which schematically visualizes the Gibbs free energy transition

during the spin-coating process. Depending on the initial composition  $\phi_m$ , the system in the ternary stable state (green region) crosses to either the metastable (beige) or the unstable (rose) regions, leading to nucleation-and-growth or spinodal decomposition, respectively. The metastable region is classified by a residual free-energy barrier, which must be overcome to nucleate a new phase, while in the unstable regime, no such barrier exists [213]. At extreme compositions, i.e.  $f_{A/B} \ll 1$ , the free energy of the mixed state remains lower than that of the separated phases, and no decomposition occurs. Note that Fig. 6.1b represents a simplified system with equal polymer weight, -volume, and solubility in the solvent, and neglects any influence of interfaces as well as the spatial confinement in the thin film. To ensure that the phase behavior is primarily governed by the intrinsic blend parameters ( $\chi$ ,  $N$ ), asymmetric interfacial energies at the substrate-blend and blend-air interfaces favoring interaction with one of the two polymers must be minimized. At the substrate level, this is easily achieved by the dehydration step. However, the composition of the atmosphere changes as the solvent evaporates during the spin coating runs, which emphasizes the need to carefully control the ambient conditions during and in-between deposition runs to warrant reproducibility.

### 6.2.3 Impact of Substrate and Ambient Conditions

To control the environmental conditions, all tools used in the process, i.e. the spin-coater, two hotplates and a cold plate (not shown) are placed in a custom-built glovebox (Fig. 6.8). To ensure similar affinity of the substrate for the adsorption of either polymer type, the substrate is pre-treated. A large number of adsorbed water molecules on the substrate increases the hydrophilicity and in turn favors the more polar PMMA polymer, which typically leads to a vertical phase separation rather than the desired lateral domains. Therefore, the substrates are pre-baked on a hotplate ( $T = 80^\circ\text{C}$ ) for 10 minutes before the deposition step. At high ambient RH > 50%, a thin film of PMMA is more likely to occur at the blend-air interface, due to its lower interfacial free energy in this condition, as well as the condensation of water molecules on the evaporating cooled polymer solution surface [210]. At intermittent relative humidity levels ( $\sim 40\% \text{RH} - 50\% \text{RH}$ ) and appropriate sample dehydration, the desired nucleation-and-growth phase is promoted [210]. Either insufficient sample dehydration or immediate re-hydration of the substrate by a high relative humidity can similarly lead to the formation of a vertically separated three-layered PMMA-PS-PMMA film [216].

Lastly, an important factor to consider is the changes in atmospheric condition after a deposition run. The evaporating MEK solvent modifies the gas composition in the glovebox, which may lead to more favorable conditions for one phase over the other, similar to extreme RH values. To address this in our routine, we flush the chamber with dehydrated nitrogen after each deposition run and subsequently wait for the input atmosphere regulator to restore the desired humidity levels. Here, we use two distinct hygrometers placed in different locations; one is placed above the spin-coater and another next to it on the floor of the glovebox. The atmosphere is considered “restored” once both RH values agree within their given tolerance of  $\pm 2\%_{\text{abs}}$ . Further details are provided in the experimental section and in Fig. 6.8.

### 6.2.4 Selective Dissolution and Etch Transfer

Using appropriate solvents, either polymer phase in the resulting mixed film can be selectively dissolved. Within our fabrication parameters, the PS phase forms island domains encapsulated in a PMMA host matrix. In here, we primarily study the route to selectively dissolve PMMA using acetic acid, leaving the remaining PS islands as an etch mask. We use a three-step reactive-ion etch routine to transfer the pattern on c-Si wafers. The three steps

consists of: i) an initial  $O_2$ -plasma step, which removes any residual organic compounds in the trenches separating the PS islands to ensure that the substrate is equally exposed in all trench regions. ii) Substrate etch to a depth of  $\sim 200$  nm, using  $SF_6$ . iii) Another  $O_2$ -plasma step to remove the remainder of the polymer mask.

The etch transfer into the substrate provides an additional tuning knob through the duration of the initial  $O_2$ -plasma step. Increasing this etch time removes smaller pillars and yields a more sparse arrangement of larger pillars. In this work, all samples were subjected to 30 s of pretreatment with  $O_2$ -plasma which removes about 73 nm of height from a flat PS thin-film on the same substrate. At a suitable etch selectivity between mask and substrate, prolonging the substrate etch until the mask has completely dissolved provides a further opportunity for tailoring, since it produces a vertical gradient of the material's filling fraction as a result of the gradually shrinking island domains as the etch depth increases. The success of obtaining the desired nucleation-and-growth phase and the ability to reproduce a particular result thus depends on careful control of the process steps and the ambient conditions. Inversely, however, the delicate dependence on macroscopic parameters presents tuning knobs to influence the formation and resulting phase-separated morphology, which we demonstrate next.

### 6.3 Results

We start by characterizing a representative structure obtained from the polymer blend process. Figure 6.4a shows an atomic force microscope (AFM) image of the PS island distribution obtained upon spin coating and selective PMMA dissolution, which reveals a dense arrangement of isolated pillars with roughly similar heights up to 500 nm. Most pillars show a homogeneous dome shape with radii varying approximately within one order of magnitude. The polymer morphology already presents a compelling opportunity to be used as an optically functional layer on its own, where the dome shape offers a gradually increasing vertical effective refractive index profile that is homogeneous across large spatial domains. The SEM image in Fig. 6.4b shows that the pattern of isolated PS islands is faithfully transferred into the substrate by the anisotropic etching. Wide-field SEM images (see appendix Fig. 6.9) corroborates a high degree of homogeneity over  $> (100 \mu\text{m})^2$ .

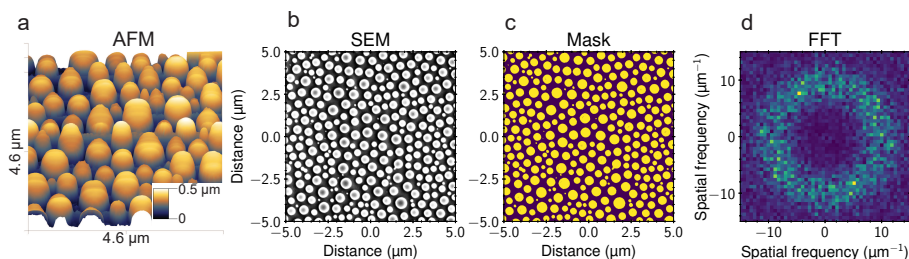


**Figure 6.4: Structural characterization**

**a** Atomic-force microscopy (AFM) image of a PS mask on a substrate after selective dissolution. The spin-coated blend consists of 8 kg/mol PMMA and 25 kg/mol in a mutual mixing ratio of 3:2 and dissolved in MEK to a total polymer concentration of 4%<sub>w</sub>. **b** Top-view scanning-electron microscopy (SEM) image of the pattern after etch transfer. **c** Binary mask obtained from (b) by Otsu-thresholding. **d** 2D Fast-Fourier transform (FFT) of the mask in (c).

To assess the structural correlations of the transferred nanopatterns, we create a binary mask from the SEM image by Otsu-thresholding (Fig. 6.4c) and obtain the power-spectral density (PSD) by calculating a 2D fast Fourier transform (FFT) of the mask (Fig. 6.4d). The resulting PSD intensity distribution shows a clear ring-like feature stemming from the aperiodic yet uniform distribution of the PS islands. The ring outer and inner boundaries delimit the minimum and maximum distances between neighboring nucleation sites, respectively, as well as their domain sizes. The PSD thus affords a spectral view on the distribution of mutual distances between the pillars at small spatial frequencies and the distribution of pillar radii at high momentum values. Specifically, the dark disk centered about the origin with a radius  $k_i \sim 6 \mu\text{m}^{-1}$  corresponds to a maximum separation distance between pillars of about  $2\pi/k_i \sim 1050 \text{ nm}$ . The average pillar diameter, on the other hand, corresponds to the outer diameter of the high-intensity ring at  $k_o \sim 12 \mu\text{m}^{-1}$  of about  $524 \text{ nm}$ .

The PSD image indicates that the phase-separation process readily produces disordered near-hyperuniform patterns (cp. with sec. 2.5.4, and [94, 95]). It must be noted, that the mathematical formulation of the hyperuniform criterion pertains to point distributions rather than real topographies with finite domain sizes. Thus, experimental realizations such as these are classified as near-hyperuniform and described by their degree of hyperuniformity instead [222, 223].

### 6.3.1 Impact on the Light Scattering Properties

We now turn towards the characterization of the scattering properties of our fabricated samples after etch transfer and their relation to the pattern's PSD. Figure 6.5a,b show the mask and the corresponding 2D FFT, respectively, of two distinctive patterns obtained by using two different PS molar weights. The top row uses a PS molar weight of  $25 \frac{\text{kg}}{\text{mol}}$ . Instead, the bottom row uses  $13 \frac{\text{kg}}{\text{mol}}$  PS, thereby reducing both the average chain length and molar weight difference between the constituents. The remaining composition and deposition parameters are kept the same. In either case, the mask images in (b) display the characteristic circles of the etched Si pillars, originating from the PS islands. At first sight, one can see clear differences in the pillar density, diameter, and diameter distribution between the two samples. The ring-shaped PSD in (b) again indicates the near-hyperuniform nature of both patterns. The denser pillar distribution in the bottom row results in a PSD ring shifted to larger momenta with respect to that in the top row.

To experimentally study the angular light scattering properties of the layer, we record the reflectance in the Fourier plane. We take one measurements at normal incidence and four at grazing incidence from orthogonal directions and construct a superposition of the five images to access a larger range in k-space. The resulting momentum-space reflectance map (Fig. 6.5c) shows a strong resemblance to the PSD in column (b). The four bright dots at large momenta on the ring are artifacts of the imaging procedure (see methods).

To better compare the scattered intensity distribution with the PSD, we radially-average the profiles from columns (b) and (c) in column (d). The resulting angular distributions reveal the direct correlation between the scattered light and the pattern's PSD. The deviation at low  $k_{\parallel}$ -values stem from a strong specular reflectance peak at  $k_{\parallel} = (0, 0)$  in the optical response, which results from the measurement at normal incidence. These results confirm that the angular scattering response is directly governed by the PSD of the polymer-blend structure, providing a clear route to tailoring its optical properties via controlled morphology design.

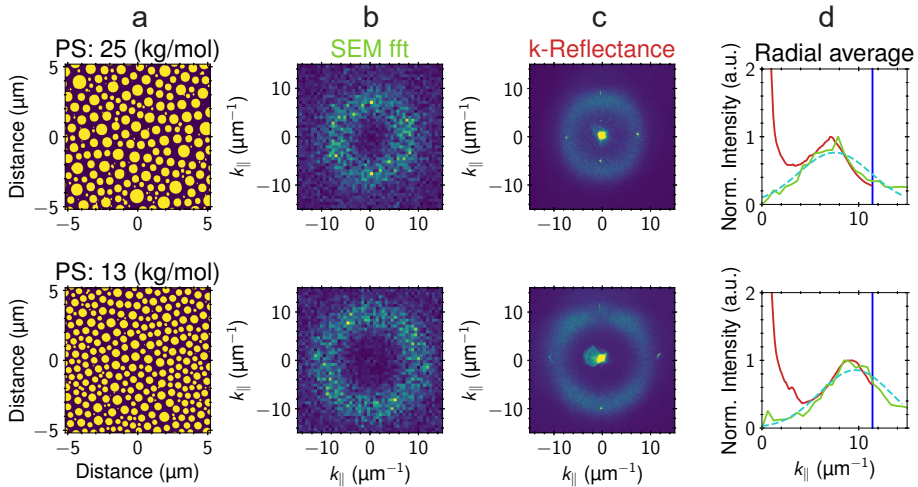


**Figure 6.5: Varying the molar weight of one polymer-blend constituent**

The polymer blends are prepared with PMMA (8 kg/mol) and PS (25 kg/mol in the top- and 13 kg/mol in the bottom row), with ratio 3:2, and dissolved in the common solvent MEK at 4%<sub>w</sub> total polymer concentration. Column **a**: Binary masks obtained through Otsu-thresholding SEM images taken after etch transfer. Column **b**: 2D PSD obtained from FFT of SEM images in **a**. Column **c**: Momentum-resolved reflectance measurement of 532 nm laser measured with  $NA = 0.95$  objective under illumination at different angles of incidence. Column **d**: Radial average of columns **b** (green) and **c** (red). A gaussian curve is fitted to the PSD radial average and displayed as a cyan dashed line. The vertical blue line denotes the light-line  $k_0 = \omega_0/c_0$  at the laser frequency  $\omega_0$  and with speed of light in vacuum  $c_0$ .

### 6.3.2 Tailored Pattern Formation through Process Parameter Variation

In the following, we map out the impact of blend composition on the pattern properties that determine light scattering. Among all experimental parameters, we systematically vary the blend composition. Specifically, we investigate three PS:PMMA weight ratios in the blend (1:1, 2:3, and 1:3) in combination with a series of molar weights ( $M_w$ ) for both PMMA and PS. For each of the samples, we perform the same PSD analysis as described above. Plots of the corresponding masks, PSDs, and fits to the radially averaged PSD for all samples are compiled in the appendix (Figs. 6.13-6.17).

Figure 6.6a plots the PSD peak position as a function of the molar ratio between PS and PMMA, i.e., the ratio of the number of polymer chains introduced into the blend. A clear power-law dependence is observed: as the PS:PMMA molar ratio decreases, the PSD peak position increases asymptotically. This behavior reflects the change in the characteristic lateral correlation length of the structure. Since the PSD peak momentum  $k_{\text{peak}}$  scales inversely with the mean inter-domain spacing ( $k_{\text{peak}} \sim 1/d$ ), reducing the relative number of PS chains effectively modifies the domain density and shifts the characteristic length scale toward smaller spacings, resulting in higher peak momenta.

The spread of inter-domain distances is reflected in the FWHM of the PSD peak (Fig. 6.6b). The ratio FWHM:peak position exhibits a clear correlation across all produced samples.

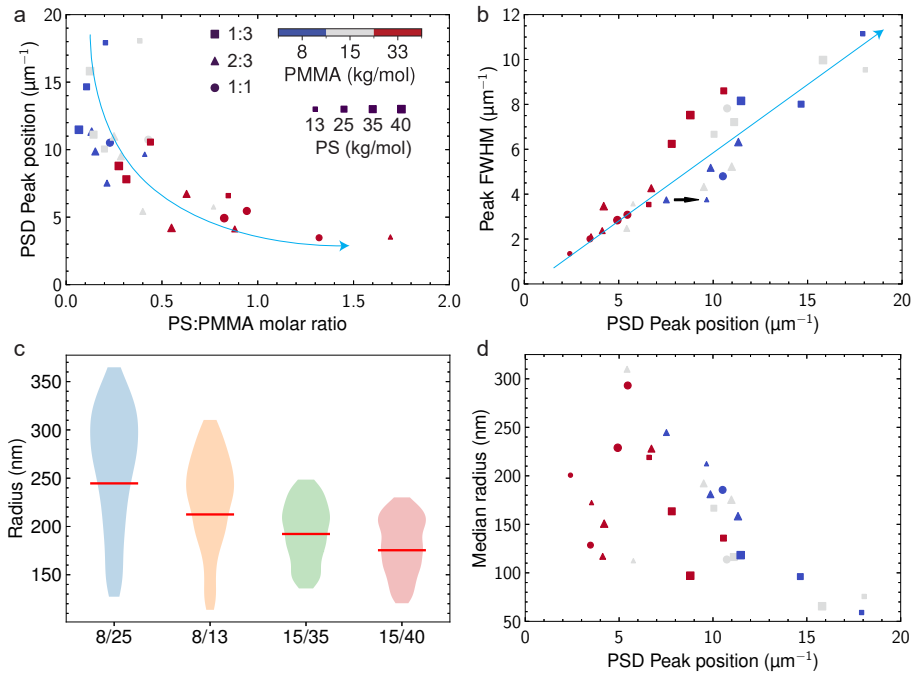


**Figure 6.6: Library of PSD signatures obtained with polymer-blend nanolithography**  
**a** PSD peak position versus molar ratio of PS:PMMA. The PMMA molar weight is color-coded and the symbol type/sizes/colors are the same in (b,d) and the blue arrows in (a,b) serve as a guide to the eye. **b** PSD peak FWHM versus peak position. The black arrow shows the phase-map trajectory corresponding to single parameter variation (Fig. 6.5, from top to bottom row). **c** Distribution of radii in selected samples, denoted by their PMMA- and PS molar weights ( $M_{\text{PMMA}}/M_{\text{PS}}$  in kg/mol) on the abscissa. The red horizontal line marks the median radius and only radii are shown that fall within one  $\sigma$  from the median value. **d** Median radius versus PSD peak position for all samples.

This can be understood by recalling the connection between number variance and size of the observation window for a HUDLE layer, i.e. that the variance  $\sigma$  in the 2D observation window of radius  $r$  scales as  $\Delta\sigma \propto d < 2$ . A larger number of points (larger PSD peak position) is equivalent to an increase in  $r$ , and the slope in (b) clearly corresponds to a scaling exponent smaller than 2. The scaling exponent  $d$  for each individual sample is plotted in the appendix Fig. 6.11, which shows values  $1.3 < d < 1.7$ , where smaller exponents (higher degree of correlations) are found mostly for distributions with small PSD peak momentum. In many instances, solutions with equal polymer weight ratios  $R$  tend to produce narrower distributions than more asymmetric polymer weights, which reflects the observations made in columns (a,b). There is no apparent general law for the effect of a single parameter variation throughout the whole parameter space. In the close vicinity of a particular coordinate, however, we often find direct dependence of either FWHM or peak position on one changing parameter, e.g. the exemplary PS-weight reduction in Fig. 6.5 produces a shift in peak

position with near-identical FWHM (black arrow in Fig. 6.6b). As such, Fig. 6.6b provides a well-established look-up table for selecting blend properties yielding certain PSD profiles, which is reproducible with equivalent control over the critical process parameters.

Beyond spatial correlations given by the PSD, the spectral response of scattered light from the patterns will also be affected by the individual scatterer's dimensions [91]. Therefore, we also analyze the island dimensions by employing a particle recognition algorithm on the AFM or SEM images [224]. Fig. 6.6c plots a selection of radii distributions for samples fabricated with different PMMA and PS molar weights. The PMMA/PS weights are indicated in the axis label. Not only the median radius is influenced by the PMMA/PS ratio, but also the spread of radii. The first and second entry from the left correspond to the samples in Fig. 6.5, top and bottom, respectively. Among these, we observe a decrease of the median radius as visually inferred from the mask images, as well as a reduction in the spread of radii within the standard deviation. The second entry confirms that the upper PSD intensity limit corresponding to  $\sim 525$  nm (Fig. 6.5b) roughly matches twice the mean radius of the extracted pillar distribution.

We find that there are varying degrees of correlations between PSD and median pillar radius, depending on the blend composition. Fig. 6.6d plots the PSD peak position as a function of median radius ( $r_m$ ) for a large range of compositional parameters: PMMA molar weight (color), PS molar weight (symbol size), and PS:PMMA mixing ratio (symbol orientation). The broad compositional parameter space allows us to access a large range of median radii, from 50 nm features up to 300 nm. We observe that the overall average separation distance (and thus PSD peak position) is intrinsically anti-correlated to the median radii. The data points of  $\sim 30$  different compositions show trends pertaining to their specific PMMA and PS molar weights, where smaller PMMA weights predominantly yield larger PSD peak momenta. In the region  $100 \text{ nm} < r_m < 250 \text{ nm}$  specifically, a large range of PSD peak positions can be targeted by adjusting the mutual mixing ratio, leading to more sparse or dense arrangements of islands with near-identical median radii. Comparing this region with the distribution of data points in (b), we confirm that the link between FWHM and PSD peak position naturally translates to an anti-correlation between median radius and FWHM as well.

By systematically varying both molar mass and blend ratio, we thus establish a comprehensive library of PSD signatures and corresponding radius distributions. This parameter space provides a practical guideline for tailoring the structural correlations — and consequently the light-scattering properties — of the polymer-blend films.

### 6.3.3 Enhanced Light Trapping with Self-Assembled HUDLE Patterns

Light that is diffracted by a surface whose corrugation contains spatial features comparable to the optical wavelength acquires in-plane momentum components corresponding to those spatial-frequencies [125, 127, 195, 225]. As such, the position and full width at half maximum (FWHM) of the PSD peak of a pattern serve as an initial prediction for the momentum distribution of light scattered by the phase-separation-induced nanopatterns. Interestingly, for PSD peak positions falling above the light line of wavelengths in the range (600 – 1200) nm, that is approximately  $k_{\parallel} \in [5, 10] \mu\text{m}^{-1}$ , Fig. 6.6b shows a wide range of attainable FWHM distributions at each targeted peak PSD momentum value. Beyond the PSD, optimizing the physical dimensions of the individual PS island domains can further increase the optical response through resonant light scattering, enhancing the pattern's scattering strengths [89, 226]. A pattern featuring a range of radii centered around an optimized value for Mie-

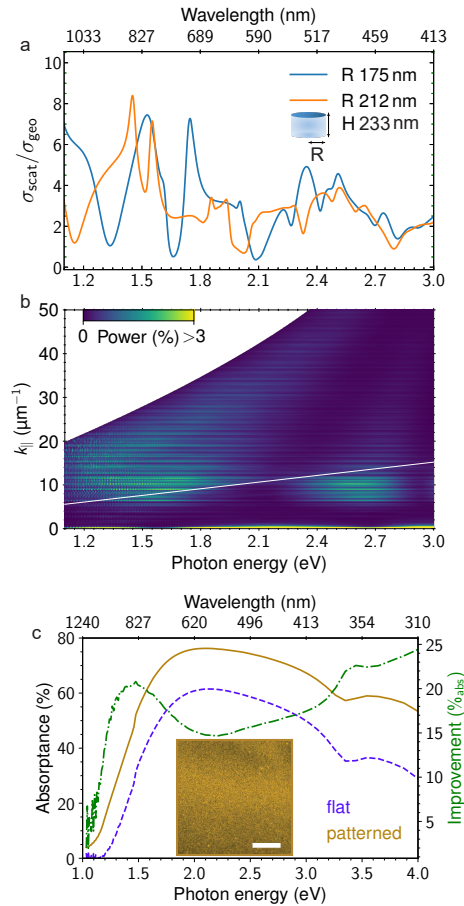


**Figure 6.7: Ensemble statistics and light-trapping capabilities of selected samples**  
**a** Scattering cross-section normalized to geometrical cross-section for a cylinder in air with median radii taken from Fig. 6.6a. **b** Spectrum- and momentum-resolved scattering analysis by FDTD simulation of a  $10\ \mu\text{m}$ -thick silicon substrate in air with an additional  $200\ \text{nm}$  layer of the pillar distribution obtained from the masked SEM image by circle detection (Sample 19, Fig. 6.16). The color of the heatmap indicates the fraction of incident power absorbed within each energy and momentum bin. **c** Absorbance measured as  $1 - \text{Reflectance} - \text{Transmittance}$  of a  $10\ \mu\text{m}$ -thick Si wafers before (dashed curve) and after deposition and etching (solid curve). The blend consists of  $15\ \frac{\text{kg}}{\text{mol}}$  PMMA and  $35\ \frac{\text{kg}}{\text{mol}}$  PS, mixing ratio 3:2, and  $4\ \%$  total polymer content dissolved in MEK. The absolute percentile improvement is plotted on the right axis as a dot-dash line. Inset: Optical microscope image of  $10\ \mu\text{m}$ -thick sample after etch transfer. Scalebar  $5\ \text{mm}$ .

resonances [81, 227] within the spectral bandwidth of interest will exhibit greater scattering efficiency across a broad wavelength range than a similar pattern with only a singular radius value. Tailoring the distribution of radii independently of the structural correlations

by adjusting macroscopic process parameters constitutes the pivotal objective of the self-assembled immiscible-blend lithography.

To elucidate the scattering response of a single nanopillar, we employ finite-difference time-domain (FDTD) simulations to calculate the spectrally-resolved scattering cross-section of a cylinder in air. We choose the cylinder's height as 233 nm based on the average height observed in the AFM measurement (Fig. 6.1e), and select as radii the the smallest and largest median values in Fig. 6.6b, specifically  $r_1 = 175$  nm and  $r_2 = 245$  nm (Fig. 6.7a). Both curves show a larger scattering cross-section than their projected areas (geometrical cross-section) for nearly all wavelengths. Due to the relatively large size of the particles, many higher-order Mie resonances are supported that give rise to strong light-matter interactions inside the high-index material, that appear as sharp peaks with irregular distribution across the spectral range. While notable differences can be observed between the two spectra, the statistical variation of radii within one pattern will result into a similar scattering efficiency throughout the wavelength range. Figure 6.7a clearly shows how optical resonances within the scattering particles can give rise to strongly enhanced scattering strengths by the pattern.

We include the effects of the underlying substrate as well as inter-particle interactions by performing additional FDTD simulations, where we incorporate a  $5 \times 5 \mu\text{m}^2$  excerpt of the scattering layer's morphology obtained from its masked SEM image into the top 200 nm of a  $10 \mu\text{m}$ -thick Si substrate in air. We place a monitor inside the substrate just underneath the scattering layer to record the local electromagnetic fields, and perform a near-to-far-field transformation (see methods of ch. 3, sec. 3.4) to filter for waves propagating the substrate. By partial integration of the far-field data at each frequency, we obtain momentum- and spectrally-resolved absorptance maps inside of the substrate (Fig. 6.7b). The slanted white line represents the light line in air, which indicates the onset of the guided-mode regime at higher  $k_{\parallel}$  values and the escape cone for lower  $k_{\parallel}$  values.

The heatmap shows a bright and broad horizontal feature centered around  $k_{\parallel} \sim 10 \mu\text{m}^{-1}$ , coinciding with the peak of the PSD (Fig. 6.16, sample 19). The observation of absorption by continuous sub-bands of the guided mode branches, rather than enhancements at specific, distinct in-plane momenta and photon energies, directly relates to the ability of (correlated-) random patterns to provide PSDs with continuous features and is therefore unattainable with periodic structures. In addition, the near-hyperuniform correlations effectively suppress small-angle scattering into the escape cone, leading to a similar response for a wide range of wavelengths and renders nanostructures of this kind particularly attractive for broad-band optoelectronic applications. Interestingly, there is low scattering into the wavevectors within the PSD at  $\sim 2.1$  eV, where most of the absorption is contributed by the zeroth order ( $k_{\parallel} \sim 0$ ). The scattering dip aligns well with the local minima seen in the scattering cross-section for the large and small radius cylinder in panel (a). In fact, all intermittent radii value exhibit a similar dip at this photon energy (Fig. 6.12) due to a Fabry-Pérot resonance within the Si pillars of height  $h = 233$  nm, which scatters light predominantly forward into the substrate.

To test the scattering and absorbing properties of the different formations in a real device, we apply the phase-separation lithography on a  $10\text{-}\mu\text{m}$ -thin silicon wafer. The inset of Fig. 6.7c shows a bright-field microscope image of the patterned sample after etch-transfer of the structure. There are slightly darker regions at the top and bottom of the excerpt, where the scattering/absorptance is larger than in the center. Overall, the phase-separated pattern reveals a homogeneous coverage of nanopillars across the whole  $\sim 4 \text{mm}^2$  area, emphasizing the large-area applicability of the method. To study the effect of the pattern on light absorption within the wafer, we performed transmission and reflectance measurements before and after the fabrication procedure (Fig. 6.7c). The nanopillar arrangement enhances absorptance substantially across the entire spectral range, increasing from  $37.0\% \rightarrow 53.1\%$  on average

(AM1.5G-averaged [228]: 32.7%  $\rightarrow$  53.1%). There is substantial improvement especially at long wavelengths, with up to 20%<sub>abs</sub> at  $\sim$  950 nm. The boost at small wavelengths is equally remarkable, since these wavelengths will be absorbed in a single pass through the device thickness. The increased absorptance is solely due to better in-coupling through the scattering layer, even in the absence of any anti-reflective coating.

## 6.4 Discussion

For implementation of phase-separation driven nanopattern generation at larger scales, spin-coating needs to be replaced by scalable deposition techniques compatible with in-line fabrication schemes, such as roll-to-roll or roll-to-plate. The spin-coating process affords rapid evaporation of the solvent, the rate of which can be controlled by ramp up times and revolutions per minute of the process, which is performed in a controlled atmosphere but otherwise ambient conditions of pressure and temperature. To obtain a similar quenching rate of the solution to its condensed state in a continuous deposition tool, e.g. slot-die coater, the solvent evaporation could be controlled by both atmospheric conditions such as ambient temperature and pressure, or through non-contact means like laser heating or flash annealing.

The scattering efficiency of the pattern depends upon the refractive index contrast between the (nanoscale) inclusions and host medium, which for PS ( $n \sim 1.5$ ) and air ( $n = 1$ ) is insufficient to provide significant scattering strength. This could readily be resolved by replacing one of the constituent polymers by a high-index dielectric, such as a sol-gel containing TiO<sub>2</sub> nanoparticles. Thereby, the functionalization of the device's surface would be achieved in a single deposition step without the need for reactive-ion etching. In cases where the deposited morphology readily constitutes the final structured layer, the thermodynamic transition during phase separation offers yet an additional opportunity to achieve truly three dimensional control over the resulting scattering layer. The binary polymer blend upon freezing produces a non-uniform surface topography, where in the case of a blend consisting of PMMA and PS in MEK, the PMMA-rich regions protrude above the PS domains after the solvent has fully evaporated. This property pertaining to the difference in relative solubility in the solvent can further be exploited in a ternary polymer blend in order to produce truly three dimensional networks with tailored properties [214].

## 6.5 Conclusion and Outlook

We present improvements in immiscible polymer blend lithography that enable correlated-structural and geometrical nanopatterns suitable for many broad-band optoelectronic applications. The fabrication procedure relies on control over temperature, humidity and atmosphere during the phase separation process and restoring the starting conditions in-between each deposition. The produced structures show correlations in their spatial arrangements belonging to the (nearly-) hyperuniform disordered class and our process allows to tailor the PSD profile, validated through FFT of masked SEM images, which in turn governs the light-scattering properties of the pattern in a real device. Here, the minimum scattering angle or in-plane momentum can be targeted to fall beyond the light line and into the guided-mode regime of the absorbing or emitting substrate. At the same time, the spread of momenta and domain sizes can be controlled partially independently of the peak position, which allows optimization of the scattering structure for arbitrary materials. We identify near-linear regimes in PSD peak position and FWHM when only one parameter is varied slightly, enabling

adjustments to the resulting pattern, and supply a library of 29 different configurations of molar weights and ratios to serve as a guide when designing scattering layers for specific applications.

Using FDTD simulations, we assess the resonant scattering behavior of the produced nanopillar geometries and highlight how localized resonances inside the nanoparticles enhance the scattering strength of the layer. Next, we employ a spectrally- and momentum-resolved absorbance analysis to quantify coupling to guided modes in a finite, weakly-absorbing substrate with an experimentally realized scattering mask is incorporated into its surface. Finally, we perform the phase-separation process directly on a thin silicon substrate and experimentally measure its optical absorbance before and after patterning its surface. The scattering into large in-plane momenta overlapping the guided-mode regime is corroborated by substantial absorption enhancements especially at long wavelengths, for which the absorption coefficient becomes very small, leading to an increase in AM1.5G-averaged absorbance of 20.4 %<sub>abs</sub>.

Overall, our results enable the reliable fabrication of tailored large-area self-assembled nanopatterns suitable for a wide range of applications and materials used. By using the process parameter library presented in this work, the selection of specific molar weights and mutual ratios is greatly accelerated and the demonstrated characterization methods allow predictions of optical performance of the created morphology before the fabrication of the device is finalized.

## 6.6 Experimental

### Polymer Blend Solutions

The polymer characteristics are summarized in Table 6.1. Each polymer is dissolved separately in MEK to a concentration of 4 %<sub>w</sub> and stirred for one hour before blending the solutions to obtain the desired mutual ratios. The blended solutions are stirred for another hour. The stirring is performed in sealed vials at ambient conditions. All investigated compositions are summarized in 6.2 and are deposited within 48 hours of their preparation.

**Table 6.1:** *Polymer properties*

Polymer	kg/mol	Supplier	PDI $((M_w)/(M_n))$
PS	13	Thermo Fisher	1.06
PS	25	Thermo Fisher	1.06
PS	35	Fraunhofer ISE	2.0–2.4
PS	40	Polysciences	unknown
PMMA	8	Thermo Fisher	unknown
PMMA	15	Sigma - Aldrich	1.05
PMMA	33	Scientific Polymer Products	2

**Table 6.2:** Synthesized Polymer Blends

PMMA (kg/mol)	PS (kg/mol)	POLYMER CONCEN- TRATION (wt %)	RATIO (PMMA:PS)
8	13	4	1:1, 3:1, 3:2
8	25	4	1:1, 3:1, 3:2
8	35	4	1:1, 3:1, 3:2
8	40	4	1:1, 3:1, 3:2
15	13	4	1:1, 3:1, 3:2
15	25	4	1:1, 3:1, 3:2
15	35	4	1:1, 3:1, 3:2
15	40	4	1:1, 3:1, 3:2
33	13	4	1:1, 3:1, 3:2
33	25	4	1:1, 3:1, 3:2
33	35	4	1:1, 3:1, 3:2
33	40	4	1:1, 3:1, 3:2

## Substrate

Standard Czochralski-grown (Cz), (100)-oriented, single-side polished, 3-inch silicon wafers (Siegert Wafer<sup>TM</sup>) with thickness 380  $\mu\text{m}$  are used as substrates for deposition trials. Thin substrates of 10  $\mu\text{m}$  thickness are obtained from Virginia Semiconductors, Silicon Cz Wafers of one inch diameter.

## Spin-Coat Deposition

The spin coater (SPS NPP Polos SPIN150i) is operated in a glovebox equipped with multiple temperature and humidity sensors (See Fig. 6.8). Relative humidity is set and maintained with a controller that mixes ambient air with dehydrated nitrogen and feeds into the glovebox. One hygrometer (Extech 445713 Big Digit Indoor/Outdoor Hygro-Thermometer) is suspended just above the spin-coater and another hygrometer B (Wireless Temp & Humidity Sensor TH05) sits next to the spin-coater on the glovebox floor. Before deposition, the substrate is placed on a hot plate at 130  $^{\circ}\text{C}$  for 10 minutes to remove any adsorbed water and subsequently cooled on a 1 cm-thick copper plate for 30 seconds. Subsequently, the substrate is transferred to the spin-coater, the solution drop-casted and the spin cycle initiated immediately. The spin parameters are listed in table 6.3.

**Table 6.3:** Spin-coating parameters

RPM	Acceleration (RPM/s)	Duration (s)
4000	400	40

The deposition is followed by soft-baking at 80°C for 2 minutes. After processing, the atmosphere in the glovebox is restored by flushing with the nitrogen/air mix within the desired relative humidity window until both hygrometers display identical values within given their tolerances (2 %<sub>abs</sub>).

### Selective Dissolution

Either polymer phase can be dissolved selectively, where acetic acid is used to dissolve PMMA and cyclohexane for PS. To dissolve the PMMA layer, samples are submerged in undiluted acetic acid glacial ( $\geq 99.9\%$ ) for 10 min without agitation. To dissolve solely the PS, the sample is placed in cyclohexane instead for 10 min without agitation.

### Reactive-Ion Etching (RIE)

A three-step etch is performed to transfer the mask into the substrate using an Oxford Instruments Plasma Technologies Plasmalab 80 system. The steps are summarized in Tab. 6.4. The first and third steps use 25 sccm O<sub>2</sub> at 5.0 torr and 20 °C for 30 s and 150 seconds, respectively. The second step uses 15 sccm SF<sub>6</sub> at 17.5 torr and 20 °C temperature for 150 seconds.

### Atomic Force Microscopy (AFM)

AFM measurements are carried out using a Bruker Dimension Icon-PT AFM operating in ScanAsyst mode, with a scanning area of 10 μm × 10 μm.

### Scanning Electron Microscopy (SEM)

SEM systems used are FEI Verios 460 and the FEI Helios NanoLab 600. Images are acquired with a 20.7 μm horizontal field of view, an accelerating voltage of 5.00 kV, and a beam current of 0.8 nA.

### Particle Analysis

The freely available analysis software Gwyddion [229] was used for image analysis. For AFM images, grain segmentation is carried out using Otsu-thresholding provided with the software.

### UV-VIS Integrated Sphere Absorption Measurements

A PerkinElmer LAMBDA 750S UV/Vis/NIR spectrophotometer is used to measure transmittance and absorbance. The setup is equipped with an integrating sphere, where the sample

**Table 6.4:** Table of reactive-ion etch parameters

Steps	RF power (W)	Gases	flow (sccm)	time (s)
1	200	O <sub>2</sub>	25	30
2	20	SF <sub>6</sub>	15	150
3	200	O <sub>2</sub>	25	120

is placed either at the front input port or the rear output port for transmission or reflection measurements, respectively. The free-standing 25.4 mm diameter 10  $\mu\text{m}$ -thick sample is bonded to a quartz wafer using a thin layer ( $\sim 200$  nm) of SU-8 photoresist. Absorbance is calculated as  $A = 1 - R - T$ . Each R,T measurement is repeated three times in immediate succession, and measurements without sample (open beam) are repeated before and after the sample measurements to obtain statistical errors for the 100 % R,T reference cases. The obtained errors are within one percent of the values and are not included in the graph to improve visibility.

## FDTD Simulations

All simulations are performed with ANSYS Lumerical 2025R1 [136] FDTD suite. The simulation runs until a pre-determined shut-off level is reached. This level quantifies the fraction of injected power still residing in the simulation volume (that has not been absorbed yet). This fraction is set to  $1e-5$  for all simulation types. The simulation uses automatic conformal meshing with a minimum mesh step given in the respective sections below.

## Scattering Cross-Section FDTD Simulation

The scattering cross-section of a single cylinder in air (Fig. 6.7a) is obtained by excitation with a total-field/scattered field (TFSF) source and collected using six 2D DFT monitors enclosing the source and scatterer, from which all scattered intensities are integrated. Simulations are performed with 4 nm minimum mesh step throughout.

## 10 $\mu\text{m}$ Silicon Simulations

We simulate a free-standing 10  $\mu\text{m}$ -thick slab of silicon in air. We add a  $5 \times 5 \mu\text{m}^2$  excerpt of the pillar structure taken from an SEM measurement mask (sample 19, Fig. 6.16) and extrude the morphology 200 nm on top of the flat Si layer. The simulation boundaries are perfectly-matched layers (PML) in the directions normal to the air-Si interface and periodic boundary conditions laterally. The minimum mesh step is 10 nm in homogeneous regions and a fixed 4 nm in the patterned region and extending  $\pm 80$  nm above and below. We place three DFT monitors recording transmitted powers and local electromagnetic fields. One is placed above the source capturing any reflectance, another is placed in the top surface of the flat Si layer just below the scattering pattern, and the final monitor is placed in air underneath the Si substrate.

## Far-Field Projection

To obtain momentum-resolved absorbance characteristics, we perform a near-to-farfield transformation on the electromagnetic fields recorded by the DFT monitor located inside the substrate just below (one mesh cell) the patterned air-Si interface. The transformation settings and procedure are thoroughly described in ch. 3, sec. 3.4.

## Momentum-Dependent Reflectance Measurements

Measurements are performed with a free-space optical setup a supercontinuum laser (NKT Whitelase Micro) used as a light source, which is filtered by a band-pass with 10 nm bandwidth and subsequently coupled into a single mode optical fiber and collimated into a Gaussian

## Self-Assembled HUDLE Patterns

beam. The beam is subsequently linearly polarized and clipped in size by a 500  $\mu\text{m}$  pinhole. The beam is then focused onto the back-focal plane of the objective and reaches the sample through a 50:50 beam splitter, where back-reflection is partially redirected through a Fourier lens and captured by a high NA (NA = 0.95) microscope objective imaging onto a C-MOS camera (Basler, acA1920–40um).

We vary the angle of incidence of the impinging laser beam by translated the beam spot on the back-focal plane to achieve unity NA. The resulting 2D maps are superpositions of five images with angles of incidence  $\in [(0, 0), (\pm k_x, 0), (0, \pm k_y)]$ , where  $k_x, k_y$  are arbitrarily chosen for each sample to lie approximately at the maximum of the intensity ring.

For overlapping pixels, the maximum value is displayed after normalization to the count number of the specular reflection at  $k_{\parallel} = (0, 0)$ . The normalization is thus arbitrary and may yield different intensity ranges for each quadrant, rendering the composed 2D image primarily qualitative. The impact on the radial averages, however, remains minute due to the statistical isotropy of the phase-separation process.

## 6.7 Supplementary Information

### Custom-Built Glovebox

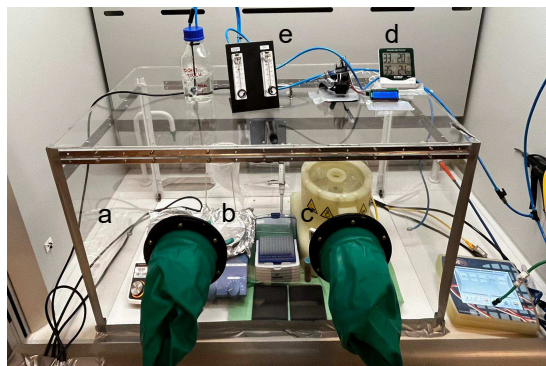


**Figure 6.8: Experimental setup**

Glovebox for humidity and temperature control by inflowing dehydrated nitrogen. The acrylic enclosure (a) contains the controlled atmosphere. Inside are two hotplates (b) for dehydration and post baking the spin-coater (c). On top of the glovebox is located one temperature and humidity meter (d) measuring above the spin-coater, the second one sits on the bottom plate next to the spin-coater (not visible). The atmosphere is controlled by a mixer (e) that regulates the inflow of a dry nitrogen and air mix into the glovebox. The setup is not sealed air tight, so that in certain regions around the bottom circumference the atmosphere can escape.

### Wide-Field View of a Polymer Blend Sample

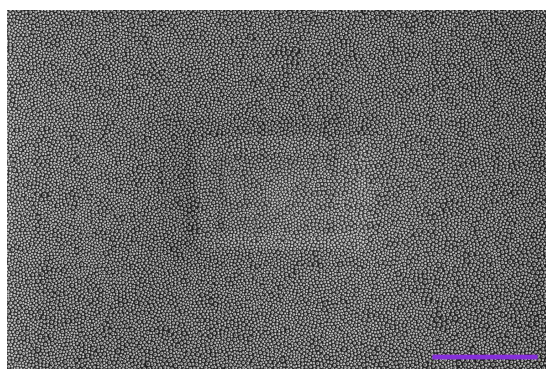


**Figure 6.9: Large-area SEM image of polymer-blend sample**

Large area SEM capture of the sample in main text Fig. 6.5, top row. Scalebar is 20  $\mu\text{m}$ . The rectangular area of brighter contrast in the center is an artifact of charging from focusing at a greater magnification level and subsequent zoom-out.

## AFM Scan of Etched Sample

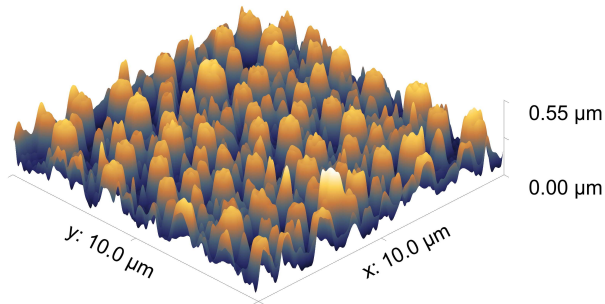


**Figure 6.10: Atomic Force Microscopy scan of a sample after selective dissolution**  
 AFM scan of a deposition on a thick wafer using identical process conditions as on the thin substrates in main text Fig. 6.7c. Grain statistical analysis reveals a median height of 233 nm, differing from the mean height of particles by less than one nanometer. This value is chosen to perform the scattering cross-section simulation in main text Fig. 6.7b.

## Variance Scaling Law

In a Poisson-random distribution, the number variance  $\sigma^2$  in the 2D observation window of radius  $r$  scales with the dimensionality  $d = 2$  of the window volume. In the presence of correlations, such as hyperuniformity, the scaling exponent  $\alpha$  is smaller than the dimensionality  $r^{\alpha < d}$  [197]. We observe in Fig. 6.11 the scaling exponent increases with PSD peak position,

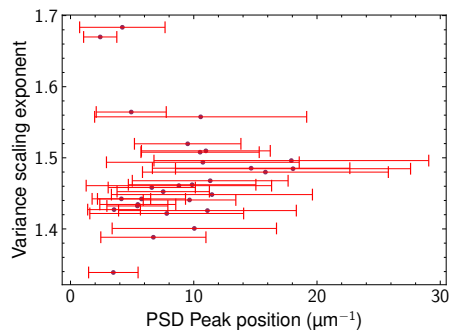


**Figure 6.11: Scaling exponent of the number variance versus observation window radius**  
 The number variance  $\sigma^2$  is extracted from each sample for different sizes of the observation window radius  $r$ . The slope is extracted from  $\ln \sigma^2 / \ln r$  and plotted versus the PSD peak position. The error bars represent the FWHM of the PSD peaks.

which reveals a more random distribution of nucleation centers when their number grows and the domains remain small. This can be understood as a consequence of the reduced polymer-polymer interactions which give rise to the correlations. The data points of the largest recorded  $\alpha$  values correspond to samples 1 ( $\alpha \sim 1.67$ ) and 2 ( $\alpha \sim 1.68$ ). From the masked SEM images in Fig. 6.13, it can be taken that the number of nucleation sites is smallest in sample 1, thus having the least statistics on the particle distribution in the observation window. Sample 2 on the other hand has a very sparse arrangement, thereby having less mutual interactions and consequently correlations. For these reasons, they can be considered as outliers.

### Scattering Cross-Section of Si Cylinders in Air

The scattering cross-section for cylinders in air of different radii and height  $h = 233$  nm is plotted in Fig. 6.12. All investigated pillars show a scattering cross-section larger than their geometrical projection for most wavelengths. There is a dip at  $\sim 590$  nm occurring for nearly all investigated radii, which corresponds to a Fabry-Pérot resonance within the cylinder due to its set height, at which the cylinders scatter light mostly in the forward direction.

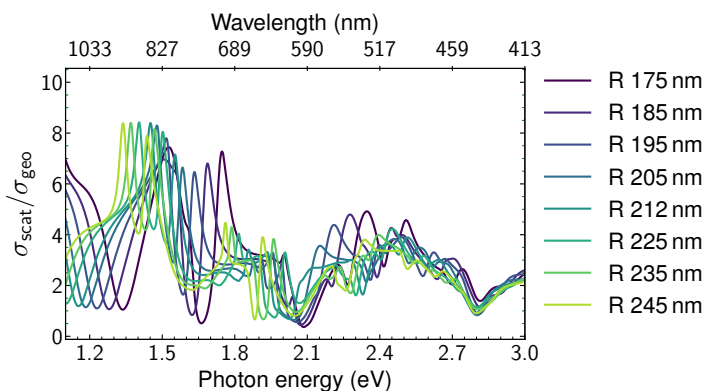


**Figure 6.12: Scattering cross-sections of cylinders in air**

Scattering cross-sections of a Si cylinder in air with height  $h = 233$  nm for different radii given in the legend.

All Samples Analysis and Fits

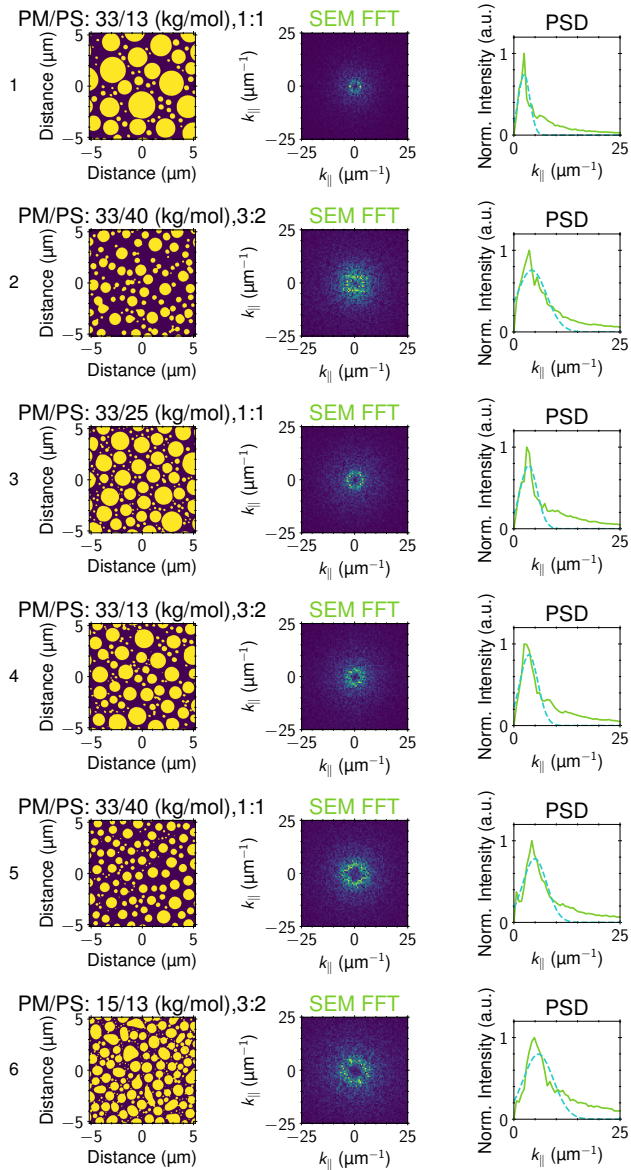


Figure 6.13: Samples #1 - #6.

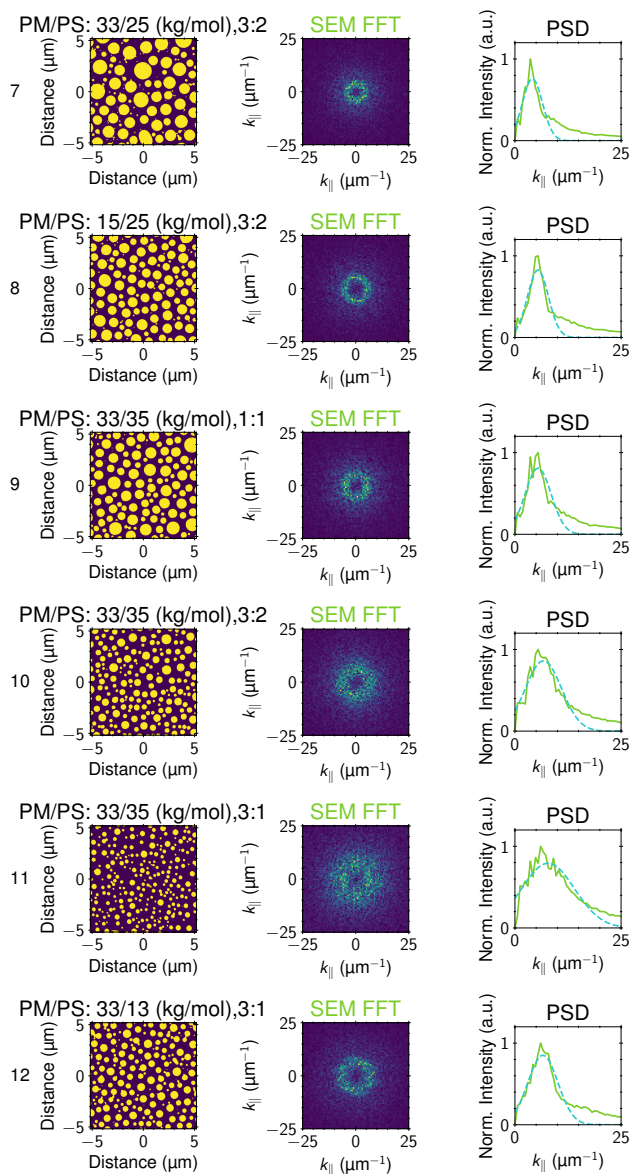
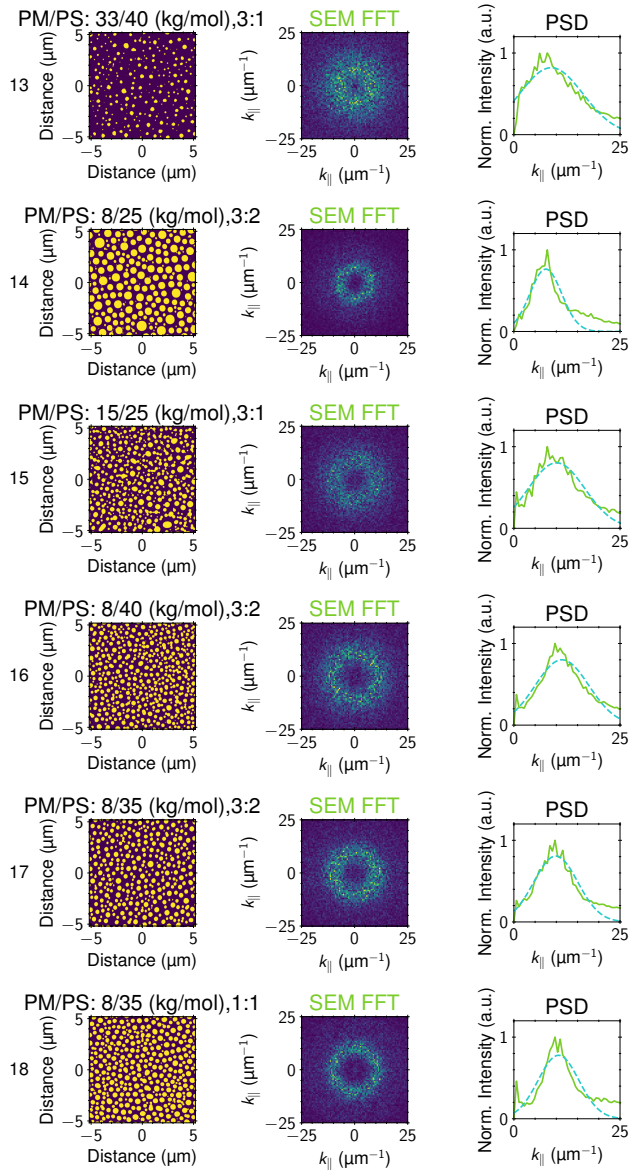


Figure 6.14: Samples #7 - #12.

# Self-Assembled HUDLE Patterns



**Figure 6.15:** Samples #13 - #18.

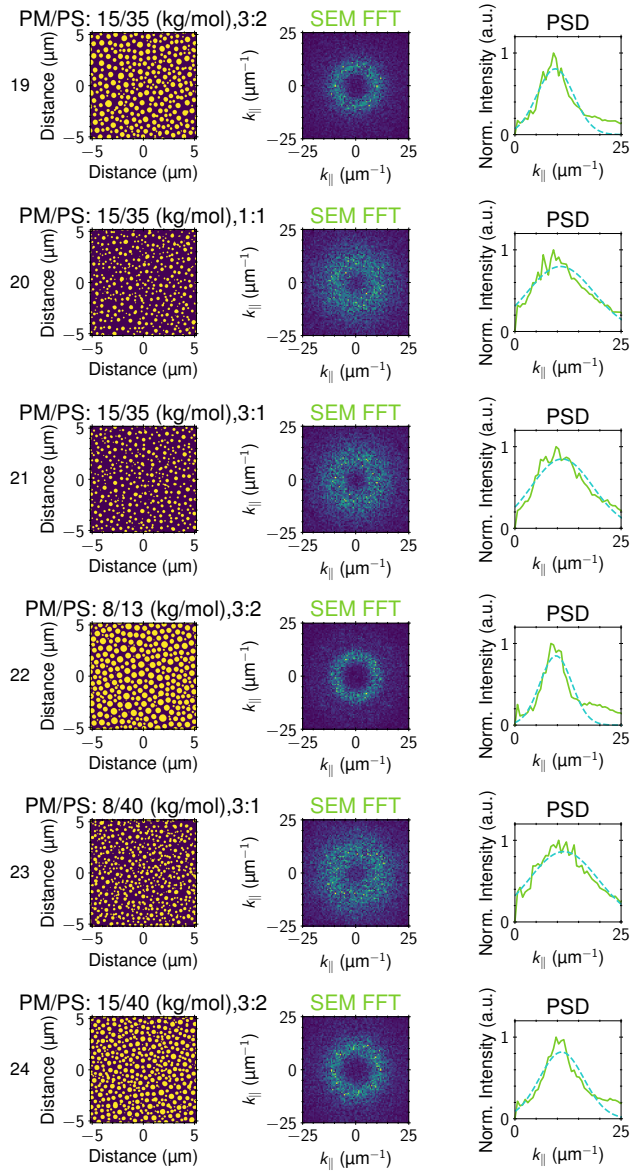
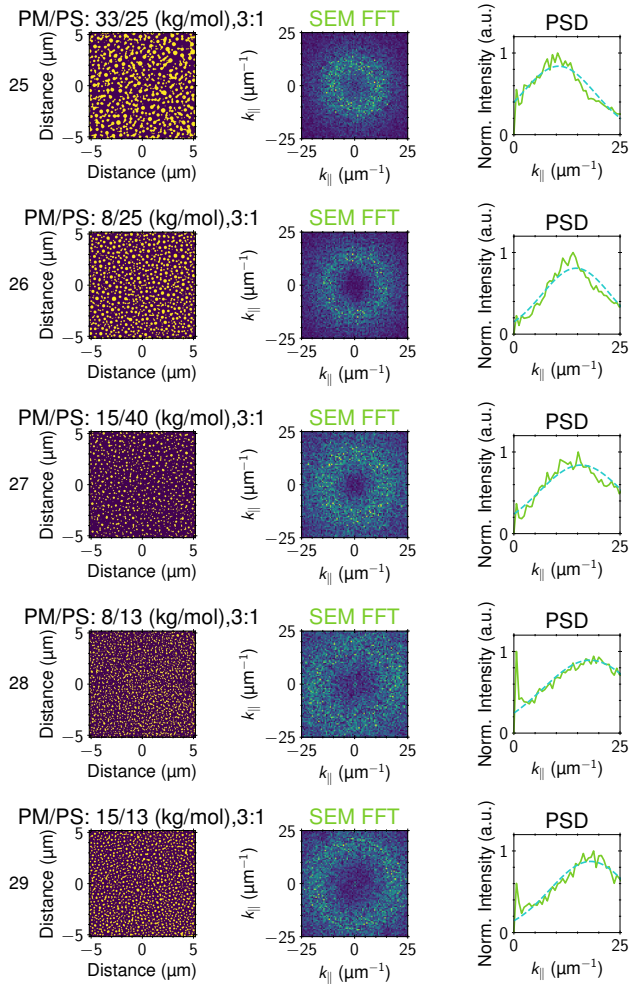


Figure 6.16: Samples #19 - #24.

# Self-Assembled HUDLE Patterns



**Figure 6.17:** Samples #25 - #29.

# List of Publications

## Related to this thesis

1. **A. Lambertz**, E. Alarcón-Lladó, J. van de Groep, *Quantifying light coupling to guided modes in semiconductor slabs with arbitrary scattering patterns*, under review in Optics Express , 2026. **(Chapter 3)**
2. **A. Lambertz**, N. Lee, V. Shautsova, A. P. M. Qoli Vafa, F. Xu, J.W. Song, N. A. Günsken, S. Selvin, M. Florescu, M. L. Brongersma, J. van de Groep, and E. Alarcón-Lladó, *Integrating Hyperuniform Disordered Light Trapping Layers in Ultrathin c-Si Solar Cells*, under review in ACS Photonics, 2026. **(Chapter 4)**
3. **A. Lambertz**, A. P. M. Qoli Vafa, M. Florescu, E. Alarcón-Lladó, J. van de Groep, *Angular Response of Ultrathin Si Solar Cells with Disordered Hyperuniform Light Trapping*, in preparation, 2026. **(Chapter 5)**
4. **A. Lambertz**, N. Urbonaite, J. Schoute, N. Feldman, J. van de Groep, E. Alarcón-Lladó, *Engineered Near-Hyperuniform Light Trapping through Phase-Separation Self-Assembly*, under review in Advanced Optical Materials , 2026. **(Chapter 6)**

## Other

5. N. Tavakoli, R. Spalding, **A. Lambertz**, P. Koppejan, G. Gkantzounis, C. Wan, R. Röhrich, E. Kontoleta, A. F. Koenderink, R. Sapienza, M. Florescu, and E. Alarcón-Lladó, *Over 65 % Sunlight Absorption in a 1  $\mu\text{m}$  Si Slab with Hyperuniform Texture*, ACS Photonics 2022, 9, 1206. <https://doi.org/10.1021/acsp Photonics.1c01668>.
6. M. Köhli, J. Weimar, S. Schmidt, F. P. Schmidt, **A. Lambertz**, L. Weber, J. Kaminski, and U. Schmidt, *Arduino-Based Readout Electronics for Nuclear and Particle Physics*, Sensors 2024, 24, 2935. <https://doi.org/10.3390/s24092935>.
7. A. Tiede, N. Feldman, **A. Lambertz**, F. Koenderink, A. Fontcuberta i Morral, and E. Alarcón-Lladó, *Blob Detection for Photonic Metasurface Designing: Angular and Spectral Control of Scattered Light*, accepted in Advanced Photonics, <https://arxiv.org/abs/2507.20857>.
8. B. Dias, R. Dziobek-Garrett, G. Mentasti, A. Gupta, **A. Lambertz**, E. Alarcon Llado, P. Schall, R. Bliem, and J. van de Groep, *Large-Area Deterministic Stamping of 2D Materials on Arbitrarily Patterned Surfaces*, under review in ACS Nano, 2026.
9. H. Song, **A. Lambertz**, B. Hoex, E. Alarcón-Lladó, and G. Conibeer, *Integration of hyperuniform disordered structures in ultrathin silicon solar cells*, in preparation.



# Author Contributions

## **Chapter 3**

Alex Lambertz developed the method, performed simulations, analyzed the data and wrote the manuscript. Esther Alarcon-Llado and Jorik van de Groep supervised the project and reviewed the manuscript.

## **Chapter 4**

Alex Lambertz fabricated the patterns and mesa structures, characterized the devices, analyzed the data and wrote the manuscript. Nayeun Lee, Viktoria Shautsova, Nicholas Gsken, Fenghao Xu, Jung-Hwan Song, and Skyler Selvin fabricated the device stack. Marian Florescu, Mark Brongersma, Jorik van de Groep, and Esther Alarcon-Llado supervised the project and reviewed the manuscript.

## **Chapter 5**

Alex Lambertz performed the measurements, analyzed data and wrote the manuscript. Ali P. Vafa performed the simulations. Marian Florescu supervised the project. Esther Alarcon-Llado and Jorik van de Groep supervised the project and reviewed the manuscript.

## **Chapter 6**

Alex Lambertz and Neda Urbonaite build the setup, and characterized the samples. Jon Schoute fabricated samples. Max Postma supported the building of the setup. Nick Feldman performed angular resolved reflectance measurements. Alex Lambertz analyzed the data and wrote the manuscript. Jorik van de Groep and Esther Alarcon-Llado supervised the project and reviewed the manuscript.



# Summary

Engineered light scattering with hyperuniform-disordered (HUD) configurations presents a compelling opportunity to enhance optical performance. This approach enables the use of thinner materials in a range of optoelectronic devices and applications, particularly those involving a broad light spectrum. Particularly for mass-produced devices such as solar cells and sensors, material expenditure and grade contribute significantly to the cost and speed of production. Reducing the thickness of active layers in these devices could further allow economical material synthesis, accelerated manufacturing, and reduced electronic losses. The optical performance of ultrathin devices is challenged, however, since the absorptance scales with the thickness of the layer. Introducing sub-wavelength scattering structures into the device can enhance absorptance through light trapping. The scattering properties must be tailored to the dimensions of the device because light trapping requires a match between its specific guided-mode structure and the momentum of the scattered light. Two main classes of structures exist: perfect order and complete disorder, each exhibiting opposite scattering properties. A periodic arrangement (perfect order) scatters light distinctly and controllably into diffractive channels, determined by the regular spacing of the scattering structures. In contrast, a Poisson-random arrangement (complete disorder) distributes light across all possible directions, offering no control. To achieve the necessary matching conditions between optical states and scattering channels, a periodic pattern provides precise control but only to a constrained set of wavelengths. In random configurations, matching conditions can occur across all wavelengths but only for a limited portion of the light intensity. In contrast to these, HUD arrangements allow controlled scattering for a broad spectral range, leading to targeted matching conditions for large fractions of light intensity.

In this thesis, we investigate how incident light interacts with ultrathin devices featuring HUD structures and leads to exceptional light trapping. We integrate HUD nanopatterns into full photovoltaic devices and study their performance compared with periodic gratings and flat reference devices. Next, we analyze light trapping in these devices with spectrally-resolved reflectance and quantum-efficiency measurements, and corroborate the experimental trends with simulations of single-particle scattering- and full-nanopattern simulations. We then test the performance of the solar cells under oblique illumination conditions, where we investigate the observed trends in the visible- and near-infrared spectral ranges separately. Subsequently, we explore a self-assembly method for creating HUD structures rapidly at large length scales, and probe the correlations between structural- and light-scattering properties with angle-resolved optical measurements. To test their light-trapping performance, we integrate these patterns in free-standing ultrathin silicon slabs and measure optical absorptance. The following provides a more detailed chapter-by-chapter description of this work.

In chapter 3, we consider the complex optical absorptance spectrum of a thin, weakly-absorbing material slab when surface corrugations are introduced. Large absorptance enhancements are observed when incident light is coupled to guided modes in the thin slab through light trapping. The precise characteristics of the guided modes and their chromatic dispersion are not easily obtained in the presence of structures and additional device layers, and asserting the coupling efficiency between incident light and a particular guided mode is not trivial. As established analytical models are constrained by a number of simplifying assumptions, they retain limited applicability when these assumptions are broken, and provide no further guidance when variations within a scattering layer are orthogonal to their

## Summary

input parameters. Even beyond analytical models, there are no numerical tools available that simultaneously accommodate non-periodic systems, calculate layer-specific absorption, determine optical band structures, and quantify coupling rates between individual guided modes and free space. Using a momentum-space approach to analyze finite-difference time-domain simulations, we develop a novel method to decompose an optical-response spectrum in the Fourier domain, which allows to extract momentum-resolved optical properties that can be traced back to specific design choices of scattering layer and device characteristics. Furthermore, we demonstrate its universal applicability by investigating purely random and HUD distributions, where we also showcase the extraction of physical parameters that directly correspond to quantities in the analytical models. Thereby, our method enables not only the quantification and characterization of arbitrary light-management strategies, but can also be employed to directly assess the assumptions in such models and advance their applicability to a wider range of systems.

Chapter 4 presents ultrathin silicon solar cells with only  $4.8\text{ }\mu\text{m}$ -thick absorption layers. Using an established platform to grow these devices on top of a silicon-on-insulator wafer, we demonstrate high solar-to-electric power conversion efficiencies already in unpatterned cells, which is afforded by minimum surface-recombination losses through a passivation layer formed by thermal oxidation. Building on the great performance of the platform, we incorporate periodic- and hyperuniform-disordered light-engineered (HUDLE) scattering layers into a great number of devices, which are all fabricated on the same wafer. Their characterization shows small statistical variation among the  $\sim 25$  cells per pattern type and warrants the attribution of emergent differences to the structural- and nanogeometric properties of the individual scattering morphologies. By employing spectrally-resolved reflectance and quantum-efficiency measurements, we find a systematic increase in the conversion efficiency of near-infrared photons in HUDLE layers compared with the periodic pattern. To assess the origins of these improvements, we apply the numerical methods developed in the previous chapter in combination with a scattering analysis of the individual scattering unit, which allows to distinguish the impact on the light trapping efficiency through local geometry and ensemble statistical properties. This analysis reveals a direct connection between the scattering response and the HUDLE momentum-space profile, which is characterized by a continuous yet delimited range of spatial frequencies. Altogether, our findings establish HUDLE principles as a superior design doctrine to enhance light trapping in ultrathin silicon solar cells, and can be extended to other materials exhibiting weak absorption over broad spectral ranges.

In chapter 5, we put the ultrathin solar cells to the test under real-world conditions. By tracking their current generation ability for a wide range of insolation angles, we simulate the performance of these devices throughout a day cycle of solar irradiance. The light absorbance and in turn current generation in solar cells is challenged by two distinct effects, namely anti-reflective properties as light enters the device, and light-trapping capabilities to prevent light from escaping before being fully absorbed. Both functionalities are combined in our light-scattering layers and optimized for normal incidence. As a consequence, widely different trends are observed among the cell types as the angle of incidence is varied. Both the anti-reflective and light-trapping properties reconfigure at oblique incidence conditions and can enhance or diminish the performance of solar cells with respect to normal incidence. Here, the two spectral ranges of visible and near-infrared light show different dependencies, since the former responds more to changes in reflectance while absorption of the latter pertains mostly to light trapping. To assess these contributions in more detail, we perform a series of angular-dependent and spectrally-resolved simulations of the full device stack involving the different pattern morphologies. The simulations corroborate the observed trends in power

conversion efficiency and provide insight into the origins of the diverging angular dependencies among the different device types. Crucially, we identify an apparent contradiction in the design process of scattering layers, which requires careful consideration when optoelectronic applications involving nanopatterns require angle-independent performance characteristics. Specifically, the in-plane momentum distribution of light scattered by an arrangement of scatterers shifts as the angle of incidence increases, and compromises the light-trapping ability beyond a certain angle. To ensure good performance for a wide range of insolation conditions, engineered HUDLE layers as well as periodic structures need to avoid overlap with the escape cone even as the in-plane momentum profiles shift with angle.

Chapter 6 explores another method of obtaining HUDLE structures compatible with large-area and high-throughput manufacturing. The approach exploits the natural tendency of many physical systems to arrange themselves into disordered hyperuniform distributions in the presence of certain types of intrinsic and external forces. A blend of two dissimilar long-chained polymers, Polystyrene (PS) and Polymethyl Methacrylate (PMMA), typically refuses to mix due to their strong difference in polarity. As a consequence, PS and PMMA tend to phase-separate and form isolated domains. The process of phase separation is controlled by a variety of factors, such as temperature, humidity, molar weight (degree of polymerization) of the constituents, and their mutual ratio. A blend is prepared in which both constituents are dissolved in a common solvent at very low concentrations, which allows to mix them. Upon casting the solution onto the substrate, the solvent evaporates and phase separation sets in. By controlling the speed of the evaporation, the resulting morphology can further be influenced. Through systematic parameter variations, we demonstrate the ability to tune the statistical distribution and sizes of the island domains separately, and analyze these by their power spectral density (PSD) and particle size distributions. With an appropriate set of parameters, the HUD-like PSD features can be tailored for light trapping in semiconductors, which we prove with angular-resolved scattering analysis. Finally, we perform the method on an ultrathin free-standing silicon film of  $10\ \mu\text{m}$  and transfer the pattern into the top  $200\ \text{nm}$  using reactive-ion etching. In comparison to a flat reference film, the patterned sample exhibits substantial absorbance enhancements throughout the whole wavelength range, with up to  $20\ \%\text{abs}$  in the near-infrared spectral range. These improvements are due to coupling incident light into the guided-mode structure of the thin substrate, which we prove with finite-difference time-domain simulations of the system, where we incorporate a  $5 \times 5\ \mu\text{m}^2$  excerpt of the experimentally realized scattering structure. Overall, our results enable the reliable fabrication of tailored large-area self-assembled nanopatterns suitable for a wide range of applications and materials used.

In summary, this thesis offers critical insights into the light-trapping capabilities of various structural types in ultrathin, weakly absorbing substrates. Focusing particularly on disordered hyperspectral uniformity (HUD), we introduce novel tools to characterize this unique class of materials and demonstrate their enhanced ability to improve absorption across a broad spectral range through tailored coupling to guided modes. Next, we incorporate HUD-like patterns into ultrathin silicon solar cells, proving that these absorption enhancements lead to systematic improvements in light-to-electrical power conversion efficiencies, achieving over  $16\ \%$  with just  $4.8\ \mu\text{m}$ -thick crystalline silicon (c-Si) absorber layers. Our testing under varying angles of incidence assesses their performance throughout a full solar cycle, enabling us to extract essential design principles for effective light-trapping solutions under real-world conditions. To maximize the impact of our findings, we further develop an advanced self-assembly method to create large-area hyperuniform disordered light-trapping patterns with customizable properties, laying the groundwork for implementing our discoveries at industrial scales.

## Summary

Overall, we elevate the significance of HUD structures from a theoretical and mathematical perspective to practical platforms capable of enhancing a diverse range of optoelectronic devices integral to our daily lives.

# Samenvatting

De toepassing van hyperuniform-wanordelijke (HUD) structuren voor de controle van verstrooid licht biedt aanzienlijke perspectieven voor de optimalisatie van optische prestaties. Deze structuren faciliteren het gebruik van ultra dunne materialen in diverse opto-elektronische apparaten, met name in toepassingen die een breed lichtspectrum gebruiken, zoals zonnecellen en sensoren. In het kader van grootschalige productie speelt het materiaalverbruik een cruciale rol in de economische haalbaarheid, de productiesnelheid en de minimalisatie van elektronische verliezen. Het reduceren van de dikte van de actieve lagen draagt bij aan deze doelen, maar brengt tevens een afname van de optische prestaties met zich mee, aangezien de lichtabsorptie schaalbaar met de laagdikte. Om deze beperking te overkomen, kan de introductie van subgolflengte-verstrooiingsstructuren de absorptie verbeteren door middel van lichtopsluiting. Hierbij is een nauwkeurige afstemming van de verstrooiingseigenschappen op de afmetingen van het apparaat essentieel, omdat effectieve lichtopsluiting een overeenkomst vereist tussen de specifieke geleide modes van het systeem en de impuls van het verstrooide licht. Er kunnen twee fundamentele categorieën van verstrooiingsstructuren worden onderscheiden: structuren met perfecte orde en structuren met complete wanorde. Een periodiek patroon (perfecte orde) zorgt voor een gecontroleerde en voorspelbare verstrooiing in discrete diffractiekkanalen, wat bepaald wordt door de regelmatige ruimtelijke verdeling van de verstrooiingselementen. Aan de andere kant resulteert een Poisson-willekeurig patroon (complete wanorde) in een isotropische verstrooiing, waarbij licht in alle richtingen wordt verspreid zonder enige vorm van controle. Hoewel periodieke patronen een precieze afstemming van de optische toestanden en verstrooiingskanalen mogelijk maken, is deze controle beperkt tot een specifiek golflengtebereik. Willekeurige patronen daarentegen bieden weliswaar een breder golflengtebereik, maar slechts voor een beperkt deel van de lichtintensiteit. HUD-patronen daarentegen combineren de voordelen van beide benaderingen: deze patronen faciliteren gecontroleerde verstrooiing over een breed spectrum, wat resulteert in gerichte koppeling van de optische modes voor een aanzienlijk deel van de lichtintensiteit.

In dit proefschrift onderzoeken we hoe ultradunne apparaten voorzien van HUD-structuren interacteren met licht, en hoe dit leidt tot uitzonderlijke lichtopsluiting. Allereerst worden HUD-nanopatronen geïntegreerd in complete fotonische apparaten, waarna hun prestaties systematisch worden vergeleken met die van periodieke patronen en vlakke referentieapparaten. Vervolgens wordt de lichtopsluiting in deze apparaten gekwantificeerd aan de hand van spectraal-opgeloste reflectie en kwantum efficiëntie metingen. De experimentele resultaten worden gevalideerd door middel van numerieke simulaties, zowel op het niveau van verstrooiing door individuele deeltjes als door het volledige nanopatroon. Daarna testen we de prestaties van de zonnecellen onder verschillende invalshoeken van belichting, waarbij we de waargenomen verbanden in het zichtbare en het nabij-infrarode licht afzonderlijk onderzoeken. Verder wordt een zelfassemblage methode onderzocht voor de efficiënte en grootschalige fabricage van HUD-structuren, waarbij de correlatie tussen structurele eigenschappen en lichtverstrooiingskenmerken wordt geanalyseerd met behulp van hoek-opgeloste optische metingen. Om de prestatie van lichtopsluiting van deze patronen te beoordelen, worden ze geïntegreerd in vrijstaande ultradunne silicium plaatjes, waarna de optische absorptie wordt gekwantificeerd. Tot slot wordt in de volgende sectie een

## Samenvatting

gedetailleerde beschrijving gegeven van de opzet en inhoud van elk afzonderlijk hoofdstuk binnen dit proefschrift.

In Hoofdstuk 3 wordt het complexe optische absorptiespectrum van een dun, zwak absorberend materiaal plak bestudeerd wanneer oppervlakteruwheden worden geïntroduceerd. Uit de analyse blijkt dat verhoogde absorptie wordt waargenomen wanneer inkomend licht wordt gekoppeld aan de lichtgeleidende modes van het dunne schrijffe. De exacte kenmerken van deze lichtgeleidende modes, inclusief hun chromatische dispersie, zijn echter moeilijk te bepalen in aanwezigheid van aanvullende structuren en materiaal lagen. Bovendien is de kwantificering van de koppelingsefficiëntie tussen het inkomend licht en de specifieke lichtgeleidende modes niet triviaal. Aangezien gevestigde analytische modellen worden beperkt door een aantal vereenvoudigde aannames, behouden zij een beperkte toepasbaarheid wanneer deze aannames worden geschonden, en bieden zij geen verdere inzichten wanneer variaties binnen de verstrooiingslaag orthogonaal staan op hun invoerparameters. Zelfs voorbij de analytische benaderingen ontbreken numerieke modellen die gelijktijdig niet-periodieke systemen kunnen modelleren, laagspecifieke absorptie kunnen berekenen, optische bandstructuren kunnen bepalen en koppelingssnelheden tussen individuele lichtgeleidende modes en de vrije ruimte kunnen kwantificeren. Om deze beperkingen te overwinnen, ontwikkelen wij een nieuwe methode gebaseerd op een impuls-ruimte benadering voor de analyse van eindige-differentie tijdsdomein-simulaties, waardoor het ons in staat stelt om het optische respons spectrum in het Fourier-domein te ontleden, waardoor impuls-opgeloste optische eigenschappen kunnen worden toegeschreven aan specifieke ontwerpkeuzes van de verstrooiingslaag en de apparaat kenmerken. Bovendien tonen we de universele toepasbaarheid ervan aan door enkel willekeurige en HUD-patronen te onderzoeken, waarbij we ook de fysische parameters die rechtstreeks overeenkomen met de grootheden in de analytische modellen achterhalen. Hierdoor faciliteert onze methode niet alleen de kwantificering en karakterisering van willekeurige lichtmanagement strategieën, maar biedt zij ook een instrument om de aannames in dergelijke modellen te evalueren en hun toepasbaarheid op een breder scala van systemen te vergroten.

Hoofdstuk 4 beschrijft de realisatie van ultradunne siliciumzonnecellen met absorptie lagen van slechts  $4.8\ \mu\text{m}$  dikte. Door gebruik te maken van een gevestigd fabricage platform voor de productie van deze apparaten op een silicium-op-isolator wafer, worden hoge omzettingsrendementen van zonne-energie naar elektriciteit gedemonstreerd in vlakke zonnecellen. Deze efficiëntie is toe te schrijven aan minimale oppervlakte-recombinatie verliezen, hetgeen dat mogelijk wordt gemaakt door een passivatielaag die gevormd wordt door thermische oxidatie. Voortbouwend op de uitstekende prestaties van dit fabricage platform worden zowel periodieke als hyperuniform-wanordelijke licht-ontworpen (HUDLE) verstrooiingslagen geïntegreerd in een groot aantal apparaten, alle gefabriceerd op dezelfde wafer. De karakterisering van de cellen onthult een beperkte statistische variatie tussen de circa 25 cellen per patroontype, wat het mogelijk maakt om waargenomen verschillen toe te schrijven aan de structurele en nano-geometrische eigenschappen van de individuele verstrooiingsmorfologieën. Bij middel van spectraal-opgeloste reflectie en kwantum-efficiëntie metingen wordt een systematische toename in het omzettingsrendement van nabij-infrarode fotonen in HUDLE-lagen geconstateerd ten opzichte van het periodieke patroon. Om de onderliggende oorzaak van deze toename te achterhalen, worden de in het vorige hoofdstuk ontwikkelde numerieke methoden toegepast, gecombineerd met een verstrooiingsanalyse van de individuele eenheid. Hierdoor kan het effect op de efficiëntie van lichtopsluiting worden gedifferentieerd tussen de lokale geometrie en de statistische eigenschappen van het geheel. Deze analyse onthult een direct verband tussen de verstrooiingsrespons en het HUDLE-impulsruimteprofiel, dat gekenmerkt wordt door een continu maar begrensd bereik

van ruimtelijke frequenties. Op basis van deze bevindingen kan worden geconcludeerd dat de HUDLE-principes een superieure ontwerpstrategie vormen voor de verbetering van lichtopsluiting in ultradunne siliciumzonnecellen, en dat het HUDLE-principe eveneens toepasbaar is voor andere materialen die gekenmerkt worden door een zwakke absorptie over een breed spectrum.

In Hoofdstuk 5 worden de ultradunne zonnecellen getest onder realistische operationele omstandigheden. Door het systematisch monitoren van de opgewekte stroom voor een breed scala aan invalshoeken van zonnestraling, simuleren we de prestaties van de cel gedurende een volledige dagcyclus. De lichtabsorptie, en derhalve de stroomopwekking in zonnecellen, wordt beïnvloed door twee fundamentele, maar distincte mechanismen, namelijk door de antireflectie-eigenschappen bij de intrede van licht in het apparaat, en het vermogen van lichtopsluiting wat gericht is op het voorkomen van het ontsnappen van licht voordat volledige absorptie is bereikt. Beide functionaliteiten zijn geïntegreerd in de ontworpen lichtverstrooiingslagen en zijn geoptimaliseerd voor loodrechte inval. Als direct gevolg hiervan worden zeer verschillende trends waargenomen tussen de diverse celtypes naarmate de invalshoek varieert. Zowel de antireflectieve als de lichtopsluitingseigenschappen ondergaan een dynamische verandering onder schuine invalshoeken, wat kan resulteren in zowel een verbetering als een verslechtering van de prestaties ten opzichte van loodrechte inval. Hierbij vertonen de twee spectraal bereiken van zichtbaar en nabij-infrarood licht verschillende afhankelijkheidsrelaties, waar het zichtbare spectrum een grotere gevoeligheid voor variaties in reflectie toont, terwijl de absorptie in het nabij-infrarode bereik primair wordt bepaald door het lichtopsluitingsvermogen. Ter verdere kwantificering van deze bijdragen wordt een reeks hoekafhankelijke en spectraal-opgeloste simulaties uitgevoerd op de volledige apparaat architectuur, inclusief de verschillende patroon structuren. Deze simulaties bevestigen de experimenteel waargenomen trends in het omzettingsrendement en bieden diepgaand inzicht in de oorsprong van de uiteenlopende hoekafhankelijkheden tussen de verschillende apparaat types. In het bijzonder identificeren wij een schijnbare tegenstelling in het ontwerpproces van verstrooiingslagen, wat een zorgvuldige afweging vereist wanneer opto-elektronische toepassingen nanopatronen bevatten die hoekafhankelijke prestatiekenmerken vereisen. Er vindt namelijk een verschuiving plaats in de in-het-vlak impulsverdeling van het verstrooide licht van een geordende configuratie van verstrooiers naarmate de invalshoek toeneemt. Voorbij een kritische hoek resulteert dit in een vermindering van het vermogen van lichtopsluiting. Om optimale prestaties te garanderen onder diverse condities, dienen zowel voor de ontworpen HUDLE-lagen als voor de periodieke structuren overlap met de ontsnappingskegel te worden vermeden, zelfs wanneer het in-het-vlak impulsprofiel als functie van de invalshoek varieert.

Hoofdstuk 6 onderzoekt een alternatieve methode voor het verkrijgen van HUDLE-structuren die compatibel zijn met grootschalige productie en hoge doorlooptijden. Deze methode benut de intrinsieke neiging van talrijke fysische systemen om zich, onder invloed van specifieke intrinsieke en externe krachten, te ordenen in wanordelijke hyperuniforme verdelingen. Een mengsel van twee verschillende lange keten polymeren, polystyreen (PS) en polymethylmethacrylaat (PMMA), vertoont doorgaans een sterke neiging tot fasescheiding als gevolg van hun aanzienlijke verschil in polariteit. Hierdoor vormen PS en PMMA geïsoleerde domeinen. Het proces van fasescheiding wordt beïnvloed door diverse factoren, waaronder temperatuur, vochtigheid, het molair gewicht (polymerisatiegraad) van de bestanddelen en hun onderlinge verhouding. Er wordt een mengsel bereid waarin beide polymeren in een gemeenschappelijk oplosmiddel bij zeer lage concentraties zijn opgelost, wat het mogelijk maakt om deze polymeren te mengen. Bij het gieten van de oplossing op het substraat verdampt het oplosmiddel, waarna de fasescheiding inzet. Door de verdampingssnelheid

## Samenvatting

te reguleren, kan de resulterende morfologie verder worden beïnvloed. Door middel van systematische variatie van de parameters demonstreren we het vermogen om afzonderlijk de statistische distributie en de afmetingen van de domeinen af te stemmen. Deze domeinen worden geanalyseerd aan de hand van hun spectrale vermogensdichtheid (PSD) en deeltjesgrootteverdelingen. Met een geschikte set parameters kunnen de HUD-achtige PSD-kenmerken worden afgestemd op lichtopsluiting in halfgeleiders, wat wordt bevestigd door middel van hoek-opgeloste verstrooiingsanalyse. Ten slotte wordt de methode toegepast op een ultradunne vrijstaande silicium folie van  $10\ \mu\text{m}$ , waarna het patroon wordt overgebracht in de bovenste 200 nm met behulp van reactief-ion etsen. In vergelijking met een vlakke referentie folie vertoont het monster met aangebrachte structuren aanzienlijke verhogingen in absorptie over het volledige golflengtebereik, met tot 20% *abs* in het nabij-infrarode spectraal bereik. Deze verbeteringen zijn toe te schrijven aan de koppeling van inkomend licht aan de structuur van lichtgeleidende-modes van het dunne substraat, wat wordt bevestigd door eindig-verschil tijdsdomein simulaties van het systeem, waarin een uittreksel van  $5 \times 5\ \mu\text{m}^2$  van de experimenteel gerealiseerde verstrooiingsstructuur is opgenomen. Ten slotte maken onze resultaten de betrouwbare fabricage van op maat gemaakte, zelf-geassembleerde nanopatronen op grote oppervlakken mogelijk, die geschikt zijn voor een breed scala aan toepassingen en materialen.

Samenvattend levert dit proefschrift fundamentele inzichten in het lichtopsluitingsvermogen van diverse structuur typen in ultradunne, zwak absorberende substraten. Door ons te richten op hyperuniform-wanordelijke (HUD) structuren introduceren wij nieuwe analytische instrumenten voor de karakterisering van deze unieke categorie van materialen en demonstreren wij hun superieure vermogen om absorptie over een breed spectraal bereik te optimaliseren door middel van op maat gemaakte koppeling aan lichtgeleidende modes. Vervolgens integreren wij HUD-achtige patronen in ultradunne silicium zonnecellen, waarbij wij aantonen dat de verhoging in absorptie resulteert in systematische verbeteringen in de omzettingsrendementen van licht naar elektrisch vermogen van meer dan 16% wat bereikt wordt met absorberende lagen van slechts  $4,8\ \mu\text{m}$  dik kristallijn silicium (c-Si). Onze experimenten die gedaan zijn onder variërende invalshoeken beoordelen de prestaties gedurende een volledige zonnecyclus, dat ons in staat stelt om essentiële ontwerpprincipes af te leiden voor effectieve lichtopsluiting onder realistische omstandigheden. Om de impact van ons onderzoek te maximaliseren, hebben wij een geavanceerde zelfassemblage methode ontwikkeld voor het maken van hyperuniform-wanordelijke lichtopsluitings structuren op grote oppervlakken met aanpasbare eigenschappen, wat de basis vormt voor het integreren van onze ontdekkingen op industriële schaal.

In het algemeen tillen wij de betekenis van HUD-structuren op van een louter theoretisch en wiskundig perspectief naar praktische platformen die in staat zijn een diverse reeks van opto-elektronische apparaten aanzienlijk te verbeteren die een integraal onderdeel vormen van ons dagelijks leven.

# Acknowledgments

The PhD program is as much a social experiment as it is a science project. A journey of self-exploration, nurturing of the rational mind, and maturing into an independent voice. As Albert said to me, the PhD students themselves are the project, and the research goals evolve in orchestration and intertwined with the students' personality. A completed PhD brings knowledge and insight to unanswered scientific questions, but a successful PhD further yields a valuable resource to the scientific community; a curious mind with a developed set of investigative tools and skilled in scientific discussion. More than anything, this evolutionary process is shaped by the supervision and guidance. Dear Esther and Jorik, the past 4.5 years with you have been an absolute blessing. It is far beyond words to describe my gratitude for your unwavering trust, inexhaustible support, and endless inspiration that carried me through every storm—like R. Wagner's Flying Dutchman. I am truly honored and grateful for this opportunity. Your decision to collaborate on this PhD project and place your trust in me means a great deal, and I deeply appreciate your mentorship.

**Esther**, you are absolutely brilliant. Even after six years, I cannot decide if I am more blown away by your cognitive or emotional intelligence—qualities that make you both a formidable scientist and the perfect person to confide in about any kind of situation. It remains an absolute mystery to me just how you manage to master so many vastly different tasks, jobs and duties all in parallel, all the while traveling sometimes three different countries in the same week, and still being always available and engaging in discussions with me as if we were in the same room. Either you must have a hidden army of clones or undisclosed magic powers. Which ever it is, I will be eternally grateful for our time together, continue to seek your advice and hope to stay close in the future.

**Jorik**, much of the same holds true for you. Your brain effortlessly surpasses the promises made by quantum computing. They could never keep up with your speed of thought and clarity of expression. I cannot even begin to summarize how much I learned from you, and how my capacity for quick thinking noticeably expanded every time I tried to keep up with your verbalized thought processes. Your mind is truly a marvel of human evolution. What strikes me even deeper, though, is your passion and kindness. Whatever the status of the scientific project, you always ask how I am doing first, and I felt safe to pour my heart out and voice my honest feelings without hesitation. This is your other superpower and to me, it is the more important one. Thank you for your warmth, patience, and supportive, optimistic guidance. You taught me to rein in my wandering thoughts, zoom out, and take a pragmatic approach to forge a clear path forward.

What I will miss the most are our (bi-)weekly triangular meetings. The sheer force of genius that was unleashed when the two of you bounce the ball back and forth with me in the middle deserves its own book to be recognized. To me, these hours together are far more valuable than the science advanced, the knowledge gained or the diplomas earned. This was our cradle of unencumbered innovation that I will cherish forever.

**Albert**, the godfather of AMOLF. You have been part of my journey as much as the samples I fabricated and characterized. Even beyond my project and the collaboration with Stefan, we organized master project workshops and ran the photovoltaics course for three years. I have learned countless skills from you and greatly appreciate the trust and confidence you placed in me and the responsibility you bestowed upon me. These experiences were truly remarkable

## Acknowledgments

and I am forever thankful for what I learned from you, and I am proud and honored to have you in my committee.

Thank you **Sander** for joining my committee, as well as for the many scientific and non-scientific discussions we held. I especially enjoyed the leisure times together at Oerknal or Polder when we unwound from the perils of scientific investigation. Your openness and gentle character create such a welcoming and comforting environment that is almost addictive. To **Mark, Rebecca** and **Christiane**, thank you for completing my committee and reading this work with such scrutiny and dedication. I could not have wished for a better committee composition with your extensive expertise and complementary scientific experience.

Dear **Femius**, with the first time I poked my head into your office seeking help with “just a quick question about coupled-mode theory” during my Msc internship, an invaluable and seemingly inexhaustible resource of wisdom, knowledge and experience was added to my ongoing scientific journey. Sometimes in these discussions, it seemed as if you have “clear voyance”, or a telepathic ability to see the erroneous links or flaw directly in my brain, rather than listening to my clumsy attempts of describing the cul-de-sac of comprehension into which I steered myself this time. At any rate, thank for helping my understanding of nanophotonics and the fun times at the photonics school in Erice.

Further to **Bruno, Erik**, and **Wiebke**, (and Esther and Albert), thank you for the wonderful times with LMPV; the certified best team of teams in the whole country! You form such a great balance among your groups and you have always been so supportive and approachable, and with the extensive use of the equipment in your labs, which you always made available to me, you have greatly accelerated my work and shaped this thesis in many subtle yet essential regards. I think to this day, I remain a ghost-like superuser of the UV-VIS and EQE setups in the shared lab of Erik and Bruno.

To **Marian**, thank you for being an integral part to my journey into hyperuniform disorder since 2020. Our many conversations and scientific discussions have greatly expanded my knowledge and deeply inspired me to continue searching for this wonderful material class in all realms of science as well as my everyday life. You are an indispensable resource to the exploration of hyperuniform disorder, and I hope to continue our collaboration in the future.

Thank you **Peter** for your trust in me as the main assistant for the PV course over many years. I greatly appreciate the level of responsibility you felt safe leaving with me, and I learned so much about conflict resolution and team building from watching your conduct, and I model my teaching style greatly after yours.

To my master students I owe profound thanks. The dedication and rigorous scientific methodology you employed led to a most beautiful chapter on the self-assembly of HUD distributions. **Jon**, you were the first to trust me as your supervisor and dove deep into the subject and beyond, revealing your passionate and thorough mindset, and the untameable drive to really understand every detail of the work you performed. I hope we stay in touch and look forward to see where life will take you. **Neda**, you are such a wonderful and kind person with a strong mind and heartfelt dedication. You have shown great trust in my guidance and proven a level of independence and leadership far beyond what I could have expected. You are nothing short of awe inspiring. I know you will continue to shine in your own PhD adventure and I will always be no further than a message away.

Being co-supervised by two PIs from different institutions entails being part of two groups, at AMOLF and the IOP at the University of Amsterdam, which of course sounds like twice the fun! Though it may also mean twice the meetings, responsibilities and duties, building bridges between both institutes has been a rewarding experience and enabled me to learn at least twice as much about other setups in the labs and access to a broader scientific community.

The 2D nanophotonics group is truly amazing and growing so fast! Not long before I

joined, there was only **Ludovica**. Though I have not yet made it to Seracruz, your fascinating personality and lively spirit bring the Sicilian warmth and sunny demeanor to every place that you go. I loved our times at Stanford together and wish you all the best for your growing family. Congratulations dr. **Tom**, you are a truly inspiring person and dedicated scientist. Thank you for all the WiTec help and setting up the EQE setup from which both of us learned so much. I am curious to see where the future will take you and long live Duckstad Radio! **Freek**, you have many qualities that make you absolutely unique. There is hardly another person with whom I enjoy disagreeing on subjects as much as I do with you. Discussing any topic where we stand on different positions has always expanded my mind and trained my debating skills in the most supportive atmosphere, for which I am eternally grateful. **Bernardo**, thank you for the fun brotherly comradery. You are so knowledgeable on all things photonics and I have learned a great deal from you and really enjoyed all the fun nights! I cannot wait to see you smash the pumpkins at your own PhD defense:) **Thomas**, the other German in the group for a long time. It was such a pleasure to have your expertise and helpful attitude around the lab, offices, and outings. I loved discussing our shared passions in science and spirits and hope to finally join for a cozy winter session of Feuerzangenbowle in the coming season of cold. **Johanna**, thank you for opening my mind about so many theoretical topics and the honest and straightforward opinions about work and otherwise. I enjoyed every meeting together and hope to see you more frequently again. **Mehmet**, not just another brother from another mother, but a really good friend and gentle soul. I admire your art skills and playful personality, and look forward to accompanying the remainder of your PhD journey. Merci beaucoup dear **Anne** for the wonderful times and best of luck with the final stretch! **Reynolds**, you are a genius! I have learned much from you about science and beyond, and your pleasant and polite attitude brings immediate calm to the hectic lab environment. **Eva**, fellow sister in photovoltaics, it is always a pleasure to be in your company and I admire your artful and creative thinking, and your shining example of a supportive friend and colleague. **Alvaro**, one of the most real blokes I have met so far. We made a deep connection from the first conversation and even after this time, I know there are many more shared interests and values left to discover. **Charly** and the three angels, arguably the most important social network in existence! Thanks for the great times together:) **David**, thank you for the fun times in the group and at the outings and all the best for your PhD, which I know you will nail. **Ershad**, despite not having spent too much time together, your dedication and thorough thought processes were evident from the first conversation we held. You are a great addition to the group, bringing additional skills and knowledge that are highly sought after. **Bauke**, thank you for your refreshing views. I loved listening to your GM presentations, you have an uncanny way to transport difficult subjects in accessible ways, which is a unique skill that I cherish. **Vera**, thank you for the fun times and interesting discussions. I love your infectious optimism and hope you will continue on your own PhD adventure. Further thanks to our previous students over the years, **Juliette, Gaby, Nella, Cian, Ruben, and Bas**. I doubt we would be the same without your contributions to the scientific and social development of the group.

The office at the UvA was a marvelous space to work and take a breather. **Susan**, my most favorite horse owner. Thank you for instructing me to take over the PV course from you, for our shared desk, and all the fun discussions and good times at AMOLF and the UvA. **Marco**, one of my favorite persons ever! Already when you gave the lab tour while I was just another student in the PV class, we made such a great connection that turned into friendship over the years. You are a marvelous person who inspired me and taught me lots about life and the Dutch culture. Further thanks to **Daan, Ina, Yingying, Abishek, Ankit, Daniel, Marie, Liu Qiuyu, Dongdong, Jasmin, Tadé** and more for all the great times and mutual support. Thank you to the technical support staff at the IOP, especially **Paul** and **Grisha** for your help,

## Acknowledgments

trainings and fun times at the Friday gatherings.

AMOLF is a place of magic, with the greatest sorcerers and witches all found in the 3D Photovoltaics group. **Yorick**, the eternal 3DPV member and my capable paranymp, the brotherhood we shared starting from my days as a master student will also keep me around much longer than my expiration date. Thank you also for translating the summary! As much as your legs never quit, this love will run forever. **Antony**, my favorite office mate and paranymp, there are no words to express my gratitude for your arrival to the group and my life. We have shared more laughter and tears and hotel rooms than any other bickering old couple in the world. I hope we will never be further apart than a bottle of Tsipourou. **Melanie**, little big one from Catania. I think the size of your heart is the greatest in a thousand years and I thank you for every minute and coffee we shared and the wonderful times in your hometown. My love is yours forever. **Daphne**, when something is off, you are always the first one to notice. Your attention and awareness are inspiring and I will never forget how you gave me the confidence to speak truth to power. Keep your spice and honesty which make your friendship essential to my life. **Jaime**, "I know, right?". I loved our acting noble and dancing together at the Christmas lunches and conferences, you are so much fun to be around and I really hope you have an easy way forward after the recent setbacks. **Margo**, thank you for TNJS! Our regular music sessions were legend and I hope we will pick it up again. You are such an interesting person and my favorite salt addict in the world. I loved our discussions about science, politics and life and there is still much more to learn from you. dr. **Anja**, queen of disorder, thank you for our fruitful collaboration and fun times together at AMOLF, EPFL and beyond. I am so curious to see where your path leads from here. **Jian**, (xiong di), I think you literally spend more time at AMOLF than anywhere else, becoming a more common sight in the building than even the green walls. You are exceptionally smart and kind and so much fun to be around, and I really enjoyed all the times at Oerknal and dancing in the small DUWO apartment. **Oleg**, "Ahh I'm sorry guys, I already have plans". Your schedule rivals that of Esther, and it seems you literally don't know the concept of rest. Traveling to the most remote places on the planet, engaging in so many sporty and cultural activities, your broad knowledge and supportive and loving conduct with everyone around you make you one of the most appreciated souls in all of AMOLF. **Mike**, you have an exceptional aura about you and I cannot imagine your face without a smile, and I doubt I will ever see it. You fit right in our team as if born for it and I greatly appreciate the calm and positivity you continue to add. **Luna**, Linux protégé, supercomputer successor, workstation operator, Lumerical Lunatic, German of the next generation, and keeper of the disordered desk. You have made such impressive advancements already since your master days that I do not dare to project where you will be at the end of your PhD. You have the most revolutionary fashion sense and I thank you for expanding my mind in many fields beyond science. **Nasim**, you were the first to ever greet me at AMOLF and your kindness and loving attitude have shaped my entire experience until now. Anything is possible if you set your mind to it, and no problem is too great to overcome. Thank you for being there always and keeping tabs on my progress even long after you set out towards new adventures. You are one of my greatest inspirations. **Daniel**, technician of specialty, sailor of the seven seas, and climber to the top of the world. You have made invaluable contributions to keep our lab running, set up the new equipment and help safeguard and maintain all the necessary equipment to keep my setups from failure. For that and the wonderful times at events, meetings and outings, I thank you for always being there. **Sunny**, bright star from down under, thank you for the wonderful collaboration and the fun times within and without the clean room. Your shining personality and meticulous conduct are awe inspiring and I hope to work with you again, soon. To our current master students, **Suus** and **Aakash**, thank you for your always positive mood and happy faces that supply the

constant liveliness and jolly moments to our lunches, borrels and outings. It is a pleasure to have you around. As people join and leave over the years, it is not always easy to stay in touch in the face of new challenges, jobs, and moving far away. Though we may rarely meet these days, the times together and the things I have learned from you continue to resonate with me. Thank you **Mark, Marco, Juliane, Mees, Blaise, Jos, Loriane, Kaj, Hallie, Nicky, Paola, Johanna, Marina, Ruerd, Chloé, Nico, Raphael, Gustavo, Donna,** and **Arthur**.

In the greater nanophotonics scheme at AMOLF, I am very thankful for all the joint poster sessions and valuable insights and discussions. **Said**, thank you for your input and interesting philosophy on obscure scientific observations. **Ewold**, thanks for pointing out various subtleties in my poster presentations and suggesting fundamental mechanisms to inspect in search for the underlying connections between theory and experiment. At these sessions and beyond, the great collaborative and supportive environment at AMOLF make working under pressure still most enjoyable, and I want to thank especially the people who made this time even more memorable. Special thanks to **Tom** for entrusting me with many of your duties and giving me a head start in so many different things, all the interesting discussions and your heartfelt dedication to the wellbeing of people at AMOLF. Thank you **Sarah, Linde, Nika, Evelijn, Matthias, Robin, Hollie, Magda, Saskia, Larissa, Imme, Stan, Elaina, Omolara, Jérôme, Daan, Marcel, Rohit, Hongyu, Jente, Deba, Nelson, Falco, Ruslan, Jesse, Julia, Jeroen, Moritz, Katharina, Roel, René, Daphne, Agustin, Lars, Larissa, Francesco, Athira, Devin, Ethan, Francesca, Nick, Masha, Harshal, Vashist, Jyoti, Christian, Timo, Menno** and **Giorgos**, and everyone else who may have slipped my mind.

Though it flew by in what felt like an instant, I have greatly enjoyed my time at Stanford in the group of Mark Brongersma. Thank you **Mark** for adopting me to your group, assigning such high priority to my tight schedule and clearing a path for me to do the almost impossible; fabricating the ultrathin solar cells in only a few weeks. None of these would have seen the light and returned a current, had it not been for your trust and support, making the right decisions under high pressure, and search for suitable alternatives when intended fabrication routes vanished. Your entire group played an essential part, and everyone contributed to my trainings, helped the brainstorming, fabrication and characterization, and made it all possible. It was an amazing time in which I learned much also about myself, and I hope to get a chance and collaborate with you again. Thank you **Nayeun** for the detailed instructions and the many small but important hints. **Vik**, you are the cornerstone of these samples, you trained me on all the necessary clean room equipment, helped to tackle emerging problems and lend your experienced hand to intermediate steps. For this and our fun times at lunches and after work, I am eternally grateful. **Nicholas**, thank you for the etcher trainings and wonderful comradery, and congratulations to your new position back in our shared home country. **Fenghao**, thank you for the great collaboration, you were always available at a moments notice to do a quick AFM, handled the dangerous wet-chemical etches and hot ovens, all the while keeping it light with interesting and fun discussions. **Qitong**, thank you for all the SEM inspection even in the late evenings and the fun times outside of the lab. **Jung-Hwan**, you are such a jolly person, I would have never believed it could be so much fun depositing nitrides or annealing contacts in the earliest morning hours. Thank you **Skyler** for so many interesting discussions, your in-depth feedback, help with the metal deposition and sample characterization, and wonderful evenings in the pub. Thank you **JP** for all the fun times at the lunches and the sample descum at precisely the required time. **Yi-Shiou**, your lively personality that even brightens up a dull Sunday afternoon in the office was a great refresher and always kept me going. And for keeping it light throughout and all the interesting conversations, thank you to **Ben, Sid, Johan, Mohammad, Eileen,** and **Juan**. For all the exceptions and accelerated access to SNF and SNFexfab equipment, I owe many thanks to **Swaroop, Graham, Maurice,**

## Acknowledgments

**Lavendra, Uli, and Bent.** Thank you for your trust and keeping the clean room safe and operational. Your work is exceptional.

The AMOLF clean room is its own little quadrant of spacetime. With its martian ambiance and white-cloaked usually cheerful and sometimes drowsy dwellers, it evokes an atmosphere of endless possibility and meticulous innovation, haunted solely by the specter of red alert. And when these should happen, the heroes and angels of NanoLab staff come to the rescue. Thank you for your unfathomable efforts, dear **Hans, Bob, Igor, Isabelle, Laura, Rilda, Dimitry, Angela, Arthur** and **Dylan**. And for leaving some of your expertise with the young newcomers in the clean room, I thank the experienced older bunny-suiters **Sven, Andrea, and Eitan**. Special thanks to Si-bro **Stefan**, your exceptional work in thinning down commercial cells and imprinting them with me for almost a year has allowed me to absorb much of your expertise and build my confidence to try more exotic fabrication approaches.

Similarly, to the awesome technicians, software- and electronics engineers, designers and mechanics, which have conceived the missing parts, built my setups, tackled emerging difficulty and accommodated my frequent and often difficult requests, I owe profound thanks for without you, many parts of this work would not have been possible. Special regards go out (but not limited) to **Dion, Hincó, Niels, Marc, Marko, Henk-Jan, Max, Ilya, Bob, Behrend, Wessel, Ricardo, Jan, and Pepijn**.

To the AMOLF IT crowd, especially **Remco, Kallinikos, Pieter, Gerben, Michiel, Sean, Rutger, Richard** and **Cees**, I owe profound thanks for helping me build and operate the four systems we set up together, the license renewal predicaments, and further thank you Stefan from SURF for the support with Snellius HPC.

Thank you to the AMOLF HR, the secretaries and PV, who organize the great events and symposia, keep a cool head over all the scheduling conflicts and aid in the smooth operation and taking care of all personnel-related tasks, **Petra, Priscilla, Lina, Linda, Sofia, Teresa, Sumaiyah, Esther, Anne, Floortje, Saskia, and Wouter**.

Thank you to the small but lovely community of correlated disorder and hyperuniformity. It was a pleasure and great honor to talk with the HUD father **Salvatore** Torquato, and all the disordered folks at the Narciso workshop, **Nicoletta, Frank, Kevin, Alexander, Remi, Massimo, Marco, and Pavel**. For more collaborative work with the CAMOLF joint venture, thank you everyone involved and for our joint project with special thanks to **Changsoon** and **Darius**.

Thanks to my sisters and larger family to make me into a six-fold uncle during the PhD, and the joy and love I received from my nieces and nephews **Luna, Noah, Romy, Ava, Carlotta, and Emil**. Thank you **Mom** and **Dieter, Dad** and **Anne, Sandra** and **Lukas, Laura** and **Christopher, Olga** and **Jens, Mona** and **Arne, Heike** und **Günter, Micha** und **Anna**, for your unwavering support and love over the years. Keeping your sanity is not guaranteed throughout the perils of breaking equipment, failing processes, senseless programming errors, and completely lost logical thought trains. For not (entirely) losing my mind, I thank especially my closest friends and soul relatives **Patrick, Roman, Jani, Ausi, Paddi, Wessel, Magda, Katerina, Filipa, Carly, and Viktoria**. Last but not least, thank you **Maren** for your love and support over the last ten years.

# Bibliography

- [1] S. Wolf, R. Bullard, J. J. Buonocore, N. Donley, T. Farrelly, J. Fleming, D. J. X. González, N. Oreskes, W. Ripple, R. Saha, and M. D. Willis, *Scientists' warning on fossil fuels*, Oxford Open Climate Change **5**, kgaf011 (2025).
- [2] N. Tesla, *Experiments with Alternate Currents of Very High Frequency and their Application to Methods of Artificial Illumination*, Transactions of the American Institute of Electrical Engineers **VIII**, 266 (1891).
- [3] Niagara Falls USA, *The Hydropower of Niagara Falls*, (2026), <https://www.niagarafallsusa.com/the-source/the-hydropower-of-niagara-falls/>, accessed: 2026-01-21.
- [4] M. Žubrinić and D. Žubrinić, *Tesla AC Technology for the Adams Power Plant Near Niagara Falls*, (2022), <https://www.croatianhistory.net/etf/teslan.html>, accessed: 2026-01-21.
- [5] C. Cleveland, A. Ni, and X. Wang, *United States electricity history in four charts*, Visualizing Energy (2023).
- [6] International Energy Agency, *Global Energy Review 2025*, (2025).
- [7] U.S. Energy Information Administration, *Annual Energy Outlook 2025*, Tech. Rep. (U.S. Energy Information Administration (EIA), 2025).
- [8] D. M. Powell, R. Fu, K. Horowitz, P. A. Basore, M. Woodhouse, and T. Buonassisi, *The capital intensity of photovoltaics manufacturing: barrier to scale and opportunity for innovation*, Energy & Environmental Science **8**, 3395 (2015).
- [9] G. Tagliabue, H. A. Atwater, A. Polman, and E. Cortés, *Photonic solutions help fight climate crisis*, Nature Photonics **18**, 879 (2024), license Number: 6215400568657.
- [10] C. Zheng *et al.*, *Enabling active nanotechnologies by phase transition: From electronics to photonics*, Chemical Reviews **122**, 523 (2022).
- [11] L. Mulko, M. Soldera, and A. F. Lasagni, *Structuring and functionalization of non-metallic materials using direct laser interference patterning: a review*, Nanophotonics **11**, 203 (2022).
- [12] F. Bonaccorso, Z. Sun, T. Hasan, and A. C. Ferrari, *Graphene photonics and optoelectronics*, Nature Photonics **4**, 611 (2010).
- [13] A. I. Kuznetsov, M. L. Brongersma, J. Yao, M. K. Chen, U. Levy, D. P. Tsai, N. I. Zheludev, and A. Faraon, *Roadmap for optical metasurfaces*, ACS Photonics (2024), 10.1021/acsp Photonics.3c00457.
- [14] E. C. Garnett, B. Ehrler, A. Polman, and E. Alarcon-Llado, *Photonics for Photovoltaics: Advances and Opportunities*, ACS Photonics **8**, 61 (2021).

## Bibliography

- [15] O. M. Halawa, E. Ahmed, M. M. Abdelrazek, Y. M. Nagy, and O. A. M. Abdelraouf, *Illuminating the Future: Nanophotonics for Future Green Technologies, Precision Healthcare, and Optical Computing*, arXiv preprint (2025).
- [16] S. Y. Nof, A. M. Weiner, and G. J. Cheng, eds., *Laser and Photonic Systems*, 0th ed. (CRC Press, 2014).
- [17] M. A. Butt, X. Mateos, and R. Piramidowicz, *Photonics sensors: A perspective on current advancements, emerging challenges, and potential solutions (Invited)*, *Physics Letters A* **516**, 129633 (2024).
- [18] K. A. Buzaverov, A. S. Baburin, E. V. Sergeev, S. S. Avdeev, E. S. Lotkov, S. V. Bukatin, I. A. Stepanov, A. B. Kramarenko, A. S. Amiraslanov, D. V. Kushnev, I. A. Ryzhikov, and I. A. Rodionov, *Silicon Nitride Integrated Photonics from Visible to Mid-Infrared Spectra*, *Laser & Photonics Reviews* **18**, 2400508 (2024).
- [19] J. S. van der Burgt and E. C. Garnett, *Nanophotonic emission control for improved photovoltaic efficiency*, *ACS Photonics* (2020), 10.1021/acsp Photonics.0c00152.
- [20] C. S. Schuster, I. Crupi, J. Halme, and M. Koç, *Empowering photovoltaics with smart light management technologies*, in *Handbook of Climate Change Mitigation and Adaptation* (2022).
- [21] E. Camarillo Abad, H. J. Joyce, and L. C. Hirst, *Light management for ever-thinner photovoltaics: A tutorial review*, *APL Photonics* **9**, 011101 (2024).
- [22] G. M. Wilson, M. Al-Jassim, W. K. Metzger, et al., *The 2020 photovoltaic technologies roadmap*, *Journal of Physics D: Applied Physics* **53**, 493001 (2020).
- [23] B. S. Richards and I. A. Howard, *Luminescent solar concentrators for building integrated photovoltaics: Opportunities and challenges*, *Energy & Environmental Science* (2023), 10.1039/D3EE00331K.
- [24] Q. Pan, Q. Zhong, J. Pu, G. Yu, J. Chen, M. Cao, and B. Feng, *Perovskite solar cells toward industrialization: Overcoming challenges with data-driven strategies*, *Nanoscale* (2026), 10.1039/D5NR05360A.
- [25] N. Jost, T. Gu, J. Hu, C. Domínguez, and I. Antón, *Integrated micro-scale concentrating photovoltaics: A scalable path toward high-efficiency, low-cost solar power*, *Solar RRL* (2023), 10.1002/solr.202300363.
- [26] V. T. Tran, H. Q. Nguyen, Y. M. Kim, G. Ok, and J. Lee, *Photonic-plasmonic nanostructures for solar energy utilization*, *Nanomaterials* **10**, 2248 (2020).
- [27] A. Anctil, M. N. Beattie, and C. Case, *Status report on emerging photovoltaics*, *Journal of Photonics for Energy* **13**, 042301 (2023).
- [28] U. E. I. A. (EIA), *Renewables Report 2024*, Tech. Rep. (U.S. Department of Energy, Washington, D.C., 2025).
- [29] S. Philipps and W. Warmuth, *Photovoltaics Report 2025 - Fraunhofer ISE*, Tech. Rep. (Fraunhofer ISE, 2025).

- [30] International Renewable Energy Agency and Climate Policy Initiative, *Global landscape of renewable energy finance, 2023* (International Renewable Energy Agency, 2023) oCLC: 1393196960.
- [31] Z. Galazka, *Czochralski Method*, in *Gallium Oxide*, Vol. 293, edited by M. Higashiwaki and S. Fujita (Springer International Publishing, Cham, 2020) pp. 15–36.
- [32] Market Research Intellect, *Global Solar Silicon Wafer Industry Market: Size, Segmented by Product Type, Technology, Application; Geographic Analysis and Forecast*, Industry report Report ID 1001917 (Market Research Intellect, 2026).
- [33] M. Woodhouse, B. Smith, A. Ramdas, and R. Margolis, *Crystalline Silicon Photovoltaic Module Manufacturing Costs and Sustainable Pricing: 1H 2018 Benchmark and Cost Reduction Roadmap*, Tech. Rep. (National Renewable Energy Laboratory, Golden, CO, 2019).
- [34] S. Schoenfelder, O. Breitenstein, S. Rissland, R. De Donno, and J. Bagdahn, *Kerfless Wafering for Silicon Wafers by Using a Reusable Metal Layer*, *Energy Procedia* **38**, 942 (2013).
- [35] D. Cheng, Y. Gao, and W. Huang, *Prediction of excess kerf loss in diamond wire sawing based on vibration source signal measurement and processing*, *Measurement* **257**, 118969 (2026).
- [36] International Energy Agency, *Net Zero by 2050: A roadmap for the global energy sector*, (2021).
- [37] M. A. Green, *Thin-film solar cells: review of materials, technologies and commercial status*, *Journal of Materials Science: Materials in Electronics* **18**, 15 (2007).
- [38] A. Aberle, *Thin-film solar cells*, *Thin Solid Films* **517**, 4706 (2009).
- [39] R. Brendel, *Thin crystalline silicon solar cells*, *Physica Status Solidi* (2018).
- [40] Z. Liu, S. E. Sofia, H. S. Laine, M. Woodhouse, S. Wieghold, I. M. Peters, and T. Buonassisi, *Revisiting thin silicon for photovoltaics: a technoeconomic perspective*, *Energy & Environmental Science* **13**, 12 (2020).
- [41] R. Saive, *Light trapping in thin silicon solar cells: A review on fundamentals and technologies*, *Progress in Photovoltaics: Research and Applications* **29**, 1125 (2021).
- [42] H.-S. Lee, J. Suk, H. Kim, J. Kim, J. Song, D. S. Jeong, J.-K. Park, W. M. Kim, D.-K. Lee, K. J. Choi, B.-K. Ju, T. S. Lee, and I. Kim, *Enhanced efficiency of crystalline Si solar cells based on kerfless-thin wafers with nanohole arrays*, *Scientific Reports* **8**, 3504 (2018).
- [43] C. Rittmann, J. Dalke, M. Drießen, C. Weiss, F. Schindler, R. Sorgenfrei, M. Schubert, and S. Janz, *Efficiency potential analysis of p- and n-type epitaxially grown Si wafers*, in *Presented at the 38th European PV Solar Energy Conference and Exhibition*, Vol. 6 (2021) p. 10.
- [44] C. Gemmel, J. Hensen, S. Kajari-Schroder, and R. Brendel, *4.5 ms Effective Carrier Lifetime in Kerfless Epitaxial Silicon Wafers From the Porous Silicon Process*, *IEEE Journal of Photovoltaics* **7**, 430 (2017).

## Bibliography

- [45] L. A. Eldada, ed., *Silicon epitaxy below 200°C: towards thin crystalline solar cells* (San Diego, California, USA, 2012).
- [46] J. H. Petermann, D. Zielke, J. Schmidt, F. Haase, E. G. Rojas, and R. Brendel, *19%-efficient and 43  $\mu\text{m}$ -thick crystalline Si solar cell from layer transfer using porous silicon*, *Progress in Photovoltaics: Research and Applications* **20**, 1 (2012).
- [47] L. Mazzarella, S. Kirner, O. Gabriel, S. S. Schmidt, L. Korte, B. Stannowski, B. Rech, and R. Schlatmann, *Nanocrystalline silicon emitter optimization for Si-HJ solar cells: Substrate selectivity and CO<sub>2</sub> plasma treatment effect: Nanocrystalline silicon emitter optimization for Si-HJ solar cells*, *physica status solidi (a)* **214**, 1532958 (2017).
- [48] Y. Kwon, C. Yang, S.-H. Yoon, H.-D. Um, J.-H. Lee, and B. Yoo, *Spalling of a Thin Si Layer by Electrodeposit-Assisted Stripping*, *Applied Physics Express* **6**, 116502 (2013).
- [49] F. Dross, J. Robbelein, B. Vandeveldel, E. Van Kerschaver, I. Gordon, G. Beaucarne, and J. Poortmans, *Stress-induced large-area lift-off of crystalline Si films*, *Applied Physics A* **89**, 149 (2007).
- [50] K. Yoshikawa, H. Kawasaki, W. Yoshida, T. Irie, K. Konishi, K. Nakano, T. Uto, D. Adachi, M. Kanematsu, H. Uzu, and K. Yamamoto, *Silicon heterojunction solar cell with interdigitated back contacts for a photoconversion efficiency over 26 %*, *Nature Energy* **2**, 17032 (2017).
- [51] H. Lin, M. Yang, X. Ru, G. Wang, S. Yin, F. Peng, C. Hong, M. Qu, J. Lu, L. Fang, C. Han, P. Procel, O. Isabella, P. Gao, Z. Li, and X. Xu, *Silicon heterojunction solar cells with up to 26.81 % efficiency achieved by electrically optimized nanocrystalline-silicon hole contact layers*, *Nature Energy* **8**, 789 (2023).
- [52] S. W. Glunz, B. Steinhauser, J. Polzin, C. Luderer, B. Grübel, T. Niewelt, A. M. O. M. Okasha, M. Bories, H. Nagel, K. Krieg, F. Feldmann, A. Richter, M. Bivour, and M. Hermle, *Silicon-based passivating contacts: The TOPCon route*, *Progress in Photovoltaics: Research and Applications* **31**, 341 (2023).
- [53] A. Richter, J. Benick, F. Feldmann, A. Fell, M. Hermle, and S. W. Glunz, *n-Type Si solar cells with passivating electron contact: Identifying sources for efficiency limitations by wafer thickness and resistivity variation*, *Solar Energy Materials and Solar Cells* **173**, 96 (2017).
- [54] J. Y. Kwon, D. H. Lee, M. Chitambar, S. Maldonado, A. Tuteja, and A. Boukai, *High Efficiency Thin Upgraded Metallurgical-Grade Silicon Solar Cells on Flexible Substrates*, *Nano Letters* **12**, 5143 (2012).
- [55] N. Tavakoli, R. Spalding, A. Lambertz, P. Koppejan, G. Gkantzounis, C. Wan, R. Röhrich, E. Kontoleta, A. F. Koenderink, R. Sapienza, M. Florescu, and E. Alarcon-Llado, *Over 65 % Sunlight Absorption in a 1  $\mu\text{m}$  Si Slab with Hyperuniform Texture*, *ACS Photonics* **9**, 1206 (2022).
- [56] E. R. Harrison, *Fluctuations at the Threshold of Classical Cosmology*, *Physical Review D* **1**, 2726 (1970).
- [57] O. H. E. Philcox and S. Torquato, *The disordered heterogeneous universe: Galaxy distribution and clustering across length scales*, *Phys. Rev. X* **13**, 011038 (2023).

- [58] Y. Zheng, L. Liu, H. Nan, Z.-X. Shen, G. Zhang, D. Chen, L. He, W. Xu, M. Chen, Y. Jiao, and H. Zhuang, *Disordered hyperuniformity in two-dimensional amorphous silica*, *Science Advances* **6**, eaba0826 (2020).
- [59] R. H. Siddique, Y. J. Donie, G. Gomard, S. Yalamanchili, T. Merdzhanova, U. Lemmer, and H. Hölscher, *Bioinspired phase-separated disordered nanostructures for thin photovoltaic absorbers*, *Science Advances* **3**, e1700232 (2017).
- [60] M. Huang, W. Hu, S. Yang, Q.-X. Liu, and H. P. Zhang, *Circular swimming motility and disordered hyperuniform state in an algae system*, *Proceedings of the National Academy of Sciences* **118**, e2100493118 (2021).
- [61] M. A. Klatt, J. Lovrić, D. Chen, S. C. Kapfer, F. M. Schaller, P. W. A. Schönhöfer, B. S. Gardiner, A.-S. Smith, G. E. Schröder-Turk, and S. Torquato, *Universal hidden order in amorphous cellular geometries*, *Nature Communications* **10**, 811 (2019).
- [62] Z.-Q. Li, Q.-L. Lei, and Y.-Q. Ma, *Fluidization and anomalous density fluctuations in 2D Voronoi cell tissues with pulsating activity*, *Proceedings of the National Academy of Sciences* **122**, e2421518122 (2025).
- [63] Y. Jiao, T. Lau, H. Hatzikirou, M. Meyer-Hermann, Joseph C. Corbo, and S. Torquato, *Avian photoreceptor patterns represent a disordered hyperuniform solution to a multiscale packing problem*, *Physical Review E* **89**, 022721 (2014).
- [64] L. Reading-Ikkanda, *Hyperuniformity Found in Birds, Math, and Physics*, (2016), <https://www.quantamagazine.org/hyperuniformity-found-in-birds-math-and-physics-20160712>, accessed: 2026-02-06.
- [65] International Electrotechnical Commission, *IEC 60904-3, photovoltaic devices – Part 3: Measurement principles for terrestrial photovoltaic (PV) solar devices with reference spectral irradiance data*, (2019), international Standard.
- [66] AMOLF, *Detailed Balance (DB) Charts*, (2026), <https://amolf.nl/research/sustainable-energy-materials/detailed-balance-charts>, accessed: 2026-03-12.
- [67] A. Polman, M. Knight, E. C. Garnett, B. Ehrler, and W. C. Sinke, *Photovoltaic materials: Present efficiencies and future challenges*, *Science* **352**, aad4424 (2016).
- [68] S. W. Tabernig, *Charge Carrier Generation Management in Photovoltaics*, Ph.D. thesis, University of Amsterdam, Amsterdam (2022).
- [69] P. Pal, V. Swarnalatha, A. V. N. Rao, A. K. Pandey, H. Tanaka, and K. Sato, *High speed silicon wet anisotropic etching for applications in bulk micromachining: a review*, *Micro and Nano Systems Letters* **9**, 4 (2021).
- [70] I. Zobel and M. Kramkowska, *Development of etch hillocks on different Si(hkl) planes in silicon anisotropic etching*, *Surface Science* **602**, 1712 (2008).
- [71] P. Campbell and M. A. Green, *Light trapping properties of pyramidally textured surfaces*, *Journal of Applied Physics* **62**, 243 (1987).
- [72] TaiyangNews, *TaiyangNews Cell & Module Technology Trends 2025*, Tech. Rep. (TaiyangNews, 2025).

## Bibliography

- [73] M. S. Branham, W. Hsu, S. Yerci, J. Loomis, S. V. Boriskina, B. R. Hoard, S. E. Han, and G. Chen, *15.7 % Efficient 10- $\mu\text{m}$ -thick crystalline silicon solar cells using periodic nanostructures*, *Advanced Materials* **27**, 2182 (2015).
- [74] M. Xue, K. N. Nazif, Z. Lyu, J. Jiang, C.-Y. Lu, N. Lee, K. Zang, Y. Chen, T. Zheng, T. I. Kamins, M. L. Brongersma, K. C. Saraswat, and J. S. Harris, *Free-standing 2.7  $\mu\text{m}$  thick ultrathin crystalline silicon solar cell with efficiency above 12.0 %*, *Nano Energy* **70**, 104466 (2020).
- [75] N. Lee, M. Xue, J. Hong, J. Van De Groep, and M. L. Brongersma, *Multi-resonant Mie resonator arrays for broadband light trapping in ultrathin c-Si solar cells*, *Advanced Materials* **35**, 2210941 (2023).
- [76] V. Depauw, C. Trompoukis, I. Massiot, W. Chen, A. Dmitriev, P. R. I. Cabarrocas, I. Gordon, and J. Poortmans, *Sunlight-thin nanophotonic monocrystalline silicon solar cells*, *Nano Futures* **1**, 021001 (2017).
- [77] A. Gaucher, A. Cattoni, C. Dupuis, W. Chen, R. Cariou, M. Foldyna, L. Lalouat, E. Drouard, C. Seassal, P. Roca i Cabarrocas, and S. Collin, *Ultrathin Epitaxial Silicon Solar Cells with Inverted Nanopyramid Arrays for Efficient Light Trapping*, *Nano Letters* **16**, 5358 (2016).
- [78] S. Jeong, M. D. McGehee, and Y. Cui, *All-back-contact ultra-thin silicon nanocone solar cells with 13.7 % power conversion efficiency*, *Nature Communications* **4**, 2950 (2013).
- [79] E. Yablonovitch, *Statistical ray optics*, *Journal of the Optical Society of America* **72**, 899 (1982).
- [80] M. R. Gonçalves, H. Minassian, and A. Melikyan, *Plasmonic resonators: fundamental properties and applications*, *Journal of Physics D: Applied Physics* **53**, 443002 (2020).
- [81] G. Mie, *Beiträge zur Optik trüber Medien, speziell kolloidaler Metallösungen*, *Annalen der Physik* **330**, 377 (1908).
- [82] H. A. Atwater and A. Polman, *Plasmonics for improved photovoltaic devices*, *Nature Materials* **9**, 205 (2010).
- [83] A. Panda, K. Palodhi, D. Prashant, Sachchidanand, M. K. Sahu, and Y. Goswami, *Optoelectronic investigation of plasmon-enhanced silicon thin-film solar cells: effect of nanoparticles geometry, periodic density, embedding position, and dielectric environment on device performance*, *Materials Science and Engineering: B* **327**, 119253 (2026).
- [84] H. Tan, R. Santbergen, A. H. M. Smets, and M. Zeman, *Plasmonic light trapping in thin-film silicon solar cells with improved self-assembled silver nanoparticles*, *Nano Letters* **12**, 4070 (2012).
- [85] W.-J. Ho, S.-Y. Su, Y.-Y. Lee, H.-J. Syu, and C.-F. Lin, *Performance-enhanced textured silicon solar cells based on plasmonic light scattering using silver and indium Nanoparticles*, *Materials* **8**, 6668 (2015).
- [86] C. Van Lare, F. Lenzmann, M. A. Verschuuren, and A. Polman, *Dielectric scattering patterns for efficient light trapping in thin-film solar cells*, *Nano Letters* **15**, 4846 (2015).

- [87] V. Neder, S. L. Luxembourg, and A. Polman, *Efficient colored silicon solar modules using integrated resonant dielectric nanoscatteers*, Applied Physics Letters **111**, 073902 (2017).
- [88] P. Spinelli and A. Polman, *Light Trapping in Thin Crystalline Si Solar Cells Using Surface Mie Scatterers*, IEEE Journal of Photovoltaics **4**, 554 (2014).
- [89] J. Van De Groep and A. Polman, *Designing dielectric resonators on substrates: Combining magnetic and electric resonances*, Optics Express **21**, 26285 (2013).
- [90] S. A. Mann and E. Alarcón-Lladó, *Nanoscale Photovoltaics*, in *Photovoltaic Solar Energy*, edited by W. Van Sark, B. Hoex, A. Reinders, P. Verlinden, and N. J. Ekins-Daukes (Wiley, 2024) 1st ed., pp. 193–215.
- [91] A. Tiede, N. Feldman, A. Lambertz, F. Koenderink, A. Fontcuberta i Morral, and E. Alarcon-Llado, *Blob Detection for Photonic Metasurface Designing: Angular and Spectral Control of Scattered Light*, arXiv preprint (2025), 10.48550/ARXIV.2507.20857.
- [92] S. S. Wang, M. G. Moharam, R. Magnusson, and J. S. Bagby, *Guided-mode resonances in planar dielectric-layer diffraction gratings*, Journal of the Optical Society of America **A 7**, 1470 (1990).
- [93] S. S. Wang and R. Magnusson, *Theory and applications of guided-mode resonance filters*, Applied Optics **32**, 2606 (1993).
- [94] S. Torquato and F. H. Stillinger, *Local density fluctuations, hyperuniformity, and order metrics*, Physical Review E **68**, 041113 (2003).
- [95] R. D. Batten, F. H. Stillinger, and S. Torquato, *Classical disordered ground states: Superideal gases and stealth and equi-luminous materials*, Journal of Applied Physics **104**, 033504 (2008).
- [96] Y. Wang and Y. Yu, *Accurate power spectrum estimation toward Nyquist limit*, Journal of Cosmology and Astroparticle Physics **2024**, 044 (2024).
- [97] S. Torquato, *Hyperuniform states of matter*, Physics Reports **745**, 1 (2018).
- [98] M. Hejna, P. J. Steinhardt, and S. Torquato, *Nearly hyperuniform network models of amorphous silicon*, Physical Review B **87**, 245204 (2013).
- [99] M. Florescu, S. Torquato, and P. J. Steinhardt, *Designer disordered materials with large, complete photonic band gaps*, Proceedings of the National Academy of Sciences **106**, 20658 (2009).
- [100] Yik-Khoon Ee, J. Biser, W. Cao, H. Chan, R. Vinci, and N. Tansu, *Metalorganic Vapor Phase Epitaxy of III-Nitride Light-Emitting Diodes on Nanopatterned AGOG Sapphire Substrate by Abbreviated Growth Mode*, IEEE Journal of Selected Topics in Quantum Electronics **15**, 1066 (2009).
- [101] J.-W. Pan, P.-J. Tsai, K.-D. Chang, and Y.-Y. Chang, *Light extraction efficiency analysis of GaN-based light-emitting diodes with nanopatterned sapphire substrates*, Applied Optics **52**, 1358 (2013).

## Bibliography

- [102] H. Helmers, E. Lopez, O. Höhn, D. Lackner, J. Schön, M. Schauerte, M. Schachtner, F. Dimroth, and A. W. Bett, *68.9 % Efficient GaAs-Based Photonic Power Conversion Enabled by Photon Recycling and Optical Resonance*, *physica status solidi (RRL) – Rapid Research Letters* **15**, 2100113 (2021).
- [103] N. A. Kalyuzhnyy, V. M. Emelyanov, V. V. Evstropov, S. A. Mintairov, M. A. Mintairov, M. V. Nahimovich, R. A. Saliy, and M. Z. Shvarts, *Optimization of photoelectric parameters of InGaAs metamorphic laser ( $\lambda = 1064$  nm) power converters with over 50 % efficiency*, *Solar Energy Materials and Solar Cells* **217**, 110710 (2020).
- [104] F. Mooshammer, X. Xu, C. Trovatiello, Z. H. Peng, B. Yang, J. Amontree, S. Zhang, J. Hone, C. R. Dean, P. J. Schuck, and D. N. Basov, *Enabling Waveguide Optics in Rhombohedral-Stacked Transition Metal Dichalcogenides with Laser-Patterned Grating Couplers*, *ACS Nano* **18**, 4118 (2024).
- [105] O. Kuster, Y. Augenstein, C. Rockstuhl, and T. J. Sturges, *A three-dimensional polarization-insensitive grating coupler tailored for 3D nanoprining*, *IEEE Journal of Selected Topics in Quantum Electronics* **32**, 1 (2026).
- [106] Q. Cai, H. You, Q. Hou, T. Tao, Z. Xie, X. Cao, B. Liu, D. Chen, H. Lu, R. Zhang, and Y. Zheng, *Self-assembly nanopillar/superlattice hierarchical structure: boosting AlGaIn crystalline quality and achieving high-performance ultraviolet avalanche photodetector*, *ACS Applied Materials & Interfaces* **14**, 33525 (2022).
- [107] X. Guo, D. Banerjee, I. M. Asuo, F.-X. Fortier, M. A. Slimani, and S. G. Cloutier, *Plasmon-enhanced photodetectors fabricated using digital inkjet-printing on chemically nanopatterned silicon wafers*, *AIP Advances* **13**, 055309 (2023).
- [108] M.-H. Li, J.-J. Chen, Y.-S. Chen, S.-T. Lin, B.-H. Lin, M.-Y. Kuo, C.-H. Lin, H. Chen, and J. Han, *Development of a broadband photodetector utilizing ZnO nanorods with grating structure fabricated via nanoimprint lithography*, *Sensors and Actuators A: Physical* **375**, 115530 (2024).
- [109] D. Pal, T. López, and A. F. Koenderink, *Metasurface-based phosphor-converted micro-LED architecture for displays-creating guided modes for enhanced directionality*, *ACS Nano* **19**, 1238 (2025).
- [110] S. Zhang, M. Liang, Y. Yan, J. Huang, Y. Li, T. Feng, X. Zhu, Z. Li, C. Xu, J. Wang, J. Li, Z. Liu, and X. Yi, *High Luminous Efficacy Phosphor-Converted Mass-Produced White LEDs Achieved by AlN Prebuffer and Transitional-Refraction-Index Patterned Sapphire Substrate*, *Nanomaterials* **12**, 1638 (2022).
- [111] B.-Y. Lin, Y.-X. Lin, S.-J. Lin, Y.-Y. Lin, S.-H. Chen, and M.-K. Wei, *Highly enhanced light extraction for organic light emitting diodes by self-assembly microlens-array films*, *Journal of Luminescence* **263**, 119986 (2023).
- [112] Y. Kuang, M. C. Van Lare, L. W. Veldhuizen, A. Polman, J. K. Rath, and R. E. I. Schropp, *Efficient nanorod-based amorphous silicon solar cells with advanced light trapping*, *Journal of Applied Physics* **118**, 185307 (2015).
- [113] J. Buencuerpo, T. E. Saenz, M. Steger, M. Young, E. L. Warren, J. F. Geisz, M. A. Steiner, and A. C. Tamboli, *Efficient light-trapping in ultrathin GaAs solar cells using quasi-random photonic crystals*, *Nano Energy* **96**, 107080 (2022).

- [114] I. Massiot, A. Cattoni, and S. Collin, *Progress and prospects for ultrathin solar cells*, *Nature Energy* **5**, 959 (2020).
- [115] P. Campbell and M. Keevers, *Light trapping and reflection control for silicon thin films deposited on glass substrates textured by embossing*, in *Conference Record of the Twenty-Eighth IEEE Photovoltaic Specialists Conference - 2000 (Cat. No.00CH37036)* (IEEE, Anchorage, AK, USA, 2000) pp. 355–358.
- [116] A. Cordaro, J. Van De Groep, S. Raza, E. F. Pecora, F. Priolo, and M. L. Brongersma, *Antireflection high-index metasurfaces combining Mie and Fabry-Pérot resonances*, *ACS Photonics* **6**, 453 (2019).
- [117] P. Molet, J. L. Garcia-Pomar, C. Matricardi, M. Garriga, M. I. Alonso, and A. Mihi, *Ultrathin semiconductor superabsorbers from the visible to the near-infrared*, *Advanced Materials* **30**, 1705876 (2018).
- [118] M. Elshorbagy, K. Abdel-Hady, H. Kamal, and J. Alda, *Broadband anti-reflection coating using dielectric Si<sub>3</sub>N<sub>4</sub> nanostructures. Application to amorphous-Si-H solar cells*, *Optics Communications* **390**, 130 (2017).
- [119] S. T. Ha, Q. Li, J. K. W. Yang, H. V. Demir, M. L. Brongersma, and A. I. Kuznetsov, *Optoelectronic metadevices*, *Science* **386**, eadm7442 (2024).
- [120] W. Wang and L. Qi, *Light management with patterned micro- and nanostructure arrays for photocatalysis, photovoltaics, and optoelectronic and optical devices*, *Advanced Functional Materials* **29**, 1807275 (2019).
- [121] M. A. Green, *Lambertian light trapping in textured solar cells and light-emitting diodes: analytical solutions*, *Progress in Photovoltaics: Research and Applications* **10**, 235 (2002).
- [122] Z. Yu, A. Raman, and S. Fan, *Fundamental limit of nanophotonic light trapping in solar cells*, *Proceedings of the National Academy of Sciences* **107**, 17491 (2010).
- [123] A. Naqavi, F.-J. Haug, C. Battaglia, H. P. Herzig, and C. Ballif, *Light trapping in solar cells at the extreme coupling limit*, *Journal of the Optical Society of America B* **30**, 13 (2013).
- [124] S. Collin and M. Giteau, *Upper bounds on broadband absorption*, arXiv preprint (2024), 10.48550/arXiv.2407.19559, arXiv:2407.19559.
- [125] P. M. Piechulla, E. Slivina, D. Bätzner, I. Fernandez-Corbaton, P. Dhawan, R. B. Wehrspohn, A. N. Sprafke, and C. Rockstuhl, *Antireflective Huygens' Metasurface with Correlated Disorder Made from High-Index Disks Implemented into Silicon Heterojunction Solar Cells*, *ACS Photonics* **8**, 3476 (2021).
- [126] H. Hauser, K. Mühlbach, O. Höhn, R. Müller, S. Seitz, J. Rühle, S. W. Glunz, and B. Bläsi, *Tailored disorder: a self-organized photonic contact for light trapping in silicon-based tandem solar cells*, *Optics Express* **28**, 10909 (2020).
- [127] M.-C. Van Lare and A. Polman, *Optimized Scattering Power Spectral Density of Photovoltaic Light-Trapping Patterns*, *ACS Photonics* **2**, 822 (2015).

## Bibliography

- [128] G. R. Neupane, J. F. Roller, S. M. Thon, S. Fu, Z. Song, Y. Yan, and B. H. Hamadani, *Insights into Transient Photovoltage Lifetimes via Dark J–V Analysis in Perovskite Solar Cells*, *The Journal of Physical Chemistry C* **128**, 16372 (2024).
- [129] P. Lalanne, M. Chen, C. Rockstuhl, A. Sprafke, A. Dmitriev, and K. Vynck, *Disordered optical metasurfaces: basics, properties, and applications*, *Advances in Optics and Photonics* **17**, 45 (2025).
- [130] Institut Optique Graduate School, LP2N, CNRS, *RETOP: near-to-far-field transformation for radiation planewaves and guided modes (Version 10)*, (2025).
- [131] T. Wu and P. Lalanne, *Rigorous Electromagnetic Quasinormal-Mode Method Made Easy for Users*, *Laser & Photonics Reviews*, e03045 (2026).
- [132] J. P. Hugonin and P. Lalanne, *RETICOLO software for grating analysis*, (2021), arXiv:2101.00901.
- [133] A. W. Snyder and J. D. Love, *Optical waveguide theory* (Chapman and Hall, London, 1991).
- [134] M. M. Werneck, R. C. d. S. B. Allil, and F. V. B. d. Nazaré, *Fiber Bragg gratings: theory, fabrication, and applications*, Tutorial texts in optical engineering No. volume TT114 (SPIE Press, Bellingham, Washington, USA, 2017).
- [135] E. A. Muljarov, W. Langbein, and R. Zimmermann, *Brillouin-Wigner perturbation theory in open electromagnetic systems*, *EPL (Europhysics Letters)* **92**, 50010 (2010).
- [136] ANSYS, *Lumerical FDTD*, (2025), version 2025R1.
- [137] COMSOL, *COMSOL Multiphysics®*, (2023).
- [138] A. Lambertz, *Modesolver and Absorption Calculator*, (2021), github.com, accessed: 2025-12-06.
- [139] G. Maxwell, *XII. Colours in metal glasses and in metallic films*, *Philosophical Transactions of the Royal Society of London. Series A, Containing Papers of a Mathematical or Physical Character* **203**, 385 (1904).
- [140] E. Allahyarov, *Theoretical Study of Nanocomposite Permittivity with a Tunable Clustering of Inclusions*, *Advanced Theory and Simulations* **3**, 2000005 (2020).
- [141] H. A. Haus, *Waves and fields in optoelectronics*, Prentice-Hall series in solid state physical electronics (Prentice-Hall, 1984).
- [142] I. Simonsen, A. Larsen, E. Andreassen, E. Ommundsen, and K. Nord-Varhaug, *Haze of surface random systems: An approximate analytic approach*, *Phys. Rev. A* **79**, 063813 (2009).
- [143] A. Bozzola, M. Liscidini, and L. C. Andreani, *Broadband light trapping with disordered photonic structures in thin-film silicon solar cells*, *Progress in Photovoltaics: Research and Applications* **22**, 1237 (2014).

- [144] C. R. Harris, K. J. Millman, S. J. Van Der Walt, R. Gommers, P. Virtanen, D. Cournapeau, E. Wieser, J. Taylor, S. Berg, N. J. Smith, R. Kern, M. Picus, S. Hoyer, M. H. Van Kerkwijk, M. Brett, A. Haldane, J. F. Del Río, M. Wiebe, P. Peterson, P. Gérard-Marchant, K. Sheppard, T. Reddy, W. Weckesser, H. Abbasi, C. Gohlke, and T. E. Oliphant, *Array programming with NumPy*, *Nature* **585**, 357 (2020), version: 2.4.2.1.
- [145] D. Georgiev, S. V. Pedersen, R. Xie, A. Fernández-Galiana, M. M. Stevens, and M. Barahona, *RamanSPy: An open-source Python package for integrative Raman spectroscopy data analysis*, (2023), version: 0.2.10.
- [146] N. M. e. a. Haegel, *Terawatt-scale photovoltaics: Transform global energy*, *Science* **364**, 836 (2019).
- [147] W. Liu, Y. Liu, Z. Yang, C. Xu, X. Li, S. Huang, J. Shi, J. Du, A. Han, Y. Yang, G. Xu, J. Yu, J. Ling, J. Peng, L. Yu, B. Ding, Y. Gao, K. Jiang, Z. Li, Y. Yang, Z. Li, S. Lan, H. Fu, B. Fan, Y. Fu, W. He, F. Li, X. Song, Y. Zhou, Q. Shi, G. Wang, L. Guo, J. Kang, X. Yang, D. Li, Z. Wang, J. Li, S. Thoroddsen, R. Cai, F. Wei, G. Xing, Y. Xie, X. Liu, L. Zhang, F. Meng, Z. Di, and Z. Liu, *Flexible solar cells based on foldable silicon wafers with blunted edges*, *Nature* **617**, 717 (2023).
- [148] H.-F. Ou, Y.-K. Lin, and C.-H. Hsueh, *Structural and Optical Properties of Textured Silicon Substrates by Three-Step Chemical Etching*, *Langmuir* **37**, 9622 (2021).
- [149] C. Trompoukis, O. El Daif, V. Depauw, I. Gordon, and J. Poortmans, *Photonic assisted light trapping integrated in ultrathin crystalline silicon solar cells by nanoimprint lithography*, *Applied Physics Letters* **101**, 103901 (2012).
- [150] A. Bozzola, P. Kowalczewski, and L. C. Andreani, *Towards high efficiency thin-film crystalline silicon solar cells: The roles of light trapping and non-radiative recombinations*, *Journal of Applied Physics* **115**, 094501 (2014).
- [151] C. Trompoukis, I. Abdo, R. Cariou, I. Cosme, W. Chen, O. Deparis, A. Dmitriev, E. Drouard, M. Foldyna, E. G. Caurel, I. Gordon, B. Heidari, A. Herman, L. Lalouat, K.-D. Lee, J. Liu, K. Lodewijks, F. Mandorlo, I. Massiot, A. Mayer, V. Mijkovic, J. Muller, R. Orobtcchouk, G. Poulain, P. Prod'Homme, P. R. I. Cabarrocas, C. Seassal, J. Poortmans, R. Mertens, O. E. Daif, and V. Depauw, *Photonic nanostructures for advanced light trapping in thin crystalline silicon solar cells: Advanced light trapping in thin crystalline silicon solar cells*, *physica status solidi (a)* **212**, 140 (2015).
- [152] J. He, M. A. Hossain, H. Lin, W. Wang, S. K. Karuturi, B. Hoex, J. Ye, P. Gao, J. Bullock, and Y. Wan, *15 % Efficiency Ultrathin Silicon Solar Cells with Fluorine-Doped Titanium Oxide and Chemically Tailored Poly(3,4-ethylenedioxythiophene):Poly(styrenesulfonate) as Asymmetric Heterocontact*, *ACS Nano* **13**, 6356 (2019).
- [153] M. Garín, T. P. Pasanen, G. López, V. Vähänissi, K. Chen, I. Martín, and H. Savin, *Black Ultra-Thin Crystalline Silicon Wafers Reach the  $4 n^2$  Absorption Limit—Application to IBC Solar Cells*, *Small* **19**, 2302250 (2023).
- [154] J. He, P. Gao, M. Liao, X. Yang, Z. Ying, S. Zhou, J. Ye, and Y. Cui, *Realization of 13.6 % Efficiency on 20  $\mu\text{m}$  Thick Si/Organic Hybrid Heterojunction Solar Cells via Advanced Nanotexturing and Surface Recombination Suppression*, *ACS Nano* **9**, 6522 (2015).

## Bibliography

- [155] E. R. Cleveland, L. C. Hirst, S. Britzman, S. Tomasulo, M. F. Bennett, A. V. Mellor, P. Pearce, P. P. Jenkins, R. J. Walters, N. J. Ekins-Daukes, and M. K. Yakes, *Enhanced Optical Absorption in an Ultra-thin Textured Solar Cell Using Nanosphere Natural Photolithography*, in *2018 IEEE 7th World Conference on Photovoltaic Energy Conversion (WCPEC) (A Joint Conference of 45th IEEE PVSC, 28th PVSEC & 34th EU PVSEC)* (IEEE, Waikoloa Village, HI, 2018) pp. 2878–2881.
- [156] A. Cattoni, H.-L. Chen, J. Goffard, R. De Lépinau, B. Behaghel, C. Dupuis, N. Bardou, and S. Collin, *Multiresonant light trapping in ultra-thin GaAs and CIGS solar cells*, in *Light, Energy and the Environment* (OSA, Boulder, Colorado, 2017) p. PW3A.2.
- [157] E. F. Pecora, A. Cordaro, P. G. Kik, and M. L. Brongersma, *Broadband antireflection coatings employing multiresonant dielectric metasurfaces*, *ACS Photonics* **5**, 4456 (2018).
- [158] E. R. Martins, J. Li, Y. Liu, V. Depauw, Z. Chen, J. Zhou, and T. F. Krauss, *Deterministic quasi-random nanostructures for photon control*, *Nature Communications* **4**, 2665 (2013).
- [159] F. Uleman, V. Neder, A. Cordaro, A. Alù, and A. Polman, *Resonant Metagratings for Spectral and Angular Control of Light for Colored Rooftop Photovoltaics*, *ACS Applied Energy Materials* **3**, 3150 (2020).
- [160] P. Spinelli, M. Verschuuren, and A. Polman, *Broadband omnidirectional antireflection coating based on subwavelength surface Mie resonators*, *Nature Communications* **3**, 692 (2012).
- [161] C. Battaglia, C.-M. Hsu, K. Söderström, J. Escarré, F.-J. Haug, M. Charrière, M. Boccard, M. Despeisse, D. T. L. Alexander, M. Cantoni, Y. Cui, and C. Ballif, *Light Trapping in Solar Cells: Can Periodic Beat Random?* *ACS Nano* **6**, 2790 (2012).
- [162] M. L. Brongersma, Y. Cui, and S. Fan, *Light management for photovoltaics using high-index nanostructures*, *Nature Materials* **13**, 451 (2014).
- [163] Z. Yu, A. Raman, and S. Fan, *Fundamental limit of light trapping in grating structures*, *Optics Express* **18**, A366 (2010).
- [164] H.-T. Kim, K. Lee, W. Jin, H.-D. Um, M. Lee, E. Hwang, T.-H. Kwon, and K. Seo, *Phosphorescent Energy Downshifting for Diminishing Surface Recombination in Silicon Nanowire Solar Cells*, *Scientific Reports* **8**, 16974 (2018).
- [165] F. Wu, H. Lin, Z. Yang, M. Liao, Z. Wang, Z. Li, P. Gao, J. Ye, and W. Shen, *Suppression of surface and Auger recombination by formation and control of radial junction in silicon microwire solar cells*, *Nano Energy* **58**, 817 (2019).
- [166] O. Breitenstein and S. Rißland, *A two-diode model regarding the distributed series resistance*, *Solar Energy Materials and Solar Cells* **110**, 77 (2013).
- [167] A. Singh, V. Umakanth, N. Tyagi, A. K. Baghel, and S. Kumar, *Comparative study of commercial crystalline solar cells*, *Results in Optics* **11**, 100379 (2023).
- [168] W. Yang, Z. Ma, X. Tang, C. Feng, W. Zhao, and P. Shi, *Internal quantum efficiency for solar cells*, *Solar Energy* **82**, 106 (2008).

- [169] A. Smets, *Solar energy: The physics and engineering of photovoltaic conversion, technologies and systems* (Bloomsbury Publishing Plc, London, 2016).
- [170] J. Henzie, J. E. Barton, C. L. Stender, and T. W. Odom, *Large-Area Nanoscale Patterning: Chemistry Meets Fabrication*, *Accounts of Chemical Research* **39**, 249 (2006).
- [171] H.-N. Barad, H. Kwon, M. Alarcón-Correa, and P. Fischer, *Large Area Patterning of Nanoparticles and Nanostructures: Current Status and Future Prospects*, *ACS Nano* **15**, 5861 (2021).
- [172] M. A. Verschuuren, M. Megens, Y. Ni, H. Van Sprang, and A. Polman, *Large area nanoimprint by substrate conformal imprint lithography (SCIL)*, *Advanced Optical Technologies* **6**, 243 (2017).
- [173] A. Cordaro, R. Müller, S. W. Tabernig, N. Tucher, P. Schygulla, O. Höhn, B. Bläsi, and A. Polman, *Nanopatterned back-reflector with engineered near-field/far-field light scattering for enhanced light trapping in silicon-based multijunction solar cells*, *ACS Photonics* **10**, 4061 (2023).
- [174] S. Suckow, T. M. Pletzer, and H. Kurz, *Fast and reliable calculation of the two-diode model without simplifications*, *Progress in Photovoltaics: Research and Applications* **22**, 494 (2014).
- [175] S. Byrnes, *Python package TMM: Transfer Matrix Method for light propagation in multilayer films*, (2024), version: 0.2.0.
- [176] M. N. Polyanskiy, *Refractiveindex.info database of optical constants*, *Scientific Data* **11**, 94 (2024).
- [177] J. M. Zavislan, *Angular scattering from optical interference coatings: scalar scattering predictions and measurements*, *Applied Optics* **30**, 2224 (1991).
- [178] N. Shanmugam, R. Pugazhendhi, R. Madurai Elavarasan, P. Kasiviswanathan, and N. Das, *Anti-reflective coating materials: A Holistic review from PV perspective*, *Energies* **13**, 2631 (2020).
- [179] D. Kray, *Hocheffiziente Solarzellenstrukturen für kristallines Silicium-Material industrieller Qualität*, PhD Thesis, Universität Konstanz, Konstanz (2004).
- [180] S.-H. Kim, S. Y. Lee, S.-M. Yang, and G.-R. Yi, *Self-assembled colloidal structures for photonics*, *NPG Asia Materials* **3**, 25 (2011).
- [181] A. A. Kulkarni and G. S. Doerk, *Hierarchical, Self-Assembled Metasurfaces via Exposure-Controlled Reflow of Block Copolymer-Derived Nanopatterns*, *ACS Applied Materials & Interfaces* **14**, 27466 (2022).
- [182] A. A. Kulkarni and G. S. Doerk, *Thin film block copolymer self-assembly for nanophotonics*, *Nanotechnology* **33**, 292001 (2022).
- [183] T. Shastry, J. Xie, C.-H. Tung, T. Y. Lynn, A. S. Panda, A.-C. Shi, and R.-M. Ho, *Sequential Self-Assembly of Polystyrene- block -Polydimethylsiloxane for 3D Nanopatterning via Solvent Annealing*, *ACS Applied Materials & Interfaces* **16**, 40263 (2024).

## Bibliography

- [184] J. F. Galisteo-López, M. Ibisate, R. Sapienza, L. S. Froufe-Pérez, Blanco, and C. López, *Self-Assembled Photonic Structures*, *Advanced Materials* **23**, 30 (2011).
- [185] P. Innocenzi, L. Malfatti, T. Kidchob, and P. Falcaro, *Order/Disorder in Self-Assembled Mesostuctured Silica Films: A Concepts Review*, *Chemistry of Materials* **21**, 2555 (2009).
- [186] Z. Li, Q. Fan, and Y. Yin, *Colloidal Self-Assembly Approaches to Smart Nanostructured Materials*, *Chemical Reviews* **122**, 4976 (2022).
- [187] A. Simonov and A. L. Goodwin, *Designing disorder into crystalline materials*, *Nature Reviews Chemistry* **4**, 657 (2020).
- [188] G. J. Aubry, L. S. Froufe-Pérez, U. Kuhl, O. Legrand, F. Scheffold, and F. Mortessagne, *Experimental tuning of transport regimes in hyperuniform disordered photonic materials*, *Physical Review Letters* **125**, 127402 (2020).
- [189] E. Church, *The measurement of surface texture and topography by differential light scattering*, *Wear* **57**, 93 (1979).
- [190] J. C. Stover and J. E. Harvey, *Limitations of Rayleigh Rice Perturbation Theory for describing surface scatter*, (San Diego, CA, 2007) p. 66720B.
- [191] V. Lotito and T. Zambelli, *Self-assembly and nanosphere lithography for large-area plasmonic patterns on graphene*, *Journal of Colloid and Interface Science* **447**, 202 (2015).
- [192] S. Yu, C.-W. Qiu, Y. Chong, S. Torquato, and N. Park, *Engineered disorder in photonics*, *Nature Reviews Materials* **6**, 226 (2021).
- [193] D. S. Wiersma, *Disordered photonics*, *Nature Photonics* **7**, 188 (2013).
- [194] Z. Hu, C. Liu, and G. Li, *Disordered optical metasurfaces: from light manipulation to energy harvesting*, *Advances in Physics: X* **8**, 2234136 (2023).
- [195] K. Vynck, R. Pierrat, R. Carminati, L. S. Froufe-Pérez, F. Scheffold, R. Sapienza, S. Vignolini, and J. J. Sáenz, *Light in correlated disordered media*, *Reviews of Modern Physics* **95**, 045003 (2023).
- [196] O. U. Uche, S. Torquato, and F. H. Stillinger, *Collective coordinate control of density distributions*, *Physical Review E* **74**, 031104 (2006).
- [197] E. Newby, W. Shi, Y. Jiao, R. Albert, and S. Torquato, *Structural properties of hyperuniform Voronoi networks*, *Phys. Rev. E* **111**, 034123 (2025).
- [198] Y.-C. Lee, C.-F. Huang, J.-Y. Chang, and M.-L. Wu, *Enhanced light trapping based on guided mode resonance effect for thin-film silicon solar cells with two filling-factor gratings*, *Optics Express* **16**, 7969 (2008).
- [199] J. Feng, X. Wang, J. Li, H. Liang, W. Wen, E. Alvianto, C.-W. Qiu, R. Su, and Y. Hou, *Resonant perovskite solar cells with extended band edge*, *Nature Communications* **14**, 5392 (2023).
- [200] T. Khaleque and R. Magnusson, *Light management through guided-mode resonances in thin-film silicon solar cells*, *Journal of Nanophotonics* **8**, 083995 (2014).

- [201] Q.-L. Lei, M. P. Ciamarra, and R. Ni, *Nonequilibrium strongly hyperuniform fluids of circle active particles with large local density fluctuations*, Science Advances **5**, eaau7423 (2019).
- [202] W. Shi, D. Keeney, D. Chen, Y. Jiao, and S. Torquato, *Computational design of anisotropic stealthy hyperuniform composites with engineered directional scattering properties*, Physical Review E **108**, 045306 (2023).
- [203] K. Ang, J. Qiu, B. Su, Z. Li, X. Yao, Z. Wang, and X. Shu, *Deep learning-based inverse design of programmable disordered metamaterials*, International Journal of Mechanical Sciences **304**, 110712 (2025).
- [204] J. A. Finkler, Y. Lin, T. Du, J. Hu, and M. M. Smedskjaer, *Inverse design of amorphous materials with targeted properties*, arXiv preprint (2025), 10.48550/ARXIV.2509.13916.
- [205] S. J. Barcelo, A. Kim, W. Wu, and Z. Li, *Fabrication of Deterministic Nanostructure Assemblies with Sub-nanometer Spacing Using a Nanoimprinting Transfer Technique*, ACS Nano **6**, 6446 (2012).
- [206] M. Salvalaglio, M. Bouabdellaoui, M. Bollani, A. Benali, L. Favre, J.-B. Claude, J. Wenger, P. De Anna, F. Intonti, A. Voigt, and M. Abbarchi, *Hyperuniform monocrystalline structures by spinodal solid-state dewetting*, Physical Review Letters **125**, 126101 (2020).
- [207] Z. Chen, X. Wang, Y. Qi, S. Yang, J. A. N. T. Soares, B. A. Apgar, R. Gao, R. Xu, Y. Lee, X. Zhang, J. Yao, and L. W. Martin, *Self-Assembled, Nanostructured, Tunable Metamaterials via Spinodal Decomposition*, ACS Nano **10**, 10237 (2016).
- [208] Y. Lei and R. Ni, *Non-equilibrium dynamic hyperuniform states*, Journal of Physics: Condensed Matter **37**, 023004 (2025).
- [209] N. P. Balsara, C. Lin, and B. Hammouda, *Early Stages of Nucleation and Growth in a Polymer Blend*, Physical Review Letters **77**, 3847 (1996).
- [210] C. Huang, M. Moosmann, J. Jin, T. Heiler, S. Walheim, and T. Schimmel, *Polymer blend lithography: A versatile method to fabricate nanopatterned self-assembled monolayers*, Beilstein Journal of Nanotechnology **3**, 620 (2012).
- [211] Y. J. Donie, M. Smeets, A. Egel, F. Lentz, J. B. Preinfalk, A. Mertens, V. Smirnov, U. Lemmer, K. Bittkau, and G. Gomard, *Light trapping in thin film silicon solar cells via phase separated disordered nanopillars*, Nanoscale **10**, 6651 (2018).
- [212] D. Laughlin, E. and W. Soffa, *Spinodal Structures*, ASM Handbook, Vol. 9 (American Society for Metals, 1985).
- [213] F. S. Bates, *Polymer-Polymer Phase Behavior*, Science **251**, 898 (1991).
- [214] S. Walheim, *Micrometer and Sub-Micrometer Structure Formation of Phase Separating Polymer Films / Mikrometer und Submikrometer Strukturierung phasenseparierender Polymerfilme*, Dissertation zur Erlangung des akademischen Grades des Doktors der Naturwissenschaften (Dr. rer. nat.), Universität Konstanz, Konstanz (2000).
- [215] S. Ebbens, R. Hodgkinson, A. J. Parnell, A. Dunbar, S. J. Martin, P. D. Topham, N. Clarke, and J. R. Howse, *In Situ Imaging and Height Reconstruction of Phase Separation Processes in Polymer Blends during Spin Coating*, ACS Nano **5**, 5124 (2011).

## Bibliography

- [216] S. Walheim, M. Böltau, J. Mlynek, G. Krausch, and U. Steiner, *Structure Formation via Polymer Demixing in Spin-Cast Films*, *Macromolecules* **30**, 4995 (1997).
- [217] S. Walheim, E. Schaffer, J. Mlynek, and U. Steiner, *Nanophase-Separated Polymer Films as High-Performance Antireflection Coatings*, *Science* **283**, 520 (1999).
- [218] K. Tanaka, A. Takahara, and T. Kajiyama, *Film Thickness Dependence of the Surface Structure of Immiscible Polystyrene/Poly(methyl methacrylate) Blends*, *Macromolecules* **29**, 3232 (1996).
- [219] A. Shultz and P. Flory, *Phase equilibria in polymer—solvent systems*1, 2, *Journal of the American Chemical Society* **74**, 4760 (1952).
- [220] M. Rubinstein and R. H. Colby, *Polymer Physics* (Oxford University Press Oxford, 2003).
- [221] N. P. Balsara, L. J. Fetters, N. Hadjichristidis, D. J. Lohse, C. C. Han, W. W. Graessley, and R. Krishnamoorti, *Thermodynamic interactions in model polyolefin blends obtained by small-angle neutron scattering*, *Macromolecules* **25**, 6137 (1992).
- [222] C. E. Maher and K. A. Newhall, *Characterizing the hyperuniformity of disordered network metamaterials*, *Physical Review E* **111**, 065420 (2025).
- [223] L. Zhong, S. Mao, and Y. Jiao, *Modeling disordered hyperuniform heterogeneous materials: Microstructure representation, field fluctuations and effective properties*, *Acta Materialia* **296**, 121218 (2025).
- [224] G. Bradski, *The OpenCV Library*, *Dr. Dobb's Journal of Software Tools* (2000).
- [225] M. Renner and G. V. Freymann, *Spatial correlations and optical properties in three-dimensional deterministic aperiodic structures*, *Scientific Reports* **5**, 13129 (2015).
- [226] S. A. Mann, R. R. Grote, R. M. Osgood, and J. A. Schuller, *Dielectric particle and void resonators for thin film solar cell textures*, *Optics Express* **19**, 25729 (2011).
- [227] C. F. Bohren and D. R. Huffman, *Absorption and Scattering of Light by Small Particles*, 1st ed. (Wiley, 1998).
- [228] C. J. Chen, *Physics of Solar Energy*, 1st ed. (Wiley, 2011).
- [229] P. Klapetek, D. Nečas, and C. Anderson, *Gwyddion data visualization and analysis software*, (2025), version: 2.68.

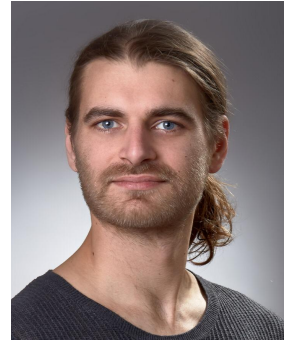
# Curriculum Vitae

## Personal Information

Alexander Lambertz

4lambertz@gmail.com  
linkedin.com/in/alex-lambertz

1990-07-08 Born in Cologne, Germany



## Education

- 2008 Lawrence North High School Diploma  
7802 Hague Road, Indianapolis, IN 46256, U.S. of America
- 2010 Otto-Hahn Gymnasium High School Diploma, Bergisch Gladbach, Germany
- 2013 Industrial Mechanic Diploma, Chamber of Commerce, Krefeld, Germany
- 2019 Bachelor of Science in Physics  
Rheinische Friedrich-Wilhelms-Universität Bonn  
*Thesis* Entwicklung eines grossflächigen Szintillator-Triggersystems mit wellenlängenschiebenden Fasern für Neutronendetektoren  
*Supervisors* Dr. Markus Köhli & Prof. dr. Jochen Kaminski & Prof. dr. Klaus Desch
- 2021 Master of Science in Physics  
Joint degree VU University Amsterdam & University of Amsterdam, The Netherlands  
*Thesis* Hyperuniform Disordered Light Trapping for Ultra-thin Solar Cells using Substrate Conformal Imprint Lithography  
*Supervisors* Dr. Nasim Tavakoli & Prof. dr. Alarcón-Lladó
- 2026 Ph.D. Candidate in Physics  
WZI Insitute of Physics, University of Amsterdam, The Netherlands  
NWO-Institute AMOLF, Amsterdam, The Netherlands  
*Thesis* Light Trapping in Solar Cells using Disordered Hyperspectral Uniformity  
*Promoters* Prof. dr. E. Alarcón-Lladó  
Dr. J. van de Groep





